XANTHORRHIZOL DERIVATIVES AS HYALURONIDASE AND LIPOXYGENASE INHIBITORS: DESIGN, SYNTHESIS, *IN VITRO* AND *IN SILICO* ANALYSES

BY

TENGKU KAMILAH BINTI TENGKU NAZMI

A dissertation submitted in fulfilment of the requirement for the degree of Master of Science in Chemistry.

Kulliyyah of Science
International Islamic University Malaysia

NOVEMBER 2024

ABSTRACT

Hyaluronidase (Hyal) and lipoxygenase (LOX) enzymes produced inflammatory inducers in the human body, making them suitable target for the design of anti-inflammatory agents. Xanthorrhizol (XNT) is a sesquiterpenoid isolated from *Curcuma xanthorrhiza* that possesses anti-inflammatory properties and holds promise as therapeutic candidate. The potential of XNT as anti-inflammatory agent can be further explored through modification of its structure. The use of computational tools can optimise the structure of XNT by precisely targeting Hyal and LOX and enhance its anti-inflammatory action. The objective of this study was to virtually screen and design potential XNT derivatives as new Hyal-1 and LOX-3 inhibitors from in-house database and *in silico* fragment-based drug design (FBDD) approaches, respectively. Then, the promising derivatives from both approaches were synthesised and characterised, followed by biological evaluation through *in vitro* enzyme inhibitory assays. The most active derivative against the enzyme in *in vitro* studies was subjected to further analysis using molecular dynamics (MD) simulation. Thirty XNT derivatives obtained from in-house database were virtually screened against Hyal-1 enzyme *via* molecular docking. Benzyl xanthorrhizyl ether **(76)** exhibited stronger binding energy (-8.0 kcal/mol) against Hyal-1 enzyme compared to XNT (-6.8 kcal/mol) and proposed to be synthesised as Hyal-1 inhibitor. Additionally, the *in silico* FBDD generated five XNT derivatives as potential Hyal-1 inhibitors, specifically (2-pyridinyl)methyl xanthorrhizyl ether **(102)**, 4-nitrobenzyl xanthorrhizyl ether **(103)**, 3-trifluoromethylbenzyl xanthorrhizyl ether **(104)**, (2-tetrahydro-2*H*-pyranyl)methyl xanthorrhizyl ether **(105)** and (2-tetrahydrofuranyl)methyl xanthorrhizyl ether **(106)**. Among the six proposed inhibitors for Hyal-1 enzyme, five derivatives **(76**, **102-105)** were successfully synthesised and characterised using spectroscopic analyses. Meanwhile, the synthesis of derivative **(106)** yielded an unexpected product, characterised as propyl xanthorrhizyloxyacetate **(117)**. The *in vitro* analysis against Hyal-1 enzyme showed that derivative **(102)** was the most active against Hyal-1 enzyme with IC_{50} value of 44.54 µg/mL compared to XNT (IC_{50} = 203.56 µg/mL). The MD simulation revealed that derivative **(102)** displayed stable interaction in the binding site of Hyal-1 enzyme throughout 100 ns simulation. Derivative **(76)** was identified as potential LOX-3 inhibitor as it exerts stronger binding energy (-8.6 kcal/mol) compared to XNT (-7.7 kcal/mol). The design of XNT derivatives through *in silico* FBDD approach generated four XNT derivatives as LOX-3 inhibitors, however, their synthesis were unsuccessful. Derivative **(76)** was synthesised, and tested *via in vitro* LOX-3 inhibitory assay, where it displayed weaker activity (IC_{50} = 619.92 µg/mL) compared to XNT (IC_{50} = 142.34 µg/mL). These findings suggest that XNT derivatives, particularly (2-pyridinyl)methyl xanthorrhizyl ether **(102)** showed promising anti-inflammatory activities through inhibition of Hyal-1 enzyme.

ملخص البحث

إنزيمات الهيالورونيداز (Hyal) والليبوكسجيناز (LOX) تنتج محفزات التهابية في جسم الإنسان، مما يجعلها هدفًا مناسبًا لتصميم عوامل مضادة للالتهابات. يُعتبر الزانثورايزول (XNT) مركبًا سيسكيتيربينويديًا معزولًا من الكركم الزانثورايزا يمتلك خصائص مضادة للالتهابات ويعد واعدًا كمرشح علاجي. يمكن استكشاف إمكانات XNT كعامل مضاد للالتهابات بشكل أكبر من خلال تعديل هيكله. يمكن استخدام الأدوات الحاسوبية لتحسين هيكل XNT عن طريق استهداف إنزيمات Hyal و LOXبدقة وتعزيز عمله المضاد للالتهابات. كان الهدف من هذه الدراسة هو الفحص الافتراضي وتصميم مشتقات XNT المحتملة كمثبطات جديدة لإنزيمات Hyal-1 و LOX-3من قاعدة بيانات داخلية ومنهجيات تصميم الأدوية القائمة على الشظايا الحاسوبية (FBDD) على التوالي. ثم تم تصنيع وتوصيف المشتقات الواعدة من كلا النهجين، تلاها تقييم بيولوجي من خلال اختبارات تثبيط الإنزيم في المختبر. تم إخضاع المشتق الأكثر نشاطًا ضد الإنزيم في الدراسات المختبرية لمزيد من التحليل باستخدام محاكاة الديناميات الجزيئية .(MD) تم فحص ثلاثين مشتقًا من XNT من قاعدة البيانات الداخلية افتراضيًا ضد إنزيم Hyal-1 عبر الربط الجزيئي. أظهر بنزيل زانثورايزيل إيثر (**76**) طاقة ارتباط أقوى (-8.0 كيلو كالوري/مول) ضد إنزيم Hyal-1 مقارنة بـ XNT (-6.8 كيلو كالوري/مول) واقترح تصنيعه كمثبط لـ .Hyal-1 بالإضافة إلى ذلك، أنتجت FBDD الحاسوبية خمسة مشتقات من XNT كمثبطات محتملة لـHyal-1 ، وهي (2-بيريدينيل)ميثيل زانثورايزيل إيثر (**102**)، 4-نيتروبنزيل زانثورايزيل إيثر (**103**)، 3-تريفلوروميثيلبنزيل زانثورايزيل إيثر (**104**)، (-2)تتراهيدرو-2H-بيرانيل(ميثيل زانثورايزيل إيثر (**105**) و(2-تتراهيدروفورانيل)ميثيل زانثورايزيل إيثر (**106**). من بين

المثبطات الستة المقترحة لإنزيمHyal-1 ، تم تصنيع وتوصيف خمسة مشتقات بنجاح باستخدام التحليلات الطيفية. في الوقت نفسه، أسفرت عملية تصنيع المشتق (**106**) عن منتج غير متوقع، تم توصيفه ك بروبيل زانثورايزيلوكسي أسيتات (**117**). أظهر التحليل في المختبر ضد إنزيم Hyal-1 أن المشتق (**102**) كان الأكثر نشاطًا ضد إنزيم Hyal-1 بقيمة IC_{50} بلغت 44.54 ميكروغرام/مل مقارنة بـ XNT (203.56 ميكروغرام/مل). كشفت محاكاة MD أن المشتق (**102**) أظهر تفاعلًا مستقرًا في موقع ارتباط إنزيم Hyal-1 طوال محاكاة 100 نانوثانية. مشتق (**76**) تم تحديده كمثبط محتمل لإنزيم3- LOX حيث يظهر طاقة ارتباط أقوى (-8.6 كيلو كالوري/مول) مقارنة بـ XNT (-7.7 كيلو كالوري/مول). تم تصميم مشتقات XNT من خلال نهج FBDD باستخدام الحاسوب، مما أنتج أربعة مشتقات XNT كمثبطات لـ LOX-3، ومع ذلك، لم تنجح عملية التخليق. تم تخليق مشتق (**76**) واختباره في اختبار تثبيط LOX-3 في المختبر، حيث أظهر نشاطًا أضعف (IC_{50} = 619.92 ميكروغرام/مل) مقارنة بـ XNT (IC_{50} = 142.34 ميكروغرام/مل). تشير هذه النتائج إلى أن مشتقات XNT، وخاصة (2-بيريدينيل) ميثيل زانثورهيزيل إيثر (**102**) أظهرت أنشطة واعدة مضادة للالتهابات من خلال تثبيط إنزيم Hyal-1.

APPROVAL PAGE

I certify that I have supervised and read this study and that in my opinion, it conforms to acceptable standards of scholarly presentation and is fully adequate, in scope and quality, as a dissertation for the degree of Master of Science in Chemistry.

…….
Nurul Iman Aminudin
Supervisor

…….
Nurasyikin Hamzah
Co-Supervisor

…….
Mazura Md Pisar
Co-Supervisor

I certify that I have read this study and that in my opinion it conforms to acceptable standards of scholarly presentation and is fully adequate, in scope and quality, as a dissertation for the degree of Master of Science in Chemistry.

…….
Zalikha Ibrahim
Examiner

…….
Noor Hidayah Pungot
External Examiner

This dissertation was submitted to the Department of Chemistry and is accepted as a fulfilment of the requirement for the degree of Master of Science in Chemistry.

…….
Mohammad Wafiuddin Ismail
Head, Department of Chemistry

This dissertation was submitted to the Kulliyyah of Science and is accepted as a fulfillment of the requirement for the degree of Master of Science in Chemistry.

…….
Zarina Zainuddin
Dean, Kulliyyah of Science

DECLARATION

I hereby declare that this dissertation is the result of my own investigations, except where otherwise stated. I also declare that it has not been previously or concurrently submitted as a whole for any other degrees at IIUM or other institutions.

Tengku Kamilah binti Tengku Nazmi

Signature…… Date…8 NOVEMBER 2024……

INTERNATIONAL ISLAMIC UNIVERSITY MALAYSIA

DECLARATION OF COPYRIGHT AND AFFIRMATION OF FAIR USE OF UNPUBLISHED RESEARCH

XANTHORRHIZOL DERIVATIVES AS HYALURONIDASE AND LIPOXYGENASE INHIBITORS: DESIGN, SYNTHESIS, *IN VITRO* AND *IN SILICO* ANALYSES

I declare that the copyright holder of this thesis/dissertation are jointly owned by the student and IIUM.

No part of this unpublished research may be reproduced, stored in a retrieval system, or transmitted, in any form or by any means, electronic, mechanical, photocopying, recording or otherwise without prior written permission of the copyright holder except as provided below

1. Any material contained in or derived from this unpublished research may only be used by others in their writing with due acknowledgement.

2. IIUM or its library will have the right to make and transmit copies (print or electronic) for institutional and academic purpose.

3. The IIUM library will have the right to make, store in a retrieval system and supply copies of this unpublished research if requested by other universities and research libraries.

By signing this form, I acknowledged that I have read and understand the IIUM Intellectual Property Right and Commercialization policy.

Affirmed by Tengku Kamilah binti Tengku Nazmi

…… 8 NOVEMBER 2024

Signature Date

This dissertation is dedicated to my beloved family.

ACKNOWLEDGEMENTS

In the name of Allah, the Most Gracious and Most Merciful.

It took me immense hard work, undying passion, and dedication to complete this dissertation. First and foremost, I thank the Almighty Allah for giving me the strength and courage to complete this research entitled "Xanthorrhizol Derivatives as Hyaluronidase and Lipoxygenase Inhibitors: Design, Synthesis, *In Vitro* and *In Silico* Analyses".

I would also like to express my deepest and sincere gratitude to my dearest supervisor, Asst. Prof. Dr. Nurul Iman binti Aminudin, for guiding me throughout the entire process of this research. I truly appreciate her dedication, encouragement, and patience to help me in completing this study. I would also like to extend my gratitude towards my co-supervisors, Asst. Prof. Dr. Nurasyikin binti Hamzah, and Dr. Mazura binti Md. Pisar. Without their constant guidance and help, this journey would not have been possible, and I would not have gained all the knowledge.

My appreciation also goes to the academic and laboratory staffs of Department of Chemistry, Kulliyyah of Science especially Br. Romizan, Sr. Azrain, Br. Arif, Br. Lazuardi, Sr. Hafiah and Br. Ikram. Not to forget the members of Biology Lab, Natural Product Division, Forest Research Institute Malaysia for the kind and warm hospitality during my short attachment there. I am also grateful to Jabatan Perkhidmatan Awam (JPA) for giving me the financial assistance to pursue my Master's degree in IIUM.

Most of all, my utmost grateful to my parents (Nor Akma binti Mohd Amin and Tengku Nazmi bin Tengku Sulaiman) and my siblings as their unwavering support, encouragement, and sacrifices have been the driving force in my academic pursuits.

Special thanks to all my postgraduate friends, especially Khadijah, Aisyah, Rashidah, Sadina, Amanina, Lisa, and Farisya, who are always there with me, rain, or shine upon completing the research. I would also like to use this opportunity to thank my beloved friends; Ainnad, Fathanah, Nazira, Aishah, Farah, Aqil, and Faiz for always giving me immense emotional support from afar. May all of us be blessed with success and love. Amin, Insya-Allah.

TABLE OF CONTENTS

Abstract……..ii
Abstract in Arabic……..iii
Approval Page …..……..v
Declaration…….....vii
Copyright……viii
Dedication……..ix
Acknowledgements…….x
Table Of Contents……..xi
List Of Tables……...xiv
List Of Figures…….xvi
List Of Schemes……xx
List Of Symbols……...xxi
List Of Abbreviations……..……...xxii
List Of Appendices……...xxvii

CHAPTER ONE: INTRODUCTION…….....1
1.1 Research Introduction…….....1
1.2 Problem Statement…….....3
1.3 Research Objectives…….....4
1.4 Research Significance……..……...4
1.5 Research Hypothesis…….....5

CHAPTER 2: LITERATURE REVIEW…….....6
2.1 Fragment-Based Drug Design (FBDD) …….....6
2.1.1 Experimental Approach in FBDD……...7
2.1.2 *In silico* Approach in FBDD……...8
2.1.3 LigBuilder software……..12
2.2 Hyaluronidase Enzyme..…….....14
2.2.1 Hyaluronidase Inhibitors……...15
2.3 Lipoxygenase Enzyme..…….....19
2.3.1 Lipoxygenase Inhibitors……20
2.4 Xanthorrhizol Derivatives…...…….....25
2.5 Anti-Inflammatory Activities of Xanthorrhizol and its Derivatives….30

CHAPTER THREE: METHODOLOGY…….....33
3.1 Chemicals and General Instrumentations……..…….... 33
3.2 Plant Materials..……..... 35
3.3 Computational Tools…….....35
3.4 Identification of Xanthorrhizol Derivatives as Hyal-1 and LOX-3 Inhibitors……...35
3.4.1 Molecular Docking of Xanthorrhizol Derivatives against Hyal-1 and LOX-3 enzymes.…….……..... 36
3.4.2 *In Silico* Fragment-Based Drug Design (FBDD)…….……37

3.5 *In Silico* Drug-Likeness and Absorption Properties……..……....39
3.6 Synthesis and Characterisation of Xanthorrhizol Derivatives……...39
3.6.1 Isolation and Purification of Xanthorrhizol from *C. Xanthorrhiza*…….39
3.6.1.1 Acetylation Reaction on CXED5 Fraction……....40
3.6.1.2 Hydrolysis of Xanthorrhizyl Acetate **(64)** …..…….41
3.6.2 Synthesis of Xanthorrhizol Derivatives as Hyal-1 Inhibitors **(76**, **102-105**, **117)**…….…….. 42
3.6.2.1 Benzyl Xanthorrhizyl Ether **(76)**……...43
3.6.2.2 (2-Pyridinyl)methyl Xanthorrhizyl Ether **(102)**……..…44
3.6.2.3 4-Nitrobenzyl Xanthorrhizyl Ether **(103)**……..45
3.6.2.4 3-Trifluoromethylbenzyl Xanthorrhizyl Ether **(104)**….46
3.6.2.5 (2-Tetrahydro-2H-pyranyl)methyl Xanthorrhizyl Ether **(105)** …….……...47
3.6.2.6 Propyl Xanthorrhizyloxyacetate **(117)**……..48
3.6.3 Attempted Synthesis Of Xanthorrhizol Derivatives **(107-110)**....49
3.6.3.1 2-(Xanthorrhizyloxy)ethyl Carbamide **(107)**……52
3.6.3.2 *N*-(2-(xanthorrhizyloxy)ethyl)-1*H*-imidazole-4-carboxamide **(108)**…… 52
3.6.3.3 *N*-(2-(xanthorrhizyloxy)ethyl)-3-aminopropanamide **(109)**……..53
3.6.3.4 3-(Xanthorrhizyloxy)propyl 1*H*-imidazole-4-carboxylate **(110)**…….. 54
3.7 Biological Evaluations of Xanthorrhizol Derivatives……55
3.7.1 *In Vitro* Hyal-1 Enzyme Assay…….…… 55
3.7.2 *In Vitro* LOX-3 Enzyme Assay……..…….. 56
3.7.3 Statistical Analysis...…….57
3.8 Molecular Dynamics Simulation……...……57

CHAPTER 4: DESIGN OF XANTHORRHIZOL DERIVATIVES AS POTENTIAL HYALURONIDASE AND LIPOXYGENASE INHIBITORS….59
4.1 Introduction……...59
4.2 Virtual Screening of In-house Database…….……..59
4.2.1 Virtual Screening of Xanthorrhizol Derivatives Against Hyal-1 Enzyme……...……..54
4.2.2 Virtual Screening of Xanthorrhizol Derivatives Against LOX-3 Enzyme…….……....65
4.2.3 *In Silico* Drug-Likeness and Absorption Profiles of Derivatives **(63-81**, **91- 101)**……..……...…70
4.3 *In Silico* Fragment-Based Drug Design (FBDD) of Xanthorrhizol Derivatives…….……...76
4.3.1 Design of Xanthorrhizol Derivatives as Hyal-1 Inhibitors…...77
4.3.2 Design of Xanthorrhizol Derivatives as LOX-3 Inhibitors…...84
4.3.3 *In Silico* Drug-Likeness and Absorption Profiles of Designed Xanthorrhizol Derivatives **(102-110)**…….……...91

CHAPTER 5: SYNTHESIS, BIOLOGICAL ACTIVITIES AND MOLECULAR DYNAMICS SIMULATION OF XANTHORRHIZOL DERIVATIVES…….94
5.1 Introduction……...94
5.2 Isolation and Purification of Xanthorrhizol **(1)** from *C. Xanthorrhiza* Essential Oil..…….…….....96
5.3 Synthesis of Xanthorrhizol Derivatives **(76**, **102-105**, **117)** as Hyal-1 Inhibitors…….…….……...100
5.4 Attempted Synthesis of Xanthorrhizol Derivatives **(107-110)** as LOX-3 Inhibitors……..……...……..111
5.5 Biological Activities of Xanthorrhizol Derivatives...……..……116
5.5.1 *In Vitro* Inhibitory Activity Against Hyal-1 Enzyme…….116
5.5.2 *In Vitro* Inhibitory Activity Against LOX-3 Enzyme…….122
5.6 Molecular Dynamics Simulation of Derivative **(102)** Against Hyal-1 Enzyme……..……123

CHAPTER 6: CONCLUSIONS AND RECOMMENDATIONS…… 131
6.1 Conclusions……..…132
6.2 Future Works Recommendations……133

REFERENCES……..…….. 133

APPENDICES……...148

LIST OF TABLES

Table 4.1	Docking results of XNT derivatives (**63-81**, **91-101**) against Hyal-1 enzyme	62-63
Table 4.2	Docking results of XNT derivatives (**63-81**, **91-101**) against LOX-3 enzyme	67-68
Table 4.3	Optimum range for physicochemical properties by SwissADME.	71
Table 4.4	*In silico* drug-likeness and absorption profile for XNT derivatives (**63-81**, **91-101**)	74-75
Table 4.5	Cavity results for Hyal-1 enzyme	78
Table 4.6	Classification of chemical groups for top fifty derivatives as Hyal-1 inhibitors	79
Table 4.7	Docking result of derivatives **(102-106)** against Hyal-1 enzyme	81
Table 4.8	CAVITY results for LOX-3 enzyme	84
Table 4.9	Classification of chemical groups for top fifty derivatives as LOX-3 inhibitors	86
Table 4.10	Docking result of derivatives **(107-110)** against LOX-3 enzyme	88
Table 4.11	*In silico* drug-likeness and absorption profile for derivatives **(102-110)**	93
Table 5.1	^{1}H and ^{13}C NMR data for xanthorrhizyl acetate **(64)** (δ in ppm, *J* in Hz)	96-97
Table 5.2	^{1}H and ^{13}C NMR data for XNT (**1**) (δ in ppm, *J* in Hz)	100
Table 5.3	^{1}H NMR derivatives **(76**, **102-104)** (δ in ppm, *J* in Hz)	102-103
Table 5.4	Hyal-1 inhibitory activities	118
Table 5.5	LOX-3 inhibitory activities	121

Table 5.6	Average RMSD and R_g values of derivative **(102)** and apigenin	125
Table 5.7	Distance between derivative **(102)** and apigenin **(17)** with the binding site of Hyal-1 enzyme	129

LIST OF FIGURES

Figure 2.1	Fragment-based drug design strategies for optimisation. A) Fragment growing, B) Fragment linking, C) Fragment merging. (Adopted from de Souza Neto et al. (2020))	7
Figure 2.2	General workflow for design strategies in LigBuilder (adapted from Qing et al., 2021)	13
Figure 2.3	a) Growing strategy b) Linking strategy (adapted from Wang et al. (2000))	14
Figure 2.4	Active site of Hyal-1 enzyme. The active site residues are coloured in maroon.	15
Figure 2.5	Active site of LOX-3 enzyme. The active site residues are coloured in yellow. Red ball represents non-heme iron.	20
Figure 4.1	A small library of reported XNT derivatives with modification at R_1 to R_4 positions.	59
Figure 4.2	Docking conformation of XNT **(1)** and its derivatives **(63-81**, **91-101)** in Hyal-1 binding site. The active site residues are coloured in maroon.	61
Figure 4.3	a) 3D docking pose of XNT **(1)** (blue) in Hyal-1 enzyme binding site; b) 2D representation for interactions of XNT **(1)** with amino acid residues of Hyal-1.	61
Figure 4.4	a) 3D docking pose of derivative (**75)** (green), (**92)** (white) and (**93)** (orange) in Hyal-1 enzyme binding site; b) 2D representation for interactions derivative (**75)** with amino acid residues of Hyal-1.	63
Figure 4.5	Summary for virtual screening of XNT derivatives for Hyal-1 enzyme.	65
Figure 4.6	a) 3D docking pose of derivative (**76)** (yellow) in Hyal-1 enzyme binding site; b) 2D representation for interactions of derivative **(76)** with amino acid residues of Hyal-1.	65

Figure 4.7	Docking conformation of XNT **(1)** and its derivatives **(63-81**, **91-101)** in LOX-3 binding site. The active site residues are coloured in yellow.	66
Figure 4.8	a) 3D docking pose of XNT **(1)** (blue) in LOX-3 enzyme binding site; b) 2D representation for interactions of XNT **(1)** with amino acid residues of LOX-3.	66
Figure 4.9	a) 3D docking pose of (**81)** (magenta) in LOX-3 enzyme binding site; b) 2D representation for interactions of **(81)** with amino acid residues of LOX-3.	68
Figure 4.10	Summary for virtual screening of XNT derivatives against LOX-3 enzyme.	70
Figure 4.11	a) 3D docking pose of derivative (**76)** (yellow) in LOX-3 enzyme binding site; b) 2D representation for interactions of derivative **(76)** with amino acid residues of LOX-3.	70
Figure 4.12	Schematic diagram of steric hindrance posed by XNT **(1)** seed structure in a) Hyal-1; b) LOX-3 binding site. The dashed line in green represents the hydrogen bonding interactions.	76
Figure 4.13	Approaches to generate seed structure for XNT **(1)** optimisation.	77
Figure 4.14	a) Overlay of Hyal-1 active site and cavity **1** surface (cyan); b) Alignment of cavity **1** surface (cyan), amino acid residues of cavity **1** (yellow) and active residues of Hyal-1 (maroon).	78
Figure 4.15	The structure of generated derivatives that inspired derivatives **(102-106)**	80
Figure 4.16	Docking conformation of derivatives **(102-106)** in Hyal-1 binding site. The active site residues are coloured in maroon.	81
Figure 4.17	(a) 3D docking pose of derivative **(104)** (green) in Hyal-1 enzyme binding site; (b) 2D representation for interactions of derivative **(104)** with amino acid residues with Hyal-1	82
Figure 4.18	2D representation for interactions with amino acid residues of Hyal-1 for derivatives; a) **(102)**, b) **(103)**, c) **(105)**, d) **(106)**	83

Figure 4.19	Overall processes for the design of Hyal-1 inhibitors using *in silico* FBDD approach.	83
Figure 4.20	a) Overlay of LOX-3 active site and cavity **3** surface (orange); b) Alignment of cavity **3** surface (orange), amino acid residues of cavity **3** (green) and binding site of LOX (yellow).	85
Figure 4.21	The structure of generated derivatives that inspired derivatives **(102-106)**	87
Figure 4.22	Docking conformation of derivatives **(107-110)** in LOX-3 binding site. The active site residues are coloured in yellow. Red ball represents non-heme iron.	88
Figure 4.23	(a) 3D docking pose of derivative **(108)** (purple) in LOX-3 enzyme binding site; (b) 2D representation for interactions of derivative **(108)** with amino acid residues of LOX-3.	89
Figure 4.24	2D representation for interactions with amino acid residues of LOX-3 for; a) derivative **(107)**, b) derivative **(109)**, c) derivative **(110)**.	90
Figure 4.25	Overall processes for the design of LOX-3 inhibitors using *in silico* FBDD approach.	90
Figure 5.1	Acetylation reaction of XNT **(1)**	95
Figure 5.2	Hydrolysis of xanthorrhizyl acetate **(64)**	93
Figure 5.3	Key HMBC (arrows) and COSY (bold) correlations of derivative **(117)**	108
Figure 5.4	Competitive inhibition of Hyal-1 activity between HA and inhibitor	117
Figure 5.5	Formation of 13*S*-HPODE from linoleic acid by LOX enzyme	120
Figure 5.6	Schematic diagram of binding pose of a) derivative **(76)** and b) 13*S*-HPODE substrate in the LOX enzyme binding pocket. The dashed line in green represents the hydrogen bonding interactions (Adapted from Ng et al. (2014)).	122
Figure 5.7	RMSD plot for a) Hyal-1-ligand complexes; b) ligand only	124

Figure 5.8	Radius of gyration plot for derivative **(102)** and apigenin **(17)**	125
Figure 5.9	RMSF plot for derivative **(102)** and apigenin **(17)**. The important amino acid residues of Hyal-1 enzyme were shown in **bold**.	126
Figure 5.10	RMSF values of important residues for Hyal-1 enzyme	126
Figure 5.11	Number of hydrogen bonds of derivative **(102)** and apigenin **(17)**	127
Figure 5.12	Hydrogen bond occupancy analysis for derivative **(102)** and apigenin **(17)**	128
Figure 5.13	Distance graph of derivative **(102)** and apigenin **(17)** with Hyal-1 enzyme	129
Figure 5.14	Visualisation state of derivative **(102)** (yellow) in binding site of Hyal-1 enzyme over 100 ns simulation.	130

LIST OF SCHEMES

Scheme 3.1	General scheme for the synthesis of XNT derivatives **(76, 102-105**, **117)**	43
Scheme 3.2	Reaction scheme for synthesis of derivative **(107)**	50
Scheme 3.3	Reaction scheme for synthesis of derivative **(108)**	50
Scheme 3.4	Reaction scheme for synthesis of derivative **(109)**	51
Scheme 3.5	Reaction scheme for synthesis of derivative **(110)**	52
Scheme 5.1	Reaction mechanism for acetylation of XNT **(1)**	95
Scheme 5.2	Reaction mechanism of hydrolysis of xanthorrhizyl acetate **(64)**	98
Scheme 5.3	Fragmentation pattern of XNT **(1)**	99
Scheme 5.4	Reaction mechanism for synthesis of derivatives **(76**, **102-104)**	101
Scheme 5.5	Fragmentation pattern of derivative **(117)**	109
Scheme 5.6	Proposed reaction mechanism for formation of derivative **(117)**	110
Scheme 5.7	Attempted synthesis of derivative **(107)**	111
Scheme 5.8	Reaction mechanism for synthesis of compound **(121)**	113
Scheme 5.9	Attempted synthesis of compound **(124)**	115
Scheme 5.10	Attempted synthesis of compound **(126)**	116

LIST OF SYMBOLS

ºC	-	degree Celsius
δ	-	chemical shift
J	-	coupling constant
Å	-	angstrom
$Å^2$	-	angstrom squared
%	-	percent
µ	-	micro
α	-	alpha
β	-	beta
±	-	plus-minus
γ	-	gamma

LIST OF ABBREVIATIONS

µg/mL	-	microgram per millilitre
^{13}C	-	Carbon
^{1}H	-	Proton
µL	-	microlitre
µM	-	micromolar
13*S*-HPODE	-	(9*Z*,11*E*)-(13*S*)-13-hydroperoxyoctadeca-9,11-dienoate
Ac	-	Acetate
ACFIS	-	Auto Core Fragment *in silico* Screening
ADME	-	Absorption, distribution, metabolism, excretion
ATR-IR	-	Attenuated Total Reflectance Infrared
Boc	-	*Tert*-butyl
br	-	broad
BSA	-	Bovine serum albumin
Bz	-	Benzoate
c	-	Concentration
CADD	-	Computer aided drug design
CC	-	Column chromatography
CI	-	Chemical ionisation
$CDCl_3$	-	Deuterated chloroform
$CHCl_3$	-	Chloroform
cm	-	Centimeter
cm^{-1}	-	Per centimeter
CO	-	Carbonyl
COSY	-	Correlation spectroscopy
COX	-	Cyclooxygenase
Cs_2CO_3	-	Cesium carbonate

d	-	Doublet
DCC	-	*N*,*N*′-dicyclohexylcarbodiimide
DCM	-	Dichloromethane
DCU	-	Dicyclohexylurea
dd	-	Doublet of doublet
ddd	-	Doublet of doublet of doublet
dddd	-	Doublet of doublet of doublet of doublet
DEPTQ	-	Distorsionless Enhancement by Polarization Transfer with Retention of Quarternaries
DFT	-	Density functional theory
DIPEA	-	*N*,*N*′-diisopropylethylamine
DMAP	-	*N*,*N*-dimethylpyridin-4-amine
DMF	-	Dimethylforamide
DMSO	-	Dimethyl sulfoxide
DMSO-D_6	-	Deuterated dimethyl sulfoxide
DSF	-	Differential scanning fluorimetry
EC_{50}	-	Half maximal effective concentration
EDC	-	1-Ethyl-3-(3-dimethylaminopropyl)carbodiimide
eq	-	Equivalent
Et_2O	-	Diethyl ether
EtOAc	-	Ethyl acetate
FBDD	-	Fragment-based drug design
g	-	gram
GC	-	Gas chromatography
H	-	Hydrogen
HA	-	Hyaluronic acid
HCl	-	Hydrochloric acid
HDAC	-	Histone deacetylases
HMBC	-	Heteronuclear Multiple Bond Correlation
HMQC	-	Heteronuclear Multiple Quantum Coherence

HPF-1	-	Human gingival fibroblast-1
HPLC	-	High-performance liquid chromatography
hrs	-	Hours
Hyal	-	Hyaluronidase
Hz	-	Hertz
I%	-	Inhibition percentage
IC_{50}	-	Half maximal inhibitory concentration
IL	-	Interleukins
i.d	-	Internal diameter
iNOS	-	Inducible nitric oxide synthase
K_2CO_3	-	Potassium carbonate
kcal/mol	-	kilocalorie per mole
kg	-	kilogram
LMW-HA	-	Low molecular weight HA
LOX	-	Lipoxygenase
LPS	-	Lipopolysaccharide
M	-	Molar
m	-	Multiplet
m/z	-	Mass-to-charge ration
MAPK	-	Mitogen-activated protein kinase
MD	-	Molecular dynamics
MeOH	-	Methanol
$MgSO_4$	-	Magnesium sulphate
MHz	-	Megahertz
min	-	Minutes
mL	-	Millilitre
mm	-	Millimetre
mM	-	Millimolar
mmol	-	Millimole

MM-PBSA	-	Molecular Mechanics-Poisson-Boltzmann Surface Area
MS	-	Mass spectroscopy
$Na_2H_2PO_4$	-	Sodium phosphate
NaCl	-	Sodium chloride
$NaHCO_3$	-	Sodium bicarbonate
NaOH	-	Sodium hydroxide
NDGA	-	Nordihydroguaiaretic acid
NF-κB	-	Nuclear factor-κB
n-hex	-	Hexane
nm	-	Nanometre
NMR	-	Nuclear magnetic resonance
NO	-	Nitric oxide
ns	-	Nanoseconds
NSAIDs	-	Non-steroidal anti-inflammatory drugs
OBn	-	Benzyloxy
OH	-	Hydroxyl
OMe	-	Methoxy
PCA	-	Principal component analysis
PDB	-	Protein data bank
PPAR-γ	-	Peroxisome proliferator-activated receptor gamma
ppm	-	Parts per million
q	-	Quartet
R_g	-	Radius of gyration
RMSD	-	Root-mean-square deviation
RMSF	-	Root-mean-square fluctuation
R_f	-	Retention factor
rt	-	Room temperature
s	-	Singlet
S.E.M	-	Standard error measurement

SARS-CoV-2	-	Severe acute respiratory syndrome coronavirus 2
SDG	-	Sustainable Development Goals
sext	-	Sextet
SiO_2	-	Silica gel
S_N2	-	Bimolecular nucleophilic substitution
SPR	-	Surface plasmon resonance
STAT3	-	Transcription 3
t	-	Triplet
TLC	-	Thin layer chromatography
TNF-α	-	Tumor necrosis factor-alpha
TPSA	-	Topological polar surface area
t_R	-	Retention time
tt	-	Triplet of triplet
UV	-	Ultraviolet
VLC	-	Vacuum liquid chromatography
VMD	-	Visual Molecular Dynamics
w/v	-	Weight per volume
XNT	-	Xanthorrhizol

LIST OF APPENDICES

A	Molecular docking result of top fifty XNT derivatives as Hyal-1 inhibitors	148-150
B	Molecular docking results for top fifty derivatives as LOX-3 inhibitors	150-152
C1	ATR-IR spectrum of xanthorrhizyl acetate **(64)**	153
C2	^{1}H NMR spectrum of xanthorrhizyl acetate **(64)**	153
C3	^{13}C NMR spectrum of xanthorrhizyl acetate **(64)**	154
C4	GC-MS spectrum of xanthorrhizyl acetate **(64)**	154
D1	ATR-IR spectrum of XNT **(1)**	155
D2	^{1}H NMR spectrum of XNT **(1)**	155
D3	^{13}C NMR spectrum of XNT **(1)**	156
D4	GC-MS spectrum of XNT **(1)**	156
E1	ATR-IR spectrum of benzyl xanthorrhizyl ether **(76)**	157
E2	^{1}H NMR spectrum of benzyl xanthorrhizyl ether **(76)**	157
E3	^{1}H NMR spectrum of benzyl xanthorrhizyl ether **(76)** (expansion)	158
E4	DEPTQ spectrum of benzyl xanthorrhizyl ether **(76)**	158
E5	GC-MS spectrum of benzyl xanthorrhizyl ether **(76)**	159
F1	ATR-IR spectrum of (2-pyridinyl)methyl xanthorrhizyl ether **(102)**	159
F2	^{1}H NMR spectrum of (2-pyridinyl)methyl xanthorrhizyl ether **(102)**	160
F3	^{1}H NMR spectrum of (2-pyridinyl)methyl xanthorrhizyl ether **(102) (**expansion)	160

F4	DEPTQ spectrum of (2-pyridinyl)methyl xanthorrhizyl ether **(102)**	161
F5	GC-MS spectrum of (2-pyridinyl)methyl xanthorrhizyl ether **(102)**	161
G1	ATR-IR spectrum of 4-nitrobenzyl xanthorrhizyl ether **(103)**	162
G2	^{1}H NMR spectrum of 4-nitrobenzyl xanthorrhizyl ether **(103)**	162
G3	^{1}H NMR spectrum of 4-nitrobenzyl xanthorrhizyl ether **(103)** (expansion)	163
G4	DEPTQ spectrum of 4-nitrobenzyl xanthorrhizyl ether **(103)**	163
G5	GC-MS spectrum of 4-nitrobenzyl xanthorrhizyl ether **(103)**	164
H1	ATR-IR spectrum of 3-trifluoromethylbenzyl xanthorrhizyl ether **(104)**	164
H2	^{1}H NMR spectrum of 3-trifluoromethylbenzyl xanthorrhizyl ether **(104)**	165
H3	^{1}H NMR spectrum of 3-trifluoromethylbenzyl xanthorrhizyl ether **(104)** (expansion)	165
H4	DEPTQ spectrum of 3-trifluoromethylbenzyl xanthorrhizyl ether **(104)**	166
H5	GC-MS spectrum of 3-trifluoromethylbenzyl xanthorrhizyl ether **(104)**	166
I1	ATR-IR spectrum of (2-tetrahydro-2*H*-pyranyl)methyl xanthorrhizyl ether **(105)**	167
I2	^{1}H NMR spectrum of (2-tetrahydro-2*H*-pyranyl)methyl xanthorrhizyl ether **(105)**	168
I3	^{1}H NMR spectrum of (2-tetrahydro-2*H*-pyranyl)methyl xanthorrhizyl ether **(105)** (expansion)	168
I4	DEPTQ spectrum of (2-tetrahydro-2*H*-pyranyl)methyl xanthorrhizyl ether **(105)**	169
I5	GC-MS spectrum of (2-tetrahydro-2*H*-pyranyl)methyl xanthorrhizyl ether **(105)**	169
J1	ATR-IR spectrum of propyl xanthorrhizyloxyacetate **(117)**	170

J2	^{1}H NMR spectrum of propyl xanthorrhizyloxyacetate **(117)**	170
J3	^{13}C NMR spectrum of propyl-2-xanthorrhizyloxyacetate **(117)**	171
J4	GC-MS spectrum of propyl xanthorrhizyloxyacetate **(117)**	171
J5	COSY spectrum of propyl xanthorrhizyloxyacetate **(117)**	172
J6	HMQC spectrum of propyl xanthorrhizyloxyacetate **(117)**	172
J7	HMBC spectrum of propyl-2-xanthorrhizyloxyacetate **(117)**	173
K1	^{1}H NMR spectrum of *N*-(2-chloroethyl)-1*H*-imidazole-4-carboxamide **(121)**	173
K2	^{1}H NMR spectrum of *N*-(2-chloroethyl)-1*H*-imidazole-4-carboxamide **(121)** (expansion)	174
L1	ATR-IR spectrum of *tert*-butyl (3-((2-chloroethyl)amino)-3-oxopropyl)carbamate **(123)**	174
L2	^{1}H NMR spectrum of *tert*-butyl (3-((2-chloroethyl)amino)-3-oxopropyl)carbamate **(123)**	175
L3	^{1}H NMR spectrum of *tert*-butyl (3-((2-chloroethyl)amino)-3-oxopropyl)carbamate **(123)** (expansion)	175
L4	^{13}C NMR spectrum of *tert*-butyl (3-((2-chloroethyl)amino)-3-oxopropyl)carbamate **(123)**	176
M	^{1}H NMR spectrum for attempted synthesis of *tert*-butyl (3-oxo-3-((2-xanthorrhizyloxyethyl)amino)propyl)carbamate **(124)**	176
N	^{1}H NMR spectrum of attempted synthesis of 3-chloropropyl-1*H*-imidazole-4-carboxylate **(126)**	177
O1	Docking conformation of seric acid A **(26)** and disodium chromoglycate **(27)** in Hyal-1 binding site. The active site residues are coloured in maroon.	177
O2	Docking results of seric acid A **(26)** and disodium chromoglycate **(27)** against Hyal-1 enzyme	178

CHAPTER ONE

INTRODUCTION

1.1 RESEARCH INTRODUCTION

Drug discovery is a long process in search of new drug for the treatment and management of diseases. This is because it involves several stages: target identification, lead identification, pre-clinical development, clinical trials, and regulatory approval (Mohs & Greig, 2017). In average, the whole process would take 12 to 15 years, and cost more than one billion US dollar for one drug to be approved (Deore et al., 2019). Despite the long time and high-cost investment, the process has low success rate (~1 in 20,000 to 30,000) (Yamaguchi et al., 2021). Concurrently, the rapid emergence of new diseases, drug resistance and the adverse side effects of currently used drug urge the need for the adaption of a faster and more accurate drug discovery process. Therefore, a cost-effective and highly efficient approach is needed (Dibyajyoti et al., 2013). One of the methods to achieve the goal of a faster identification of drug candidates is through *in silico* studies, or specifically computer aided drug design (CADD).

CADD is a method for discovering and analysing drug compounds through the computers and mathematical tools (Yu & Mackerell, 2017). It includes computational chemistry, molecular modelling, and rational drug design (Arya & Coumar, 2021). CADD approach is more targeted compared to traditional screening and therefore is effective to generate hits (Osakwe, 2016). Hits are the compound that possessed desired biological activity during screening process after target modification, and confirmed upon retesting (Hughes et al., 2011). Hits will be refined and modified to improve the potency and selectivity of the compound before advancing to lead optimisation process.

CADD also helps to describe the pharmacological activity exhibited by potential drug compound on molecular basis. In addition, the possible analogues with improved therapeutic activity can be elucidated based on the variables predicted (Osakwe, 2016). CADD facilitates in filtering the large compound libraries to narrow down the number of potential drug compounds as well as for the optimisation process to improve the

pharmacokinetics properties of the compounds (Sliwoski et al., 2014). CADD greatly helps in reducing the cost and time consumption for drug discovery and development compared to traditional approaches (Usha et al., 2017).

Molecular docking is one of the most commonly used CADD tools, in which it helps to predict the binding orientation of drug molecules in the biological target of interest. The scoring function is then employed to estimate the binding affinity of each ligand pose generated from docking studies (Yang et al., 2022). Molecular dynamics (MD) simulation plays essential role in drug design process as it evaluates the movements and interactions of drug molecules in the protein system. This allows the monitoring of the ligand conformation in protein binding site over prolonged timescale. Therefore, MD simulation was also used to validate the docking pose results (Ahmed et al., 2023; Mohs & Greig, 2017).

Another emerging technique of CADD is *in silico* fragment-based drug design (FBDD), which utilised the fragments of small molecules that exhibited weak affinity towards the protein target. The affinity of the protein target then can be improved by several strategies including fragment growing, linking, and merging (Rachman et al., 2021). The incorporation of *in silico* tools in FBDD pipeline facilitate the identification of binding site of target protein, screening of fragment libraries and the optimisation of fragment-to-lead process (Bissaro et al., 2020).

Inflammation is a result of immune system's response to maintain the integrity of human body after exposure to pathogens or external injury (Furman et al., 2019). There are many enzymes responsible for inflammatory response and one of it is lipoxygenase (LOX) and hyaluronidase (Hyal). LOX is one of two major pathways of eicosanoids biosynthesis. In human body, LOX is responsible for the formation of leukotrienes, the potent inducers of inflammatory response. (Giménez-Bastida et al., 2021). Meanwhile, Hyal is the enzyme responsible to degrade hyaluronic acid (HA) and plays a significant role in tissue remodelling, modulation of wound healing through cell migration and proliferation as well as regulating dendritic cell maturation in several organs (Dokoshi et al., 2018; Fronza et al., 2014). Therefore, targeting Hyal can be a good strategy for designing anti-inflammatory and anticancer agent.

Xanthorrhizol (XNT) is a bisabolene-type sesquiterpenoids, most abundantly compound found in *C. xanthorrhiza.* XNT **(1)** made up more than 92 % of rhizome of *C. xanthorrhiza* essential oil (Jantan et al., 2012). XNT was reported to exhibit multiple biological effects including anti-inflammatory activity through inhibition of several inflammatory mediators like cyclooxygenase (COX) and interleukins (IL) (Chung et al., 2007; Lim et al., 2005), proving that this compound has strong potential to be developed as anti-inflammatory drugs. The use of natural product as building block for drug modification, by removing or adding some of the moieties will improve the ligand efficacy to be used as drug compound (Guo, 2017). Therefore, XNT can be further optimised as potent anti-inflammatory agents through the modification of its functional group.

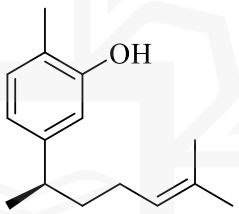

(1)

1.2 PROBLEM STATEMENT

Inflammation is a response to triggers by pathogens or tissue damage in human body. The disruption during acute inflammatory response can lead to chronic inflammation. Chronic inflammatory diseases, like strokes, arthritis and cancer are the most significant cause of death in the world. Non-steroidal anti-inflammatory drugs (NSAIDs) and steroids are the most common drugs used to treat inflammatory-related conditions. However, the use of these drugs posed risk towards the consumers as it is associated with adverse side effects like stomach ulsers, acute renal dysfunction and atrial fibrillation. Therefore, there is an unmet demand in search for new anti-inflammatory agents as alternatives to cater for the currently faced issue. XNT exhibited promising anti-inflammatory properties, yet there have been any studies on its inhibitory effect on Hyal and LOX enzymes particularly Hyal-1 and LOX-3. These two enzymes

contributed to the inflammatory response in human body. Despite its potential, XNT does not fulfil the drug-likeness properties, hampering its development as new drug candidates. Structural modifications of XNT are needed to optimise its activity against the protein target of interest and achieve suitable properties as a drug compound. The utilisation of CADD tools can expedite the optimisation process since it provides a more targeted approach and avoids arduous synthesis of XNT derivatives in a random manner.

1.3 RESEARCH OBJECTIVES

1. To virtually screen and design XNT derivatives as potential Hyal-1 and LOX-3 inhibitors from in-house database using molecular docking and *in silico* FBDD methods, respectively.
2. To synthesise and characterise the most promising XNT derivatives through spectroscopic analyses such as nuclear magnetic resonance (NMR), infrared (IR) and mass spectrometry (MS).
3. To evaluate the inhibitory activities of the synthesised XNT derivatives against Hyal-1 and LOX-3 enzymes through *in vitro* enzyme inhibitory assays.
4. To assess the stability of the most active XNT derivatives within enzymes' binding sites using MD simulation.

1.4 RESEARCH SIGNIFICANCE

Adverse side effects associated with the currently used drug for inflammation like NSAIDs and corticosteroids has caused the urgent need for development of new drugs. Therefore, this study will contribute to society as the potential new drug for inflammatory-related disease can be identified by targeting Hyal-1 and LOX-3 enzymes. Moreover, this research can give insights to medicinal chemists on important substituents needed for improved activities of the enzyme inhibitors. Furthermore, since natural products are one of the main sources of new drugs, the use of CADD in this study for the optimisation of the compounds as scaffold provided a more efficient and

targeted approach for the drug discovery process. The study aligns with the Sustainable Development Goals (SDGs), namely Good Health and Well Being (SDG 3) as well as Industry, Innovation, and Infrastructure (SDG 9), as it contributes towards healthcare benefits for the public community as well as adapting the currently advances in technology and innovation for the drug design process.

1.5 RESEARCH HYPOTHESIS

The potential XNT derivatives as Hyal-1 and LOX-3 inhibitors can be identified through combination of virtual screening from published literatures and *in silico* FBDD technique. All the designed derivatives can be synthesised using XNT as starting material. It was expected that the synthesised derivatives will display improved inhibitory activities against the enzymes compared to XNT.

CHAPTER 2

LITERATURE REVIEW

2.1 FRAGMENT-BASED DRUG DESIGN (FBDD)

Fragment-based drug design is one of the powerful approaches for identification of new bioactive compounds. FBDD involves screening of low molecular weight fragments that have weak affinities towards the biological target. These fragments served as the starting point for subsequent development of the lead compounds (de Souza Neto et al., 2020). Fragment libraries were built to sample diverse chemical structures for targeting the binding site of protein of interest.

The common practice to build fragments libraries is by following the "Rules of Three", where the fragments should have molecular weight less than 300 Da, ClogP value less than three, and possess less than three hydrogen donors and acceptors (Congreve et al., 2003; Erlanson et al., 2016). Fragments have low affinity towards the binding site of the protein, hence structural modification needs to be done to optimise the fragments and enhance their binding affinities towards the protein target. The screening of fragments can be done through experimental or *in silico* approaches.

There are three strategies that can be used in optimising fragments, namely fragment growing, fragment linking, and fragment merging. The most common approach in optimisation of fragments is fragment growing. This strategy involves expanding of the initial fragment hits to occupy the chemical space within the binding pocket. Fragment linking refers to assembling different fragments that occupied different part of the binding pocket using chemical linkers. On the other hand, fragment merging combined the structural features of different ligands occupying the same binding pocket of the protein (Lamoree & Hubbard, 2017; Villemagne et al., 2023). The strategies for fragment optimisation are illustrated in **Figure 2.1**.

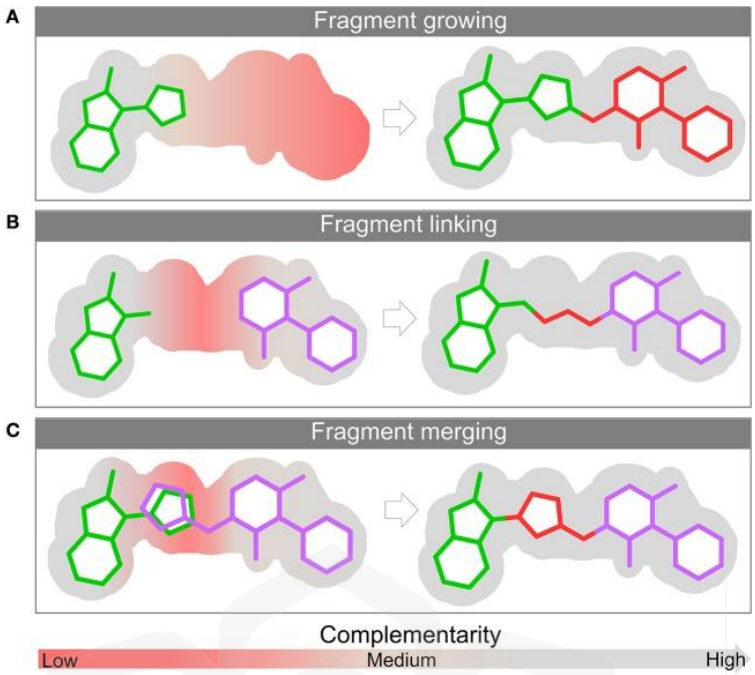

Figure 2.1: Fragment-based drug design strategies for optimisation. A) Fragment growing, B) Fragment linking, C) Fragment merging. (Adopted from de Souza Neto et al. (2020)).

2.1.1 Experimental Approach in FBDD

The experimental FBDD can be conducted by using X-ray crystallography, differential scanning fluorimetry (DSF), surface plasmon resonance (SPR) and nuclear magnetic resonance (NMR). These techniques allow detection of fragments binding and protein-ligand interactions (Li, 2020). For example, Asciminib, a newly approved anti-cancer drug targeting the tyrosine kinase of BCR-ABL1 oncoprotein, was developed by fragment-based screening approach using NMR and X-ray crystallography (Novartis, 2021; Schoepfer et al., 2018). NMR and crystallographic fragment screening also play important roles for the development of other approved drugs i.e. venetoclax (brand name, Venclexta) (Fairbrother et al., 2019), vemurafenib (brand name, Zelboraf) (Bollag et al., 2012), and pexidatinib (brand name, Turalio) (Zhang et al., 2013).

However, experimental FBDD imposed several challenges that can limit the use of this approach. The most common difficulty faced by the experimental FBDD is the high-cost consumption from the instrumentations and the sample preparation. The

examples of costly sample preparation are the isotope labelling of protein for NMR and protein immobilisation method required for SPR (Kumar et al., 2012). Another problem that encountered during the fragment screening process when performing experimental FBDD is the unability of the weak interaction between the fragment and residues to be detected due to the small size of individual fragment. Experimental FBDD also demands highly soluble fragments for screening, which greatly limits the number of suitable fragments that can be used (Bian & Xie, 2018).

2.1.2 *In silico* Approach in FBDD

The use of *in silico* tools in FBDD can come in handy to overcome the limitations of the experimental approach. It is a fast and cost-effective approach that can be applied to protein targets whose three-dimensional structure obtained from Protein Data Bank (PDB) or generated using homology modelling approach (Kumar et al., 2012). *In silico* FBDD approach utilises fragment libraries from commercially available databases such as ZINC, MayBridge or ChemBridge databases. It is then followed by screening of fragments, most commonly using molecular docking. Virtual screening using molecular docking is complementary to the fragment screening step using X-ray crystallography, NMR or SPR techniques in experimental FBDD. Virtual screening has an advantage over experimental techniques because it can screen a larger number of fragments in short time (Sheng et al., 2015). Softwares like AutoGrow, LigBuilder and Gandi can facilitate in the fragment optimisation to build new compounds that fit into the defined binding site of protein of interest (de Souza Neto et al., 2020; Moinul et al., 2022).

The example of successful application of *in silico* FBDD specifically *via* fragment linking strategy is the design of new signal transducer and activator of transcription 3 (STAT3) inhibitors. Two libraries were built from known STAT3 inhibitors, which consist of fragments that bind to pTyr705 and the side pocket of the STAT3 catalytic domain. Screening of pTyr705 library using molecular docking resulted in fragment naphthalene-5,8-dione-1-sulfonamide **(2)** to be randomly linked with fragments from the side pocket library using dimethyl amine group as linker to generate new compounds. All compounds generated were subjected to molecular

docking against STAT3 to select top five compounds to be synthesised based on their docking scores and conformations. 5,8-Dioxo-6-(pyridine-3-yl-amino)-5,8-dihydronaphtlene **(3)** exhibited strongest inhibition against human osteosarcoma cell lines U2OS (IC_{50} = 0.52 µM), compared to known STAT3 inhibitor, 5-hydroxy-9,10-dioxo-9,10-dihydroanthracene-1-sulfonamide **(4)**. Moreover, the compound **(3)** was also able to downregulate STAT3 phosphorylation and inhibit tumour growth in *in vivo* studies (Yu et al., 2013).

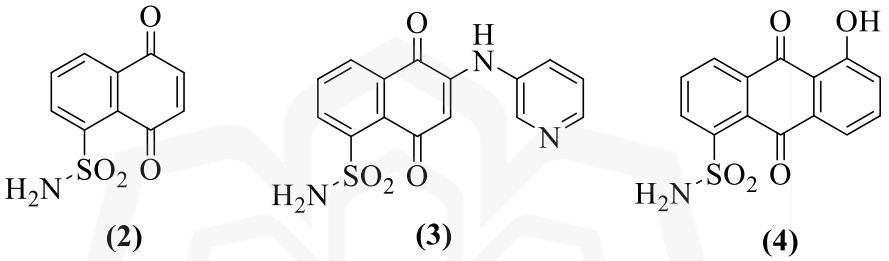

The fragment growing approach in *in silico* FBDD were demonstrated in designing potential anti-diabetic agent by targeting peroxisome proliferator-activated receptor gamma (PPAR-γ), which played pivotal role in glucose metabolism. Thiazolidine-2,4-dione **(5)** was identified as the scaffold for structural optimisation where the design of its new derivatives was conducted using Schrodinger Maestro software. A total of 1000 fragments were docked against the active site of PPAR-γ. Then, the screened fragments were linked with compound **(5)** at different substitution positions to generate 7000 compounds. From the initial pool of 7000 compounds, series of virtual screening based on the Lipinski's rule of Five, docking scores and conformation resulted in twelve compounds with favourable interaction with PPAR-γ. All twelve compounds were synthesised and tested on PPAR-γ transactivation assay. Compound **(6)** demonstrated the strongest potency among all synthesised derivatives with EC_{50} of 739.0 nM, which were comparable to reference compound, pioglitazone **(7)** (EC_{50} = 575.2 nM). Compound **(6)** also showed remarkable reduction in glucose levels of pre-treated swiss albino mice with value of 134.1 mg/dl, similar to pioglitazone **(7)** (132.2 mg/dl) (Gupta et al., 2023).

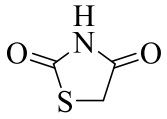

(5)

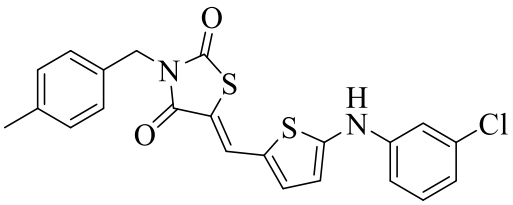

(6)

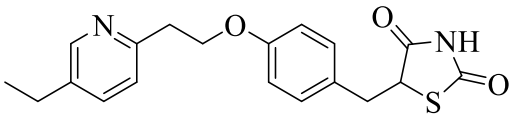

(7)

The design of new histone deacetylases (HDACs) inhibitors for cancer treatment also utilised the *in silico* FBDD approach. In the study, the approved HDAC inhibitor, vorinostat **(8)** was used as core structure for design of new compounds, in which the modification was aimed at the phenyl ring of vorinostat **(8)** (Liu et al., 2020). A total of 11809 fragments were screened using molecular docking against HDAC2 protein. In the protocol, the docking of fragments was constrained at the spatial position of the phenyl ring. The screening resulted in eight fragments with good docking score and similar binding conformation with vernostat **(8)**. Based on the synthetic feasibility, 6-phenyl-1*H*-indazole **(9)** was chosen to be hydridised with phenyl ring of vernostat **(8)**, and a series of indazole derivatives were synthesised to furnish twenty-two new derivatives. *N*-Hydroxy-*N*-(6-(4-methoxyphenyl)-1*H*-indazol-3-yl)octanediamide **(10)** and *N*-(6-(4-chlorophenyl)-1*H*-indazol-3-yl)-*N*-hydroxyoctanediamide **(11)** were the most active derivatives against HDAC1 (IC_{50} = 2.7 and 3.1 nM), HDAC2 (IC_{50} = 4.2 and 3.6 nM) and HDAC8 (IC_{50} = 3.6 and 3.3 nM). The activities of compound **(10)** and **(11)** against HDAC1, HDAC2 and HDAC3 were stronger compared to vernostat **(14)** (IC_{50} = 13.0, 70.0, 44.0 nM, respectively).

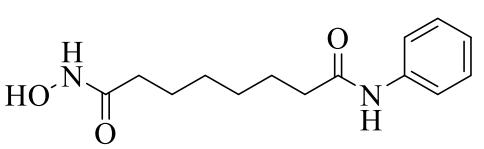

(8)

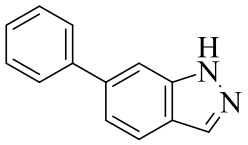

(9)

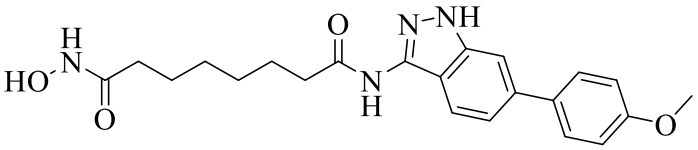

(10)

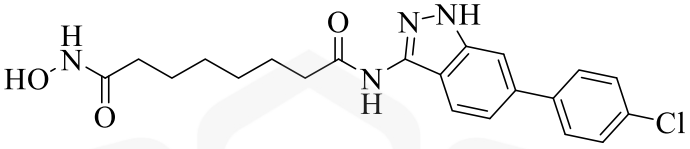

(11)

In silico FBDD approach was also employed to design novel severe acute respiratory syndrome coronavirus 2 (SARS-CoV-2) main protease inhibitors. In the study, baicalein **(12)**, a known SARS-CoV-2 inhibitor was used as the reference compound for the FBDD process. Baicalein **(12)** was fragmented to form two fragments, chromene ring **(13)** and phenyl ring **(14)** (**Scheme 2.1**). The chromene ring fragment **(13)** was subjected to FBDD using Auto Core Fragment *in silico* Screening (ACFIS) webserver. This is because chromene ring **(13)** interacted with several amino acid residues *via* hydrogen bonding in the binding site of the protein. The newly generated compounds were subjected to molecular docking, absorption, distribution, metabolism, excretion, toxicity (ADMET) screening, MD simulation, and principal component analysis (PCA), resulting in generation of compound 5,6,7-trihydroxy-2-(isoxazole-5-ylmethyl)-4*H*-chromen-4-one **(15)**. Compound **(15)** exhibited binding free energy of -55.296 kJ/mol comparable to baicalein **(12)** (-57.370 kJ/mol) in Molecular Mechanics Poisson-Boltzmann Surface Area (MM-PBSA) analysis, indicating its potential as SARS-CoV-2 main protease inhibitor (Andola et al., 2022).

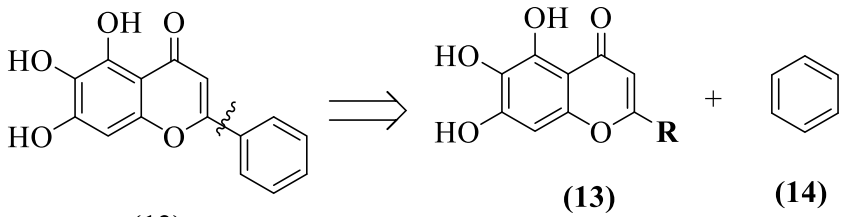

(12) **(13)** **(14)**

R = Linking site

Scheme 2.1: Fragmentation of baicalein **(12)**

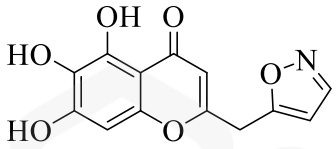

(15)

2.1.3 Ligbuilder software

Ligbuilder is a software developed to facilitate drug designing process, especially through structure-based drug design (Wang et al. (2000). There are two major programmes, known as Cavity and Build mode. The general workflow in LigBuilder is illustrated in **Figure 2.2**. Firstly, the crystal structure of the protein is subjected to the Cavity mode for detection of potential binding sites by predicting protein ligandability and druggability. Druggability refers to the ability of drug-like molecules to bind to the protein target site with high affinity, making them suitable for drug discovery. Ligandability refers to the likelihood of finding a small molecule that binds to the target and reflected in the Cavity mode by the pK_d value. Cavity output will show predicted Drugscore and pK_d values. A high DrugScore reflects good druggability, with a score higher than 600 indicating that the binding site is "Druggable", whereas the maximum and average pK_d value of higher than 6 are good indicator for suitable target for drug design (Xu et al., 2018; Zhang et al., 2015).

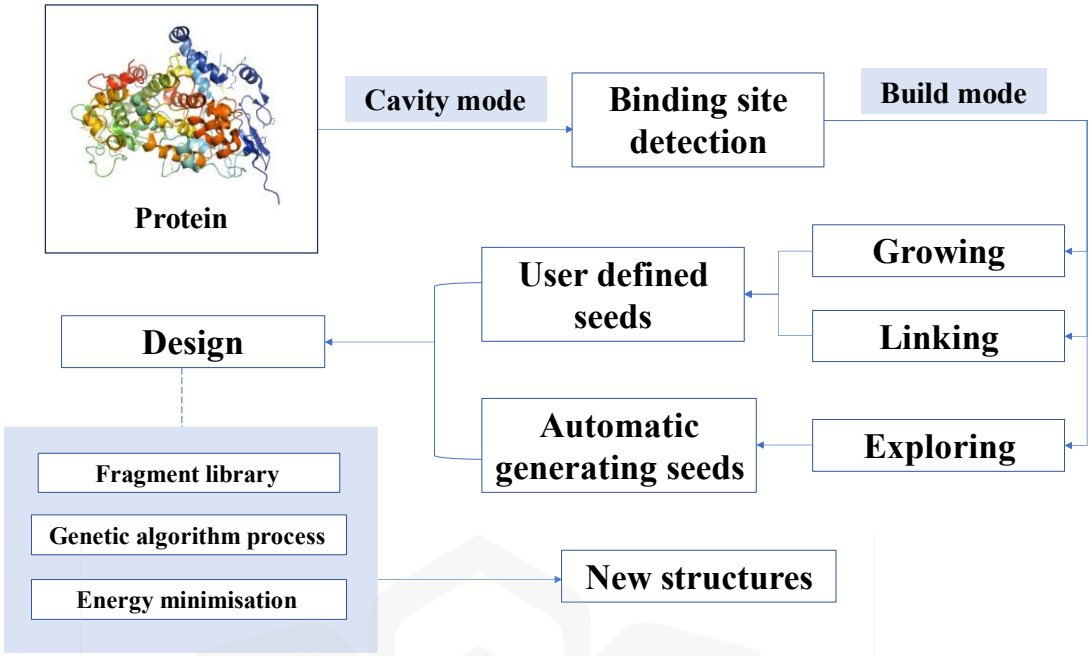

Figure 2.2: General workflow for design strategies in LigBuilder (adapted from Qing et al., 2021).

Then, the selected cavity or binding site was used for the design process in the Build mode. There were three strategies available for constructing new ligands, which were growing, linking and exploring. The growing and linking strategies required a seed structure inside the binding site before the addition of fragments. The seed structure refers to starting or original structure of a compound, which will then be designed by using the fragment library in the LigBuilder software. The fragments library of Ligbuilder software assembled chemical groups and rings that are commonly observed in organic compounds (Qing et al., 2021). Exploring strategy can be used for *de novo* design of new drug compound it required no seed structure to construct the ligand. Growing strategy involves expansion of seed structure at the assigned growing site with new fragments. Meanwhile, linking strategy involves fragmentation of the seed structure into several pieces. These pieces of seed structure will be linked with possible linkers until they integrated into a new structure. The ligand construction process using all strategies were controlled by genetic algorithm and the energy minimisation was incorporated in the design process to ensure minimal errors for the designed ligands (Yuan et al., 2011). The design using both strategies was illustrated in **Figure 2.3**.

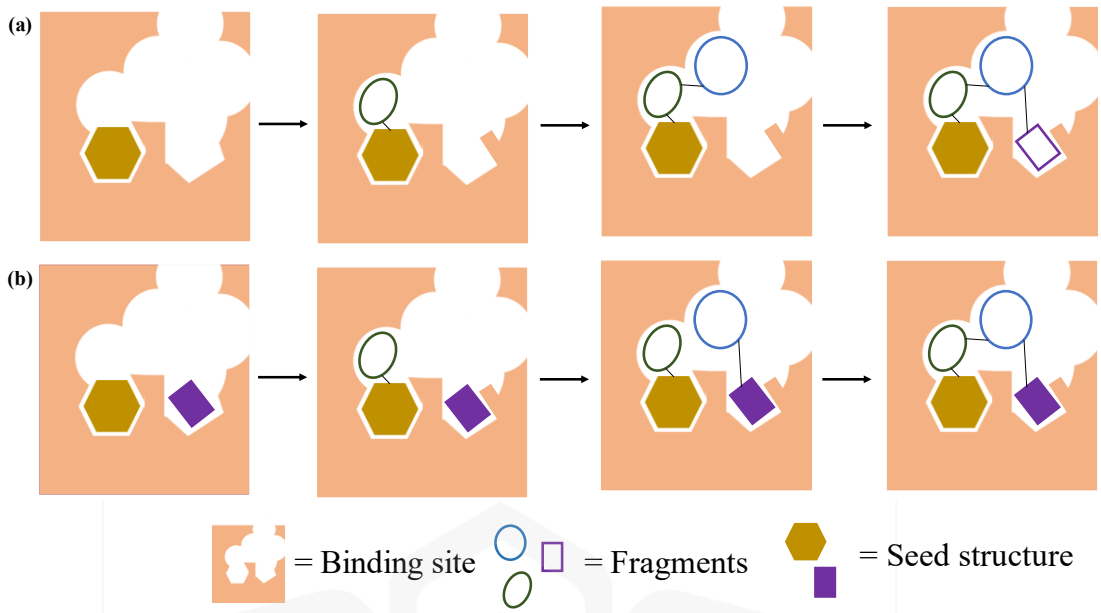

Figure 2.3: a) Growing strategy b) Linking strategy (adapted from Wang et al. (2000))

2.2 HYALURONIDASE ENZYME

Hyaluronidase (Hyal) is an enzyme responsible for hyaluronic acid (HA) degradation in the extracellular matrix. It is an important enzyme for physiological functions in which the disturbance of its regulation can lead to disease progression, including tumor metastasis (Isoyama et al., 2006). HA metabolism can result in production of low molecular weight HA (LMW-HA) fragments that can contribute to inflammatory and immunosuppressive response (Lengers et al., 2020). Increased expression of chemokines and inducible nitric oxide synthase (iNOS) were observed in presence of LMW-HA. Moreover, it can also stimulate dendritic cell signaling pathways to produce interleukins (IL)-1β, IL-12, and tumor necrosis factor-alpha (TNF-α) (Garantziotis & Savani, 2019; McQuitty et al., 2020). Therefore, targeting Hyal is one of the strategies to develop novel anti-inflammatory agents. In the human body, there are five Hyal isozymes identified, namely Hyal-1, Hyal-2, Hyal-3, Hyal-4 and Hyal PH-20. Among them, Hyal-1 and Hyal-2 are the key enzymes involved in the degradation of HA (Žádníková et al., 2022).

The binding site of human Hyal-1 enzyme composed of arginine side chains (Arg134, Arg265), aromatic amino acid residues (Tyr75, Trp141, Tyr202, Tyr208, Tyr210, Tyr247, Tyr261, Tyr286, Tyr321), serine residues (Ser245) and acidic amino acid residues (Asp129, Glu131) (Chao et al., 2007). Among these, Asp129 and Glu131 residues were found to be directly involved in the catalytic cleavage of the β1-4 linkage of *N*-acetylglucosamine and glucuronic acid of HA polymers, suggesting its important role on enzyme inhibitory activity. Moreover, mutagenesis of Tyr247 to Phe247 diminished the substrate catalysis, showing that Tyr247 was responsible for the catalytic activity of Hyal-1 enzyme. Additionally, residues Tyr202 and Ser245 supported the binding of substrate in the active site of Hyal-1 enzyme by positioning the substrate for the catalytic cleavage process (Zhang et al., 2009). The visualisation of active site for Hyal-1 enzyme was depicted in **Figure 2.4**.

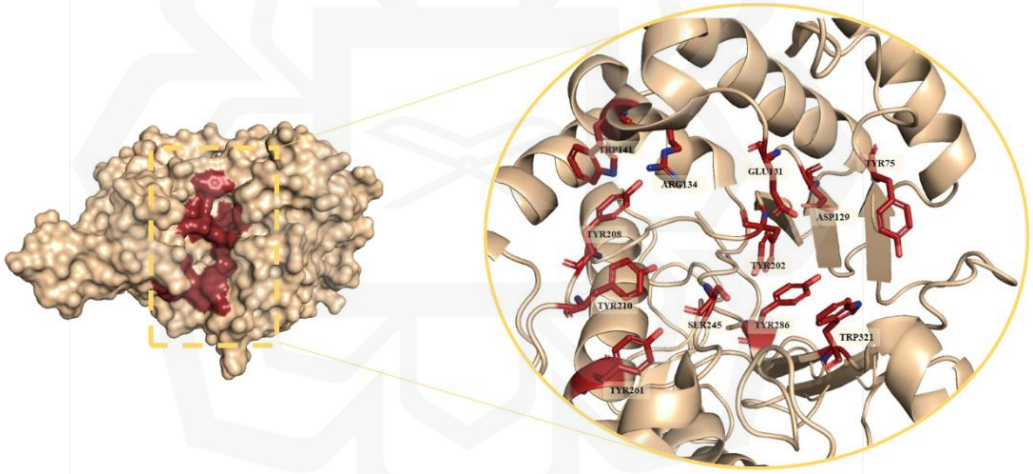

Figure 2.4: Active site of Hyal-1 enzyme. The active site residues are coloured in maroon.

2.2.1 Hyaluronidase Inhibitors

Ursolic acid **(16)**, a pentacyclic triterpenoid isolated from *Prismatomeris tetrandra* (Roxb.) K. Schum was reported to possess Hyal inhibitory activity (Abdullah et al., 2016). The inhibitory activity of **(16)** (IC_{50} = 103.18 µM) was stronger than the positive control apigenin **(17)** (IC_{50} = 214.74 µM). Its synthetic analogue, carbonexolone **(18)** (IC_{50} = 56.83 µM) exhibited stronger inhibitory activity against Hyal enzyme compared

to ursolic acid **(16)** and apigenin **(17)**. The molecular docking studies showed that carbonexolone **(18)** exhibited lower binding energy towards human Hyal-1 enzyme (-8.5 kcal/mol) compared to apigenin **(17)** (-7.8 kcal/mol). Moreover, carbonexolone **(18)** interacted with amino acid residue Asp129, which is important for the enzyme inhibition. In contrast, the interaction with Asp129 was not observed in the apigenin **(17)** containing complex (Abdullah et al., 2016).

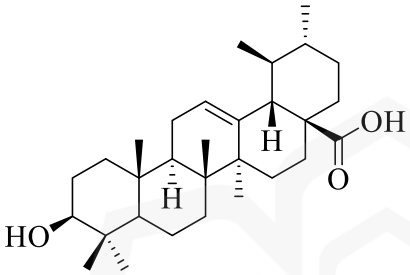

(16)

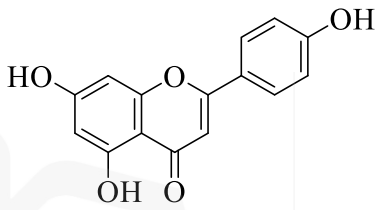

(17)

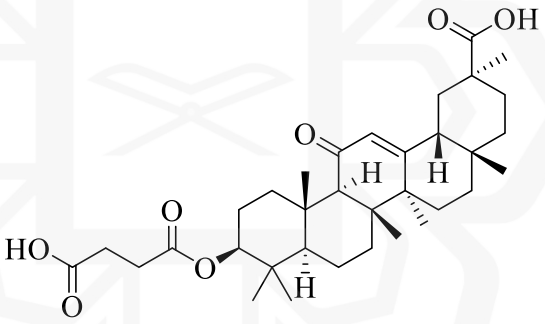

(18)

Coclaurine **(19)**, an alkaloid isolated from the flower buds of *Nelumbo nucifera* or lotus flower exhibited strong Hyal inhibition activity, with IC_{50} of 11.4 µM. Other isolated alkaloids called nornuciferine **(20)**, asimilobine **(21)**, norarmepavine **(22)** and norjuziphine **(23)** also inhibited Hyal enzyme (IC_{50} values of 22.5, 11.7, 26.4, and 24.3 µM, respectively) (Morikawa et al., 2019). Meanwhile, *β*-sitosterol **(24)** isolated from rhizome of *Aglaonema simplex* Blume exhibited moderate Hyal inhibition, with IC_{50} 885.5 µg/mL, compared to 6-*O*-palmitoylascorbic acid **(25)** (IC_{50} = 86.1 µM) as the control (Khammee et al., 2020). Concurrently, the binding energy of 6-*O*-palmitoylascorbic acid **(25)** (-8.70 kcal/mol) is lower than *β*-sitosterol **(24)** (-5.93 kcal/mol) evaluated from molecular docking analysis.

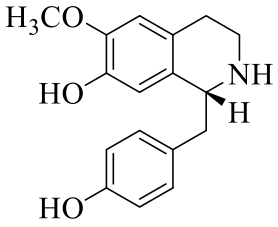

(19)

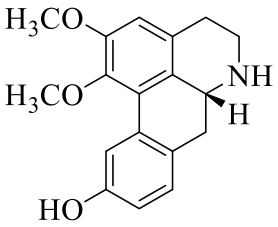

(20)

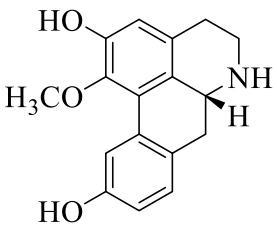

(21)

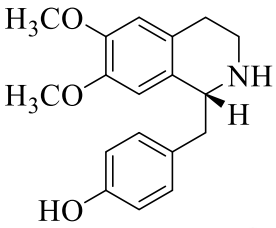

(22)

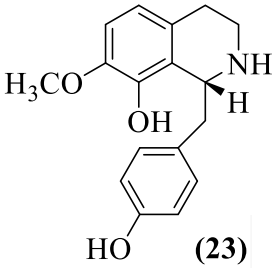

(23)

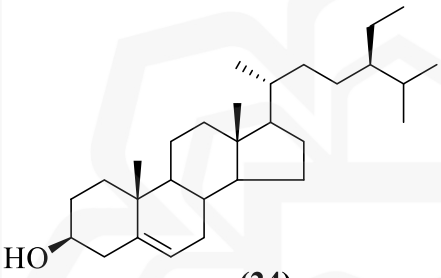

(24)

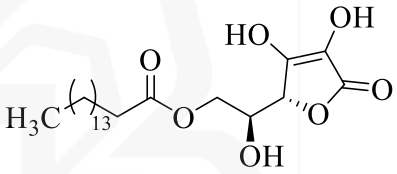

(25)

Seric acid A **(26)** isolated from *Oenanthe javanica* roots showed inhibition towards Hyal enzyme with IC_{50} 0.19 mM and had better activity in *in vitro* assay compared to the positive control disodium chromoglycate **(27)** (0.39 mM) (Murata et al., 2021). An alkyl benzoquinone, embelin **(28)** from *Lysimacia puntata* L. exhibited Hyal inhibition with IC_{50} 275.1 µg/mL, which is almost two-fold stronger than the reference compound, quercetin **(29)** (517.3 µg/mL) (Wróbel-Biedrawa et al., 2020).

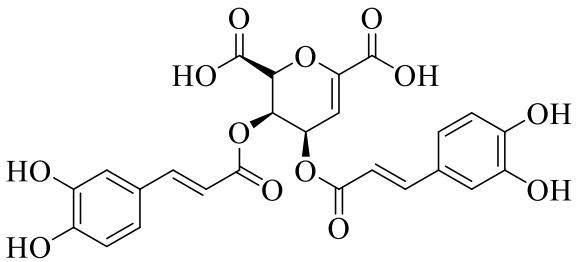

(26)

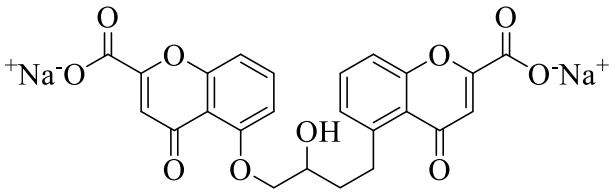

(27)

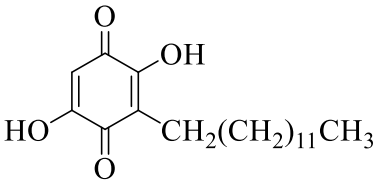

(28)

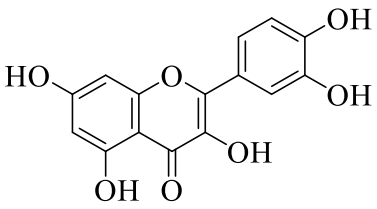

(29)

A synthetic compound, namely 3-(4-bromophenyl)-6,7-dihydroxycoumarin **(30)** exhibited strong inhibition against Hyal enzyme with IC_{50} 112.0 µM, compared to oleanolic acid **(31)** (IC_{50} = 212.4 µM) (Pintus et al., 2022) as the reference compound. Meanwhile, biphenyl triazole compounds, (*R*)-2-((((9*H*-fluoren-9-yl)methoxy)carbonyl)amino)-3-(1-(4′-acetyl-[1,1′-biphenyl]-3-yl)-1*H*-1,2,3-triazol-4-yl)propanoic acid **(32)** and 1-(3′-(4-(4-((7-chloroquinolin-4-yl)amino)phenyl)-1*H*-1,2,3-triazol-1-yl)-[1,1′-biphenyl]-4-yl)ethan-1-one **(33)** demonstrated better inhibitory activities against Hyal enzyme (IC_{50} =16.3 and 9.1 µM, respectively) compared to positive control **(25)** (IC_{50} =31.7 µM) (Qin et al., 2024).

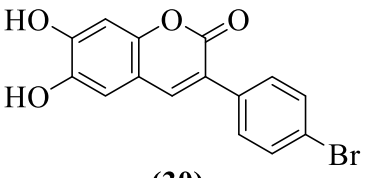

(30)

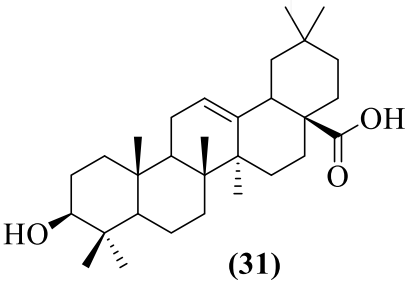

(31)

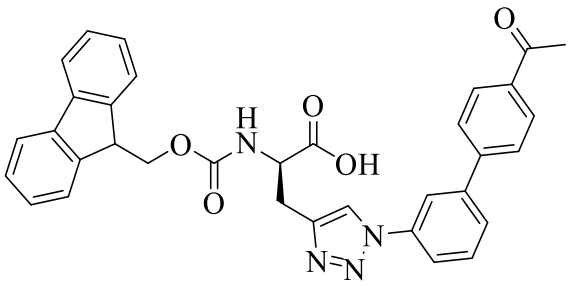

(32)

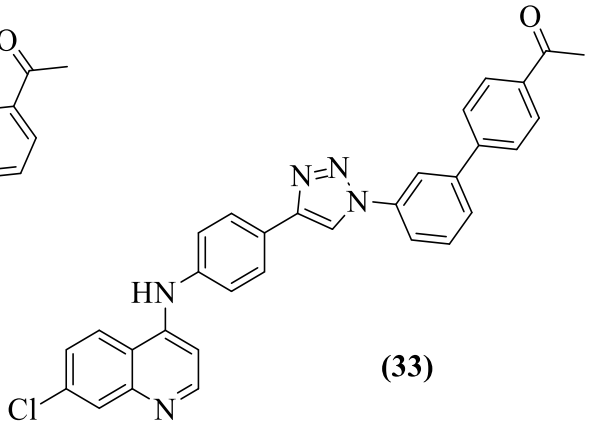

(33)

2.3 LIPOXYGENASE ENZYME

Lipoxygenase (LOX) is also one of the biological targets for designing anti-inflammatory agents. LOX is involved in the conversion of arachidonic acid to leukotrienes involved in modulation of immune response (Martel-Pelletier et al., 2003). There are several isoforms of LOX that exist in the human body, including 5-LOX, 15-LOX, 15-LOX-2, 12-LOX and 12R-LOX. These isoforms are classified based on their selectivity to oxygenate fatty acids in a specific position (Jameson et al., 2014). There are two domains in lipoxygenases enzyme called C-terminal catalytic domain and N-terminal domain. C-terminal domain consisted of the non-heme iron atom and N-terminal domain is essential for translocation to the nuclear membrane (Wisastra & Dekker, 2014). Zileuton **(34)** is the approved 5-LOX inhibitor approved for the treatment of prophylaxis and chronic treatment of asthma. However, it is reported to be associated with liver toxicity (Rossi et al., 2010).

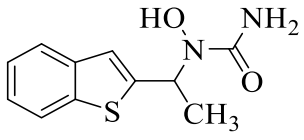

(34)

Soybean LOX-3 is often used as the model for human 5-LOX due to its structural similarity and mechanism of action (Muñoz-Ramírez et al., 2020). The active

pocket of LOX-3 enzyme composed of amino acid residues His509, His518, His523, Asn713 and Ile857, which were buried inside the protein close to the non-heme iron site, as depicted in **Figure 2.5**. Of these, the hydrophobic channel of the active site is composed of Leu273, Thr274, Leu277, Ile557, Ile772 and Ile857 amino acid residues to facilitate in the stabilisation of the substrate-protein complex. The active pocket also included hydrophilic region composed of Ser510, Gln716, Gly720, Arg726 and Asp766 residues that can form hydrogen bonding network with the substrate (Koukoulitsa et al., 2007).

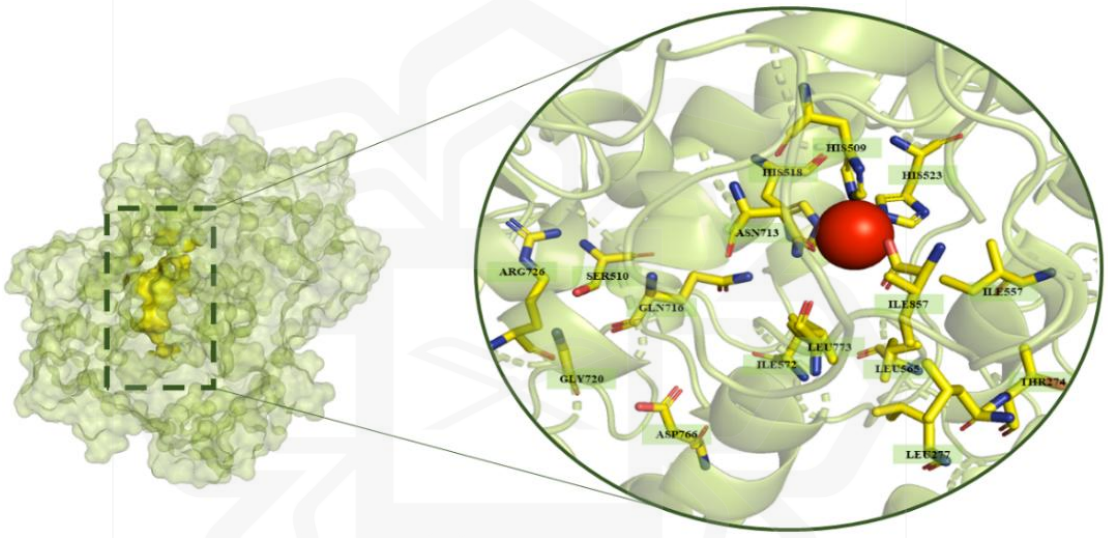

Figure 2.5: Active site of LOX-3 enzyme. The active site residues are coloured in yellow. Red ball represents non-heme iron.

2.3.1 Lipoxygenase Inhibitors

There were several reports on the development of potential soybean LOX inhibitors based on the structure of known NSAIDs. Naproxen **(35)** derivatives, namely 4-(2,4-dichlorophenyl)-1-(2-(6-methoxynaphthalen-2-yl)propanoyl) thiosemicarbazide **(36)**, 4-(3-fluorophenyl)-5-(1-(6-methoxynaphthalen-2-yl)ethyl)-4*H*-1,2,4-triazole-3-thiol **(37)**, and *N*-(2-fluorophenyl)-5-(1-(6-methoxynaphthalen-2-yl)ethyl)-1,3,4-oxadiazol-2-amine **(38)** inhibited soybean LOX enzymatic activities with IC_{50} value of 1.13, 1.19, and 1.72 µM, respectively and stronger than baicalein **(12)** (IC_{50} = 2.24 µM) as the reference compound (Sardar et al., 2022a). A diclofenac **(39)** derivative, namely *N*'-(1-

benzyl-5-chloro-2-oxoindolin-3-ylidene)-2-(2-((2,6-dichlorophenyl)amino)phenyl) acetohydrazide **(40)** exhibited inhibitory activity against soybean LOX with IC_{50} 4.61 µM, comparable to the positive control quercetin **(29)** (4.84 µM) (Sardar et al., 2022b).

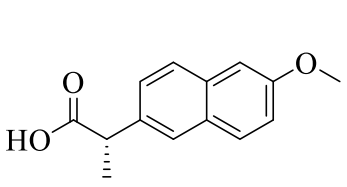

(35)

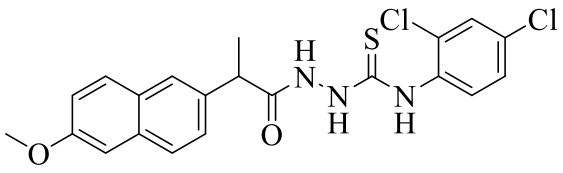

(36)

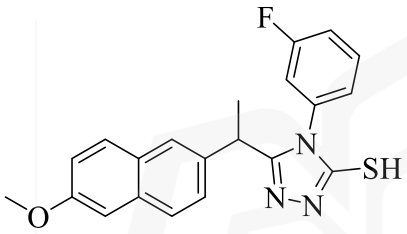

(37)

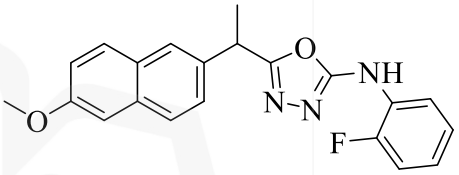

(38)

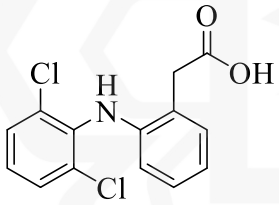

(39)

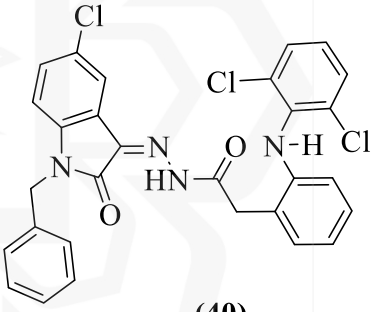

(40)

Inspired by the structure of NSAID suprofen **(41)**, thienopyrimidine derivative namely (*Z*)-4-oxo-4-(2-(2-((5,6,7,8-tetrahydrobenzo-[4,5]-thieno-[2,3-d]-pyrimidin-4-yl)amino)acetyl)hydrazinyl)but-2-enoic acid **(42)** showed stronger inhibition (IC_{50} = 1.17 µM) against soybean LOX than positive control nordihydroguaiaretic acid (NDGA) **(43)** (IC_{50} = 1.28 µM). Other derivatives, namely (*E*,*Z*)-2-((5,6,7,8-tetrahydrobenzo[4,5]thieno[2,3-d]pyrimidin-4-yl)amino)-*N*'-(thiophen-2-ylmethylene) acetohydrazide **(44)** and (*E*,*Z*)-*N*'-(4-methoxybenzylidene)-2-((5,6,7,8-tetrahydrobenzo [4,5]thieno[2,3-d]pyrimidin-4-yl)amino)acetohydrazide **(45)** exhibited similar inhibitory activities to NDGA **(43)**, with IC_{50} 1.29 and 1.30 µM, respectively (Abdelkhalek et al., 2023).

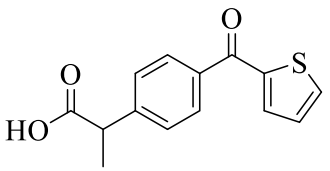

(41)

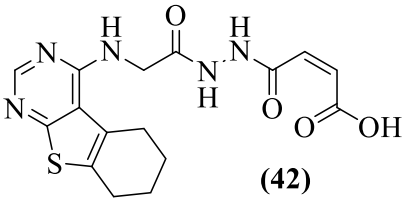

(42)

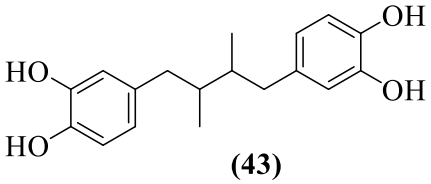

(43)

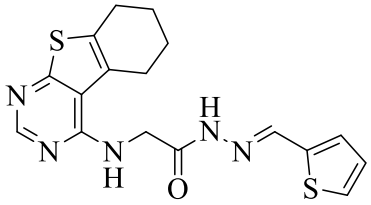

(44)

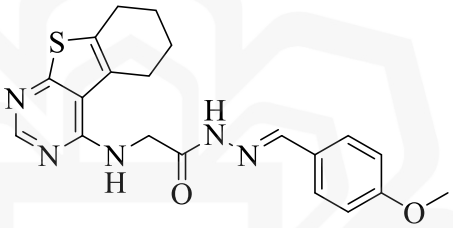

(45)

A series of benzimidazole derivatives, *N*-(2-((3,4-diphenylthiazol-2(3*H*)-ylidene)hydrazono)propyl)-4-(2-(methylthio)-1*H*-benzo[d]imidazole-1-yl)thiazol-2-amine **(46)**, *N*-(2-((4-(4-chlorophenyl)-3-phenylthiazol-2(3*H*)-ylidene)hydrazono) propyl)-4-(2-(methylthio)-1*H*-benzo[d]imidazol-1-yl)thiazol-2-amine **(47)**, 4-(2-(methylthio)-1*H*-benzo[d]imidazol-1-yl)-*N*-(2-((-3-phenyl-4-(p-tolyl) thiazol-2(3*H*)-ylidene)hydrazono)propyl)thiazol-2-amine **(48)** also inhibited soybean LOX with IC_{50} 1.85, 1.67 and 2.14 µM, respectively, which were stronger compared to positive control, quercetin **(29)** (IC_{50} 3.34 µM). The molecular docking study revealed that the most potent compound **(47)** was bound to the active site of human 15-LOX enzyme with binding energy of -9.27 kcal/mol, stronger than quercetin **(29)** (-6.89 kcal/mol). Moreover, compound **(47)** possessed three hydrogen bond interactions with residues Cys106, Arg407, and Asp625 (Maghraby et al., 2020).

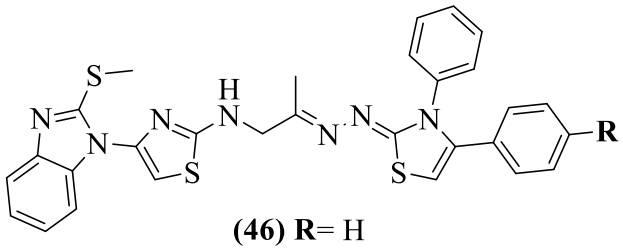

(46) R= H
(47) R= Cl
(48) R= CH_3

Ethyl-6-(4-(cyclohexylmethyl)-1*H*-1,2,3-triazol-1-yl)pyridine-3-carboxylate **(49)**, a triazole compound showed inhibition towards soybean LOX with IC_{50} value of 37.50 µM, compared to positive control indomethacin **(50)**. Compound **(49)** was docked into the active pocket of LOX-3 enzyme with binding energy of -9.5 kcal/mol in the similar binding conformation to indomethacin **(50)** (-6.5 kcal/mol). The docking analysis revealed that compound **(49)** formed hydrogen bonding with His513 and Arg726, as well as pi-pi stacking bond with Phe576 in the hydrophobic channel of LOX-3 enzyme (Ahmed et al., 2021).

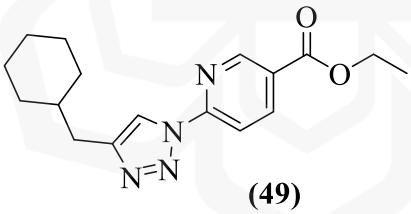

(49)

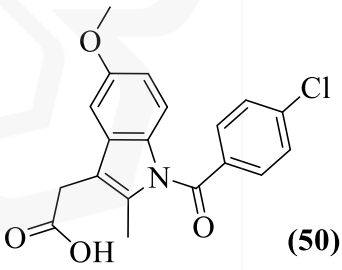

(50)

The search for LOX inhibitors were also performed through natural product sources. Clerodane diterpenes isolated from the eeds of *Polyalthia longifolia* or Ashoka plant also inhibited human 5-LOX enzyme. Three compounds, namely 16-hydroxy-cleroda-4(18),13-dien-16,15-olide **(51)**, 3*α*,16*α*-dihydroxy-cleroda-4(18),13(14)*Z*-dien-15,16-olide **(52)**, and 16*α*-hydroxy-cleroda-3,13(14)*Z*-dien-15,16-olide **(53)** exhibited inhibition with IC_{50} values of 12.73, 16.94, and 14.38 µM, respectively stronger than diclofenac (IC_{50} = 23.28 µM), (Nguyen et al., 2020).

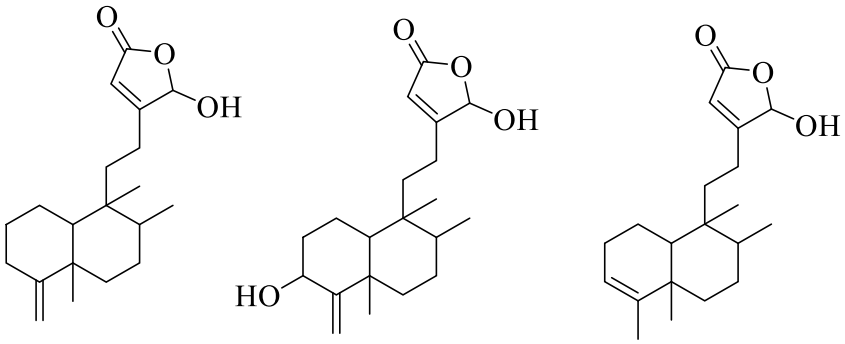

(51) **(52)** **(53)**

In addition, two bioactive compounds isolated from the leaves of *Alstonia scholaris*, namely schloraicine **(54)** and *β*-sitosterol glucoside **(55)** demonstrated strong inhibitory activities against soybean LOX enzyme with IC_{50} 15.2 and 18.5 µM, respectively, which is better than the reference compound baicalein **(12)**. Molecular docking studies revealed that both isolated schloraicine **(54)** and *β*-sitosterol glucoside **(55)** were bound in the active site of soybean LOX-3 enzyme through hydrogen bonding with residues Gln514 and His518, as well as residues Val571 and Asp766, respectively (Ghansenyuy et al., 2023). Human 5-LOX inhibitory activities were also reported by several natural pentacyclic triterpenoids, i.e 30-hydroxy-11-oxo-*β*-amyrin **(56)** (25.7 µM), glycyrrhetinic acid **(57)** (24.8 µM) and 11-keto-*β*-boswellic acid **(58)** (28.3 µM), comparable to the standard drug zileuton **(34)** (23.9 µM) (Vo et al., 2019).

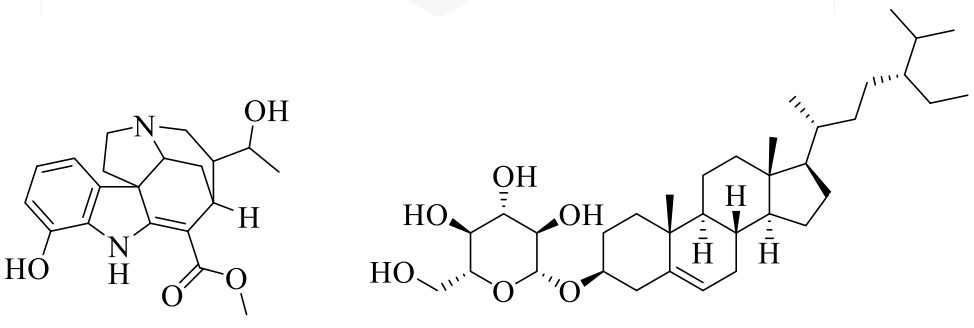

(54) **(55)**

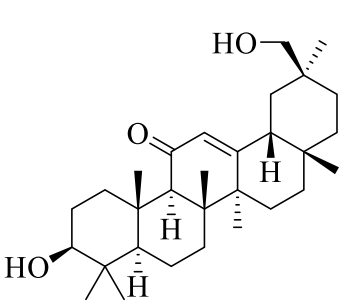

(56)

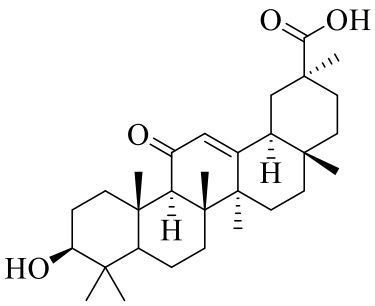

(57)

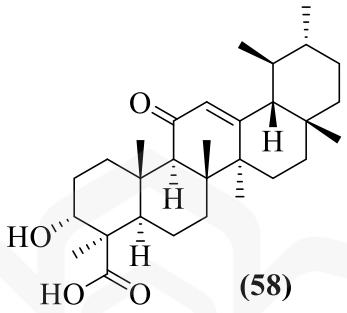

(58)

2.4 XANTHORRHIZOL DERIVATIVES

XNT **(1)** is a natural product compound that can be isolated abundantly from the rhizome of *C. xanthorrhiza*. It possesses a wide range of biological activities, including antibacterial, antioxidant, anti-hyperglycemic as well as anti-inflammatory (Oon et al., 2015). There were several reports on its derivatives, which spawned from the modification of its hydroxy and alkene functional group.

XNT derivatives called (10*R*/10*S*)-10,11-epoxyxanthorrhizol **(59)**, and (10*R*/11*S*)-10,11-dihydro-10,11-dihydroxyxanthorrhizol **(60)** were isolated as minor compounds from the chloroform ($CHCl_3$) extract of *Iostephane heterphylla* (Cav.) Hemsl. (Asteraceace) roots. Based on the analytical HPLC and NMR signals of C-10, it was suggested that both compounds existed as epimeric mixture and cannot be separated by using conventional column chromatography technique (Aguilar et al., 2001).

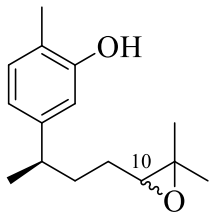

(59)

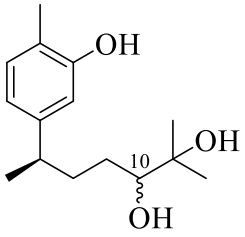

(60)

XNT derivatives can also be produced from chemical reactions. The bromination of XNT **(1)** using *N*-bromo-succinimide afforded two isomers, 2-bromo xanthorrhizol **(61)** and 6-bromo xanthorrhizol **(62)**. 10,11-dihydroxanthorrhizol **(63)** were also synthesised by catalytic hydrogenation using 10% palladium on carbon (Pd/C) as catalyst. Modification of hydroxyl group using acetic anhydride and benzoyl chloride afforded xanthorrhizyl acetate **(64)** and xanthorrhizyl benzoate **(65)**, respectively (Aguilar, Delgado, & Villarreal, 2001). The α-hydroxyl ketone derivatives were synthesised from derivatives **(64)** and **(65)**. Oxidation of derivatives **(64)** and **(65)** using potassium permanganate afforded α-hydroxyl ketone derivative characterised as 5-(6-hydroxy-6-methyl-5-oxoheptan-2-yl)-2-methylphenyl acetate **(66)** and 5-(6-hydroxy-6-methyl-5-oxoheptan-2-yl)-2-methylphenyl benzoate **(67)**, respectively.

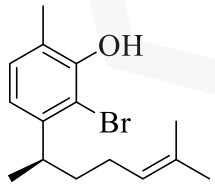

(61)

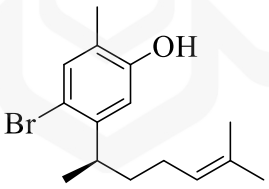

(62)

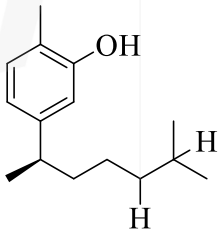

(63)

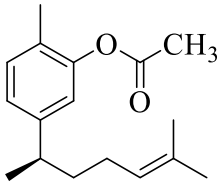

(64)

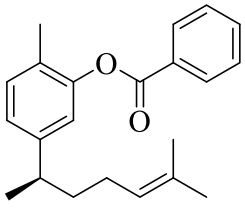

(65)

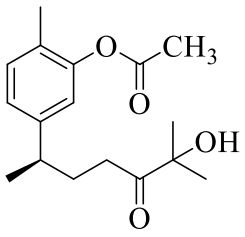

(66)

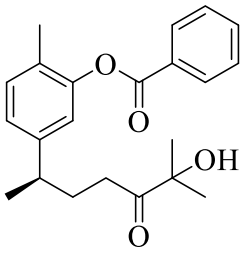

(67)

Synthesis of xanthorrhizol derivatives were conducted extensively by Ngai and Sirat (2004). Two stereoselective diols derivatives, (10*S*)-10,11-dihydroxanthorrhizyl acetate **(68)** and (10*S*)-10,11-dihydro xanthorrhizyl acetate **(69)** were synthesised using Sharpless asymmetric dihydroxylation (AD) reactions of derivative **(64)** with AD-mix-*α* and AD-mix-*β*, respectively. Deprotection of both compounds using aqueous sodium carbonate afforded (10*S*)-10,11-dihydro-10,11-dihydroxyxanthorrhizol **(70)** and (10*R*)-10,11-dihydro-10,11-dihydroxyxanthorrhizol **(71)**.

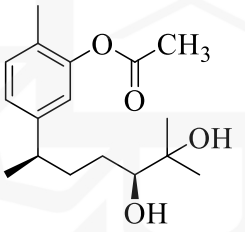

(68)

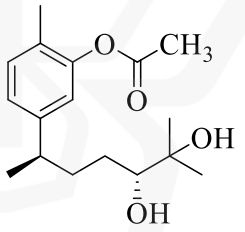

(69)

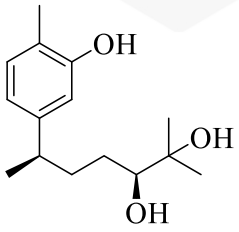

(70)

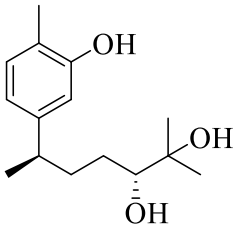

(71)

Oxidation of XNT **(1)** using Fremy's salt afforded curcuquinone **(72)**, followed by reduction reaction furnished curcuhydroquinone **(73)**. Subsequent acetylation

reaction of derivative **(73)** resulted in formation of curcuquinone diacetate **(75)**. In addition, the reaction of derivative **(73)** with benzyl bromide yielded dibenzyloxy curcuquinone **(75)**.

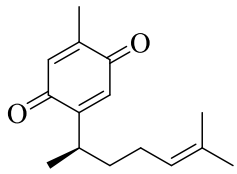

(72)

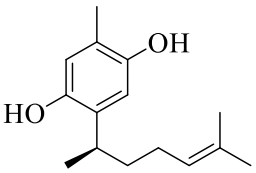

(73)

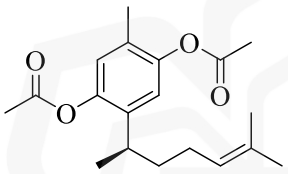

(74)

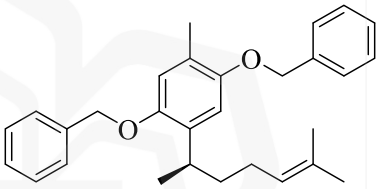

(75)

The hydroxyl group of XNT **(1)** can also be substituted to benzyloxy and methoxy functionalities through Williamson ether synthesis reaction, which afforded benzyl xanthorrhizyl ether **(76)** and methyl xanthorrhizyl ether **(77)**, respectively. Several modifications were made to the alkene functionality from derivative **(76)** through sequential reactions. Firstly, (10*S*)-10,11-dihydro-benzyloxy xanthorrhizol **(78)** was synthesised through Sharpless AD reaction. Then, acetylation of derivative **(78)** afforded monoacetate derivative **(79)** and followed by subsequent dehydration reaction to yield allylic acetate derivative **(80)**. Then, the hydrolysis of derivative **(80)** using potassium carbonate in methanol to furnish allylic alcohol derivative **(82)** (Sirat et al., 2007).

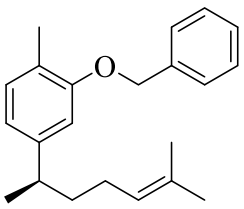

(76)

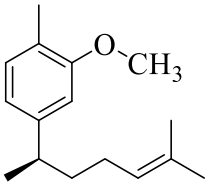

(77)

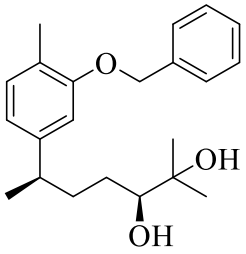

(78)

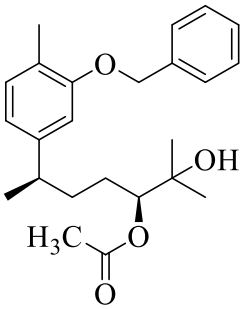

(79)

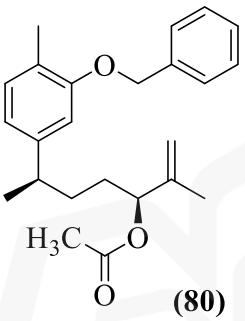

(80)

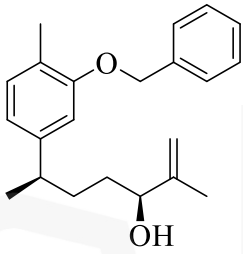

(81)

A series of nitrogen-containing XNT derivatives, namely 3-(morpholino)propyl xanthorrhizol **(82)**, 3-(6,7-dimethoxyquinazolin-4(3*H*)-onepropyl xanthorrhizol **(83)**, and 3-(benzylamino)propyl xanthorrhizol **(84)** were also synthesised (Purnamasari et al., 2024). The derivatives were prepared using two-step synthesis. Firstly, the synthesis of respective alkyl halides as substituents was prepared, followed by reaction of the synthesised alkyl halides with XNT **(1)** through Williamson ether synthesis. In addition, another two isomers derivatives called 6-nitroxanthorrhizol **(85)** and 4-nitroxanthorrhizol **(86)** were synthesised using nitration reaction.

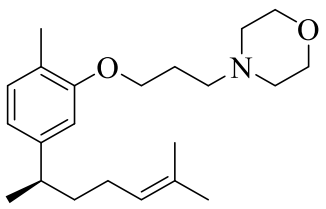

(82)

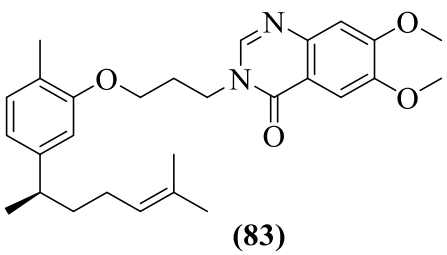

(83)

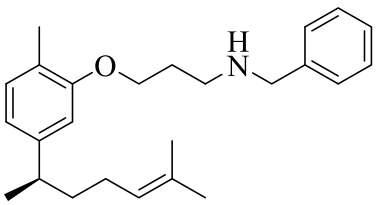

(84)

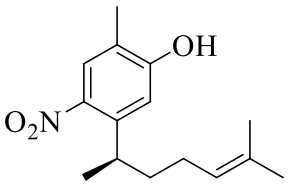

(85)

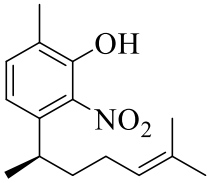

(86)

2.5 ANTI-INFLAMMATORY ACTIVITIES OF XANTHORRHIZOL AND ITS DERIVATIVES

XNT **(1)** exhibited inhibitory activities on inflammatory mediators, IL-6 and TNF-α. The secretion of IL-6 and TNF-α in activated microglial cells were reduced by 98% and 96%, respectively in the presence of 10 µM of XNT **(1)**. Moreover, the concentration of nitric oxide (NO) in lipopolysaccharide (LPS) treated microglial cells were also reduced by 98% upon treatment with XNT **(1)** (Lim et al., 2005). XNT **(1)** also inhibited cyclooxygenase-2 (COX-2) (IC_{50} = 0.2 γ/mL) and inducible nitric oxide synthase (iNOS) (IC_{50} = 1.0 γ/mL) enzymes in prostaglandin E2 and NO production assay (Lee et al., 2002). The level of COX-2 and iNOS expressions were also suppressed for 12-*O*-tetradecanoylphorbol-13-acetate (TPA)-induced acute inflammation that was pre-treated with XNT **(1)**. It was also demonstrated that XNT **(1)** blocked the nuclear factor-κB (NF-κB), a signaling molecule that regulates the expression of COX-2 and iNOS expression (Chung et al., 2007).

The potential anti-inflammatory activity of XNT **(1)** was further proved through a study on LPS-treated human gingival fibroblast-1 (HPF-1) cell. It was found that expression of NF-κB and IL-1β on LPS-treated HPF-1 cells was suppressed by action of XNT **(1)** (Kim et al., 2018). The suppression of NF-κB and IL-1β were attributed to the downregulation of mitogen-activated protein kinase (MAPK) signaling pathway. Similar findings on the effect of XNT **(1)** on the suppression of TNF-α, IL-1β, and IL-6 were reported in other studies by Liao et al. (2019), Zhou et al. (2022), and (Sun et al., 2023). XNT **(1)** also inhibited the IL-5-, IL-13-and IL-17-expressing T helper (CD4-positive) cells frequency in dose-dependent manner (Liao & Wong, 2022).

Three XNT derivatives **(64)**, **(66)**, and (**67)** exhibited higher IC_{50} (73.85, 354.05, and 97.19 µM, respectively) in NO inhibition assay in LPS-induced RAW 246.7 cell compared to XNT **(1)** (IC_{50} = 31.82 µM). Meanwhile, derivative **(65)** did not exhibit any activity in the assay. This indicated that substitution of hydroxyl and alkene functionalities of XNT **(1)** hindered the activities. However, the toxicity of substituted XNT against RAW 264.7 macrophage cells was reduced compared to XNT **(1)**. In the cytotoxicity assay study, derivative **(64-67)** exhibited higher LD_{50} (31.15 to 117.86 µM, respectively) compared to XNT **(1)** (LD_{50} = 30.97 µM) (Rahayu et al., 2020).

Anti-inflammatory activities of XNT **(1)** were also evaluated using *in silico* studies. XNT **(1)** interacted with both COX-1 (PDB ID: 1EQG) and COX-2 (PDB ID: 3LN1) with binding energies of -8.85 and -10.11 kJ/mol, respectively. The molecular docking also revealed that XNT **(1)** was formed hydrogen bonding with several amino acid residues important for activity in both enzymes. XNT **(1)** interacted with COX-1 through hydrogen bonding with Arg120 and Tyr335 residues. Meanwhile, hydrogen bond interactions were observed with residues Gln178 and Leu338 of COX-2 enzyme. The docking pose of XNT **(1)** in COX-2 was similar pattern to the pose of reference compound celecoxib **(87)** (Dinata et al., 2014).

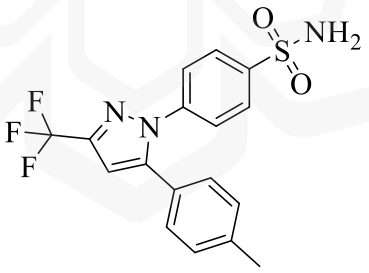

(87)

Additionally, XNT **(1)** was also docked against the 5-LOX (PDB ID: 308Y) with binding energy of -5.41 kcal/mol. XNT **(1)** also exhibited comparable binding energy towards 5-LOX receptor compared other active compounds found in *C. xanthorrhiza*, i.e. *β*-curcumene **(88)** (5.31 kcal/mol), *α*-terpineol **(89)** (-5.65 kcal/mol), and *β*-turmerone **(90)** (-5.70 kcal/mol) (Gadnayak et al., 2022).

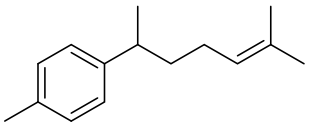

(88)

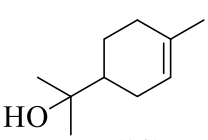

(89)

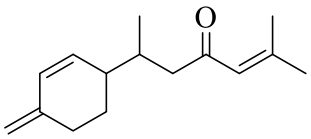

(90)

The activity of XNT **(1)** against several enzymes and inflammatory mediators showed that it is indeed a good anti-inflammatory agent. To the best of our knowledge, there has yet been any research on Hyal enzyme inhibitory activity of XNT **(1)**, specifically through Hyal-1 inhibition.

CHAPTER THREE

METHODOLOGY

3.1 CHEMICALS AND GENERAL INSTRUMENTATIONS

All organic solvents used for in this research were from Q-rec (analytical grade). The dry solvents i.e. dry pyridine was prepared by soaking in sodium hydroxide (NaOH) overnight, followed by distillation. Meanwhile, dry acetone was furnished by mixing the acetone with 1M NaOH and silver nitrate before drying over anhydrous magnesium sulphate ($MgSO_4$) and distilled (Furniss et al., 1989).

The chemicals used in this study were acetic anhydride (Merck), anhydrous potassium carbonate (K_2CO_3) (Bendosen), benzyl bromide (98%, Sigma-Aldrich), 4-nitrobenzyl bromide (99% Sigma-Aldrich), 2-(chloromethyl)pyridine hydrochloride (98%, Sigma-Aldrich), 3-(trifluoromethyl)benzyl chloride (97%, Sigma-Aldrich), 2-(chloromethyl)tetrahydro-2*H*-pyran (99 %, Sigma-Aldrich), tetrahydrofurfuryl chloride (≥97%, Sigma-Aldrich), cesium carbonate (Cs_2CO_3) (99%, Sigma-Aldrich), *N*-(2-chloroethyl)urea (Sigma-Aldrich), 4-imidazolecarboxylic acid (98%, Sigma-Aldrich), *N*,*N*′-diisopropylethylamine (DIPEA) (98%, Acros Organics), *N*,*N*′-dicyclohexylcarbodiimide (DCC) (99%, Sigma-Aldrich), *N*,*N*-dimethylpyridin-4-amine (DMAP) (99%, Sigma-Aldrich), 1-bromo-3-chloropropane (99%, Sigma-Aldrich), ethylamine hydrochloride (98%, Sigma-Aldrich) and Boc-*β*-alanine (99%, Sigma-Aldrich). Hydrochloric acid (HCl), sodium bicarbonate ($NaHCO_3$), sodium chloride (NaCl), and anhydrous magnesium sulphate ($MgSO_4$) were from analytical grade.

Thin layer chromatography (TLC) experiment was conducted on silica gel F_{254} plates (Merck) as the stationary phase. The spots were visualised under ultraviolet (UV) light (λ 254 and 365 nm). In addition, the developed TLC plates were also visualised using TLC stains. Vanillin-sulphuric acid reagent was sprayed on the TLC plate and heated on a hot plate. Meanwhile, iodine staining was conducted by placing the TLC plate in developing beaker containing evaporated iodine chip. TLC plate staining were

also done by immersion of the developed plate into bromocresol green and Dragedorff's reagent. Vacuum liquid chromatography (VLC) was performed by using silica gel 60 (230-400 mesh ASTM; Merck), while column chromatography (CC) was carried out by using silica gel 60 (70-230 mesh ASTM; Merck) as the stationary phase. Evaporation of organic solvents were carried out by using IKA® RV 10 Control rotary evaporator.

The chemicals used for Hyal-1 enzymatic inhibitory assay were hyaluronidase enzyme type 1-S from bovine testes (EC 3.2.1.35), sodium phosphate ($Na_2H_2PO_4$) buffer, hyaluronic acid, apigenin and bovine serum albumin (BSA). Meanwhile, the chemicals for LOX-3 enzymatic inhibitory assay included soybean lipoxygenase type 1-B (EC 1.13.11.12), sodium phosphate ($Na_2H_2PO_4$) buffer, nordihydroguaiaretic acid (NDGA) and linoleic acid sodium salt. All chemicals were purchased from Sigma-Aldrich. The absorbance data for both assays was recorded by BioTek Epoch 2 microplate spectrophotometer.

The Attenuated Total Reflectance Infrared (ATR-IR) spectrum was recorded on Perkin-Elmer spectrophotometer at wavelength from 4000 to 600 cm^{-1}. The ^{1}H and ^{13}C Nuclear Magnetic Resonance (NMR) analysis were performed by using JEOL ECS 400 MHz spectrometer (Institute of Science, Universiti Teknologi MARA), Bruker Ultra Shield Plus 500 MHz spectrometer (Universiti Malaysia Pahang Al-Sultan Abdullah) and Bruker Ascend 600 MHz spectrometer (Forest Research Institute Malaysia, FRIM). Chemical shifts (δ) were obtained in parts per million (ppm) in deuterated chloroform ($CDCl_3$) and deuterated dimethyl sulfoxide (DMSO-D_6) as the solvents.

Gas Chromatography-Mass Spectrometry (GC-MS) analysis was carried out on GC-MS Perkin Elmer (ClarusTM 680/GC SQ8T/MS) (Kulliyyah of Science, IIUM) equipped with Elite-5MS capillary column (30 m x 0.25 mm id, 0.25 µm film thickness;Perkin Elmer) and GC-MS Agilent Technologies 7890A/5975C equipped with HP-5MS (30 m x 0.25 mm id, 0.25 µm film thickness;Agilent) (FRIM). The column temperature was set from 60 °C (10 min), at 3 °C min^{-1} to 230 °C (10 min). Specific rotation values for chiral compounds were recorded in methanol (MeOH) at 25ºC by using Anton Paar Modular compact polarimeter (MCP 100) in polarimeter tube with cell length of 2.5 mm and volume of 0.05 mL.

3.2 PLANT MATERIALS

The rhizome of *Curcuma xanthorrhiza* (20.0 kg) was purchased from the Chow Kit market, Kuala Lumpur. The plant specimen was identified by a botanist, Dr Shamsul bin Khamis and deposited at UKMB herbarium, Universiti Kebangsaan Malaysia (voucher number: ID008/2021). The extraction of *C. xanthorrhiza* essential oil was conducted by using Turbo Extractor at Institute Bioproduct Development (IBD), Universiti Teknologi Malaysia (UTM), Skudai.

3.3 COMPUTATIONAL TOOLS

All the crystal structures of enzymes in this study were retrieved from Protein Data Bank (PDB) (https://rcsb.org). The software used for the computational studies are ChemDraw Professional 15.0, Avogadro 2.0 (Hanwell et al., 2012), OpenBabel v2.3.1 (O'Boyle et al., 2011), AutoDockTools 1.5.6. (Goodsell & Olson, 1990), AutoDock Vina (Trott & Olson, 2010), PyMOL 2.5.2 (The PyMOL Molecular Graphics System, Version 2.0 Schrödinger, LLC.), Discovery Studios Visualizer (BIOVIA, Dassault Systèmes, 2021), and LigBuilder V3 (Yuan et al., 2020). The drug-likeness profiles of all compounds were predicted using SwissADME (https://swissadme.ch). The software used for molecular dynamics studies are CHARMM-GUI server (Brooks et al., 2009; Jo et al., 2008; Lee et al., 2016), GROMACS 2022.6 (Baeuer et al., 2022), Visual Molecular Dynamics (VMD) (Humphrey et al., 1996), and Grace5.1.25 software (Turner, 2005).

3.4 IDENTIFICATION OF XANTHORRHIZOL DERIVATIVES AS HYAL-1 AND LOX-3 INHIBITORS

The structures of XNT derivatives were obtained *via* two strategies, which are mining from in-house database using molecular docking and *in silico* fragment-based drug design (FBDD). From these strategies, the XNT derivatives were synthesised, characterised and subjected to *in vitro* enzymatic inhibitory assay against both enzymes.

3.4.1 Molecular Docking of Xanthorrhizol Derivatives against Hyal-1 and LOX-3 enzymes

A total of thirty XNT derivatives **(63-81**, **91-101)** obtained from literatures (Aguilar, Delgado, & Villarreal, 2001; Ngai & Sirat, 2004; Rahayu et al., 2020; Sirat et al., 2007) were treated as ligands and subjected to virtual screening using molecular docking against Hyal-1 and LOX-3 enzymes. Apigenin **(17)**, seric acid A **(26)** and disodium chromoglycate **(27)** were chosen as control compounds for docking against Hyal-1. All ligands were drawn using ChemDraw Professional 15.0 and optimised using AutoOptimize Tools in Avogadro 2.0. The ligands were then computed with Gasteiger charge by using AutoDockTools 1.5.6 software and saved as PDBQT format.

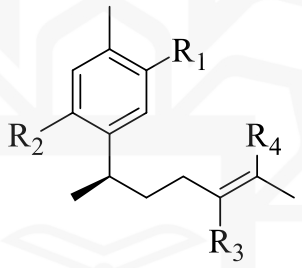

(1) = R_1-OH, R_2-H, R_3-H, R_4-CH_3
(63) = R_1-OH, R_2-H, R_3-H, R_4-H
(64) = R_1- Ac, R_2-H, R_3-H, R_4-CH_3
(65) = R_1-Bz, R_2-H, R_3-H, R_4-CH_3
(66) = R_1- Ac, R_2-H, R_3-Ac, R_4-OH
(67) = R_1-Bz, R_2-H, R_3-Ac, R_4-OH
(68) = R_1- Ac, R_2-H, R_3-(*S*)-OH, R_4-OH
(69) = R_1- Ac, R_2-H, R_3-(*R*)-OH, R_4-OH
(70) = R_1-OH, R_2-H, R_3-(*S*)-OH, R_4-OH
(71) = R_1-OH, R_2-H, R_3-(*R*)-OH, R_4-OH
(72) = R_1- CO, R_2-CO, R_3-H, R_4-H
(73) = R_1-OH, R_2-OH, R_3-H, R_4-CH_3
(74) = R_1-Ac, R_2-Ac, R_3-H, R_4- CH_3
(75) = R_1-OBn, R_2-OBn, R_3-H, R_4- CH_3
(76) = R_1-OBn, R_2-H, R_3-H, R_4-CH_3
(77) = R_1-OMe, R_2-H, R_3-H, R_4-CH_3
(78) = R_1-OBn, R_2-H, R_3-(*S*)-OH, R_4-OH
(79) = R_1-OBn, R_2-H, R_3-Ac, R_4-OH
(80) = R_1-OBn, R_2-H, R_3-Ac, R_4-CH_2
(81) = R_1-OBn, R_2-H, R_3-OH, R_4-CH_2
(91) = R_1-Ac, R_2-Ac, R_3-(*S*)-OH, R_4-OH
(92) = R_1-OBn, R_2-OBn, R_3-(*S*)-OH, R_4-OH
(93) = R_1-OBn, R_2-OBn, R_3-(*R*)-OH, R_4-OH
(94) = R_1-OH, R_2-OH, R_3-(*S*)-OH, R_4-OH
(95) = R_1-OH, R_2-OH, R_3-(*R*)-OH, R_4-OH
(96) = R_1-OBn, R_2-H, R_3-(*R*)-OH, R_4-OH
(97) = R_1-OMe, R_2-H, R_3-(*S*)-OH, R_4-OH
(98) = R_1-OMe, R_2-H, R_3-Ac, R_4-OH
(99) = R_1-OMe, R_2-H, R_3-Ac, R_4-CH_2
(100)= R_1-OMe, R_2-H, R_3-OH, R4-CH_2
(101)= R_1- OH, R_2-H, R_3-OH, R_4-CH_2

*(OBn= benzyloxy, Ac = acetate, Bz = benzoate, OMe = methoxy, OH = hydroxyl, H = hydrogen, CO =carbonyl)

The crystal structure of human Hyal-1 (PDB ID: 2PE4) (Chao et al., 2007) and soybean LOX-3 (PDB ID: 1IK3) (Skrzypczak-Jankun et al., 2001) enzymes were directly obtained from Protein Data Bank. All bound ligands and water molecules of the enzymes were removed by using PyMOL software. Then, Kollman charges and polar hydrogen atoms were computed into the enzymes by using AutoDockTools software and saved as PDBQT format.

All ligands were subjected to molecular docking studies using AutoDock Vina. For Hyal-1 enzyme, the grid box was set at 62, 58 and 58 Å (x, y, z, axes respectively) and centred at 37.045, -17.292, -11.844 (x, y, z, respectively). Meanwhile, the grid box for LOX-3 was set at 20, 26 and 26 Å (x, y, z axes respectively) with center of grid box was set as 20.950, 0.657 and 18.863 (x, y, z respectively). The spacing used for the grid boxes were 1 Å. These grid boxes were specified to cover all the amino acid residues in the active site of the protein as stated in **Section 2.2** and **Section 2.3**. Each docking runs generated ten ligand conformation, ranked based on their binding energies score (kcal/mol). The docking conformations and interactions with amino acid residues were visualised using PyMOL and Discovery Studios Visualizer.

3.4.2 *In Silico* Fragment-Based Drug Design (FBDD)

The *in silico* FBDD approach was performed on target proteins Hyal-1 and LOX-3 enzymes to generate potential inhibitors with XNT **(1)** as the chemical scaffold. Firstly, the crystal structure of Hyal-1 and LOX-3 enzymes were submitted to Cavity mode in LigBuilder software to predict their potential binding sites or cavities. The detected cavities were ranked based on the CavityScore and cavities that was identical with the reported binding sites were selected for further study.

The structure of XNT **(1)** and the cavities selected were then utilised as seed structure and target site, respectively for FBDD in the Build mode. The conversion from PDBQT format to MOL2 format and addition of hydrogen atoms of XNT **(1)** were done by using OpenBabel software. The growing site was defined by changing the atom type of the corresponding hydrogen from "H" to "H.spc" in MOL2 input file. The fragment library readily available in LigBuilder software composed of 2928 fragments were then

utilised as the building blocks to be linked to the assigned growing site for the generation of new XNT derivatives.

A total of 1159 and 1887 XNT derivatives were generated as Hyal-1 and LOX-3 inhibitors, respectively, followed by screening using molecular docking. The top fifty derivatives for Hyal-1 inhibitors **(Appendix A)** and LOX-3 inhibitors **(Appendix B)** were ranked from the lowest to the highest binding energies. The structures of all derivatives were further screened and modified based on their synthetic tractability. Finally, a total of five **(102-106)** and four **(107-110)** new XNT derivatives were proposed to be synthesised as Hyal-1 and LOX-3 inhibitors, respectively.

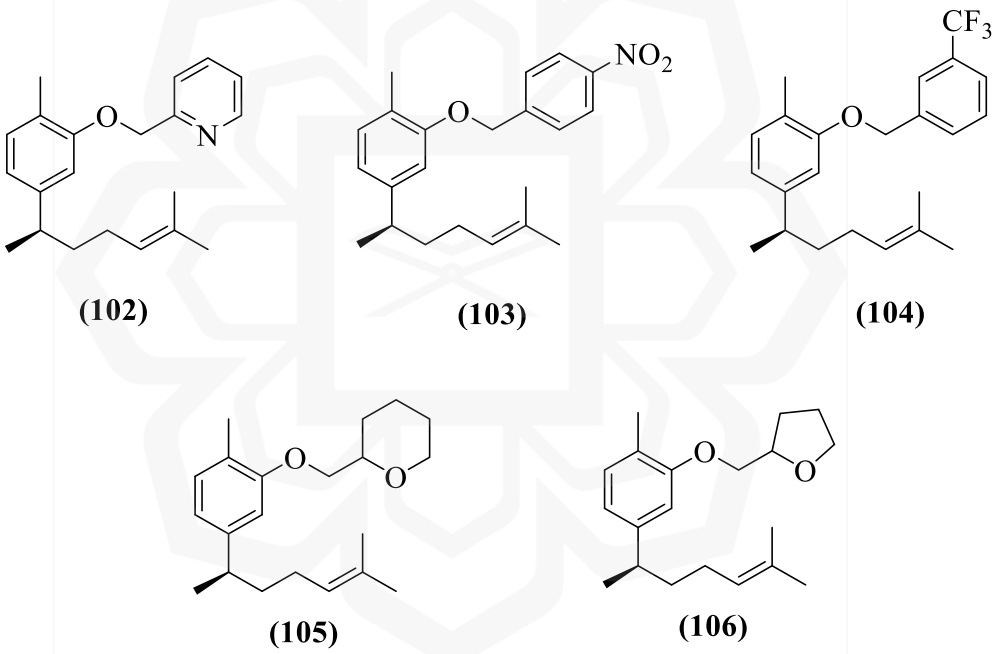

(102) **(103)** **(104)**

(105) **(106)**

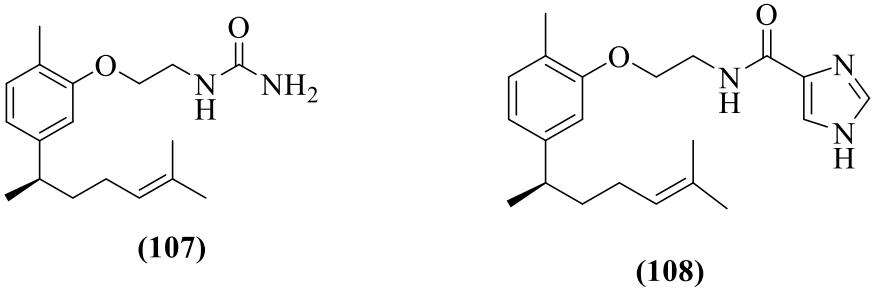

(107) **(108)**

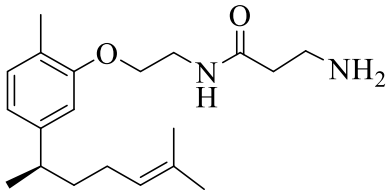

(109)

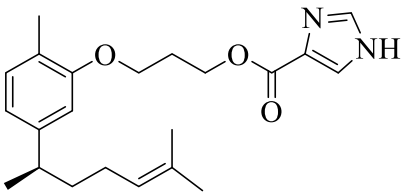

(110)

3.5 *IN SILICO* DRUG-LIKENESS AND ABSORPTION PROPERTIES

The drug-likeness and prediction of its absorption properties of all derivatives were generated by using SwissADME tools to predict their physicochemical properties and absorption in human body. Each derivative was evaluated based on the molecular weight, solubility, lipophilicity, topological polar surface area (TPSA), carbon saturation, and flexibility parameters that contributed to the drug absorption in the human body.

3.6 SYNTHESIS AND CHARACTERISATION OF XANTHORRHIZOL DERIVATIVES

Prior to the synthesis of the derivatives, XNT **(1)** was isolated and purified from *C. xanthorrhiza* essential oil. XNT **(1)** was then used as the starting material for the synthesis of its derivatives. All derivatives were characterised by using NMR, ATR-IR, GC-MS and polarimeter.

3.6.1 Isolation and Purification of Xanthorrhizol from *C. Xanthorrhiza.*

The essential oil of *C. xanthorrhiza* (9.0115 g) was subjected to VLC over silica gel (286.44 g), with mixture of hexane (*n*-hex) and diethyl ether (Et_2O) as the solvent system. The solvent polarity was increased by 2% from *n*-hex:Et_2O 200:0 to 190:10, followed by 1% from 190:10 until 180:20, 10% from 180:20 to 100:100, and finally, 50% from 100:100 to 0:200. A total of 25 fractions were collected. The fractions with similar TLC profiles were combined to afford eight major fractions labelled as CXED1

to CXED8. The fraction CXED5 having XNT **(1)** as the major product were further subjected for purification through two-step chemical synthesis method, which were acetylation and hydrolysis.

3.6.1.1 Acetylation Reaction on CXED5 fraction

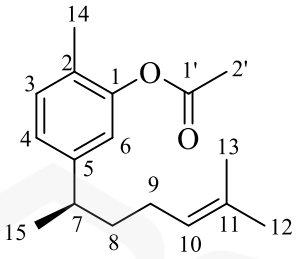

(64)

The CXED5 fraction (1.2371 g) was dissolved in Et_2O (10 mL). The solution was subjected to acetylation reaction by adding dry pyridine (4.0 eq, 22.67 mmol, 1.82 mL), and acetic anhydride (3.5 eq, 19.83 mmol, 1.77 mL) into a 50 mL-round bottom flask. The reaction mixture was stirred continuously for 24 hours at room temperature. The reaction was monitored by using TLC with *n*-hex:Et_2O, (4:1) as the solvent system. Upon reaction completion, distilled water (5 mL) was added, and the reaction mixture was stirred for another 10 minutes. The reaction mixture was washed with 1 M HCl solution (20 mL x 3 times), saturated sodium Na_2CO_3 solution (20 mL x 3 times), and brine solution (20 mL) once. The organic layer was collected and dried with anhydrous magnesium sulphate. The organic solvent was evaporated *in vacuo* to yield a yellow oil (1.1429 g).

The yellow oil was purified over *via* CC (20 mm x 240 mm, 40.7180 g SiO_2) using a mixture of *n*-hex:Et_2O as the solvent to afford 188 fractions. Fractions 1 to 75 eluted with mobile phase ratio (*n*-hex:Et_2O, 99:1 to 98:2) were combined to afford a major fraction labelled as AX-1. Fraction AX-1 showed the presence of a purple spot on TLC over vanilin-sulphuric acid reagent afforded xanthorrhizyl acetate (**64**) as a colourless oil (1.2229 g, 79.12%) with R_f value of 0.825 (*n*-hex:Et_2O, 4:1).

Spectral data: IR (ATR) ν_{max} cm^{-1}; 2957.87 and 2871.92 (sp^3 CH), 1768.06 (C=O ester), 1210.68 (C-O ester) (**Appendix C1**); ^{1}H-NMR (500 MHz, $CDCl_3$): δ_H 1.20 (3H, d, *J* =7.0 Hz, H-15), 1.52 (3H, s, H-12), 1.54-1.60 (2H, m, H-8), 1.67 (3H, s, H-13), 1.84-1.90 (2H, m, H-9), 2.14 (3H, s, H-14), 2.31 (3H, s, H-2'), 2.66 (1H, sext, *J* = 7.0 Hz, H-7), 5.07 (1H, tt, *J* = 7.1 Hz, 1.4 Hz, H-10), 6.81 (1H, d, *J* = 1.7 Hz, H-6), 6.96 (1H, dd, *J* = 1.7, 7.7 Hz, H-4), 7.12 (1H, d, *J* = 7.7 Hz, H-3) (**Appendix C2**); ^{13}C-NMR (125 MHz, $CDCl_3$): δ_C 15.78 (C-14), 17.66 (C-12), 20.83 (C-2'), 22.15 (C-15), 25.69 (C-13), 26.07 (C-9), 38.33 (C-8), 38.85 (C-7), 120.34 (C-6), 124.38 (C-4), 124.71 (C-2), 127.17 (C-10), 130.83 (C-3), 131.52 (C-11), 146.94 (C-5) 149.30 (C-1), 169.20 (C-1') (**Appendix C3**); GC-MS (97.31%): t_R 50.71 min, *m/z* 260 (16) [M^+] ($C_{17}H_{24}O_2$), 177 (14), 148 (39), 136 (100), 121 (30) (**Appendix C4**); $[\alpha]_D^{25}$ –35.64 (*c* 1.01, MeOH).

3.6.1.2 Hydrolysis of Xanthorrhizyl Acetate (64)

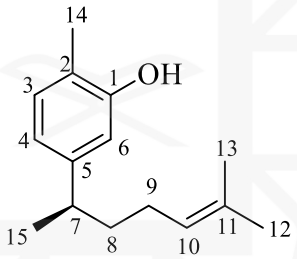

(1)

Xanthorrhizyl acetate **(64)** (1.2230 g, 4.70 mmol), anhydrous K_2CO_3 (3.0 eq, 14.11 mmol, 1.9486 g), MeOH (7 mL) and distilled water (1 mL) were mixed in 50 mL-round bottom flask and left for stirring at room temperature for 7 hours. The reaction was monitored by using TLC with *n*-hex:Et_2O (4:1) as the solvent system. Distilled water (5 mL) was then added to the reaction mixture and washed with ethyl acetate (EtOAc) (10 mL x 3 times). The organic phase was obtained and dried over anhydrous $MgSO_4$ before evaporated to drying to yield XNT **(1)** as a light yellow oil (0.9128 g, 88.88%) with R_f value of 0.525 (*n*-hex:Et_2O, 4:1).

Spectral data: IR (ATR) ν_{max} cm^{-1}; 3378.37 (-OH), 2961.65 and 2918.05 (C-H sp^3), 1620.71 and 1454.76 (C=C aromatic) **(Appendix D1)**; ^{1}H-NMR (500 MHz, $CDCl_3$): δ_H 1.19 (3H, d, *J* = 7.0 Hz, H-15), 1.53 (3H, s, H-12), 1.53-1.60 (2H, m, H-8), 1.67 (3H, s, H-13), 1.84-1.90 (2H, m, H-9), 2.21 (3H, s, H-14), 2.61 (1H, sext, *J* = 7.0 Hz, H-7), 4.62 (1H, s, H-1), 5.07 (1H, tt, *J* = 7.7 Hz, 1.4 Hz, H-10), 6.60 (1H, d, *J* = 1.6 Hz, H-6), 6.66 (1H, dd, *J* = 7.7, 1.6 Hz, H-4), 7.01 (1H, d, *J* = 7.7 Hz, H-3) (**Appendix D2**); ^{13}C-NMR (125 MHz, $CDCl_3$): δ_C 15.31 (C-12), 17.68 (C-14), 22.38 (C-15), 25.71 (C-13), 26.16 (C-9), 38.38 (C-8), 39.04 (C-7), 113.54 (C-6), 119.45 (C-4), 120.79 (C-2), 124.52 (C-10), 130.76 (C-3), 131.43 (C-11), 147.25 (C-5), 153.61 (C-1) (**Appendix D3**); GC-MS (97.74%): t_R 49.21 min, *m/z* 218 (25) [M^+] ($C_{15}H_{22}O$), 148 (38), 136 (100), 121 (18) (**Appendix D4**); $[\alpha]_D^{25}$ –59.26 (*c* 1.08, MeOH) [lit. (Ngai & Sirat, 2005); $[\alpha]_D$ –49.4 (*c* 1.00, MeOH)]

3.6.2 Synthesis of Xanthorrhizol Derivatives as Hyal-1 Inhibitors (76, 102-105, 117)

The XNT derivatives (**76, 102-105**, **117**) were synthesised using Williamson ether synthesis, following method from Huang et al. (2019) with slight modifications. In this reaction, XNT **(1)** was refluxed with base for one hour, followed by addition of respective alkyl halides; benzyl bromide **(111)**, 2-(chloromethyl) pyridine hydrochloride **(112)**, 4-nitrobenzyl bromide **(113)**, 3-(trifluoromethyl)benzyl chloride **(114)**, 2-(chloromethyl) tetrahydro-2*H*-pyran **(115)**, tetrahydrofurfuryl chloride **(116)**. The reactions were monitored using TLC until completion. After the reaction was completed, distilled water (5 mL) was added, and the reaction mixture was washed with EtOAc (10 mL x 3 times), followed by extraction of the organic layer. The organic layer was dried over $MgSO_4$ and evaporated to dryness. The purification of crude products by CC afforded xanthorrhizol derivatives **(76, 102-105**, **117)**. The general reaction scheme for the reactions were shown in **Scheme 3.1**.

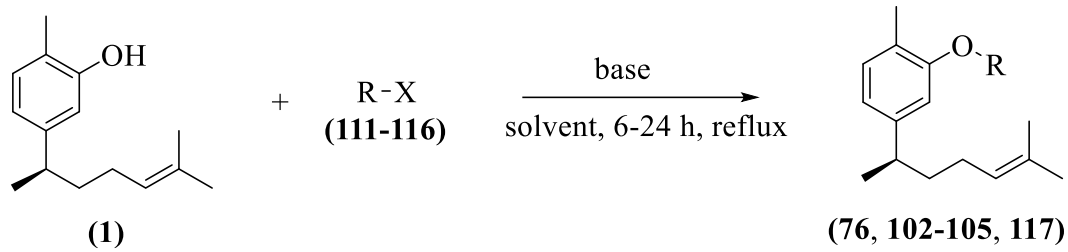

(1) **(76**, **102-105**, **117)**

(111) R= benzyl, X= Br

(112) R= 2-methyl pyridine, X= Cl

(113) R= 4-nitrobenzyl, X= Br

(114) R= 3-(trifluoromethyl)benzyl, X= Cl

(115) R= 2-methyltetrahydro-2*H*-pyran, X= Cl

(116) R= tetrahydrofurfuryl, X= Cl

(76) R= methylbenzene

(102) R= 2-methylpyridine

(103) R= 4-nitrobenzene

(104) R = 3-(trifluoromethyl)benzene

(**105)** R= methyltetrahydro-2*H*-pyran

(117) R = propyl acetate

Scheme 3.1 General scheme for the synthesis of XNT derivatives **(76, 102-105**, **117)**

3.6.2.1 Benzyl Xanthorrhizyl Ether (76)

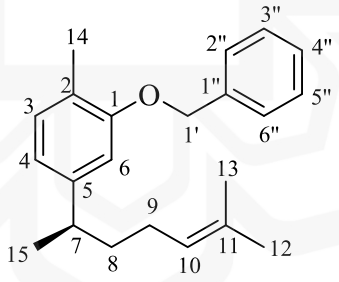

(76)

XNT **(1)** (0.500 g, 2.29 mmol) and K_2CO_3 (3.0 eq, 6.87 mmol, 0.9495 g) in dry acetone (10 mL) was refluxed in oil bath at 90 ºC for 1 hour. Benzyl bromide **(111)** (1.5 eq, 3.44 mmol, 0.4080 g) was then added dropwise into the reaction mixture. The reaction mixture was stirred at 90°C for another 6 hours. The reaction mixture was then washed and work up following the general procedure in **Section 3.6.2** to afford crude product. The crude product was then purified by CC using *n*-hex as eluent to yield derivative **(76)** with IUPAC name 1-(benzyloxy)-2-methyl-5-(6-methylhept-5-en-2-yl)benzene as yellow oil (0.3151 g, 63.02%) with R_f value of 0.85 (*n*-hex:Et_2O 4:1).

Spectral data: IR (ATR) ν_{max} cm^{-1}; 2960.04 and 2919.05 (C-H sp^3), 1610.85 and 1452.11 (C=C aromatic), 1252.58 (C-O) (**Appendix E1**); ^{1}H-NMR (600 MHz, $CDCl_3$): δ_H 1.23 (3H, d, *J* = 7.0 Hz, H-15), 1.55 (3H, s, H-12), 1.56-1.65 (2H, m, H-8), 1.70 (3H, s, H-13), 1.85-1.95 (2H, m, H-9), 2.27 (3H, s, H-14), 2.67 (1H, sext, *J* = 7.0 Hz, H-7), 5.10 (2H, s, H-1'), 5.12 (1H, tt, *J* = 7.1 Hz, 1.2 Hz, H-10), 6.72 (1H, d, *J* = 1.2 Hz, H-6), 6.74 (1H, dd, *J* = 7.2, 1.2 Hz, H-4), 7.09 (1H, d, *J* = 7.2 Hz, H-3), 7.34 (1H, t, *J* = 7.4, 1.2 Hz, H-4"), 7.40 (2H, t, *J* = 7.4 Hz, H-3"/H-5"), 7.48 (2H, dd, *J* = 7.4, 1.2 Hz, H-2"/H-6") (**Appendix E2** and **E3**); DEPTQ (150 MHz, $CDCl_3$): δ_C 15.99 (C-12), 17.69 (C-14), 22.50 (C-15), 25.70 (C-13), 26.16 (C-9), 38.42 (C-8), 39.44 (C-7), 69.85 (C-1'), 110.50 (C-6), 119.09 (C-4), 124.36 (C-2), 124.54 (C-10), 127.17 (C-3"/C-5"), 127.65 (C-3), 128.44 (C-2"/C-6"), 130.44 (C-4"), 131.36 (C-1"), 137.64 (C-11), 146.62 (C-5), 156.78 (C-1) (**Appendix E4**); GC-MS (98.77%): t_R 63.11 min, *m/z* 308 (23), [M^+] ($C_{22}H_{28}O$), 226 (20), 135 (20), 91 (100) (**Appendix E5**); $[\alpha]_D^{25}$ –27.27 (*c* 0.88, MeOH).

3.6.2.2 (2-Pyridinyl)methyl Xanthorrhizyl Ether (102)

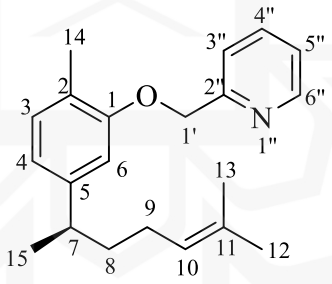

(102)

XNT **(1)** (0.050 g, 22.90 mmol) and anhydrous K_2CO_3 (5.0 eq, 0.1583 g, 1.145 mmol) in dry acetone (10 mL) was refluxed for 1 hour, followed by addition of 2-(chloromethyl)pyridine hydrochloride **(112)** (4.0 eq, 0.1503 g, 91.60 mmol). The reaction mixture was stirred for another 12 hours. The reaction mixture was then washed and work up following the general procedure in **3.6.2** to yield the crude product. The crude product was purified over CC using 100% *n*-hex to afford derivative **(102)** with IUPAC name 2-((methyl-5-(6-methylhept-5-en-2-yl)phenoxy)methyl pyridine as a yellow oil (0.02891 g, 40.79%) with R_f value of 0.58 (*n*-hex:Et_2O, 3:2).

Spectral data: IR (ATR) ν_{max} cm^{-1}; 2959.60 and 2925.80 (C-H sp^3), 1613.70 and 1456.98 (C=C aromatic), 1591.20 (C=N), 1262.11 (C-O), 1133.65 (C-N) (**Appendix F1**); ^{1}H-NMR (500 MHz, $CDCl_3$): δ_H 1.17 (3H, d, *J* = 6.9 Hz, H-15), 1.51 (3H, s, H-12), 1.52-1.58 (2H, m, H-8), 1.66 (3H, s, H-13), 1.77-1.89 (2H, m, H-9), 2.30 (3H, s, H-14), 2.62 (1H, sext, *J* = 6.9 Hz, H-7), 5.05 (1H, tt, *J* = 7.1, 1.2 Hz, H-10), 5.22 (2H, s, H-1'), 6.71 (1H, s, H-6), 6.72 (1H, s, H-4), 7.07 (1H, d, *J* = 7.6 Hz, H-3), 7.20-7.26 (1H, m, H-5"), 7.57 (1H, d, *J* = 7.8 Hz, H-3"), 7.72 (1H, ddd, *J* = 7.8, 7.6, 1.6 Hz, H-4"), 8.58 (1H, dd, *J* = 4.8, 1.6 Hz, H-6") (**Appendix F2** and **F3**); DEPTQ (125 MHz, $CDCl_3$): δ_C 16.05 (C-12), 17.70 (C-14), 22.47 (C-15), 25.71 (C-13), 26.12 (C-9), 38.41 (C-8), 39.40 (C-7), 70.44 (C-1'), 110.39 (C-6), 119.35 (C-4), 120.94, (C-5"), 122.42 (C-3"), 124.08 (C-2), 124.51 (C-10), 130.51 (C-3), 131.38 (C-11), 136.81 (C-4"), 146.82 (C-5), 149.03 (C-6"), 156.33 (C-1), 157.94 (C-2") (**Appendix F4**); GC-MS (90.05%): t_R 63.90 min, *m/z* 309 (36), [M^+] ($C_{21}H_{27}NO$), 227 (38), 135 (38), 93 (100), 65 (10) (**Appendix F5**); $[\alpha]_D^{25}$ –25.00 (*c* 0.25, MeOH).

3.6.2.3 4-Nitrobenzyl Xanthorrhizyl Ether (103)

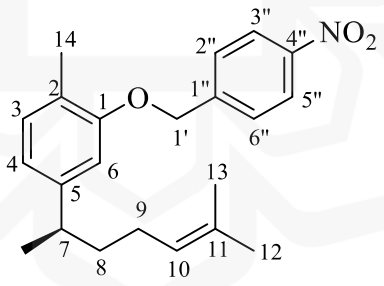

(103)

XNT **(1)** (0.100 g, 45.80 mmol) and anhydrous K_2CO_3 (2.5 eq, 0.1580 g, 1.145 mmol) was refluxed in dry acetone (10 mL) for 1 hour, followed by addition of 4-nitrobenzyl bromide **(113)** (1.5 eq, 0.1484 g, 68.70 mmol). The reaction mixture was stirred for another 6 hours, followed by work up procedure using the general procedure in **3.6.2** to furnish crude product. The crude product was purified *via* CC using *n*-hex as mobile phase to afford derivative **(103)** with IUPAC name 1-((2-methyl-5-(6-methylhept-5-en-2-yl)phenoxy)methyl)-4-nitrobenzene as a yellow oil (103.20 mg, 63.74%) with R_f value of 0.575 (*n*-hex:Et_2O, 4:1).

Spectral data: IR (ATR) ν_{max} cm^{-1}; 2960.16 and 2922.71 (C-H sp^3), 1607.49 and 1453.29 (C=C aromatic), 1520.67 and 1344.57 (N=O), 1255.54 (C-O) (**Appendix G1**); ^{1}H-NMR (600 MHz, $CDCl_3$): δ_H 1.20 (3H, d, *J* = 6.9 Hz, H-15), 1.52 (3H, s, H-12), 1.54-1.59 (2H, m, H-8), 1.70 (3H, s, H-13), 1.80-1.90 (2H, m, H-9), 2.30 (3H, s, H-14), 2.66 (1H, sext, *J* = 6.9 Hz, H-7), 5.06 (1H, tt, *J* = 7.1 Hz, 1.2 Hz, H-10), 5.18 (2H, s, H-1'), 6.66 (1H, s, *J* = 1.3 Hz, H-6), 6.75 (1H, dd, *J* = 7.1, 1.3 Hz, H-4), 7.10 (1H, d, *J* = 7.1 Hz, H-3), 7.63 (2H, d, *J* = 8.9 Hz, H-2"/H-6"), 8.26 (2H, d, *J* = 8.9 Hz, H-3"/H-5") (**Appendix G2** and **G3**); DEPTQ (150 MHz, $CDCl_3$): δ_C 15.99 (C-12), 17.69 (C-14), 22.50 (C-15), 25.71 (C-13), 26.15 (C-9), 38.44 (C-8), 39.46 (C-7), 68.57 (C-1'), 110.30 (C-6), 119.73 (C-4), 123.79 (C-2"/C-6"), 124.30 (C-2), 124.41 (C-10), 127.40 (C-3), 130.78 (C-3"/C-5"), 131.50 (C-1"), 145.13 (C-11), 146.85 (C-5), 147.47 (C-4"), 156.13 (C-1) (**Appendix G4**); GC-MS (57.98%): t_R 54.99 min, *m/z* 242 (100), 207 (16), 183 (18), 131 (20), 107 (47), 91 (80), 79 (46) (**Appendix G5**); $[\alpha]_D^{25}$ –44.44 (*c* 0.72, MeOH).

3.6.2.4 3-Trifluoromethylbenzyl Xanthorrhizyl Ether (104)

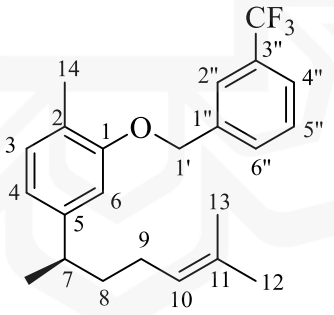

(104)

XNT **(1)** (0.100 g, 45.80 mmol) and anhydrous K_2CO_3 (3.0 eq, 0.1580 g, 1.374 mmol) in dry acetone (10 mL) were refluxed for 1 hour. 3-(trifluoromethyl)benzyl chloride **(114)** (2.0 eq, 0.142 mL, 91.40 mmol) was then added and stirred for additional 12 hours. The reaction mixture was then washed and work up following the general procedure in **3.6.2** to afford crude product. The crude product was purified *via* CC using *n*-hex as mobile phase to yield derivative **(104)** with IUPAC name 1-(3-

trifluoromethyl)benzyloxy)-2-methyl-5-(6-methylhept-5-en-2-yl)benzene as colourless oil (98.40 mg, 57.07%) with R_f value of 0.83 (*n*-hex:Et_2O, 4.5:0.5).

Spectral data: IR (ATR) ν_{max} cm^{-1}; 2962.17 and 2964.03 (C-H sp^3), 1613.31 and 1451.23 (C=C aromatic), 1329.15 (C-F), 1254.53 (C-O) (**Appendix H1**); ^{1}H-NMR (600 MHz, $CDCl_3$): δ_H 1.21 (3H, d, *J* = 7.0 Hz, H-15), 1.53 (3H, s, H-12), 1.55-1.60 (2H, m, H-8), 1.68 (3H, s, H-13), 1.82-1.93 (2H, m, H-9), 2.27 (3H, s, H-14), 2.66 (1H, sext, *J* = 7.0 Hz, H-7), 5.08 (1H, tt, *J* = 7.1, 1.4 Hz, H-10), 5.13 (2H, s, H-1'), 6.66 (1H, d, *J* = 1.3 Hz, H-6), 6.75 (1H, dd, *J* = 7.6, 1.3 Hz, H-4), 7.09 (1H, d, *J* = 7.6 Hz, H-3), 7.52 (1H, t, *J* = 7.6 Hz, H-5"), 7.59 (1H, d, *J* = 7.6 Hz, H-6"), 7.65 (1H, d, *J* = 7.6 Hz, H-4"), 7.73 (1H, s, H-2") (**Appendix H2** and **H3**); DEPTQ (150 MHz, $CDCl_3$): δ_C 15.96 (C-12), 17.70 (C-14), 22.51 (C-15), 25.72 (C-13), 26.17 (C-9), 38.44 (C-8), 39.46 (C-7), 69.13 (C-1'), 110.44 (C-6), 119.54 (C-4), 123.21 (C-7"), 123.87 (C-4"), 124.39 (C-2), 124.49 (C-10), 124.54 (C-2"), 128.98 (C-3), 130.35 (C-5"), 130.65 (C-6"), 130.98 (C-3"), 131.45 (C-1"), 138.69 (C-11), 146.79 (C-5), 156.45 (C-1) (**Appendix H4**); GC-MS (99.52%): t_R 61.77 min, *m/z* 376 (38) [M^+] ($C_{23}H_{27}F_3O$), 294 (74), 159 (100), 135 (46), 91 (37) (**Appendix H5**); $[\alpha]_D^{25}$ –11.43 (*c* 1.05, MeOH).

3.6.2.5 (2-Tetrahydro-2H-pyranyl)methyl Xanthorrhizyl Ether (105)

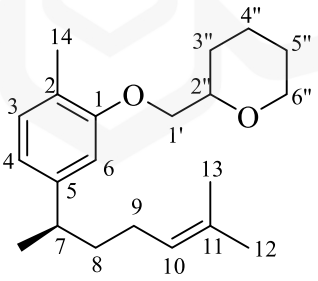

(105)

XNT **(1)** (0.050 g, 22.90 mmol) and NaOH (4.0 eq, 0.0403 g, 91.60 mmol) were refluxed in absolute ethanol (15 mL) for 1 hour. 2-(chloromethyl)tetrahydro-2*H*-pyran **(115)** (4.0 eq, 0.1230 g, 91.60 mmol) were then added and stirred for another 24 hours. The reaction mixture was then washed and work up following the general procedure in **3.6.2** to afford crude product. The crude product was purified *via* CC using *n*-hex as

mobile phase to yield derivative **(105)** with IUPAC name 2-((2-methyl-5-(6-methylhept-5-en-2-yl)phenoxy)methyl)-tetrahydro-2*H*-pyran as a colourless oil (4.4 mg, 6.29%) with R_f value of 0.77 (*n*-hex:Et_2O 4:1).

Spectral data: IR (ATR) ν_{max} cm^{-1} 2956.70 and 2923.97 (C-H sp^3), 1611.83 and 1454.08 (C=C aromatic), 1255.81 (C-O) (**Appendix I1**); ^{1}H-NMR (600 MHz, $CDCl_3$) δ_H 1.20 (3H, d, *J* = 6.9 Hz, H-15), 1.44-1.49 (1H, m, H-3"a), 1.52 (3H, s, H-12), 1.53-1.55 (2H, m, H-8), 1.55-1.66 (4H, m, H-4", H-5"), 1.67 (3H, s, H-13), 1.78-1.80 (2H, m, H-3"b), 1.82-1.90 (2H, m, H-9), 2.20 (3H, s, H-14), 2.63 (1H, sext, *J* = 6.9 Hz, H-7), 3.52 (1H, td, *J* = 11.4, 2.2 Hz, H-6"b), 3.72 (1H, dtd, *J* = 10.9, 5.4, 2.2 Hz, H-2"), 3.83 (1H, ddd, *J* = 9.5, 5.4, 2.2 Hz, H-1'a), 4.02 (1H, ddd, *J* = 9.5, 5.4, 2.2 Hz, H-1'b), 4.04 (1H, dddd, *J* = 11.4, 4.4, 2.2, 1.8 Hz, H-6"a), 5.08 (1H, tt, *J* =7.1 Hz, 1.4 Hz, H-10), 6.61 (1H, d, *J* = 1.6 Hz, H-6), 6.67 (1H, dd, *J* = 7.7, 1.6 Hz, H-4), 7.01 (1H, d, *J* = 7.7 Hz, H-3) (**Appendix I2** and **I3**); DEPTQ (150 MHz, $CDCl_3$) δ_C 15.85 (C-12), 17.72 (C-14), 22.50 (C-15), 23.12 (C-4"), 25.73 (C-13), 26.09 (C-5"), 26.19 (C-9), 28.79 (C-3"), 38.45 (C-8), 39.44 (C-7), 68.59 (C-6"), 71.58 (C-1'), 76.19 (C-2"), 110.50 (C-6), 119.07 (C-4), 124.33 (C-2), 124.56 (C-10), 130.33 (C-3), 131.39 (C-11), 146.62 (C-5), 156.95 (C-1) (**Appendix I4**); GC-MS (98.45%): t_R 63.16 min, *m/z* 217 (14), 135 (69), 91 (100) (**Appendix I5**); $[\alpha]_D^{25}$ –69.57 (c 0.23, MeOH).

3.6.2.6 Propyl Xanthorrhizyloxyacetate (117)

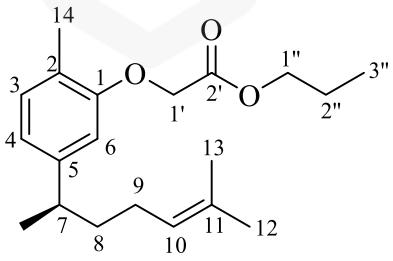

(117)

XNT **(1)** (0.100 g, 45.80 mmol) and Cs_2CO_3 (2.5 eq, 0.3731 g, 1.145 mmol) were mixed in acetonitrile (10 mL) and refluxed for 1 hour. Tetrahydrofurfuryl chloride **(116)** (4.0 eq, 0.2209 g, 1.832 mmol) was added into the reaction mixture and stirred for additional

12 hours. The reaction mixture was then washed and work up following the general procedure in **3.6.2** to afford crude product.The crude product was purified *via* CC using *n*-hex as mobile phase to furnish derivative **(117)** with IUPAC name propyl 2-(2-methyl-5-(6-methylhept-5-en-2-yl)phenoxy)acetate as a colourless oil (10.4 mg, 7.79%) with R_f value of 0.70 (*n*-hex:Et_2O 4:1).

Spectral data: IR (ATR) ν_{max} cm^{-1}; 2964.20 and 2925.62 (sp^3 CH), 1762.43 (C=O ester), 1616.10 and 1455.33 (C=C aromatic), 1198.41 (C-O) (**Appendix J1**); ^{1}H-NMR (400 MHz, $CDCl_3$): δ_H 0.92 (3H, t, *J* = 7.4 Hz, H-3"), 1.17 (3H, d, *J* = 7.0 Hz, H-15), 1.51 (3H, s, H-12), 1.52-1.58 (2H, m, H-8), 1.65 (2H, sext, *J* = 7.4 Hz, H-2"), 1.66 (1H, s, H-13), 1.81-1.90 (2H, m, H-9), 2.24 (3H, s, H-14), 2.61 (1H, sext, *J* = 6.9 Hz, H-7), 4.14 (2H, t, *J* = 6.7 Hz, H-1"), 4.63 (2H, s, H-1'), 5.06 (1H, tt, *J* = 7.1 Hz, 1.3 Hz, H-10), 6.52 (1H, d, *J* = 1.4 Hz, H-6), 6.72 (1H, dd, *J* = 7.6, 1.4 Hz, H-4), 7.05 (1H, d, *J* = 7.6 Hz, H-3) (**Appendix J2** and **J3**); ^{13}C-NMR (100 MHz, $CDCl_3$): δ_C 10.38 (C-3"), 15.92 (C-14), 17.79 (C-12), 22.03 (C-2"), 22.55 (C-15), 25.82 (C-13), 26.23 (C-9), 38.49 (C-8), 39.48 (C-7), 65.88 (C-1'), 66.83(C-1"), 110.28 (C-6), 120.04 (C-4), 124.54 (C-2), 124.66 (C-10), 130.85 (C-3), 131.56 (C-11), 146.74 (C-5), 156.14 (C-1), 169.59 9 (C-2') (**Appendix J4**); GC-MS (75.73%): t_R 50.51 min, *m/z* 318 (55) [M^+] ($C_{20}H_{30}O_3$), 248 (30), 236 (100), 193 (53), 148 (30) (**Appendix J5**); $[\alpha]_D^{25}$ –12.50 (*c* 0.32, MeOH).

3.6.3 Attempted Synthesis of Xanthorrhizol Derivatives (107-110)

In this study, XNT derivatives **(107-110)** were attempted to be synthesised as LOX-3 inhibitors. Derivative **(107)** was proposed to be synthesised using Williamson ether synthesis as described in **Scheme 3.2**. The formation of derivatives **(108)** and **(109)** required the synthesis of *N*-(2-chloroethyl)-1*H*-imidazole-4-carboxamide **(121)** (**Scheme 3.3**) and *tert*-butyl (3-((2-chloroethyl)amino)-3-oxopropyl)carbamate **(123)** (**Scheme 3.4**) as alkylating agents, respectively by using Steglich esterification method (Bol'shakov et al., 2012) with minor modifications. Meanwhile, the synthesis of derivative **(110)** required the synthesis of alkylating agent 3-chloropropyl-1*H*-imidazole-4-carboxylate **(126)**. The synthesis of compound **(126)** was attempted using esterification method (Lee et al., 1996) (**Scheme 3.5**). All alkylating agents were reacted with XNT **(1)** *via* Williamson ether synthesis to furnish derivative **(107-108**, **110**, **124)**.

The derivative **(124)** would be subjected to deprotection of *tert*-butyloxycarbonyl (Boc) group through hydrolysis in acidic condition to afford derivative **(109)**.

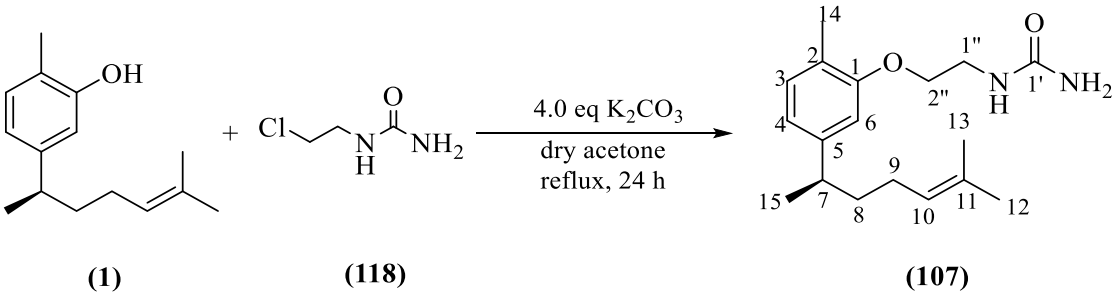

(1) **(118)** **(107)**

Scheme 3.2: Reaction scheme for synthesis of derivative **(107)**

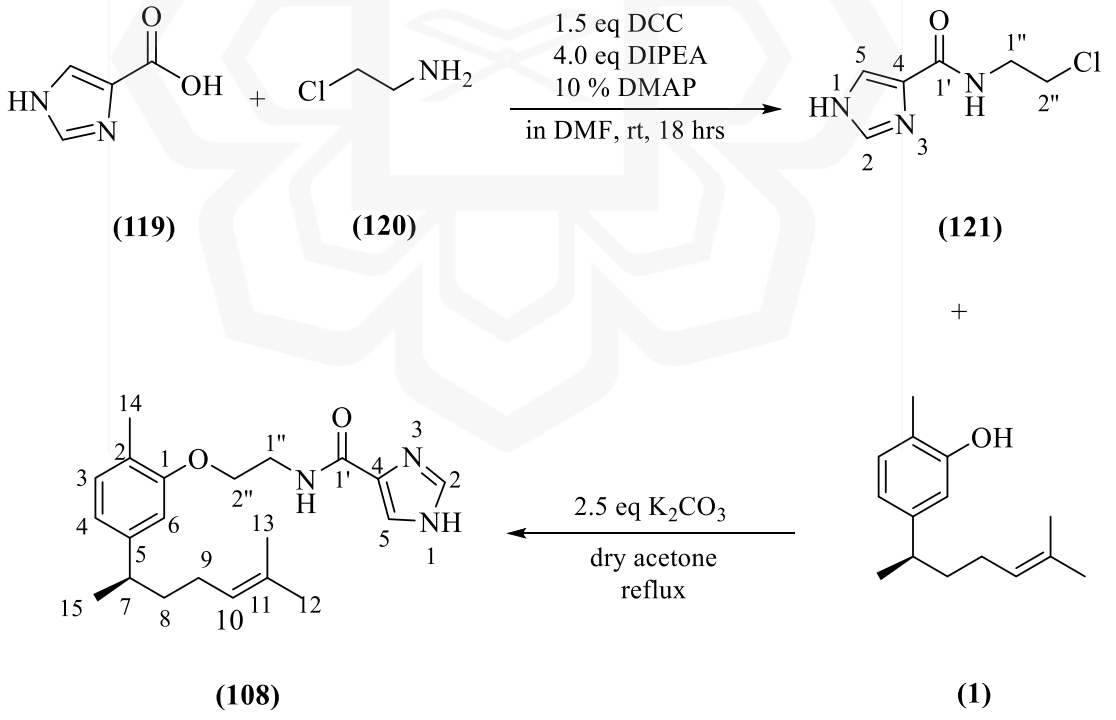

(119) **(120)** **(121)** **(108)** **(1)**

Scheme 3.3: Reaction scheme for synthesis of derivative **(108)**

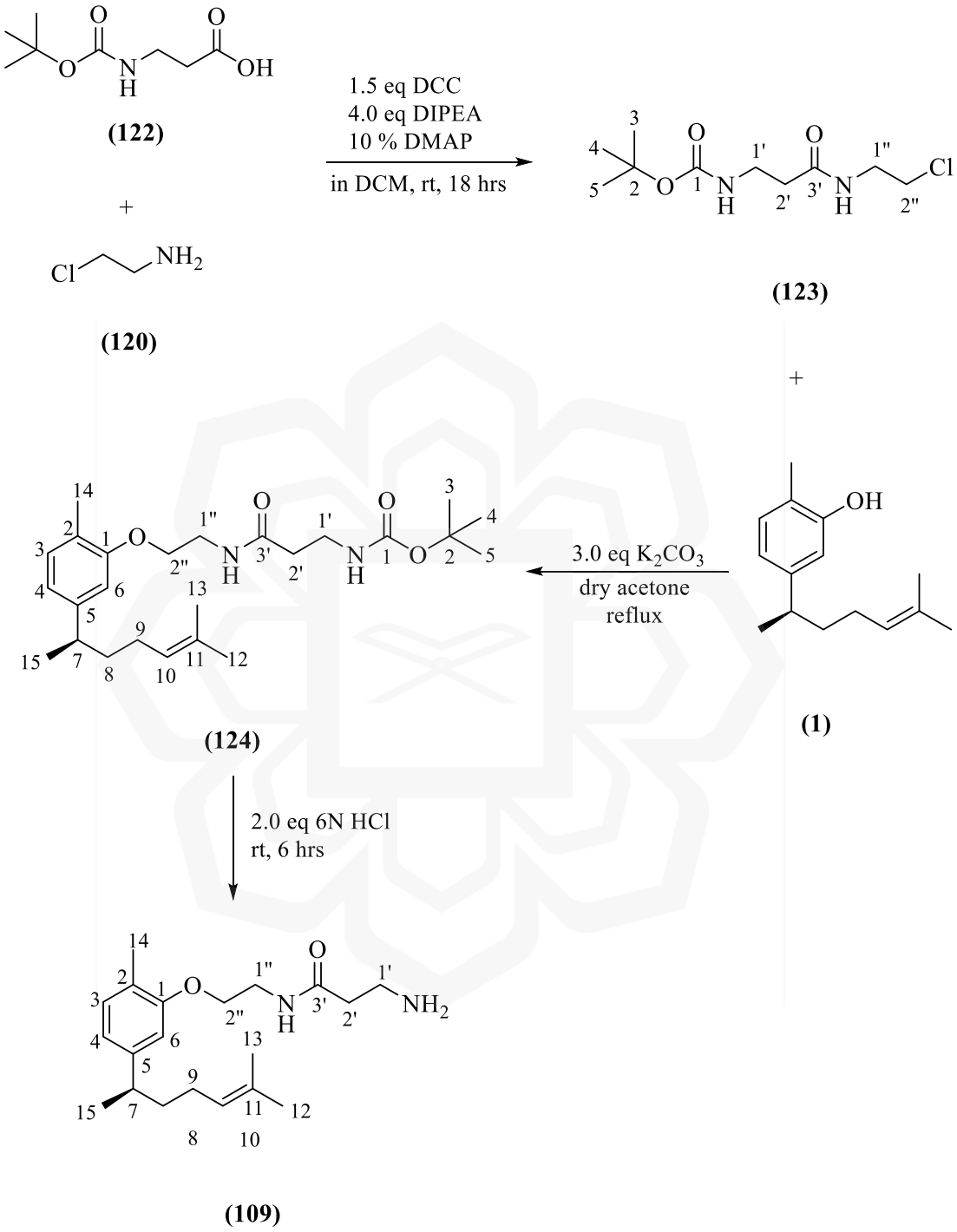

Scheme 3.4: Reaction scheme for synthesis of derivative **(109)**

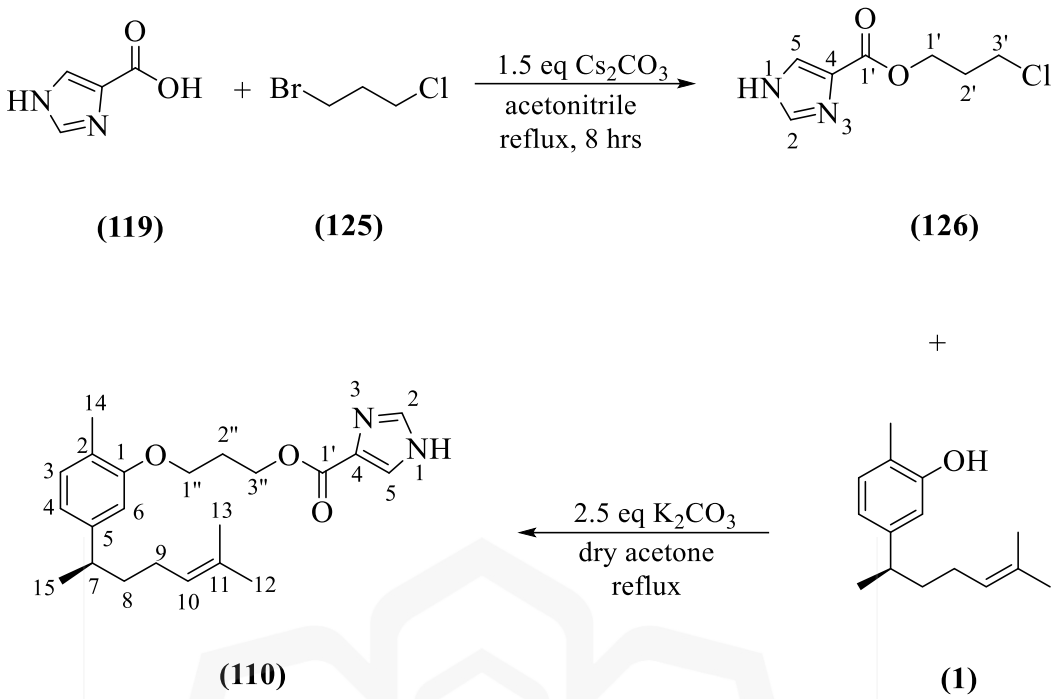

Scheme 3.5: Reaction scheme for synthesis of derivative **(110)**

3.6.3.1 2-(Xanthorrhizyloxy)ethyl carbamide (107)

XNT **(1)** (0.1 g, 45.80 mmol) and anhydrous K_2CO_3 (4.0 eq, 0.2532 g, 1.83 mmol) were refluxed in dry acetone (15 mL) for 1 hour. *N*-(2-chloroethyl)urea **(118)** (2.5 eq, 0.1403 g, 1.46 mmol) was then added to the reaction mixture and stirred for at least 12 hours. The reaction was monitored using TLC with solvent system *n*:hex:EtOAc (4:1). However, the reaction failed to furnish derivative **(107)**.

3.6.3.2 N-(2-(xanthorrhizyloxy)ethyl)-1H-imidazole-4-carboxamide (108)

In an attempt to synthesis derivative **(108)**, the preparation of alkylating agent, *N*-(2-chloroethyl)-1*H*-imidazole-4-carboxamide **(121)** as the starting material was performed. 4-Imidazolecarboxylic acid **(119)** (0.05 g, 44.61 mmol) was dissolved with ethylamine hydrochloride **(120)** (2.5 eq, 0.1293 g, 1.12 mmol), DIPEA (4.0 eq, 0.31 mL, 1.78 mmol), and DMAP (5.45 g, 10% mol) in dimethylformamide (DMF) (10 mL) and stirred at 0ºC. After the mixture has dissolved, DCC (1.5 eq, 0.1381 g, 66.91 mmol)

was then added into the reaction mixture and stirred continuously at 0 ºC for 1 hour. The reaction mixture was then allowed to stir at room temperature with TLC monitoring using bromocresol green and iodine staining. The reaction mixture was filtered, and the filtrate was washed with saturated $NaHCO_3$ solution (5 mL) and extracted with EtOAc (5 mL x 3 times). The organic layer was dried over $MgSO_4$ and evaporated to dryness under *vacuo*. The purification of crude products by CC afforded *N*-(2-chloroethyl)-1*H*-imidazole-4-carboxamide **(121)** as white solid (6.5 mg, 8.39%) with R_f value of 0.83 (*n*-hex:EtOAc, 1:4). However, compound **(121)** was obtained in low yield and impure, thus hampered the subsequent synthesis of derivative **(108)**.

Spectral data: ^{1}H-NMR (500 MHz, $CDCl_3$): δ_H 2.31 (2H, ddd, *J* = 16.0, 12.5, 3.5 Hz, H-2"), 3.72 (2H, m, H-1"a), 4.14 (1H, dddd, *J* = 16.0, 12.5, 4.5, 3.9 Hz, H-1"b), 7.40 (1H, s, H-5), 7.95 (1H, s, H-2) (**Appendix K1** and **K2**).

3.6.3.3 N-(2-(xanthorrhizyloxy)ethyl)-3-aminopropanamide (109)

The synthesis of derivative **(109)** was attempted by the preparation of alkylating agent, *tert*-butyl-(3-((2-chloroethyl)amino)-3-oxopropyl)carbamate **(123)** as starting material. Boc-*β*-alanine **(122)** (0.10 g, 52.85 mmol) were dissolved with ethylamine hydrochloride **(120)** (2.5 eq, 0.1531 g, 1.32 mmol), DIPEA (4.0 eq, 0.37 mL, 12.11 mol), and catalytic amount of DMAP (10% mol, 6.5 mg) in dichloromethane (DCM) (15 mL) at 0ºC. DCC (1.5 eq, 0.1635 g, 79.28 mmol) was then added into the dissolved reaction mixture and stirred continuously at 0 ºC for 1 hour. The reaction mixture was then allowed to stir at room temperature with TLC monitoring using bromocresol green and iodine staining. The reaction mixture was filtered and washed with saturated $NaHCO_3$ solution (5 mL) and extracted with EtOAc (10 mL x 3 times). The organic layer was dried over $MgSO_4$ and evaporated to dryness under *vacuo*. The purification of crude products by CC afforded precursor *tert*-butyl(3-((2-chloroethyl)amino)-3-oxopropyl)carbamate **(123)** as white solid (37.2 mg, 28.08%).

Spectral data: IR (ATR) ν_{max} cm^{-1}; 3325.58 and 3239.31 (N-H), 2928.43 and 2852.23 (CH sp^3), 1715.94 and 1642.22 (C=O) (**Appendix L1**); ^{1}H-NMR (500 MHz, $CDCl_3$): δ_H 1.44 (9H, s, H-3, H-4, H-5), 1.97 (2H, m, H-2"), 2.62 (2H, t, *J* = 5.7 Hz, H-

2'), 3.41 (2H, qt, H-1', J = 5.7 Hz), 3.67 (1H, m, H-1"a), 3.88 (1H, t, J = 11.3 Hz, H-1"b), 5.20 (1H, br s, NH), 7.08 (1H, br s, NH) (**Appendix L2** and **L3**); ^{13}C-NMR (125 MHz, $CDCl_3$): δ_C 28.49 (C-3/C-4/C-5), 33.21 (C-2'), 34.04 (C-1'), 48.35 (C-2"), 49.19 (C-1"), 79.43 (C-2), 156.88 (C-1), 170.41 (C-3') (**Appendix L4**).

Then, the synthesis of intermediate **(124)** was attempted using Williamson ether synthesis method. XNT **(1)** (1.3 eq, 0.040 g, 18.14 mmol) and K_2CO_3 (3.0 eq, 0.0579 g, 41.88 mmol) were refluxed in dry acetone (15 mL) for 1 hour. Compound **(123)** (0.035 g, 13.96 mmol) was then added and stirred for another 24 hours. The reaction was monitored using TLC using solvent system *n*:hex:EtOAc (4:1) and vanillin-sulphuric acid reagent. The reaction mixture was washed using EtOAc (10 mL x 3 times). The organic layer was dried over anhydrous $MgSO_4$ and evaporated to dryness using rotary evaporator. The purification of crude product using CC was attempted using 100% *n*-hex. However, the ^{1}H-NMR analysis (**Appendix M**) of isolated compound showed no evidence of successful synthesis for intermediate **(124)**. Therefore, the following step for the synthesis of derivative **(109)** was not resumed.

3.6.3.4 3-(Xanthorrhizyloxy)propyl 1H-imidazole-4-carboxylate (110)

In order to attempt the synthesis of derivative **(110)**, 3-chloropropyl 1*H*-imidazole-4-carboxylate **(126)** as the starting material was prepared. 4-Imidazolecarboxylic acid **(119)** (0.01 g, 89.21 mmol) was mixed with Cs_2CO_3 (1.5 eq, 0.4360 g, 1.34 mmol) in acetonitrile (10 mL) followed by the addition of 1-bromo-3-chloropropane **(125)** (5.0 eq, 0.44 mL, 4.46 mmol). The mixture was allowed to stir under reflux for at least 8 hours. The reaction was monitored using TLC with solvent system *n*:hex:EtOAc (1:4) and staining using bromocresol green and iodine. The reaction mixture was washed using EtOAc (10 mL x 3 times). The organic layer was dried over anhydrous $MgSO_4$ and evaporated to dryness under *vacuo*. The attempt to purify the crude product *via* CC was conducted using 100% *n*-hex. However, the ^{1}H-NMR analysis (**Appendix N**) of isolated compound showed no evidence of targeted compound **(126)**. Hence, the synthesis of derivative **(110)** was not performed.

3.7 BIOLOGICAL EVALUATIONS OF XANTHORRHIZOL DERIVATIVES

The XNT derivatives **(76**, **102-105**, **117)** were subjected to *in vitro* Hyal-1 inhibitory assay. Then, the most active XNT derivative with strongest inhibitory activity underwent further analysis *via* an *in silico* approach, specifically through MD simulation. Meanwhile, derivative **(76)** was subjected to *in vitro* LOX-3 inhibitory assay.

3.7.1 *In Vitro* Hyal-1 Enzyme Assay

The assay was conducted by using Sigma protocol with slight modifications (Ling et al., 2003). The stock solutions of derivatives **(76**, **102-105**, **117)** were prepared at 400 µg/mL in dimethyl sulfoxide (DMSO). The stock solution of each test compound was diluted to achieve final concentrations of 200, 100, 50 and 25 µg/mL. The assay was carried out in 48-well flat bottom plate. The Hyal-1 enzyme from bovine testes was prepared in $Na_2H_2PO_4$ buffer (1400 U, 100 µL, 20 mM, pH 7.0). The Hyal-1 enzyme (100 µL) was pre-incubated with each test compound (25 µL) for 10 minutes at 37 ºC. The assay was initiated by addition of hyaluronic acid solution (100 µL, 0.03%, pH 5.35) to the mixture and incubated for another 40 minutes. The undigested hyaluronic acid was precipitated with acid albumin solution (1 mL), which made up of sodium acetate trihydrate (24 mM), acetic acid (79 mM) and BSA (0.1% w/v). The reaction mixture was allowed to stand at room temperature for 10 minutes. The absorbance of the reaction mixture was measured at 600 nm by using a microplate reader. Apigenin **(17)** was used as positive control in this experiment. All assays were conducted in triplicate. The average inhibition percentage (I%) was calculated by using the following formula:

$$\text{Inhibition (I\%)} = \frac{(A_{sample} - A_{blank})}{A_{RF}} \times 100\ \%$$

where the A_{sample} is the absorbance of reaction mixture containing all reagents including test compounds, enzyme, and substrate, A_{blank} is the absorbance of reaction mixture containing all reagents excluding test compounds, enzyme and substrate, and A_{RF} is the absorbance of reaction mixture containing all reagents except test compound and enzyme.

3.7.2 *In Vitro* LOX-3 Enzyme Assay

The assay was performed following the method with minor modifications by Azhar-Ul-Haq et al. (2004). The stock solution of derivative **(76)** was prepared at 400 µg/mL in DMSO. The stock solution of test compound was diluted to achieve final concentrations of 200, 100, 50, 25, 12.5 and 6.25 µg/mL. The stock solution of soybean LOX-3 enzyme was prepared by diluting LOX-3 enzyme (1 mg) in $Na_2H_2PO_4$ buffer (1 mL, pH 8.0). The working solution of LOX-3 enzyme was freshly prepared by mixing the LOX stock solution (60 µL) with buffer (1940 µL). The assay was conducted in 96-well flat bottom plate. The test compound (10 µL), LOX-3 enzyme solution (100 µL), and $Na_2H_2PO_4$ buffer (160 µL, pH 8.0) were pre-incubated for 15 minutes at 25 ºC. The assay was then initiated by the addition of linoleic acid solution (20 µL, 0.03 mM) to the reaction mixture and incubated for additional 10 minutes. The absorbance of the reaction mixture was measured at 234 nm by using a microplate reader. NDGA **(43)** was used as positive control in this experiment. The assay was carried out in triplicate. The average inhibition (I%) percentage was calculated by using the following formula:

$$\text{Inhibition (I\%)} = \frac{[(A_{DMSO} - A_{blank\ DMSO}) - (A_{sample} - A_{blank\ sample})]}{(A_{DMSO} - A_{blank\ DMSO})} \times 100\ \%$$

where the A_{DMSO} is absorbance of reaction mixture containing all reagents including buffer DMSO, enzyme and substrate, while $A_{blank\ DMSO}$ is the absorbance of reaction mixture containing all reagents excluding enzyme. Meanwhile, A_{sample} is the absorbance of reaction mixture containing all reagents including test compound, buffer, enzyme

and substrate, while $A_{blank\ sample}$ is the absorbance of reaction mixture containing all reagents without enzyme.

3.7.3 Statistical Analysis

All *in vitro* experiments were performed in triplicate and each data represents mean ± standard error measurement (S.E.M). All statistical analysis were done using GraphPad Prism 8.0 software. The IC_{50} values were determined using the non-linear regression curve. The normality of each data was determined using the Shapiro-Wilk test. The significant difference of the derivatives with XNT **(1)** and positive controls for respective assays were analysed using independent *t*-test. The data was considered as significantly different if $P < 0.05$.

3.8 MOLECULAR DYNAMICS SIMULATION

The MD simulation for derivative **(102)**, which shows the lowest IC_{50} value in the Hyal-1 inhibitory enzyme assay was performed. Apigenin **(17)**, which was the positive control used in the *in vitro* assay was also subjected to the simulation as positive control.

The input files were prepared using the solution builder module in CHARMM-GUI server. The topology and coordinates of the models were generated using CHARMM36m force field, while the derivative **(102)** and apigenin **(17)** was parameterised using CHARMM general force field. The system was solvated with TIP3 water molecules in rectangular waterbox with edge distance of 10.0 Å. Sodium and chloride counterions were added to the final concentration of 0.15 M to neutralise the system. Subsequently, the solvated model was subjected to energy minimisation using steepest gradient method for 5000 steps. The equilibration of the system was conducted by the canonical (NVT) and isothermal-isobaric (NPT) ensemble. The temperature coupling was performed using Nose-Hoover thermostat at 300 K, while the pressure coupling was conducted by employing Parrinello-Rahman barostat at 1 atm.

The production run was performed at 100 ns simulation using GROMACS software. The trajectory of the simulation was visualised using VMD software. Post-simulation trajectories analysis was conducted using GROMACS utilities, to calculate the root-mean-square deviation (RMSD), root-mean-square fluctuation (RMSF), radius of gyration (R_g), hydrogen bonds, and pair distance between ligand and protein. The graphs for each analysis were plotted using Grace software whereas the hydrogen bond occupancy was analysed using VMD package.

CHAPTER 4

DESIGN OF XANTHORRHIZOL DERIVATIVES AS POTENTIAL HYALURONIDASE AND LIPOXYGENASE INHIBITORS

4.1 INTRODUCTION

This study employed two approaches to identify potential XNT derivatives as Hyal and LOX enzyme inhibitors. The first approach involved virtual screening of XNT derivatives from in-house database. The second approach involved designing new XNT derivatives *via in silico* FBDD using LigBuilder software. The drug-likeness properties of all XNT derivatives obtained from both approaches were evaluated using SwissADME server.

4.2 VIRTUAL SCREENING OF IN-HOUSE DATABASE

The virtual screening of in-house database consisting of thirty XNT derivatives **(63-81**, **91-101)** collected from literatures (Aguilar, Delgado, & Villarreal, 2001; Ngai & Sirat, 2004; Rahayu et al., 2020; Sirat et al., 2007) against Hyal-1 and LOX-3 enzymes were performed using molecular docking. These derivatives were modified *via* chemical synthesis at different positions of XNT moiety, represented as R_1 to R_4 position (**Figure 4.1**).

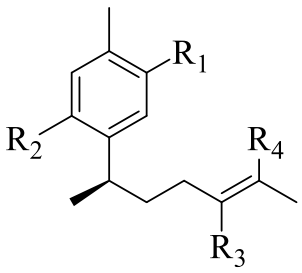

Figure 4.1: A small library of reported XNT derivatives with modification at R_1 to R_4 positions.

A grid box needs to be set prior to docking in AutoDock Vina protocol. There are two approaches for the preparation of grid boxes, depending on the docking strategy to be used. Blind docking is the docking of ligands which took place with the whole surface of the protein and used particularly for the exploration of the binding pockets of the protein due to insufficient information of the binding pockets (Grasso et al., 2022).

Meanwhile, site-targeted molecular docking is utilised when the information on the important pockets for the enzyme activity was already established, hence the grid box will be set to cover the important amino acid residues (Torres et al., 2019). In this study, site-targeted molecular docking was used to make sure that the compounds would be docked in the active site of the respective proteins. The information on the binding sites for Hyal-1 and LOX-3 were obtained from the published literatures for the respective enzymes.

4.2.1 Virtual Screening of Xanthorrhizol Derivatives Against Hyal-1 Enzyme

XNT **(1)** and its derivatives **(63-81**, **91-101)** were docked against Hyal-1 enzyme to predict their binding affinities. Due to the lack of co-crystallised ligand in Hyal-1 enzyme crystal structure, seric acid A **(26)** and disodium chromoglycate **(27)** were docked as the control compounds with same parameters for the docking studies. The docking result (**Appendix O1** and **O2**) showed that seric acid A **(26)** bound stronger in the Hyal-1 binding site with binding energy (-8.8 kcal/mol) compared to disodium chromoglycate **(27)** (-8.3 kcal/mol). The docking result corresponded to the IC_{50} value of seric acid A **(26)** (0.19 mM) and disodium chromoglycate **(27)** (0.39 mM) (Murata et al., 2021) showing that the parameters set for the docking protocol were reliable. Apigenin **(17)**, another known Hyal-1 inhibitor used as positive control for *in vitro* Hyal-1 enzyme assay was also docked as the reference compound for the docking studies. All docked compounds were bound in the active site of Hyal-1 enzyme (**Figure 4.2**) with binding energies ranging from -8.5 to -5.6 kcal/mol (**Table 4.1**). XNT **(1)** exhibited binding energy of -6.5 kcal/mol and the hydroxyl group interacted with Tyr261 *via* hydrogen bonding. Moreover, it also formed pi-alkyl interactions with Arg134 and Pro249, as well as pi-hydrogen bond interactions with Tyr210 (**Figure 4.3**).

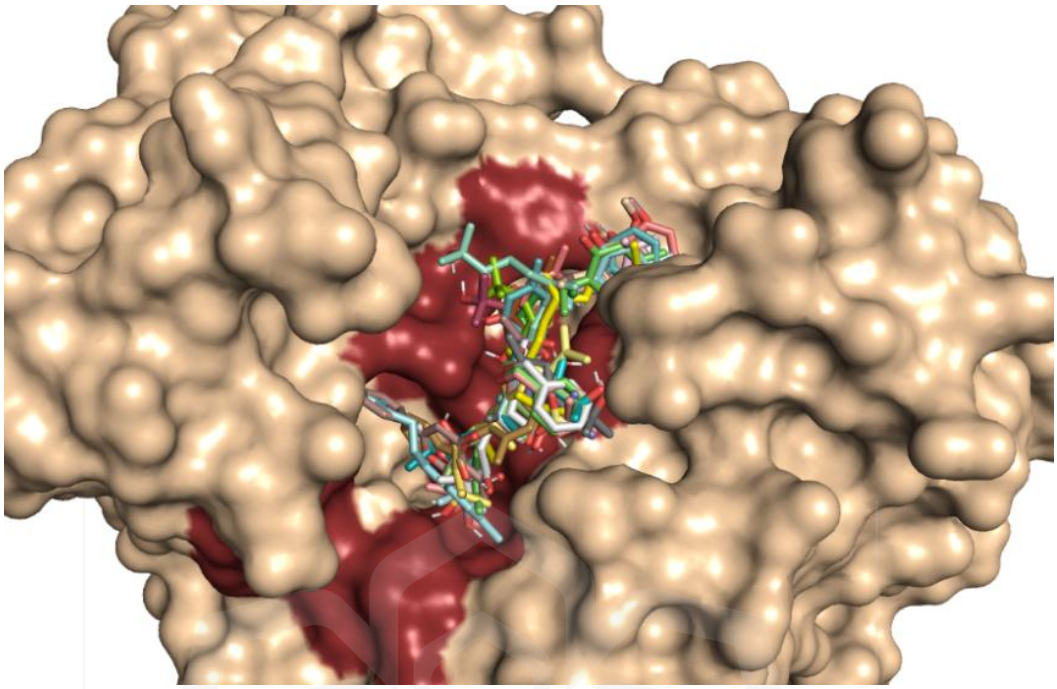

Figure 4.2: Docking conformation of XNT **(1)** and its derivatives **(63-81**, **91-101)** in Hyal-1 binding site. The active site residues are coloured in maroon.

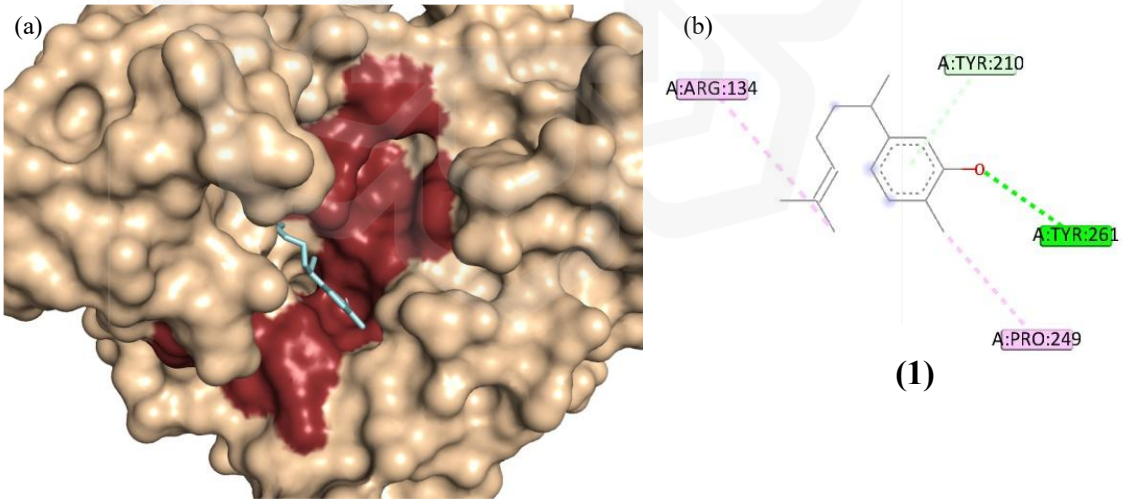

Figure 4.3: a) 3D docking pose of XNT **(1)** (blue) in Hyal-1 enzyme binding site; b) 2D representation for interactions of XNT **(1)** with amino acid residues of Hyal-1.

Table 4.1: Docking results of XNT derivatives (**63-81**, **91-101**) against Hyal-1 enzyme

Derivatives	Binding energy (kcal/mol)	Interacting amino acid residues
(75)	-8.5 ± 0.00	Ile73, **Asp129, Glu131**, **Tyr247**, Tyr286, Trp321
(93)	-8.4 ± 0.12	Ile73, **Asp129**, **Glu131**, Tyr286, Trp321
(65)	-8.3 ± 0.21	Pro62, Tyr75*, **Asp129**, Trp321*
(92)	-8.3 ± 0.06	**Asp129**, **Glu131**, **Tyr202***, Tyr210*, Tyr286, Trp321
(79)	-8.3 ± 0.00	Ile73, **Asp129**, **Glu131**, Gly203, Tyr210*, **Ser245**, Tyr286, Trp321
(80)	-8.0 ± 0.20	Ile73, **Asp129**, **Glu131**, **Tyr202**, **Ser245**, Tyr286, Trp321
(78)	-8.0 ± 0.10	Ile73, Val127, **Asp129**, **Glu131**, **Tyr247**, Arg265, Tyr286, Trp321, Trp324*
(76)	-8.0 ± 0.06	Pro62, **Asp129**, **Glu131**, **Tyr247**, Tyr286, Trp321
(81)	-8.0 ± 0.06	Ile73, **Asp129**, **Glu131**, **Tyr202***, Tyr286, Trp321
Apigenin (17)	-7.9 ± 0.00	Trp130*, **Glu131**, **Tyr202***, Tyr210*, **Ser245***, Arg265*, Tyr261*
(67)	-7.9 ± 0.10	**Tyr247***, Trp321
(96)	-7.6 ± 0.15	**Asp129**, **Glu131**, **Tyr202***, **Tyr247**, Tyr286
(66)	-6.9 ± 0.15	Ser76*, **Asp129***, **Glu131**, Trp321
(74)	-6.8 ± 0.20	Trp75*, Trp321*
(64)	-6.8 ± 0.10	Tyr75*, **Asp129**, **Glu131**, **Tyr202**, Trp321*
(91)	-6.6 ± 0.30	**Glu131***, **Tyr202***, **Ser245***, **Tyr247***
(68)	-6.6 ± 0.12	Tyr75*, **Asp129**, **Glu131**, Trp321*
(71)	-6.6 ± 0.10	Asn37*, Ile73, Tyr75*, Val127, **Asp129***, **Tyr202**, Tyr286, Trp321
(73)	-6.6 ± 0.06	Pro62, **Tyr202**, Tyr286, Trp321*, Val322*, Trp324
(97)	-6.5 ± 0.21	Tyr75, **Asp129**, **Glu131**, **Tyr202**, Asp292, Trp321
(69)	-6.5 ± 0.15	Ser76, **Asp129**, **Glu131**, Trp321
(101)	-6.5 ± 0.10	Ile73, Tyr75*, **Asp129**, **Tyr202**, Tyr286, Asp292*, Trp321
(1)	-6.5 ± 0.06	Arg134, Tyr210*, Pro249, Tyr261
(70)	-6.5 ± 0.00	Ile73*, Tyr75, **Asp129***, **Glu131***, **Tyr247***, Tyr286, Trp321
(72)	-6.4 ± 0.42	**Tyr202**, Tyr286, Trp321*, Trp324*

(63)	-6.3 ± 0.38	Asn37, Tyr75*, **Asp129**, Trp321
(95)	-6.2 ± 0.21	**Asp129***, **Glu131***, **Tyr202**, Trp321
(77)	-6.2 ± 0.12	Tyr75*, **Asp129**, **Tyr202**, Trp321
(100)	-6.0 ± 0.21	Tyr75, **Asp129**, **Glu131**, Asp292*, Trp321
(98)	-5.9 ± 0.46	Pro62, **Glu131***, **Tyr247***
(94)	-5.9 ± 0.25	Asn37*, Tyr75, **Asp129***, **Glu131***, **Tyr247***, Tyr286*
(99)	-5.6 ± 0.62	Pro62, Trp321

Notes. The essential interacting amino acid residues were shown in **bold**. The hydrogen bonding interactions were marked with (*).

There were nine XNT derivatives **(65**, **75-76**, **78-81**, **92-93)** exhibited stronger binding affinities (-8.5 to -8.0 kcal/mol) towards Hyal-1 enzyme compared to apigenin **(17)** (-7.9 kcal/mol). Among all derivatives, derivative **(75)** exhibited the strongest binding energy of -8.5 kcal/mol. It is bound to the active site of Hyal-1 through pi-anion interactions between aromatic ring from XNT scaffold and benzyloxy moiety substituted at R_1 position with residues Asp129 and Glu131. Meanwhile, no interactions with important residues were observed from the benzyloxy moiety at R_2 position. The interactions of derivative **(75)** with Hyal-1 enzyme are shown in **Figure 4.4**. The same docking pattern of interactions was also observed for derivative **(92)** and **(93)**, where both derivatives also possess benzyloxy moieties at R_1 and R_2 positions.

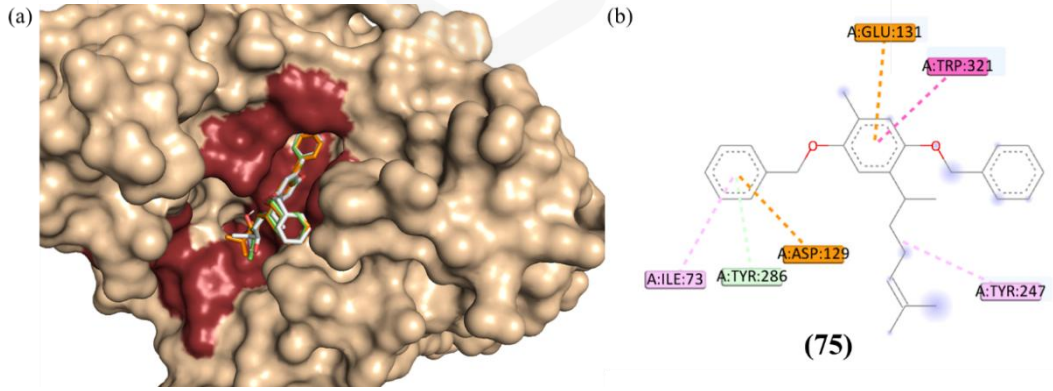

Figure 4.4: a) 3D docking pose of derivative (**75)** (green), (**92)** (white) and (**93)** (orange) in Hyal-1 enzyme binding site; b) 2D representation for interactions derivative (**75)** with amino acid residues of Hyal-1.

Moreover, derivatives **(76**, **79-81**, **91)**, which bear only one benzyloxy moiety at R_1 position and xanthorrhizyl benzoate **(65)** also exhibited favourable binding energy with Hyal-1 enzyme. This pattern suggested that substitution of aromatic ring at R_1 improved the binding energy of the derivatives against Hyal-1 enzyme. Additional substitution of benzyloxy moiety at R_2 position provides conformational stability of the derivatives towards the binding site of the enzyme.

The substitution of hydroxyl group to smaller functional groups at R_1 position, such as acetate XNT derivatives **(68-69)** and methoxy XNT derivatives **(77**, **97-100)** exhibited lower affinities (-6.5 to -5.6 kcal/mol) compared to XNT **(1)**. The substitution of alkene functionalities at R_3 and R_4 positions of XNT scaffold to diols and enols to derivatives **(71-73)** and **(101)**, respectively did not exert significant effect on the binding interaction of the derivatives against Hyal-1 enzyme. This negligible influence of substitution at R_3 and R_4 positions can be further affirmed by similar binding energies exhibited by derivatives **(92)** and **(93)**, as both derivatives have benzyloxy moieties at R_1 and R_2 positions while bearing different in substitution at R_3 and R_4 positions.

The summary for virtual screening of XNT derivatives against Hyal-1 enzyme was described in **Figure 4.5**. Only benzyloxy and benzoyl moiety at R_1 position showed significant influence towards the binding energies of XNT derivatives towards the enzyme, while addition of benzyloxy moiety at R_2 position contributed to conformational stability towards the bound molecule. On the other hand, no significant improvement of the binding energies towards Hyal-1 enzyme for derivatives with enol, diol or α-hydroxyl ketone functionalities at R_3 and R_4 positions.

The virtual screening result demonstrated that the presence of the benzyloxy moiety at R_1 position is important for Hyal-1 enzyme activity. Therefore, benzyl xanthorrhizyl ether **(76)**, was synthesised due to its strong affinity towards Hyal-1 enzyme (-8.0 kcal/mol). Derivative **(76)** bound to the enzyme through several hydrophobic interactions, including pi-anion interactions with Asp129 and Glu131 residues (**Figure 4.6**). Moreover, it also formed carbon-hydrogen bond interaction with Tyr247. These three residues were reportedly essential for the Hyal-1 enzyme activity; hence these interactions were necessary to inhibit the enzyme action (Zhang et al., 2009).

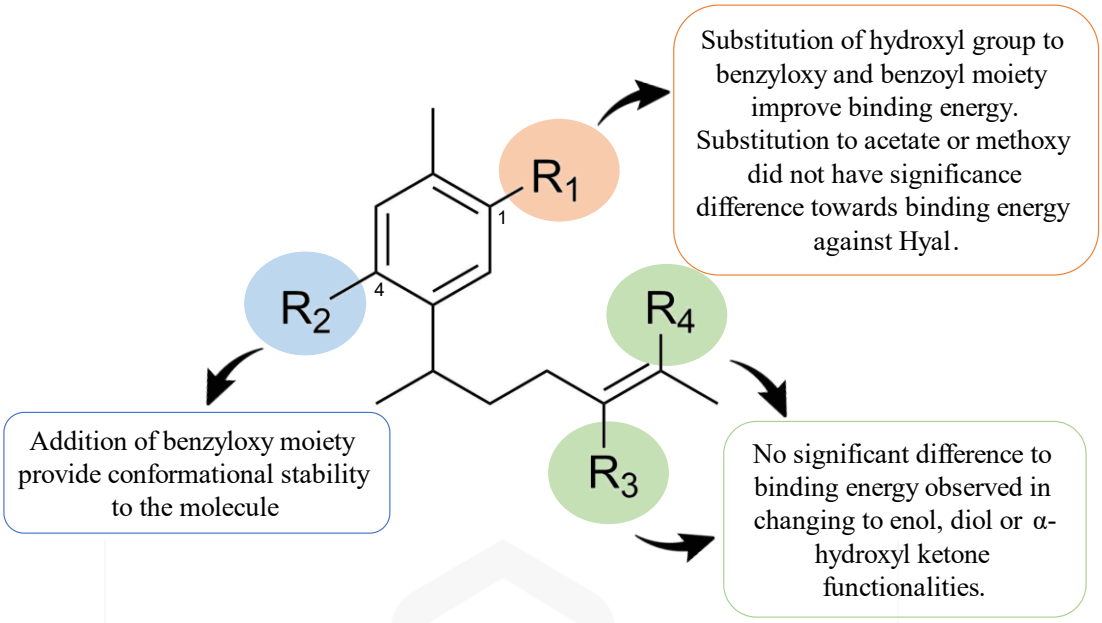

Figure 4.5: Summary for virtual screening of XNT derivatives for Hyal-1 enzyme.

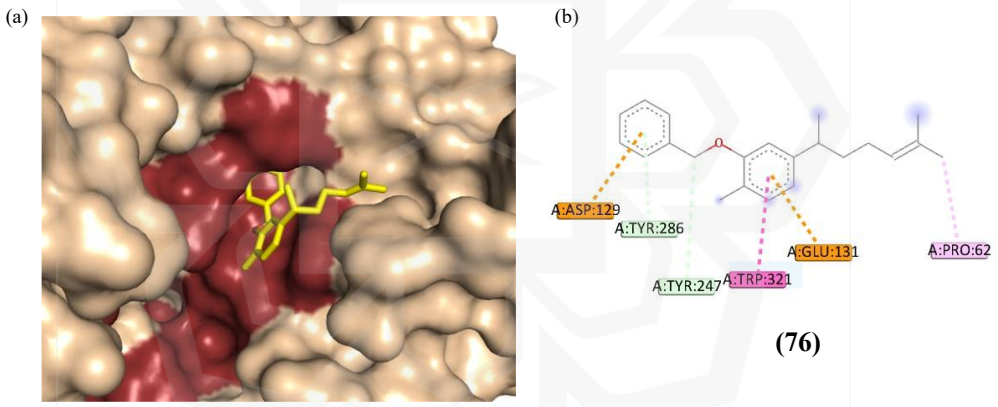

Figure 4.6: a) 3D docking pose of derivative (**76)** (yellow) in Hyal-1 enzyme binding site; b) 2D representation for interactions of derivative **(76)** with amino acid residues of Hyal-1.

4.2.2 Virtual Screening of Xanthorrhizol Derivatives Against LOX-3 Enzyme

The XNT derivatives were also virtually screened against the LOX-3 enzyme using site-targeted docking approach. From the virtual screening, it can be observed that all derivatives were able to be docked inside the binding site of LOX-3 enzyme with binding energies ranging from -8.8 to -4.6 kcal/mol (**Figure 4.7**). The docking results

were tabulated in **Table 4.2**. The docking of XNT **(1)** against LOX-3 enzyme showed that it bound to the active site of LOX-3 with binding energy of -7.7 kcal/mol. The hydroxyl group of XNT **(1)** interacted with Gln514 *via* hydrogen bonding, while the aromatic ring had hydrophobic interaction with His518 and Ile572 (**Figure 4.8**).

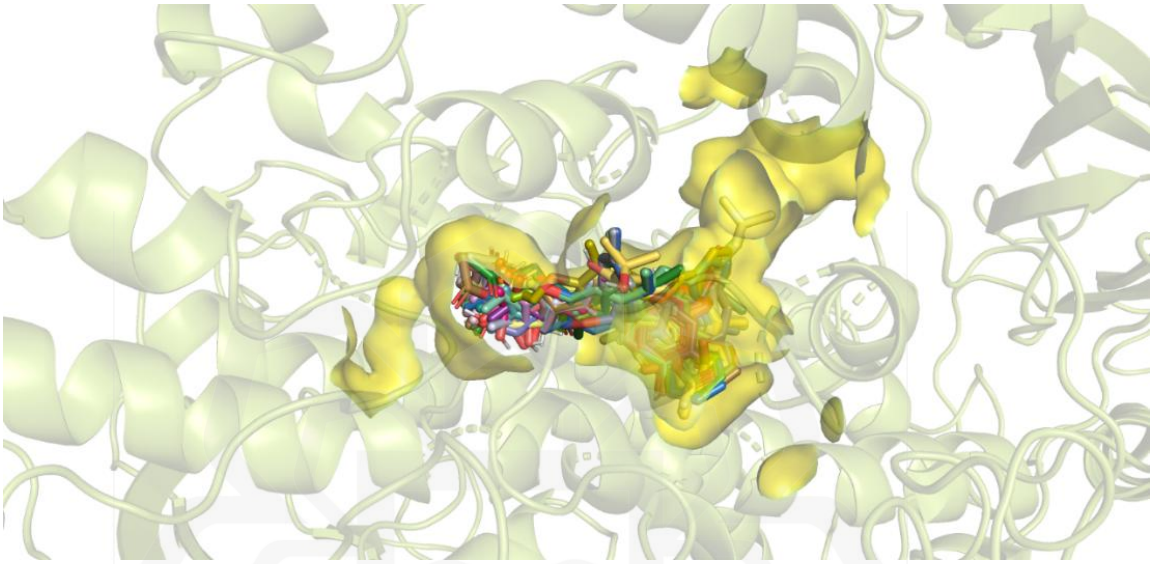

Figure 4.7: Docking conformation of XNT **(1)** and its derivatives **(63-81**, **91-101)** in LOX-3 binding site. The active site residues are coloured in yellow.

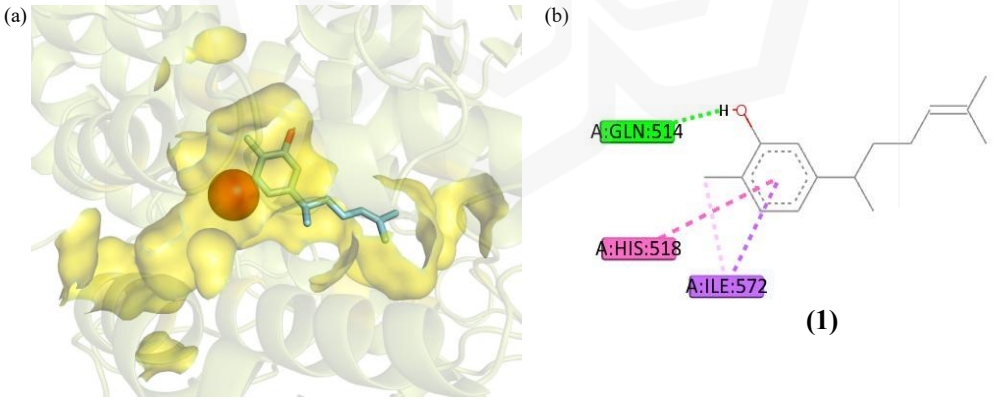

Figure 4.8: a) 3D docking pose of XNT **(1)** (blue) in LOX-3 enzyme binding site; b) 2D representation for interactions of XNT **(1)** with LOX-3.

Table 4.2: Docking results of XNT derivatives (**63-81**, **91-101**) against LOX-3 enzyme

Derivatives	Binding energies (kcal/mol)	Interacting amino acid residues
(81)	-8.8 ± 0.06	Gln516, Trp519, Ile572, **Arg726***
(76)	-8.6 ± 0.10	Val372, Gln514, Trp519, Leu565, Ile770, **Arg726**
(67)	-8.5 ± 0.06	His513*, **His518***, Trp519, Ile572, Val566
(66)	-8.4 ± 0.15	**Ser510***, His513*, **His518**, Ile572
(74)	-8.4 ± 0.06	**His523**, Val769
(68)	-8.4 ± 0.00	His513*, **His518**, Ile572, Gln716*, **Asp766**
(78)	-8.3 ± 0.12	Gln514, Trp519, Ile572, **Gly720**
(69)	-8.2 ± 0.12	**His518**, Ile572
(72)	-8.1 ± 0.06	**His523**, Val769
(96)	-8.1 ± 0.00	Gln514, Trp519, Ile572, Gln716*
(80)	-8.0 ± 0.06	Ile572
(65)	-8.0 ± 0.06	**His513***, Ile572
NDGA (43)	-8.0 ± 0.00	**Ser510***, Gln514*, Ile572, **Asp766***
(99)	-7.9 ± 0.06	His513*, Ile572, **Arg726***
(63)	-7.8 ± 0.29	Gln514, Ile572
(73)	-7.8 ± 0.12	Ala561, Val769
(64)	-7.8 ± 0.06	**His518**, Ile572
(70)	-7.8 ± 0.00	His513*, Ile572, Gln716*, **Asp766***, Leu773
(97)	-7.7 ± 0.06	Ile572, Asp766
(71)	-7.7 ± 0.06	**Ser510***, His513*, Gln514*, **His518**, Ile572, Leu773
(101)	-7.7 ± 0.00	Ile572, Leu773
(1)	-7.7 ± 0.00	Gln514*, **His518**, Ile572
(100)	-7.6 ± 0.06	His513*, Ile572, Gln716*
(77)	-7.5 ± 0.21	Val769, Leu773
(98)	-7.4 ± 0.06	His513*, Ile572, **Gly720**
(94)	-7.3 ± 0.12	His513, Gln514*, Ile572, Gln716, **Asp766***
(79)	-7.3 ± 0.06	**Ser510***, Gln514, Trp519, Ile572, Gln716*
(95)	-7.0 ± 0.23	Gln514*, Thr575*, **Asp766***
(91)	-6.8 ± 0.10	**Asp766***

(75)	-6.5 ± 0.06	Gln514, Leu565, Gln716, Leu773
(93)	-5.4 ± 0.06	Gln514, **His518**, Ile572, Gln716
(92)	-4.6 ± 0.06	**His518**, Trp519, Leu565, Leu773, Val769

Notes. The essential interacting amino acid residues were shown in **bold**. The residues with hydrogen bond interactions were marked with (*).

Eight derivatives **(66-69**, **72**, **74**, **76**, **81)** exhibited lower binding energies compared to positive control, NDGA **(43)** (-8.0 kcal/mol). Derivative **(81)** exhibited the strongest binding energy (-8.8 kcal/mol) compared to other derivatives and NDGA **(43)**. The hydroxyl group from enol functionality interacted with Arg726 through hydrogen bonding interaction. Moreover, substituted benzyloxy moiety at R_1 position also contributed to hydrophobic interactions with Gln 514, Trp519 and Ile572 (**Figure 4.9**).

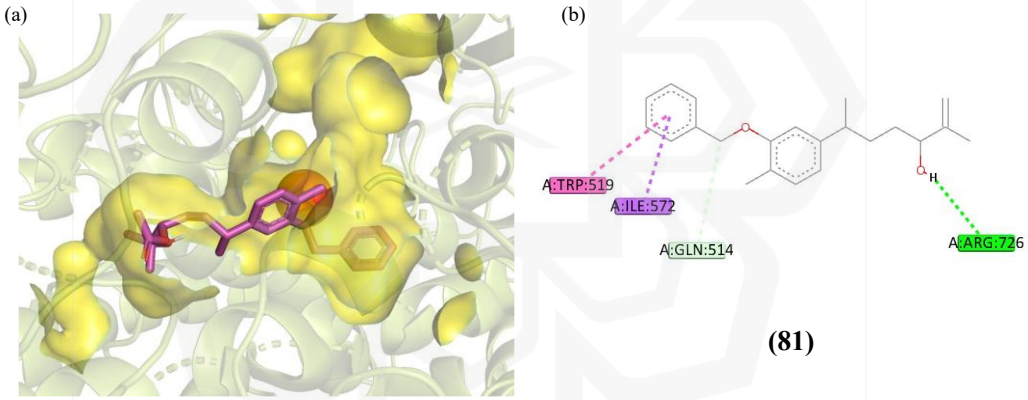

Figure 4.9: a) 3D docking pose of (**81)** (magenta) in LOX-3 enzyme binding site; b) 2D representation for interactions of **(81)** with amino acid residues of LOX-3.

Similar patterns of hydrophobic interactions with Trp591 and Ile572 were also observed for derivatives **(76**, **78-81**, **96)** as they shared benzyloxy moiety at R_1 position with different substituents at R_3 and R_4. This substitution resulted in improved binding energy compared to XNT **(1)**. However, additional benzyloxy moiety substituted at R_2 position showed significant decrease in binding affinity, as exhibited by derivatives **(75)** (-6.5 kcal/mol), **(92)** (-4.6 kcal/mol), and **(93)** (-5.4 kcal/mol). These interactions suggested that the benzyl ring at R_1 position contributed to the stabilisation of the

derivatives with the binding site, while addition of benzyloxy moiety at R_2 position might impose steric effect, which reduced the binding energy significantly.

The substitution of hydroxyl group (R_1 position) to acetate and methyl moieties for derivatives **(64)** and **(77)** did not enhance the binding affinities towards LOX-3 enzyme. The binding energies displayed by derivative **(64)** (-7.8 kcal/mol) and derivative **(77)** (-7.5 kcal/mol) were comparable to XNT **(1)** (-7.7 kcal/mol). Meanwhile, the substitution of alkene group (R_3 and R_4 position) of xanthorrhizyl acetate **(64)** (-7.8 kcal/mol) to diols for derivatives **(68-69)** and α-hydroxyl ketone for derivative **(66)** improved the binding energies (-8.4 to -8.2 kcal/mol). The presence of α-hydroxyl ketone in benzoyl derivative **(67)** also exhibited positive influence towards its binding energy as it improved from -8.0 kcal/mol to -8.5 kcal/mol. No significant changes in binding energies were observed upon substitution at R_3 and R_4 position for other derivatives.

The summary for virtual screening of XNT derivatives against LOX-3 enzyme was depicted in **Figure 4.10**. Similar to Hyal-1 enzyme, only substitution of hydroxyl group to benzyloxy and benzoyl moieties at R_1 position showed improvement of the binding energies. Meanwhile, xanthorrhizyl acetate derivatives **(64)** showed improvement upon substitution at R_3 and R_4 positions to α-hydroxyl ketone and diols for derivatives **(66-67)** and **(68-69)**, respectively. The substitution at R_3 and R_4 position showed negligible influence for other derivatives.

Therefore, based on the virtual screening studies, derivative **(76)** was selected to be synthesised as LOX-3 inhibitor due to the positive influence of substitution of hydroxyl group to benzyloxy moiety at R_1 position. Derivative **(76)** exhibited strong binding energy (-8.6 kcal/mol) towards LOX-3 enzyme through stable interactions of aromatic ring with hydrophobic channel (Trp519, Leu565, Ile572) and carbon hydrogen bond with Gln514 (**Figure 4.11**).

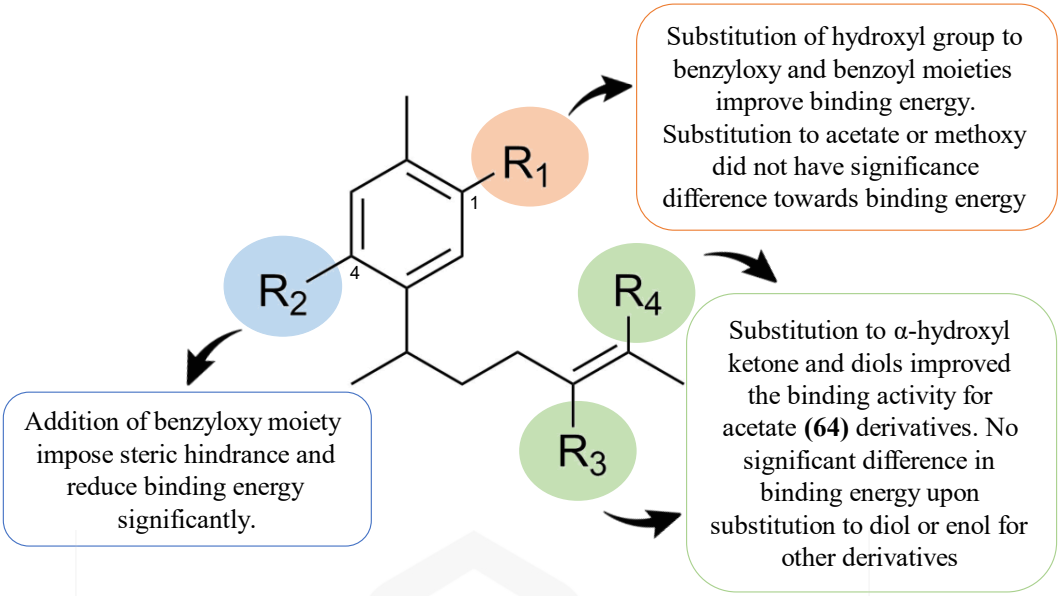

Figure 4.10: Summary for virtual screening of XNT derivatives against LOX-3 enzyme.

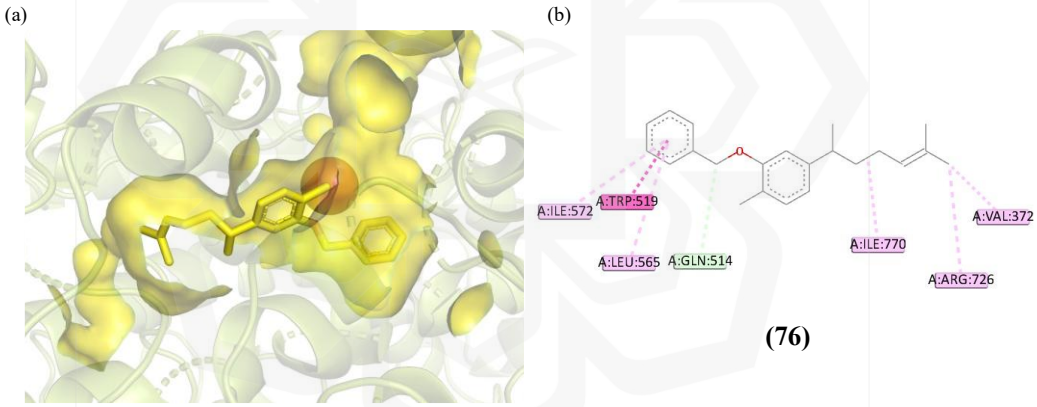

Figure 4.11: a) 3D docking pose of derivative (**76)** (yellow) in LOX-3 enzyme binding site; b) 2D representation for interactions of derivative **(76)** with amino acid residues of LOX-3.

4.2.3 *In Silico* Drug-Likeness and Absorption Profiles of Derivatives (63-81, 91-101)

One of the factors that contributed to the failure of drug candidates to pass clinical trials is attributed to the poor ADME profile of the drug compounds, which leads to poor bioavailability in human body. In the 1990s, this issue had caused approximately 40%

drug attrition during clinical phase (Tsaioun et al., 2009). Therefore, the ADME properties has become one of the crucial factors to be assessed in the early stage of drug discovery process. Drug-like classifiers, such as Lipinski's Rule of Five (Lipinski et al., 2001) and Veber's rule (Veber et al., 2002) were established to define the limit for physicochemical parameters of compounds to exhibit suitable pharmacokinetics profile of a drug (Loureiro et al., 2019). Consequently in 2022, the rate of failure due to the drug-likeness issues has improved from 40% to 15% (Sun et al., 2022).

In recent years, the ADME assessment studies has been developed for both *in vitro* and *in vivo* experiments. However, the experiments can be costly to be performed for a large number of compounds. Therefore, *in silico* ADME prediction models serve as the suitable alternative to be used for a fast and cost-effective method to identify potential drug compounds (Wu et al., 2020). In this study, SwissADME was utilised to evaluate the drug-likeness and absorption profiles of each XNT derivative. SwissADME assessed the drug-likeness properties of the drug compounds based on six physicochemical descriptors; molecular weight, lipophilicity, solubility, topological polar surface area (TPSA), carbon bond saturation, and flexibility (Daina et al., 2017). The optimum range of each descriptor for good absorption in human body were described in **Table 4.3**.

Table 4.3: Optimum range for physicochemical properties by SwissADME

Descriptors	Range
Lipophilicity	$-0.7 \leq$ XLOGP3 $\leq +5.0$
Molecular weight	150 g/mol $\leq$ MW $\leq$ 500 g/mol
Topological polar surface area (TPSA)	20 Å$^2 \leq$ TPSA $\leq$ 130 Å^2
Water solubility	Log $S \geq -6$
Carbon bond saturation	Fraction of carbons in the sp^3 hybridization not less than 0.25
Flexibility	0 < Number of rotatable bonds < 10

Lipophilicity and water solubility are two important parameters for the absorption and distribution of drug compound in human body. The administered drug needs to pass through hydrophobic cell membrane to be distributed and bind to the receptor of target protein (Morak-Młodawska et al., 2023). XLOGP3 descriptor was utilised to predict the lipophilicity of the structure. The optimum range for XLOGP3 is between -0.7 to 5.0. In addition, drug compounds should also possess water solubility to achieve the sufficient drug needed in systemic circulation after the drug administration. Up to 70% of orally administered drugs have decreased effectiveness because they have low solubility and do not dissolve well in the gastrointestinal tract, leading to poor bioavailability (Bhalani et al., 2022). The solubility of compound was predicted with ESOL LogS, where the LogS value lower than -6.0 were classified as poorly soluble compound (Daina et al., 2017).

Meanwhile, TPSA parameter has direct influence towards the drug absorption in biological system, including gastrointestinal, blood brain barrier as well as nerve cells in central nervous system (Karami et al., 2022). For the design of orally active drug, the TPSA should be less than 140 $Å^2$ to ensure the oral absorption in human body (Clark, 2011). The flexibility from rotatable bond in a compound can improve drug permeation as it travels from an aqueous environment to the lipid interior of the plasma membrane. Unsaturation of the compounds helped to improve receptor-ligand complimentary (Lovering et al., 2009). However, a compound that is too flexible failed to achieve high bioavailability. This is due to the high energy required to achieve stable conformation and enter the membrane (Ahmad et al., 2023; Wang et al., 2021). Hence, Veber's rule suggested that the number of rotatable bonds for a drug candidate should be less than 10 (Veber et al., 2002).

The results from **Table 4.4** showed that 19 derivatives (**66-74**, **78**, **91**, **94-101**) fulfilled all six drug-likeness parameters, thus predicted to possess good absorption in the gastrointestinal intestinal tract of the human body. While derivatives **(63-65**, **75-77**, **79-81**, **92-93**) violated at least one of parameters, all of them were still classified as moderately soluble compounds and have high absorption in GI tract.

Derivative **(75)** showed the best binding affinity towards Hyal-1 enzyme. However, this derivative violated four parameters, which were lipophilicity, solubility, number of rotatable bonds and TPSA (**Table 4.4**). This is due to the presence of two benzyloxy moieties at R_1 and R_2 positions and alkene functionality at R_3 and R_4 positions resulted in high hydrophobicity as indicated by the low TPSA (18.36 $Å^2$) and XLOGP (8.31) values. Derivative **(75)** is classified as poorly soluble compound with low absorption in gastrointestinal tract.

Derivative **(76)** was also expected to possess low absorption in gastrointestinal tract as it only consisted of benzyloxy moiety at R_1 position which lowered the TPSA (9.23 $Å^2$), thus increased the lipophilicity (XLOGP = 6.84) values. Despite being classified as moderately soluble, its low TPSA value leads to poor absorption and membrane permeability (Rajalakshmi et al., 2021). However, the substitution of alkene functionality with diols as derivative **(78)** improved the absorption profile, resulting in the increase of TPSA value to 49.69 $Å^2$ and the XLOGP3 value lowered to 4.37. Derivative **(81**) with the strongest binding affinity towards LOX-3 enzyme only violated lipophilicity parameter (XLOGP= 5.67). This is because derivative **(81)** only bears one benzyloxy moiety at R_1 position and two hydroxyl moieties at R_3 and R_4 positions, which are able to increase its solubility in the gastrointestinal tract.

From the summary of virtual screening as shown **Figure 4.5** and **Figure 4.10**, it can be concluded that substitution to enols or diols at R_3 and R_4 position had a minimal effect on binding activity of the derivatives towards both Hyal-1 and LOX-3 enzymes. Nevertheless, the favourable absorption profile demonstrated by derivatives **(78)** and **(81)** implied that the incorporation of the polar functional groups at R_3 and R_4 positions in the XNT scaffold is necessary to enhance its drug-likeness properties, especially in solubility issues. However, benzyl xanthorrhizyl ether **(76)** was still chosen to be synthesised despite the poor absorption profile as this study only focused on optimisation of XNT **(1)** at the hydroxyl functionality (R_1 position) to establish the effect on substitution of aromatic ring in the XNT **(1)** scaffold against Hyal-1 and LOX-3 enzymes.

Table 4.4: *In silico* drug-likeness and absorption profile for XNT derivatives **(63-81**, **91-101)**

Compounds	Molecular weight (MW ≤ 500)	Carbon bond saturation ($Csp^3 \geq 0.25$)	No of rotatable bonds (n < 9)	TPSA (20 $Å^2 \leq$ TPSA ≤ 130 $Å^2$)	XLOGP3 (XLOGP3 ≤ +5.0)	ESOL Log S (Log S ≥ -6)	Solubility class	GI absorption
(1)	218.33[a]	0.47[a]	4[a]	20.23 [a]	5.46[b]	-4.65[a]	Moderately soluble	High
(63)	220.35[a]	0.60[a]	5[a]	20.23 [a]	5.91[b]	-4.88[a]	Moderately soluble	High
(64)	260.37[a]	0.47[a]	6[a]	26.3 [a]	5.13[b]	-4.52[a]	Moderately soluble	High
(65)	322.44[a]	0.32[a]	7[a]	26.3 [a]	6.79[b]	-6.02[b]	Poorly soluble	High
(66)	292.37[a]	0.53[a]	7[a]	63.6 [a]	2.58[a]	-3.03[a]	Soluble	High
(67)	354.44[a]	0.36[a]	8[a]	63.6 [a]	4.24[a]	-4.52[a]	Moderately soluble	High
(68)	294.39[a]	0.59[a]	7[a]	66.76 [a]	2.66[a]	-3.09[a]	Soluble	High
(69)	294.39[a]	0.59[a]	7[a]	66.76 [a]	2.66[a]	-3.09[a]	Soluble	High
(70)	252.35[a]	0.60[a]	5[a]	60.69 [a]	2.98[a]	-3.20[a]	Soluble	High
(71)	252.35[a]	0.60[a]	5[a]	60.69 [a]	2.98[a]	-3.20[a]	Soluble	High
(72)	232.32[a]	0.47[a]	4[a]	34.14 [a]	4.17[a]	-3.64[a]	Soluble	High
(73)	234.33[a]	0.47[a]	4[a]	40.46 [a]	4.67[a]	-4.23[a]	Moderately soluble	High
(74)	318.41[a]	0.47[a]	8[a]	52.60 [a]	4.88[a]	-4.55[a]	Moderately soluble	High
(75)	414.58[a]	0.31[a]	10[b]	18.46[b]	8.31[b]	-7.42[b]	Poorly soluble	Low
(76)	308.46[a]	0.36[a]	7[a]	9.23[b]	6.84[b]	-5.99[a]	Moderately soluble	Low

(77)	232.36[a]	0.50[a]	5[a]	9.23[b]	5.35[b]	-4.58[a]	Moderately soluble	High
(78)	342.47[a]	0.45[a]	8[a]	49.69 [a]	4.37[a]	-4.54[a]	Moderately soluble	High
(79)	384.51[a]	0.46[a]	10[b]	55.76 [a]	4.94[a]	-4.99[a]	Moderately soluble	High
(80)	366.49[a]	0.38[a]	10[b]	35.53 [a]	6.25[b]	-5.72[a]	Moderately soluble	High
(81)	324.46[a]	0.36[a]	8[a]	29.46 [a]	5.67[b]	-5.27[a]	Moderately soluble	High
(91)	352.42[a]	0.58[a]	9[a]	93.06 [a]	2.41[a]	-3.13[a]	Soluble	High
(92)	448.59[a]	0.38[a]	11[b]	58.92 [a]	5.84[b]	-5.98[a]	Moderately soluble	High
(93)	448.59[a]	0.38[a]	11[b]	58.92 [a]	5.84[b]	-5.98[a]	Moderately soluble	High
(94)	268.35[a]	0.60[a]	5[a]	80.92 [a]	2.20[a]	-2.79[a]	Soluble	High
(95)	268.35[a]	0.60[a]	5[a]	80.92 [a]	2.20[a]	-2.79[a]	Soluble	High
(96)	342.47[a]	0.45[a]	8[a]	49.69 [a]	4.37[a]	-4.54[a]	Moderately soluble	High
(97)	266.38[a]	0.62[a]	6[a]	49.69 [a]	2.88[a]	-3.14[a]	Soluble	High
(98)	308.41[a]	0.61[a]	8[a]	55.76 [a]	3.45[a]	-3.60[a]	Soluble	High
(99)	290.40[a]	0.50[a]	8[a]	35.53 [a]	4.75[a]	-4.32[a]	Moderately soluble	High
(100)	248.36[a]	0.50[a]	6[a]	29.46 [a]	4.18[a]	-3.86[a]	Soluble	High
(101)	234.33[a]	0.47[a]	5[a]	40.46 [a]	4.29[a]	-3.93[a]	Soluble	High

*Notes.*The optimum range based on SwissADME parameters; [a]No violation; [b]Violation.

4.3 *IN SILICO* FRAGMENT-BASED DRUG DESIGN (FBDD) OF XANTHORRHIZOL DERIVATIVES

In this study, the design of new XNT derivatives using *in silico* FBDD focused on modification of the hydroxyl group of XNT structure. Therefore, the growing strategy was applied with XNT **(1)** as the seed structure. Ideally, the hydrogen atom from hydroxyl group of XNT (**1**) structure was assigned as the growing site to generate new derivatives. However, the docking result of XNT **(1)** against both enzymes that hydroxyl group of XNT **(1)** interacted with Tyr210 of Hyal-1 (**Figure 4.12.a**) and Gln514 of LOX-3 (**Figure 4.12.b**). These interactions created steric hindrance between the seed structure and assigned growing site, causing failure of generating new derivatives.

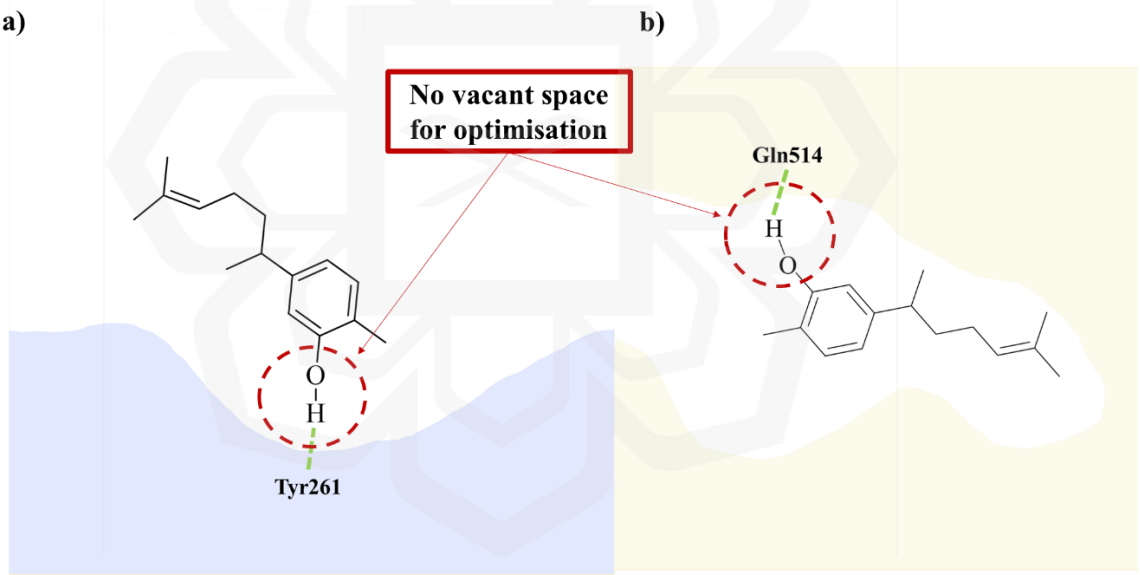

Figure 4.12: Schematic diagram of steric hindrance posed by XNT **(1)** seed structure in a) Hyal-1; b) LOX-3 binding site. The dashed line in green represents the hydrogen bonding interactions.

Therefore, two approaches were adapted to generate suitable seed structure for the structural optimisation of XNT **(1)**, to create vacant chemical space in the binding site and allowed for its growing. The first approach was by replacing the hydroxyl group of XNT **(1)** to a hydrogen atom (**Figure 4.13.a**). The second approach was done by

substituting the hydroxyl group to methoxy functionality. Then, the hydrogen atoms of the methoxy group were set as the growing site (**Figure 4.13.b**).

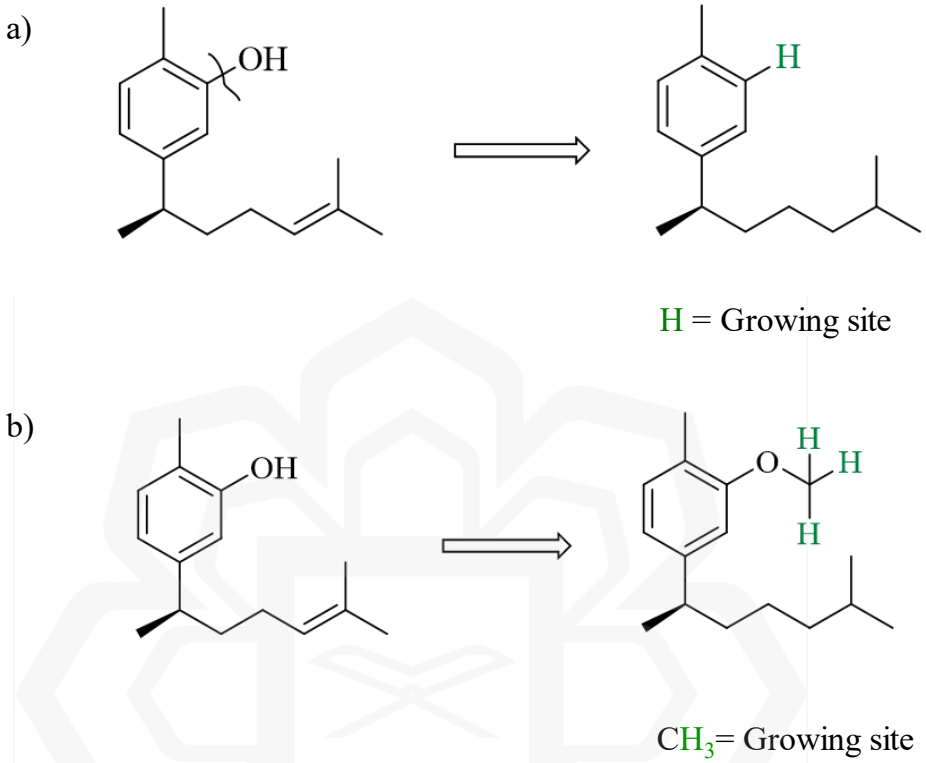

Figure 4.13: Approaches to generate seed structure for XNT **(1)** optimisation.

4.3.1 Design of Xanthorrhizol Derivatives as Hyal-1 Inhibitors

There were four potential binding sites identified for Hyal-1 enzyme as tabulated in **Table 4.5**. Among them, cavities **1** and **2** were identified as "Druggable" in Cavity mode. Cavity **1** was chosen since it displayed the highest Drugscore (1222.00) compared to the cavity **2** (DrugScore 941.00), suggesting that small molecules can possibly bind to this cavity and suitable to be used as target. Moreover, the maximum (6.22) and average pK_d (5.93) value also indicated that cavity **1** was suitable to be used as drug target. Furthermore, cavity **1** was also located at the same position as the reported binding site for Hyal-1 enzyme (Chao et al., 2007). The location of cavity **1** and its comparison to binding site of Hyal-1 enzyme was depicted in **Figure 4.14**.

Table 4.5: Cavity results for Hyal-1 enzyme

Cavity	Maximum pK_d	Average pK_d	DrugScore	Druggability
1	6.22	5.93	1222.00	Druggable
2	6.05	5.43	941.00	Druggable
3	-4.82	4.71	-1560.00	Undruggable
4	-0.45	4.48	-1665.00	Undruggable

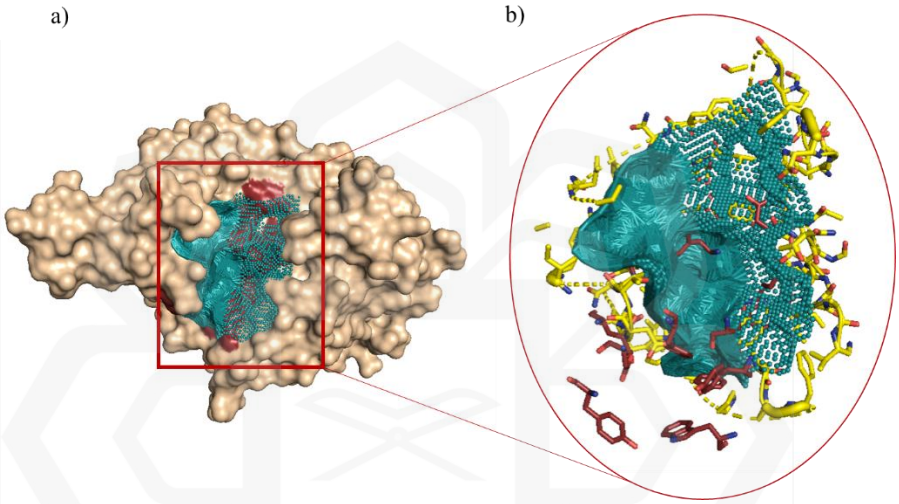

Figure 4.14: a) Overlay of Hyal-1 active site and cavity **1** surface (cyan); b) Alignment of cavity **1** surface (cyan), amino acid residues of cavity **1** (yellow) and active residues of Hyal-1 (maroon).

The utilisation of cavity **1** and XNT **(1)** as seed structure successfully generated a total of 1159 new XNT derivatives in Build mode. All derivatives were subjected to molecular docking against Hyal-1 enzyme and only top fifty derivatives with lowest binding energies were selected for further analysis (**Appendix A**). These fifty derivatives showed binding energies ranging from -8.9 to -7.9 kcal/mol and they were further classified according to structures of fragments bonded to XNT **(1)** structure. It can be observed that the derivatives (labelled with **H** for Hyal-1 inhibitors) consisted of a variety of ring systems, including heterocyclic ring, aromatic ring as well as pentacyclic substituents. In addition, alkyl chain with different functional groups like hydroxyl, alkene system, amide and amine were also observed (**Table 4.6**).

Table 4.6: Classification of chemical groups for top fifty derivatives as Hyal-1 inhibitors

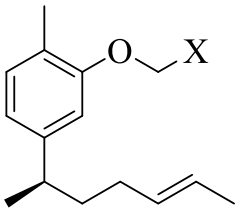

X= fragments

Chemical structures of the fragments, X	Number of derivatives generated
Heterocyclic five-membered ring	24
Five-membered ring	12
Six-membered ring	1
Alkyl chain with functional group	13

The synthetic tractability of these derivative need to be carefully considered, since a feasible synthetic route was essential for the synthesis of the compounds. Therefore, the generated derivatives were modified based on the commercially available chemicals for the substituents, while ensuring that the newly designed derivatives still possessed stronger binding energies towards Hyal-1 enzyme compared to XNT **(1)** (-6.5 kcal/mol).

Nine generated derivatives, labelled as **H026**, **H131**, **H343**, **H371**, **H552**, **H672**, **H819**, **H868**, and **H910** (**Figure 4.15**) were selected as the reference compounds to be modified with a good synthetic tractability. From the modification of generated derivatives, five XNT derivatives, namely (2-pyridinyl)methyl xanthorrhizyl ether **(102)**, 4-nitrobenzy xanthorrhizyl ether **(103)**, 3-(trifluoromethyl) benzyl xanthorrhizyl ether **(104**), (2-tetrahydro-2*H*-pyranyl)methyl xanthorrhizyl ether **(105)** and (2-tetrahydrofuranyl)methyl xanthorrhizyl ether **(106)** were proposed to be synthesised. The structures of derivatives **(102-106)** can be referred in **Section 3.4.2**. These derivatives were composed of ring systems with different heteroatoms as the substituents.

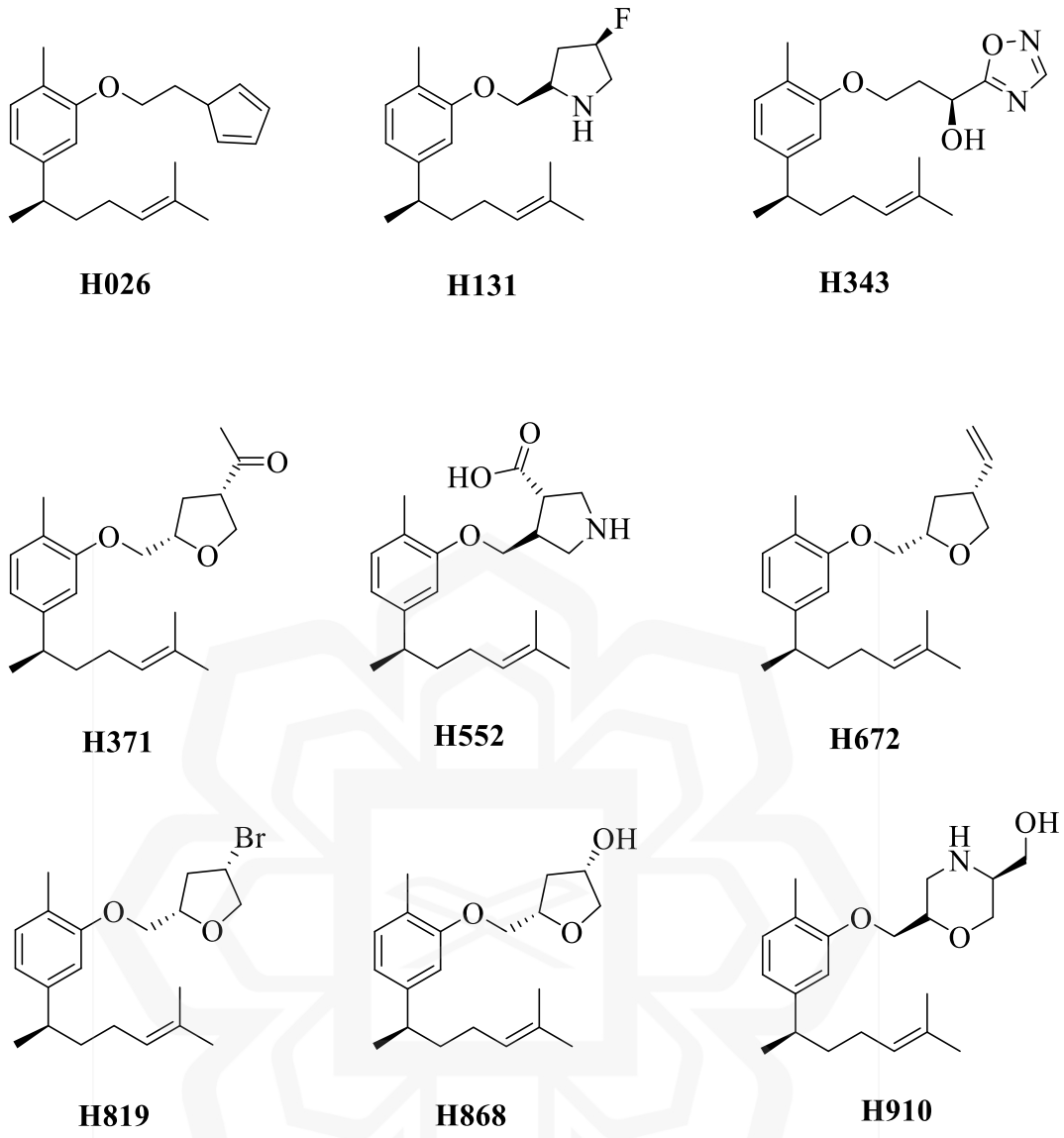

Figure 4.15: The structure of generated derivatives that inspired derivatives **(102-106)**

The derivatives **(102-104)** were proposed based on the inspiration from the structures of **H026**, **H131**, **H343**, **H552** and **H910**. These structures of these derivatives included the presence of heterocyclic ring containing oxygen and nitrogen, and substituents containing nitrogen and oxygen atom. Meanwhile, derivative **(105)** and **(106)** were inspired from the structure of including **H371**, **H672**, **H868**, and **H819**, which were composed of substituted oxygen heterocycles.

Then, to further confirm the ability of newly proposed derivatives **(102-106)** to possess good binding interactions against Hyal-1 enzyme, they were subjected to molecular docking analysis. The docking results showed that all derivatives were bound to the active site of Hyal-1 enzyme (**Figure 4.16**) and exhibited better binding energies compared to XNT (-6.5 kcal/mol) (**Table 4.7**).

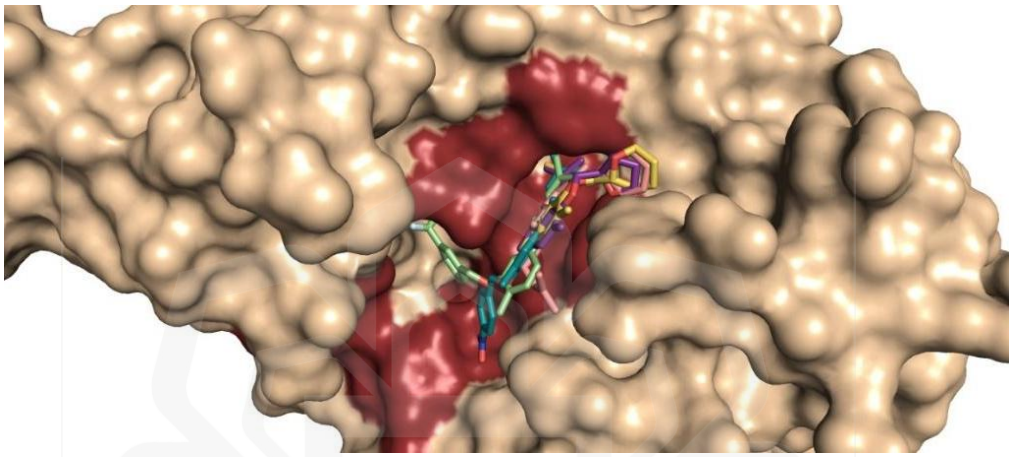

Figure 4.16: Docking conformation of derivatives **(102-106)** in Hyal-1 binding site. The active site residues are coloured in maroon.

Table 4.7: Docking result of derivatives **(102-106)** against Hyal-1 enzyme

Derivatives	Binding energies (kcal/mol)	Interaction with amino acid residues
(102)	-7.9 ± 0.06	Pro62, Tyr75*, **Asp129**, Trp321
(103)	-8.2 ± 0.31	**Glu131**, Tyr210*, **Ser245**
(104)	-8.9 ± 0.06	Trp130, **Glu131**, **Tyr202***, Gly203
(105)	-7.7 ± 0.10	Pro62, Tyr75, **Tyr202**, Trp321*, Val322
(106)	-7.5 ± 0.17	**Tyr202***, Trp321
(1)	-6.5 ± 0.06	Arg134, Tyr210*, Pro249, Tyr261

Notes. The essential interacting amino acid residues were shown in **bold**. The residues with hydrogen bond interactions were marked with (*).

Among them, derivative **(104)** exhibited strongest affinity against the enzyme with binding energy -8.9 ± 0.06 kcal/mol. It interacted with important Tyr202 and Glu131 residues *via* hydrogen bonding interaction and carbon hydrogen bonding, respectively. Moreover, the trifluoromethyl group also displayed halogen interactions with Trp130 and Gly203 (**Figure 4.17**). These findings were predicted to lead to good inhibitory activity against Hyal-1 enzyme in the *in vitro* studies.

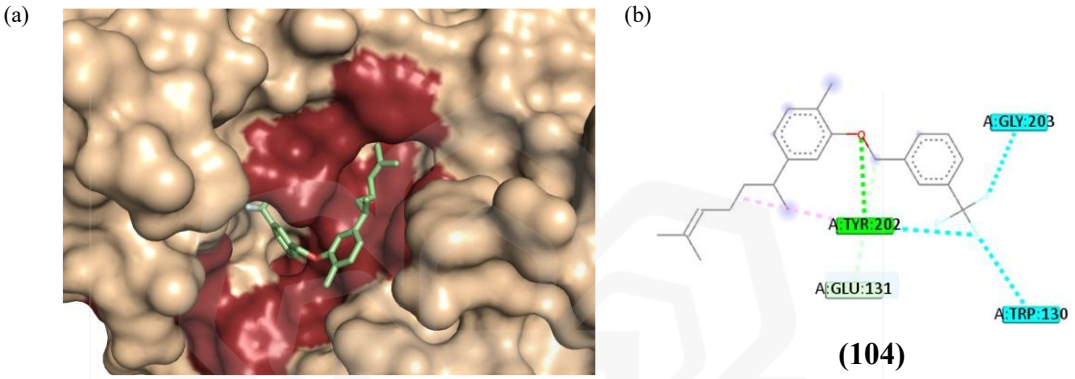

(104)

Figure 4.17: (a) 3D docking pose of derivative **(104)** (green) in Hyal-1 enzyme binding site; (b) 2D representation for interactions of derivative **(104)** with amino acid residues of Hyal-1.

Moreover, derivatives **(102-106)** also displayed good binding energies with Hyal-1 enzyme with binding energies ranging from -8.1 to -7.5 kcal/mol. These derivatives also capable of forming hydrogen bonding interactions with important residues essential for enzyme activity in binding site of Hyal-1 enzyme (Tyr202, Asp129, Glu131 and Ser245) (**Figure 4.18**). The results indicated their potential as Hyal-1 inhibitors. The improved result in terms of binding energies and interactions between the derivatives and Hyal-1 enzyme compared to XNT **(1)** suggested that the substitution of hydroxyl group to ring system can enhance the potential of XNT **(1)** as Hyal-1 inhibitors. The summary for the overall processes of designing new XNT derivatives as Hyal-1 inhibitors were depicted in **Figure 4.20**.

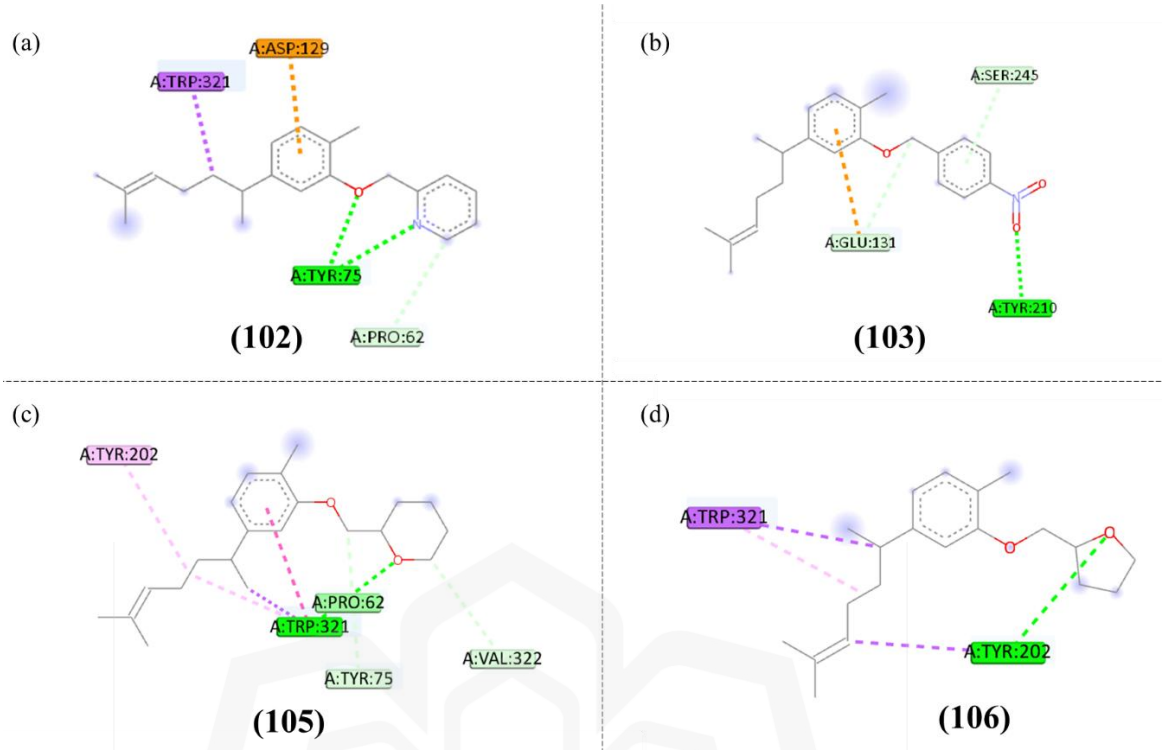

Figure 4.18: 2D representation for interactions with amino acid residues of Hyal-1 enzyme for derivatives; a) **(102)**, b) **(103)**, c) **(105)**, d) **(106)**

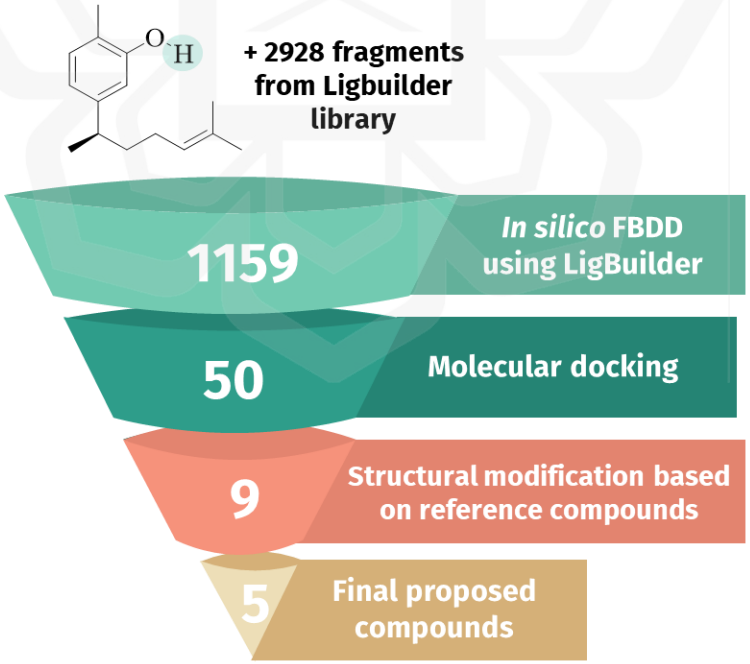

Figure 4.19: Overall processes for the design of Hyal-1 inhibitors using *in silico* FBDD approach.

4.3.2 Design of Xanthorrhizol Derivatives as LOX-3 Inhibitors

The design of XNT derivatives using *in silico* FBDD as LOX-3 inhibitors was conducted using similar steps as Hyal-1 inhibitors as in **Section 4.3.1**. Cavity mode predicted ten potential binding sites for LOX-3 enzyme as shown in **Table 4.8**. Among them, only cavity **3** was identified as "Druggable" (DrugScore 1356.00) with maximum and average pK_d value of 10.63 and 6.95, respectively. Thus, it was selected as the target binding site for designing XNT **(1)** derivatives. The location of cavity **3** was also consistent with the binding site of LOX-3 enzyme near the non-heme iron atom as described by Koukoulitsa et al. (2007). Cavity **3** and its comparison with LOX-3 binding site is shown in **Figure 4.20**.

Table 4.8: CAVITY results for LOX-3 enzyme

Cavity	Maximum pK_d	Average pK_d	DrugScore	Druggability
1	8.56	6.81	-1235.00	Undruggable
2	9.59	6.88	-361	Undruggable
3	10.63	6.95	1356.00	Druggable
4	11.40	6.99	-117.00	Amphibious
5	11.40	6.40	-603.00	Undruggable
6	10.03	6.06	-895.00	Undruggable
7	6.69	4.91	-1557.00	Undruggable
8	6.69	4.91	-1353.00	Undruggable
9	6.00	4.68	-1540.00	Undruggable
10	5.57	4.53	-1498.00	Undruggable

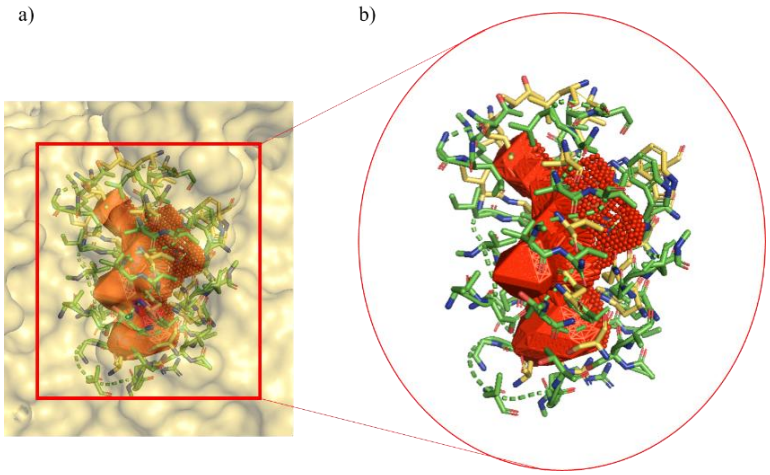

Figure 4.20: a) Overlay of LOX-3 active site and cavity **3** surface (orange); b) Alignment of cavity **3** surface (orange), amino acid residues of cavity **3** (green) and active residues of LOX-3 (yellow).

The utilisation of two seed structures as mentioned in **Section 4.3** generated 1887 new XNT derivatives in the Build mode. The screening of the derivatives revealed that the top fifty derivatives was bound to LOX-3 with binding energies ranging from -9.0 to -8.4 kcal/mol (**Appendix B**). The classification for the chemical groups of the derivatives were shown in **Table 4.9**. The derivatives (labelled with **L** for LOX-3 inhibitors) were composed of long alkyl chain, with presence of diverse substitution with polar functional group in the chain, including ring system, carbonyl group, and heteroatoms, including nitrogen and oxygen.

The derivatives generated as LOX-3 inhibitors were designed with alkyl chain, which conformed to hydrophobic channel of the enzyme (Koukoulitsa et al., 2007). Consequently, the derivatives had increased number of rotatable bonds and lipophilicity, compromising their drug-like properties. Therefore, some modifications were implemented on the design of the derivatives to resolve this issue, which included reducing the length of the alkyl chain while keeping the polar functional groups and ring system. This strategy helped to retain the hydrogen bonding networks with the hydrophilic region as well as stabilisation of the protein-ligand complex through interactions with the hydrophobic pocket of LOX-3 binding site. Moreover, the modifications were also made by considering the feasible synthetic route of each derivative.

Table 4.9: Classification of chemical groups for top fifty derivatives as LOX-3 inhibitors

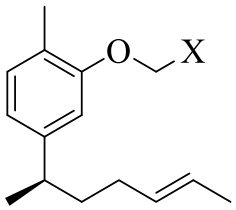

X= fragments

Chemical structures of the fragments, X	Number of structures generated
Hydrophobic alkyl chain	14
Alkyl chain with five-membered ring	13
Alkyl chain with aromatic ring	2
Alkyl chain with nitrogen heterocycles	5
Alkyl chain with functional group	16

Four new derivatives were proposed as LOX-3 inhibitors, namely 2-(xanthorrhizyloxy)ethyl carbamide **(107)**, *N*-(2-(xanthorrhizyloxy)ethyl)-1*H*-imidazole-4-carboxamide **(108)**, *N*-(2-(xanthorrhizyloxy)ethyl)-3-aminopropanamide **(109)** and 3-(xanthorrhizyloxy)propyl 1*H*-imidazole-4-carboxylate **(110)**. The structures of derivatives **(107-110)** can be referred in **Section 3.4.2**. These derivatives featured alkyl chain bonded to polar functional group (amide and ester).

The design of XNT derivatives for LOX-3 enzymes were inspired by the structure of six generated derivatives **L101**, **L102**, **L167**, **L321**, **L843** and **L922** (**Figure 4.21**). Derivative **(107)** was modified based on **L843**, where the length of alkyl chain was shortened to 1-ethylurea group. Meanwhile, derivatives **(108)** and **(110)** were consisted of imidazole ring, attached to *N*-ethylacetamido and propylacetate group, respectively, inspired by the structure of **L101, L102, L321, L922** with different five-membered ring. Derivative **(109)** was derived from **L167**. Originally composed of long alkyl chain linked with two acetamido groups, it was modified to have shorter chain with only one acetamido and amino group to improve the drug-likeness properties of the derivatives.

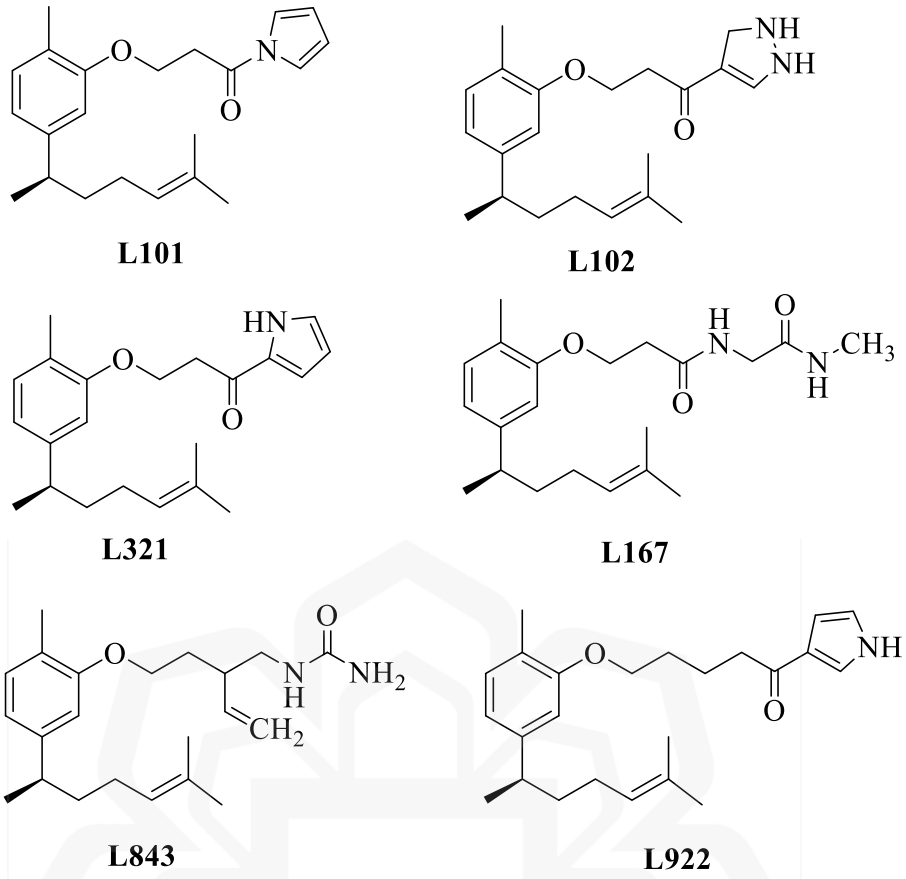

Figure 4.21: The structure of generated derivatives that inspired derivatives **(102-106)**

All designed derivatives were subjected to molecular docking to validate their binding affinities towards LOX-3 enzyme. The docking results showed that all derivatives were docked inside the binding pocket of LOX-3 enzyme (**Figure 4.22**). All derivatives also exhibited stronger binding energy compared to XNT **(1)** (-7.7 kcal/mol), ranging from -8.3 to -7.9 kcal/mol (**Table 4.10**).

Derivative **(108)** showed the strongest binding towards LOX-3 enzyme, with binding energy -8.3 kcal/mol. The derivative had hydrogen bonding interactions with His513 and Arg726 as depicted in **Figure 4.23**. The hydrogen bond interaction with Arg726 was reportedly important for stabilisation of ligand-enzyme complex in LOX-3 binding site, thus contributing to strong inhibitory activity in *in vitro* studies (Lavrentaki et al., 2023). Moreover, the imidazole ring in the structure also interacted with Gly720 and Asp766 through carbon-hydrogen bond and pi-anion bond, respectively. The XNT backbone was stabilised at the hydrophobic channel of LOX-3

enzyme binding pocket *via* hydrophobic interactions with His523, Ala561, Ile572 and Leu773.

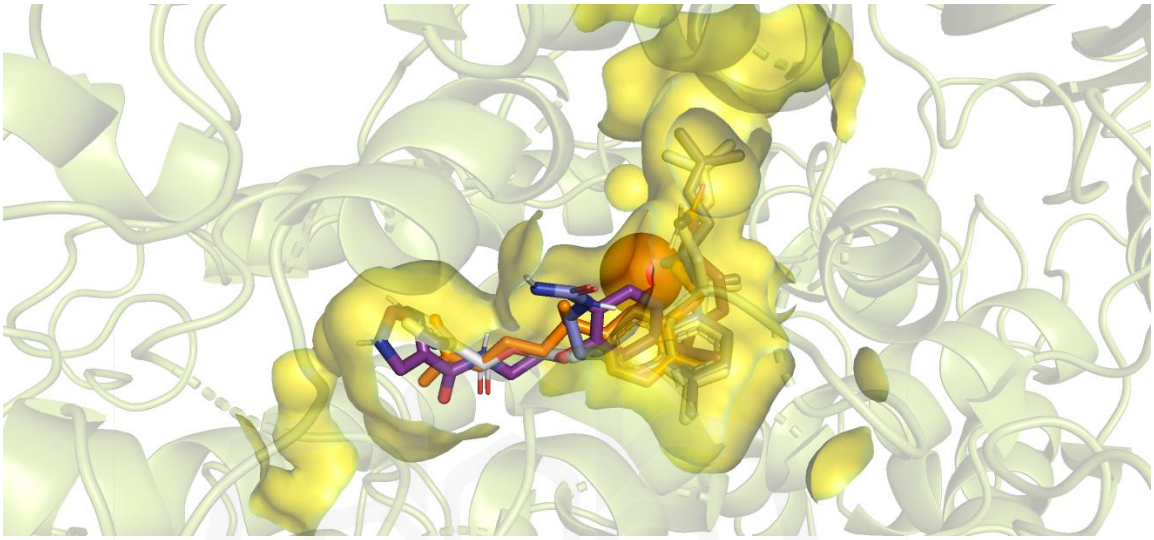

Figure 4.22: Docking conformation of derivatives **(107-110)** in LOX-3 binding site. The active site residues are coloured in yellow. Red ball represents non-heme iron.

Table 4.10: Docking result of derivatives **(107-110)** against LOX-3 enzyme

Compounds	Binding energies (kcal/mol)	Interaction with amino acid residues
(107)	-7.9 ± 0.15	Val372, His513, **His518**, Ile572, Ile770, **Ile857***, **Fe858**
(108)	-8.3 ± 0.15	His513*, **His523**, Ala561, Ile572, **Gly720**, **Arg726***, **Asp766**, Leu773
(109)	-8.0 ± 0.20	Ile572, Gln716*, **Gly720***, **Arg726***, **Asp766***
(110)	-8.2 ± 0.06	Leu227, His513*, His523, Ile572, Gln716*, Ile770, **Asp766**
(1)	-7.7 ± 0.00	Gln514*, Ile572

Notes. The essential interacting amino acid residues were shown in **bold**. The residues with hydrogen bond interactions were marked with (*).

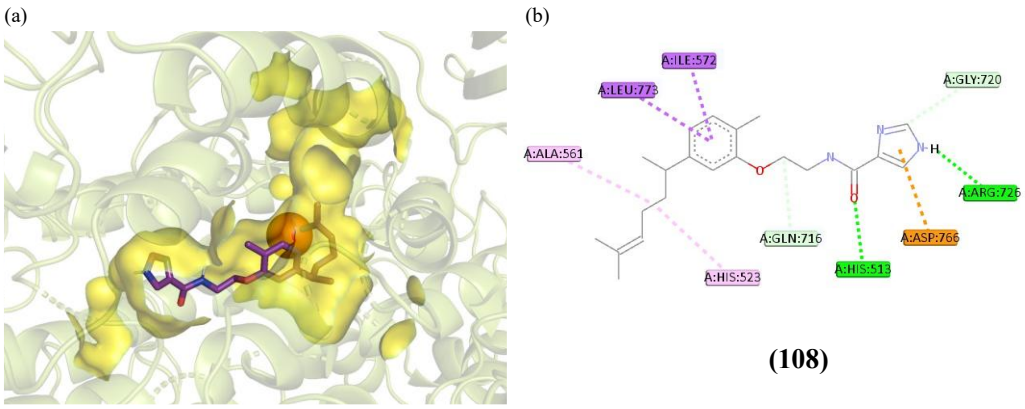

Figure 4.23: (a) 3D docking pose of derivative **(108)** (purple) in LOX-3 enzyme binding site; (b) 2D representation for interactions of derivative **(108)** with amino acid residues of LOX-3.

Derivatives **(109-110)** were also bound to the binding site of LOX-3 through hydrogen bonding interactions in the hydrophilic region with stabilisation in the hydrophobic channel as observed in **Figure 4.24**. Nitrogen atom from acetamido and amino group in derivative **(109)** contributed to four hydrogen bonding interactions with Gln716, Gly720, Arg726 and Asp766. Meanwhile, derivative **(110)** formed hydrogen bonding with His513 and Gln716, and also interacted with Leu227, His523, Ile572, Ile770, and Asp766 through hydrophobic interactions.

The XNT backbone of derivative **(107)** was also stabilised in hydrophobic channel through interactions with Val372, His513, His518, Ile572, and Ile770 (**Figure 4.24**). However, substituent 1-ethylurea interacted with Ile857, which was one of the residues that coordinates with the iron atom in the catalytic site of the LOX-3 enzyme, instead of residues in hydrophobic region. Carbon hydrogen bond was also formed with the iron atom. Previous studies suggested that hydrophobic interactions with iron atom contribute to the enhanced inhibitory activity in *in vitro* studies (Lavrentaki et al., 2023). Based on the docking analyses, it can be observed that the introduction of polar functional groups for the design of XNT derivatives as LOX-3 inhibitors showed promising result as they demonstrated improved binding energies and interactions. The overall processes for designing new XNT derivatives as LOX-3 inhibitors was summarised in **Figure 4.25**.

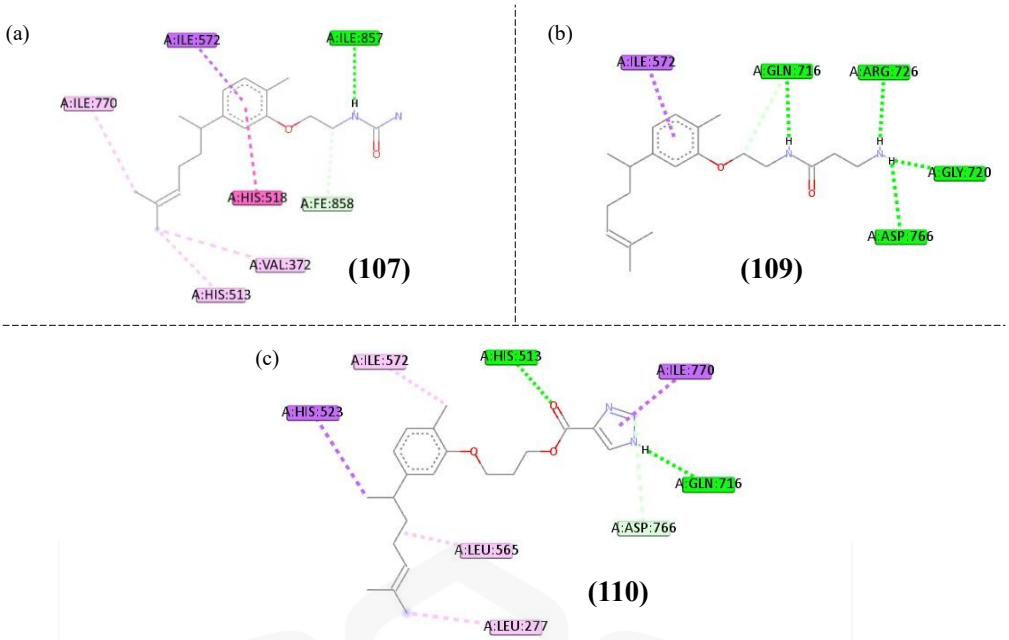

Figure 4.24: 2D representation for interactions with amino acid residues of LOX-3 for; a) derivative **(107)**, b) derivative **(109)**, c) derivative **(110)**.

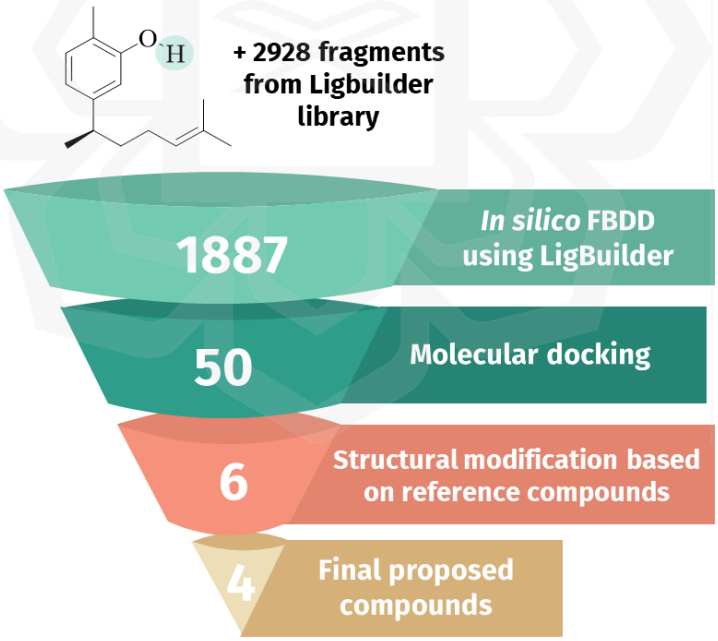

Figure 4.25: Overall processes for the design of LOX-3 inhibitors using *in silico* FBDD approach.

4.3.3 *In Silico* Drug-Likeness and Absorption Profiles of Designed Xanthorrhizol Derivatives (102-110)

All proposed derivatives were submitted to SwissADME server to evaluate its drug-likeness properties. The proposed Hyal-1 inhibitors, derivative **(102-106)** violated at least one pharmacokinetic descriptor for good drug absorption in human body **(Table 4.11)**. Derivative **(102)** displayed the best drug-like properties compared to other derivatives, as it only violated lipophilicity rule with XLOGP3 value of 5.81. All derivatives also classified as moderately soluble and expected to have high absorption in GI tract, except for derivative **(104)**. Derivative **(104)** violated three parameters, lipophilicity (XLOGP3= 7.73), TPSA (9.23 $Å^2$), and solubility (LogS= -6.84) and its effect was reflected in its classification as poorly soluble and predicted to possess low gastrointestinal tract absorption. The incorporation of trifluoromethyl group in the methylbenzene substituent has significantly increased the lipophilicity of derivative **(104)** due to high hydrophobicity from fluorine (Jeffries et al., 2018).

Meanwhile, the drug-likeness profiles of the proposed LOX-3 inhibitors revealed that only derivative **(107)** satisfied all parameters for good absorption in human body **(Table 4.11)**. Derivatives **(108-110)** failed to comply optimum number of rotatable bonds less than 9, as derivative **(108)** consisted of 10 rotatable bonds, while derivative **(109)** and **(110)** had 11 rotatable bonds. Derivative **(107)** also had higher lipophilicity compared to other derivatives that might be attributed to the increased hydrophobic character due to the propyl alkyl chain and ester group possessed by derivative **(110)**. Nevertheless, all derivatives proposed for LOX-3 enzyme were expected to have good absorption in gastrointestinal tract.

From the result in **Table 4.11**, it can be observed that the drug-likeness profiles of the designed derivatives **(102-106)** for Hyal-1 enzyme did not improve compared to XNT **(1)**. The substitution from hydroxyl group to ring system had increased the hydrophobic characteristics of the derivatives. This is because LigBuilder generated the derivatives based on the binding site of the enzyme. Hence, the non-polar attributes of Hyal-1 binding site (Chao et al., 2007) has likely contributed to the non-polar derivatives generated for Hyal-1 enzyme.

Meanwhile, the design for LOX-3 inhibitors was generally more polar compared to Hyal-1 inhibitors, which might be attributed to the hydrophilic region around the catalytic site of LOX-3 enzyme (Koukoulitsa et al., 2007). Therefore, the derivatives **(107-110)** designed for LOX-3 enzyme showed significant improvement in its drug-like properties due to the incorporation for polar functional groups like amides and esters.

Table 4.11: *In silico* drug-likeness and absorption profile for derivatives **(102-110)**.

Compounds	Molecular weight (MW ≤ 500)	Carbon bond saturation ($Csp^3 \geq 0.25$)	No of rotatable bonds (n < 9)	TPSA (20 $Å^2 \leq$ TPSA ≤ 130 $Å^2$)	XLOGP3 (XLOGP3 ≤ +5.0)	ESOL Log S (Log S ≥ -6)	Solubility class	GI absorption
(102)	309.45[a]	0.38[a]	7[a]	22.12[a]	5.81[b]	-5.34[a]	Moderately soluble	High
(103)	353.45[a]	0.36[a]	8[a]	55.05[a]	6.67[b]	-6.05[b]	Moderately soluble	High
(104)	376.46[a]	0.39[a]	8[a]	9.23[b]	7.73[b]	-6.84[b]	Poorly soluble	Low
(105)	316.48[a]	0.62[a]	7[a]	18.46[b]	6.11[b]	-5.38[a]	Moderately soluble	High
(106)	302.45[a]	0.60[a]	7[a]	18.46[b]	5.76[b]	-5.08[a]	Moderately soluble	High
(107)	304.43[a]	0.50[a]	9[a]	64.35[a]	4.09[a]	-3.91[a]	Soluble	High
(108)	355.47[a]	0.43[a]	10[b]	67.01[a]	4.80[a]	-4.72[a]	Moderately soluble	High
(109)	332.48[a]	0.55[a]	11[b]	64.35[a]	3.66[a]	-3.67[a]	Soluble	High
(110)	370.49[a]	0.45[a]	11[b]	64.21[a]	5.73[b]	-5.32[a]	Moderately soluble	High

*Notes.*The optimum range based on SwissADME parameters; [a]No violation; [b]Violation

CHAPTER 5

SYNTHESIS, BIOLOGICAL ACTIVITIES AND MOLECULAR DYNAMICS SIMULATION OF XANTHORRHIZOL DERIVATIVES

5.1 INTRODUCTION

In this chapter, XNT **(1)** was isolated and purified from *C. xanthorrhiza* essential oil. The purified XNT **(1)** was then used as the starting material for the synthesis of derivatives **(102-106)** as potential Hyal-1 inhibitors and derivatives **(107-110)** as potential LOX-3 inhibitors. The synthesised compounds were characterised using spectroscopic analyses including NMR, MS and IR spectroscopy. The synthesised derivatives were then subjected to *in vitro* assays against Hyal-1 and LOX-3 enzymes. The most active derivative against the enzyme was then subjected to MD simulation to further analyse the interactions of the derivative against the enzyme.

5.2 ISOLATION AND PURIFICATION OF XANTHORRHIZOL (1) FROM *C. XANTHORRHIZA* ESSENTIAL OIL

The essential oil of *C. xanthorrhiza* were subjected to fractionation *via* VLC. The TLC profile of subfraction CXED5 showed the presence of two spots; a major spot for XNT **(1)** and a minor spot identified as mixture of sesquiterpenoids. To purify the XNT **(1)**, two-step synthesis method, which were acetylation of XNT **(1)** in the subfraction CXED5 to xanthorrhizyl acetate **(64)**, followed by hydrolysis of **(64)**.

The subfraction CXED5 was subjected to acetylation reaction (**Figure 5.1**) to afford xanthorrhizyl acetate **(64)**. In this reaction, pyridine was used as a base to abstract a proton from XNT **(1)** to form nucleophilic phenoxide ion **(127)**. The ion would attack the electrophilic carbonyl of acetic anhydride to produce intermediate **(128)**. Removal

of acetate ion from intermediate **(128)** due to the electron's delocalisation afforded xanthorrhizyl acetate **(64)**. The reaction mechanism was shown in **Scheme 5.1**.

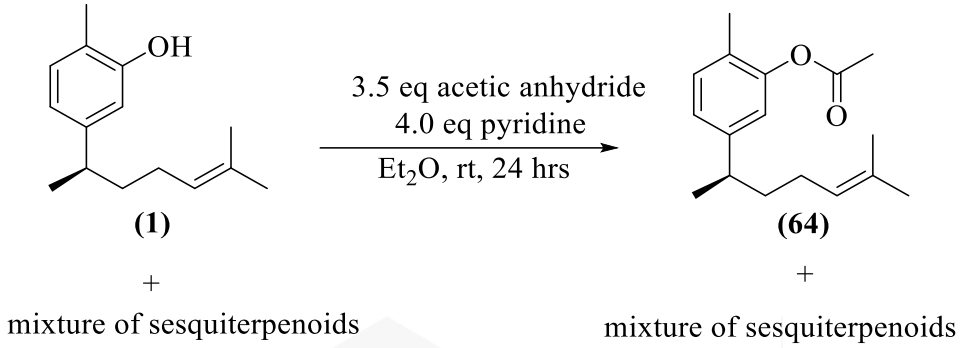

Figure 5.1: Acetylation reaction of XNT **(1)**

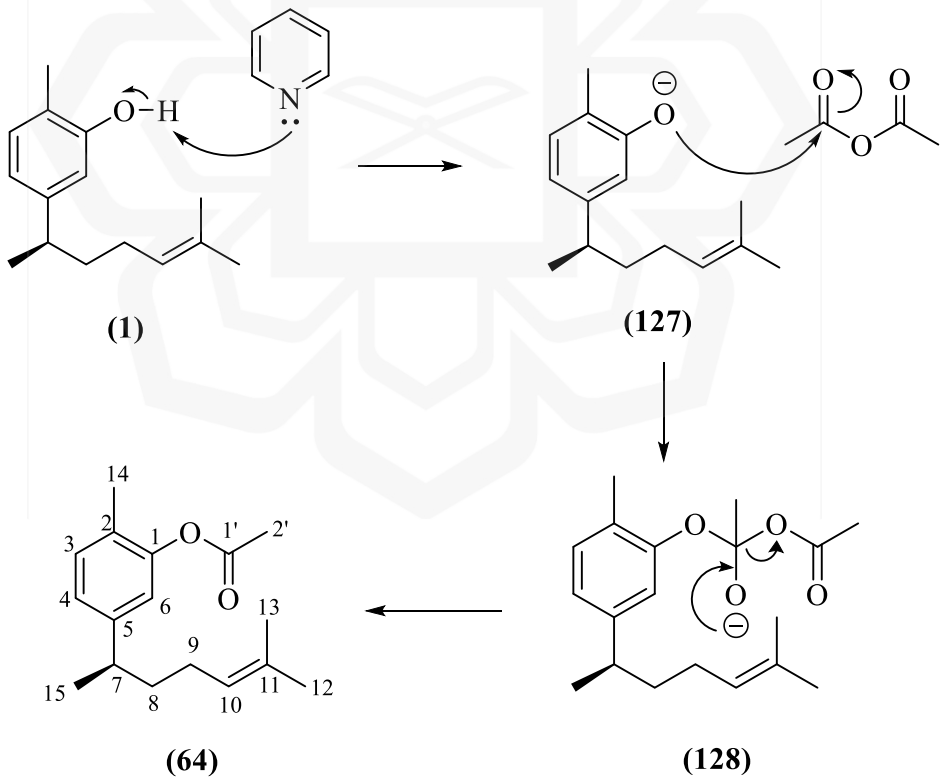

Scheme 5.1: Reaction mechanism for acetylation of XNT **(1)**

The ^{1}H NMR spectrum of compound **(64)** (**Appendix C2**) showed a doublet signal at δ_H 1.20 (3H, *J* = 7.0 Hz) assigned for H-15 due to coupling with methine proton, H-7 (δ_H 2.66, 1H, *J* = 7.0 Hz, sextet). Two sets of singlet peaks at δ_H 1.52 and 1.67, integrated for three protons each corresponded to methyl protons H-12 and H-13, respectively. Moreover, two sets of multiplets resonated at δ_H 1.54-1.60 and 1.84-1.90 were assigned to methylene protons H-8 and H-9, respectively. The slightly deshielded singlet peak at δ_H 2.14 was assigned as methyl protons H-14 bonded to the aromatic ring. The signals of aromatic protons H-6 and H-3 arised as doublets at δ_H 6.81 (*J* = 1.7 Hz) and δ_H 7.14 (*J* = 7.7 Hz). The signal of H-4 appeared as doublet of doublet signal (δ_H 6.96, *J* = 1.7 and 7.7 Hz), due to the meta and ortho coupling with H-6 and H-3, respectively. Additional singlet peak integrated for three protons at δ_H 2.31 was assigned for acetate methyl protons H-2'.

Meanwhile, ^{13}C NMR spectrum (**Appendix C3**) showed a total of seventeen carbon peaks, which corresponded to the total number of carbons in compound **(64)**. The most deshielded signal at δ_c 169.20 (C-1') was assigned to the carbonyl of ester. The appearance of strong absorption peak at 1768.06 cm^{-1} in the IR spectrum (**Appendix C1**) further confirmed the presence of acetate functionality. The signals resonated at δ_C 120.34 (C-6), 124.38 (C-4), 124.71 (C-2), 130.83 (C-3), 146.94 (C-5) and 149.30 (C-1) indicated the presence of aromatic carbons. The molecular ion peak at *m/z* 260 in the MS spectrum (**Appendix C4**) corresponded with the molecular formula of xanthorrhizyl acetate **(64)**, $C_{17}H_{24}O_2$. All spectroscopic data obtained for compound **(64)** were in agreement with the published data of similar compound from Ngai & Sirat (2004) as tabulated in **Table 5.1**.

Table 5.1 ^{1}H and ^{13}C NMR data for xanthorrhizyl acetate **(64)** (δ in ppm, *J* in Hz)

No	δ_H[a]	δ_H[b]	δ_C[a]	δ_C[b]
1	-	-	149.30	149.3
2	-	-	124.71	124.7
3	7.13 (1H, d, *J* = 7.7)	7.16 (1H, d, *J* = 7.8)	130.83	130.8
4	6.96 (1H, dd, *J* =1.7, 7.7)	6.99 (1H, dd, *J* =7.8, 1.8)	124.38	124.4

5	-	-	146.94	146.9
6	6.81 (1H, d, *J* =1.7)	6.84 (1H, d, *J* = 1.8)	120.34	120.3
7	2.66 (1H, sext, *J* = 7.0)	2.69 (1H, sext, *J* = 6.9)	38.85	38.9
8	1.54-1.60 (2H, m)	1.55-1.66 (2H, m)	38.33	38.3
9	1.84-1.90 (2H, m)	1.88-1.95 (2H, m)	26.07	26.1
10	5.07 (1H, tt, *J* = 7.1, 1.4)	5.10 (1H, tt, *J* = 7.2, 1.2)	127.71	127.2
11	-	-	131.52	131.5
12	1.52 (3H, s)	1.53 (3H, s)	17.66	17.7
13	1.67 (3H, s)	169 (3H, s)	25.69	25.7
14	2.14 (3H, s)	2.16 (3H, s)	15.78	15.8
15	1.20 (3H, d, *J* = 7.0)	1.24 (3H, d, *J* = 6.9)	22.15	22.2
1'	-	-	169.20	169.3
2'	2.31 (3H, s)	2.33 (3H, s)	20.83	20.9

Notes.[a] experimental data measured at 500 MHz for ^{1}H NMR and 125 MHz for ^{13}C NMR in $CDCl_3$; [b] lit data (Ngai & Sirat, 2004) measured at 300 MHz for ^{1}H NMR and 75 MHz for ^{13}C NMR in $CDCl_3$.

XNT **(1)** were recovered from its acetate derivative **(64)** through hydrolysis reaction (**Figure 5.2**) to obtain pure XNT **(1)**. In this base-catalysed reaction, carbonate ion from K_2CO_3 abstracted proton from MeOH to produce methoxy ion. The methoxy ion then attacked the carbonyl carbon in compound **(64)** to form anionic intermediate **(129)**. The movement of lone pair in intermediate **(129)** leads to production of phenoxide ion **(127)** and loss of methyl acetate **(130)**. Phenoxide ion **(127)** underwent deprotonation of water molecule to afford XNT **(1)**, while potassium hydroxide (KOH) was removed as leaving group. The reaction mechanism was shown in **Scheme 5.2**. XNT **(1)** is an optically active compound due to the presence of chiral center of C-7. The absolute configuration of naturally occurring XNT **(1)** was established as *R*-configuration (John & Rao, 1985). The specific rotation of purified XNT **(1)** was $[\alpha]_D^{25}$ –59.26 (*c* 1.08, MeOH).

The formation of XNT **(1)** from xanthorrhizyl acetate **(64)** was characterised by using IR spectrum (**Appendix D1**) through the appearance of broad peak at 3378.37 cm^{-1}, indicating the presence of hydroxyl group. The XNT **(1)** structure could also be

confirmed through the ^{1}H NMR spectrum (**Appendix D2**) through the appearance of a singlet peak at δ_H 4.62 assigned for hydroxyl proton H-1 and the disappearance of a singlet peak attributed for the methyl acetate protons H-2' (δ_H 2.31) of compound **(64)** (**Appendix C2**).

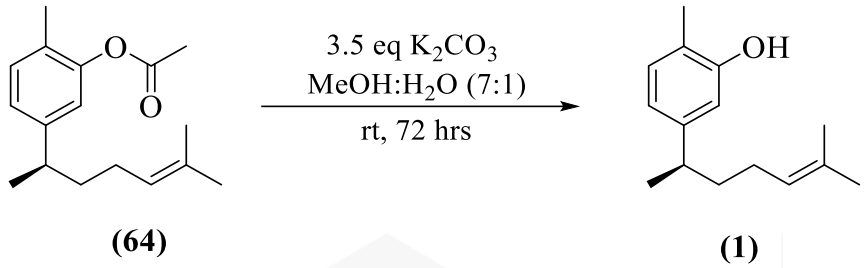

(64) **(1)**

Figure 5.2: Hydrolysis of xanthorrhizyl acetate **(64)**

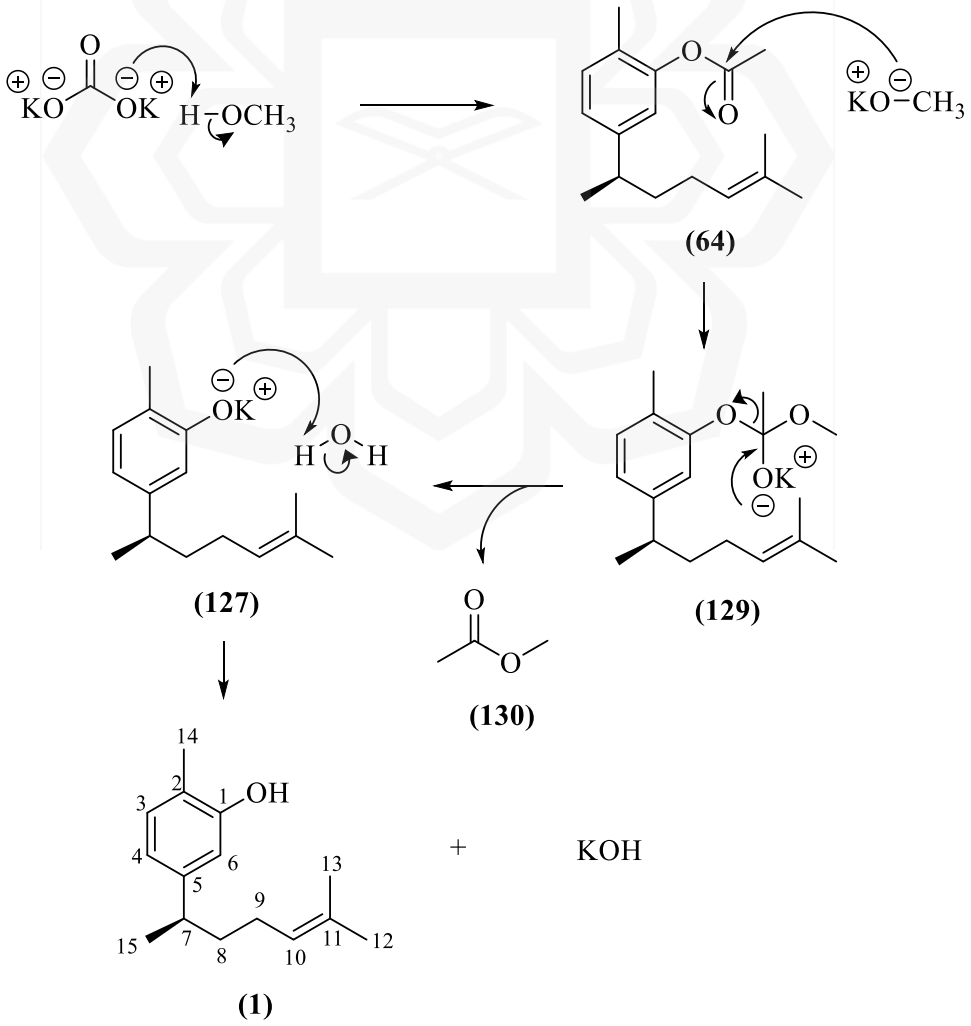

(64) **(127)** **(129)** **(130)** **(1)**

Scheme 5.2: Reaction mechanism of hydrolysis of xanthorrhizyl acetate **(64)**

The ^{13}C NMR spectrum for XNT **(1)** (**Appendix D3**) exhibited fifteen signals consistent with the total of fifteen carbons in the structure. The peaks for acetate functionality were no longer present in this spectrum. Instead, a deshielded signal at δ_C 153.61 supported the presence of hydroxyl group at C-1. The structure of XNT **(1)** was further confirmed with the presence of molecular ion (M^+) peak *m/z* 218 corresponding its molecular formula of $C_{15}H_{22}O$ in the MS spectrum (**Appendix D4**). It was deduced that XNT **(1)** possibly underwent collision with other ions in the ion trap or 'self-chemical ionisation' (self-CI) (Pavia et al., 2015). This phenomenon resulted in hydrogen transfer and yielded M+H peak of *m/z* 219. It was followed by the homolytic cleavage at C-7 position to afford fragment with *m/z* 136 as illustrated in **Scheme 5.3**. There is also another possibility that XNT **(1)** underwent homolytic cleavage at C-7 position, followed by self-CI and resulted in fragment with *m/z* 136. All spectroscopic data obtained for XNT **(1)** were consistent with the published data of same compound from Ngai & Sirat (2004) as tabulated in **Table 5.2**.

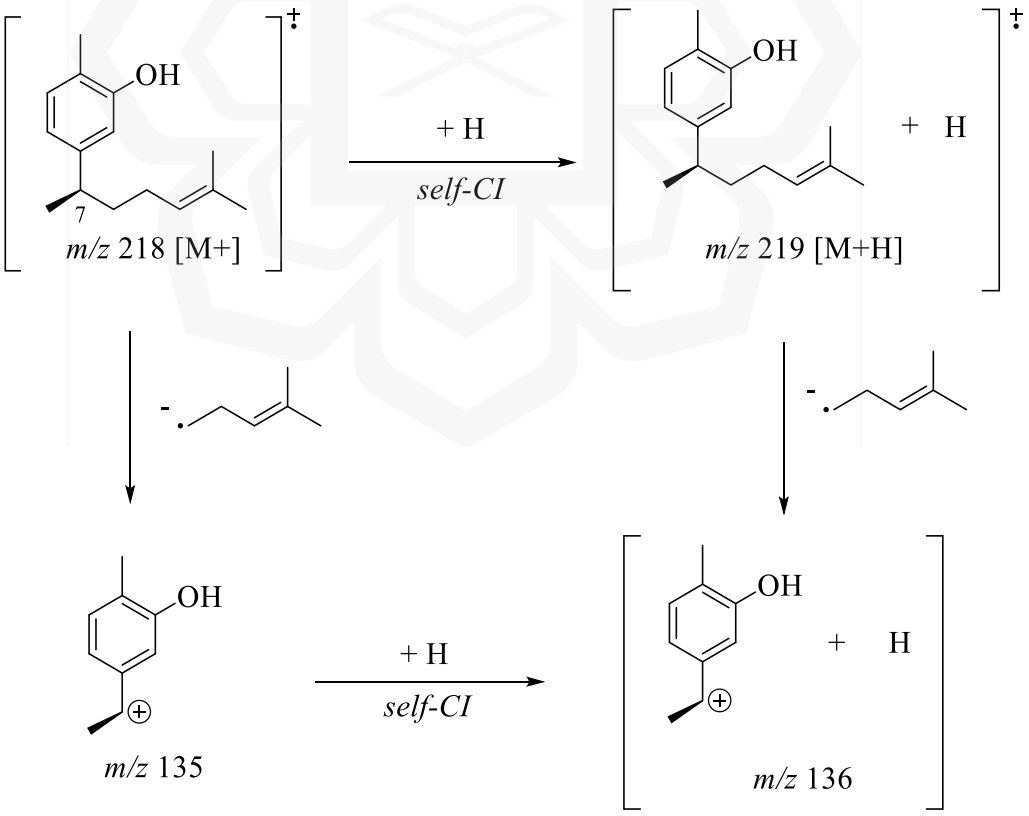

Scheme 5.3: Fragmentation pattern of XNT **(1)**

Table 5.2: ^{1}H and ^{13}C NMR data for XNT (**1**) (δ in ppm, *J* in Hz)

No	δ_H[a]	δ_H[b]	δ_C[a]	δ_C[b]
1	4.62 (1H, s)	4.69 (1H, s)	153.61	153.6
2	-	-	120.79	120.8
3	7.01 (1H, d, *J* = 7.7)	7.05 (1H, d, *J* =7.8)	130.76	130.3
4	6.66 (1H, dd, *J* = 7.7, 1.6)	6.70 (1H, d, *J* =7.8)	119.45	119.4
5	-	-	147.25	147.2
6	6.60 (1H, d, *J* = 1.6)	6.63 (1H, d, *J* =1.8)	113.54	113.5
7	2.61 (1H, sext, *J* = 7.0)	2.63 (1H, sext)	39.04	39.0
8	1.53-1.60 (2H, m)	1.62 (2H, m)	38.38	38.4
9	1.84-1.90 (2H, m)	1.89 (2H, m)	26.16	26.1
10	5.07 (1H, tt, *J* = 7.7, 1.4)	5.11 (1H, tt, *J* = 4.6)	124.52	124.5
11	-	-	131.43	131.4
12	1.53 (3H, s)	1.55 (3H, s)	15.31	15.3
13	1.67 (3H, s)	167 (3H, s)	25.71	25.7
14	2.21 (3H, s)	2.24 (3H, s)	17.68	17.7
15	1.19 (3H, d, *J* = 7.0)	1.22 (3H, d, *J* = 6.9)	22.38	22.4

Notes.[a] experimental data measured at 500 MHz for ^{1}H NMR and 125 MHz for ^{13}C NMR in $CDCl_3$; [b] lit data (Ngai & Sirat, 2004) measured at 300 MHz for ^{1}H NMR and 75 MHz for ^{13}C NMR in $CDCl_3$.

5.3 SYNTHESIS OF XANTHORRHIZOL DERIVATIVES (76, 102-105, 117) AS HYAL-1 INHIBITORS

The derivatives **(76**, **102-105**, **117)** were successfully synthesised using Williamson ether synthesis reaction. Derivatives **(102-105)** and **(117)** were new XNT derivatives while derivative **(76)** had been reported by Sirat et al. (2007). In general, the synthesis of derivatives **(76**, **102-104)** proceeded *via* bimolecular nucleophilic substitution (S_N2) reaction as illustrated in **Scheme 5.4**. XNT **(1)** was deprotonated by carbonate ion to produce phenoxide ion **(127)**. The phenoxide ion acted as nucleophile and attacked the electrophilic benzylic carbon of alkyl halides **(111-114)**, followed by the loss of halide ion. This reaction resulted in the formation of alkyl xanthorrhizyl ether derivatives **(76**, **102-104)**.

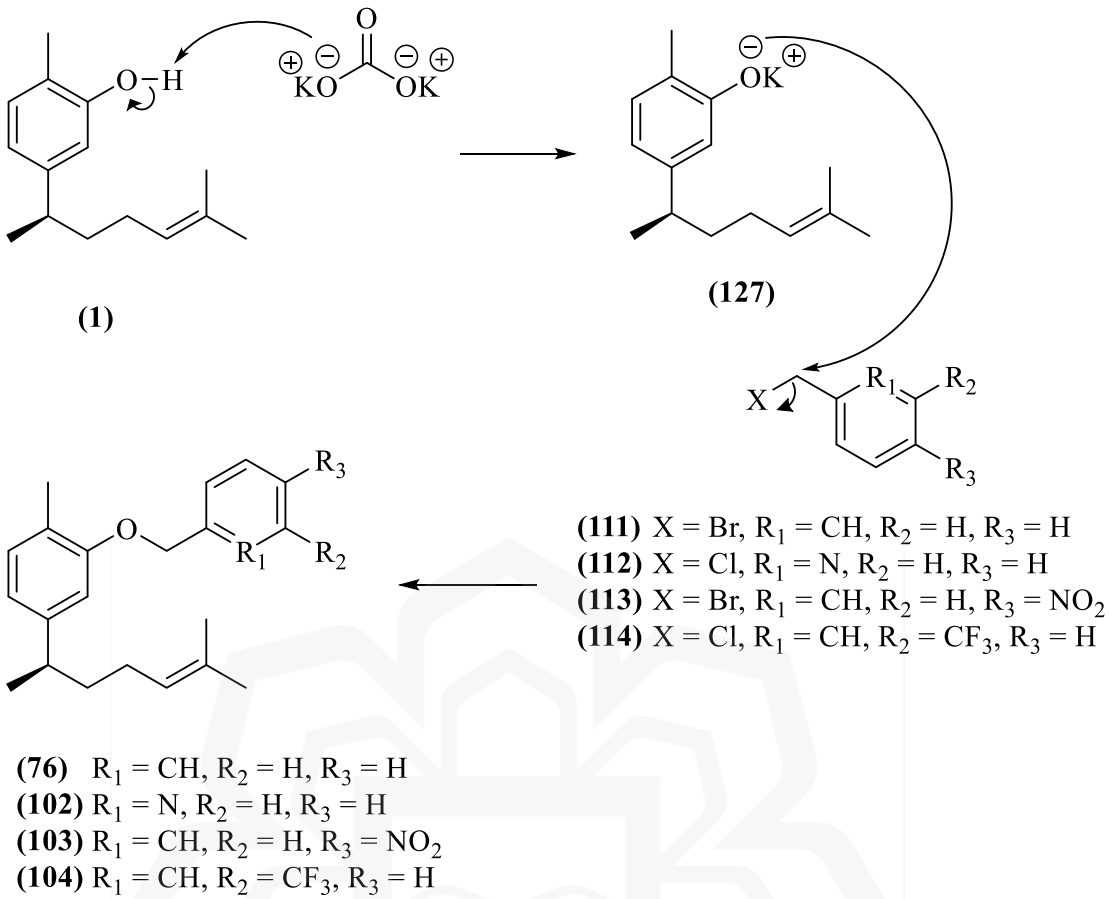

Scheme 5.4: Reaction mechanism for synthesis of derivatives **(76**, **102-104)**

The ^{1}H NMR spectral data for derivatives **(76**, **102-104)** were tabulated in **Table 5.3**. All proton signals of XNT **(1)** (H-1 to H-15) were observed in the ^{1}H NMR spectra. The presence of singlet signal integrated for two protons in the range of δ_H 5.07 to 5.18, indicating successful reaction. The rise of new signals at the aromatic region in the spectra of all derivatives signifies a successful formation of the derivatives (**Table 5.3**).

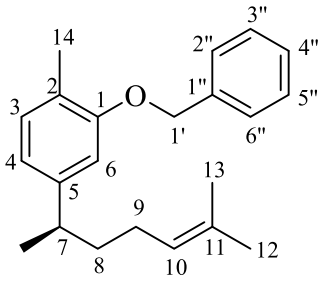

(76)

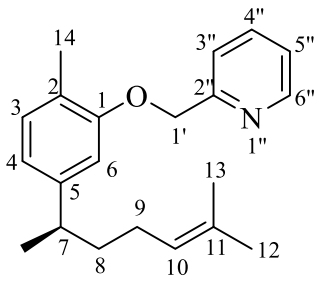

(102)

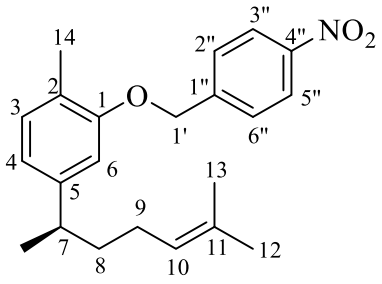

(103)

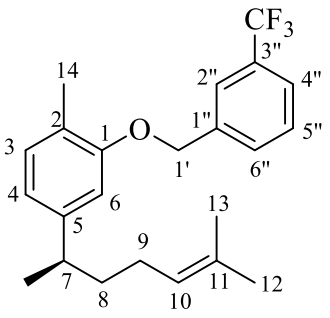

(104)

Table 5.3: ^{1}H NMR derivatives **(76**, **102-104)** (δ in ppm, *J* in Hz)

No	(76)[a]	(102)[b]	(103) [a]	(104) [a]
1	-	-	-	-
2	-	-	-	-
3	7.09 (1H, d, *J* = 7.2)	7.07 (1H, d, *J* = 7.6)	7.10 (1H, d, *J* = 7.1)	7.09 (1H, d, *J* = 7.6)
4	6.74 (1H, dd, *J* = 7.2, 1.2)	6.72 (1H, s)	6.75 (1H, dd, *J* = 7.1, 1.3)	6.75 (1H, dd, *J* = 7.6, 1.3)
5	-	-	-	-
6	6.72 (1H, d, *J*= 1.2)	6.71 (1H, s)	6.66 (1H, d, *J*= 1.3)	6.66 (1H, d, *J*= 1.3)
7	2.67 (1H, sext, *J* = 7.0)	2.62 (1H, sext, *J* = 6.9)	2.66 (1H, sext, *J* = 6.9)	2.66 (1H, sext, *J* = 7.0)
8	1.56-1.65 (2H, m)	1.52-1.58 (2H, m)	1.54-1.59 (2H, m)	1.55-1.60 (2H, m)
9	1.85-1.95 (2H, m)	1.77-1.89 (2H, m)	1.80-1.90 (2H, m)	1.82-1.93 (2H, m)
10	5.11 (1H, tt, *J* = 7.1, 1.2)	5.05 (1H, tt, *J* = 7.1, 1.2)	5.06 (1H, tt, *J* = 7.1, 1.2)	5.08 (1H, tt, *J* = 7.1, 1.4)
11	-	-	-	-
12	1.55 (3H, s)	1.51 (3H, s)	1.52 (3H, s)	1.53 (3H, s)
13	1.70 (3H, s)	1.66 (3H, s)	1.70 (3H, s)	1.68 (3H, s)
14	2.27 (3H, s)	2.30 (3H, s)	2.30 (3H, s)	2.27 (3H, s)

15	1.23 (3H, d, *J* = 7.0)	1.17 (3H, d, *J* = 6.9)	1.20 (3H, d, *J* = 6.9)	1.21 (3H, d, *J* = 7.0)
1'	5.10 (2H, s)	5.22 (2H, s)	5.18 (2H, s)	5.13 (2H, s)
1''	-	-	-	-
2''	7.48 (2H, dd, *J* = 7.4, 1.2)	-	7.63 (2H, d, *J* = 8.9)	7.73 (1H, s)
3''	7.40 (2H, t, *J* = 7.4)	7.57 (1H, d, *J*= 7.8)	8.26 (2H, d, *J* = 8.9)	-
4''	7.34 (1H, tt, *J* = 7.4, 1.2)	7.72 (1H, ddd, *J* = 7.8, 7.6, 1.6)	-	7.65 (1H, d, *J* = 7.6)
5''	7.40 (2H, t, *J* = 7.4)	7.20-7.26 (1H, m)	8.26 (2H, d, *J* = 8.9)	7.52 (1H, t, *J* = 7.6)
6''	7.48 (2H, dd, *J* = 7.4, 1.2)	8.58 (1H, dd, *J* = 4.8, 1.6)	7.63 (2H, d, *J* = 8.9)	7.59 (1H, d, *J* = 7.6)

Notes.[a] experimental data measured at 600 MHz in $CDCl_3$; [b] experimental data measured at 500 MHz in $CDCl_3$.

The ^{1}H NMR spectrum of derivative **(76)** shows a triplet of triplet signal resonated at δ_H 7.34 (*J* = 1.2 and 7.4 Hz) with integration for one proton attributed to H-4". The equivalent aromatic protons H-3"/H-5" (δ_H 7.41, *J* = 7.4 Hz) appeared as a triplet signal due to ortho coupling with H-4" and H-2"/H-6". A doublet of doublet peak at δ_H 7.48 (*J* = 1.2 and 7.4 Hz) was assigned to another equivalent aromatic protons H-2"/H-6" due to ortho and meta coupling interactions with H-3"/H-5" and H-4", respectively (**Appendix E3**). The structure of derivative **(76)** was further confirmed with analysis of DEPTQ spectrum (**Appendix E4**), which showed presence of four methyl, three methylene, eight methine and five quaternary carbon peaks. The methine peaks at δ_C 127.17 and 128.44 were assigned to two sets of equivalent carbon, C-3"/C-5" and C-2"/C-6", respectively. The IR spectrum (**Appendix E1**) showed the presence of a strong absorption band at 1258.58 cm^{-1}, corresponded to the C-O functional group. Additionally, the MS spectrum revealed the presence of molecular ion peak at *m/z* 308 in agreement with the molecular formula of derivative **(76)** ($C_{22}H_{28}O$) (**Appendix E5**). The analysis of spectral data concluded the successful synthesis of derivative **(76)**, namely benzyl xanthorrhizyl ether.

The chemical shifts of the aromatic protons for derivatives **(102-104)** shifted to more deshielded region upon replacement of different type of aromatic rings compared to derivative **(76)**. The presence of singlet signal (δ_H 5.22) attributed to methyleneoxy protons, H-1' signified successful conversion of XNT **(1)** to its xanthorrhizyl ether derivative. Another four signals (δ_H 7.20-8.58) integrated for one proton each, indicate the presence of four sets of unequivalent aromatic protons of the pyridine ring (H-3"-H-6") as depicted in the ^{1}H NMR spectrum (**Appendix F3**). The multiplet (δ_H 7.20-7.26) and doublet (δ_H 7.57, *J* = 7.8 Hz) signals were assigned to H-5" and H-3", respectively. Meanwhile, a doublet of doublet of doublet signal (δ_H 7.72, *J* = 7.8, 7.6, 1.6 Hz) was assigned to H-4" due to ortho coupling with H-3" and H-5" as well as meta coupling with H-6". The signal for H-6" appeared at to be more deshielded (δ_H 8.58, *J* = 4.8, 1.6 Hz) due its position that is bonded to the nitrogen atom of pyridine. The DEPTQ data of derivative **(102)** also correlates with the total number of twenty-one carbons for derivative **(102)**, corresponding to five methyl, three methylene, five methine, and eight quaternary carbons. The signals at δ_C 157.94 and 149.03, were assigned to aromatic carbons, C-2" and C-6" respectively (**Appendix F4**). The analysis of all spectral data concluded that derivative **(102)**, namely (2-pyridinyl)methyl xanthorrhizyl ether was successfully synthesised.

The substitution of nitro group at C-4" position in derivative **(103)** deshield the chemical shifts of equivalent aromatic protons of H-3"/H-5" to δ_H 8.26 compared to derivative **(76)** (δ_H 7.40). Two sets of doublet signal (δ_H 8.26 and 7.63) with coupling constant of 8.9 Hz each were corresponded to ortho coupling between H-3"/H-5" and H-2"/H-6", respectively (**Appendix G3**). A total of twenty peaks composed of six methyl, three methylene, five methine and five quaternary carbons were depicted in DEPTQ sprectrum (**Appendix G4**). Although derivative **(103)** consisted of a total of twenty-two carbons, the signals at δ_C 123.79 and 130.78 were attributed to equivalent carbons C-2"/C-6" and C-3"/C-5", respectively. A quaternary carbon peak at δ_C 147.47 was assigned to C-4", attached to nitro group. The spectral data obtained thus affirmed the successful synthesis of derivative **(103)**, namely 4-nitrobenzyl xanthorrhizyl ether.

Meanwhile, the ^{1}H NMR spectra for derivative **(104)**, namely 3-trifluoromethylbenzyl xanthorrhizyl ether indicated the successful substitution of (3-trifluoromethyl) methylbenzene in XNT **(1)**. The presence of four signals (δ_H 7.52-7.73)

attributed to four aromatic protons H-2", H-4", H-5" and H-6", and a singlet signal (δ_H 5.13, 2H) assigned for methyleneoxy proton H-1' (**Appendix H3**). Two sets of doublet peaks (δ_H 7.59 and 7.65) and a triplet peak at δ_H 7.52 were contributed by ortho coupling between H-4", H-5" and H-6". A singlet peak at δ_H 7.73 was ascribed to H-2". The DEPTQ spectrum (**Appendix H4**) also showed the presence of peak for trifluoromethyl carbon at δ_C 123.21 ppm.

The conversion of hydroxyl group to methyleneoxy group as indicator of successful synthesis reaction were affirmed through IR analysis. The IR spectra of all derivatives (**Appendix F1-H1**) revealed the absence of hydroxyl band at 3358.31 cm^{-1} and presence of C-O absorption band at range of 1262.11 to 1252.58 cm^{-1}, compared to XNT **(1)** (**Appendix D1**). Moreover, strong stretching frequencies also appeared corresponding to each substituent, for example, absorption bands at 1591.20 cm^{-1} and 1133.65 cm^{-1} corresponding to C=N and C-N, respectively showed the presence of pyridine ring for derivative **(102)** (**Appendix F1**). The IR spectrum for derivative **(103)** (**Appendix G1**) demonstrated the appearance of nitro stretching band at wavelength 1520.67 cm^{-1} and 1344.57 cm^{-1}, indicating the presence of nitro (N=O) group in derivative **(103)**. Meanwhile, the appearance of strong band at 1329.15 cm^{-1} (C-F) revealed the presence of trifluoromethyl group for derivative **(104)** (**Appendix H1**).

The synthesis of derivative **(105)** utilised NaOH as base for the reaction. The yield for this reaction is very low, as it only afforded 6.29% of the final product. The lower yield of derivative **(105)** compared to derivatives **(76**, **102-105)** can be attributed to the less reactive aliphatic nature of the alkyl halide. On the other hand, benzyl carbon in the transition state of S_N2 reaction of derivative **(76**, **102-105)** were stabilised by resonance due to presence of the aromatic ring.

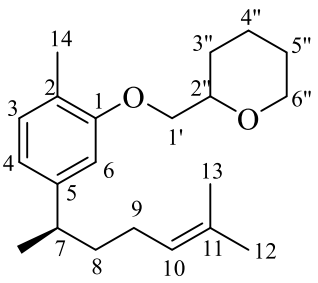

(105)

The characterisation of derivative **(105)** using ^{1}H NMR (**Appendix I3**) revealed the appearance of two sets of doublet of doublet of doublet signals (J = 9.5, 5.4, 2.2 Hz) at δ_H 3.83 and 4.02, which were ascribed for non-equivalent methylene protons of H-1'a and H-1'b. The multiplet signals at the downfield region δ_H 1.55-1.66 were ascribed to the methylene protons of H-4" and H-5" of the ring. Meanwhile, the signals for H-3"a and H-3"b arised as multiplets at δ_H 1.44-1.49 and 1.78-1.80. The signals at δ_H 3.72 (dtd, J = 10.9, 5.4, 2.2 Hz) was ascribed to H-2" as a result of coupling with H-1'a (J = 5.4 Hz), H-3"a and H-6"a (J = 10.9 and 2.2 Hz). A signal at δ_H 4.04 (dddd, J = 11.4, 4.4, 2.2, 1.8 Hz) was ascribed to H-6"a. H-6"a coupled with its geminal proton H-6"b (J = 11.4 Hz), H-5"a and H-5"b (J = 4.4 and 2.2 Hz) and H-4"a (J = 1.8 Hz). Meanwhile, the peak for H-6"b arised at δ_H 3.52 as triplet of doublet (J =11.4 and 2.2 Hz) due to coupling with H-6"a and H-5"a with same coupling constant, 11.4 Hz and H-5"b (J = 2.2 Hz).

The DEPTQ spectrum (**Appendix I4**) further confirmed the structure of derivative **(105)**, as twenty-one peaks composed of four methyl, seven methylene, six methine and four quaternary carbons of derivative **(105)** were observed. The carbon peaks for XNT scaffold were detected, while additional methylene peaks observed at δ_C 23.12, 26.09 and 28.79 were assigned to C-4", C-5", and C-3", respectively. Meanwhile, two more deshielded methylene peaks at δ_C 71.58 and 68.59 were ascribed to C-1' and C-6", respectively. The peak at δ_C 76.19 identified as methine carbon was assigned to C-2".

The synthesis of (2-tetrahydro-2*H*-furanyl)methyl xanthorrhizyl ether **(106)** were attempted using K_2CO_3 and NaOH as the bases. However, no product was formed upon reaction monitoring with TLC. Then, the synthesis was carried out using Cs_2CO_3 as the base in acetonitrile. The formation of product was finally observed at R_f 0.7 (*n*-hex:Et_2O, 4:1). The reaction mixture was purified, and derivative **(117)** was obtained as colourless oil.

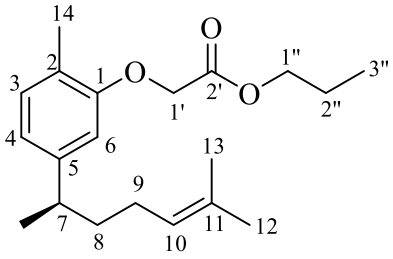

(117)

The characterisation of derivative **(117)** using ^{1}H NMR (**Appendix J2**) revealed that all characteristics signals for the XNT **(1)** structure were present. Interestingly, the characteristics signals for tetrahydrofuran ring were not observed. Instead, *n*-propyloxy moiety was detected represented by a triplet signal (δ_H 0.92, J = 7.4 Hz) for terminal methyl protons, H-3", a sextet signal (δ_H 1.65, J = 7.4 Hz) for internal methylene protons, H-2", and a triplet signal (δ_H 4.14, J = 6.7 Hz) for methyleneoxy protons, H-1". The assignation was further confirmed through COSY analysis (**Appendix J5**), which clearly depicted cross peaks for ^{1}H-^{1}H coupling between H-1", H-2" and H-3" (**Figure 5.3**). A singlet signal resonated at δ_H 4.63 integrated for two protons was assigned to methyleneoxy protons, H-1'. The ^{13}C NMR analysis (**Appendix J3**) revealed a total of twenty signals, corresponding to five methyl, five methylene, five methine, and five quaternary carbons of derivative **(106)**. Direct correlation between ^{1}H-^{13}C analysed through HMQC analysis (**Appendix J6**) allowed the assignation of signals δ_C 10.38, 22.03, 65.88 and 66.83 for H-3", H-2", H-1' and H-1", respectively.

A deshielded quaternary carbon peak observed at δ_C 169.5 suggested the presence of carbonyl ester for the product. Analysis of the IR spectrum (**Appendix J1**) indicated the presence of a strong absorption band at 1740.14 cm^{-1} which further confirmed the assignation of ester group in the structure. The HMBC analysis (**Appendix J7**) displayed a ^{1}H-^{13}C long-range correlation between H-1' and C-1 indicating successful conversion of XNT **(1)** to become ether derivative. Other two correlations observed for methyleneoxy protons H-1" and H-1' both to carbonyl of C-2' further proved the structure of derivative **(117)** (**Figure 5.3**).

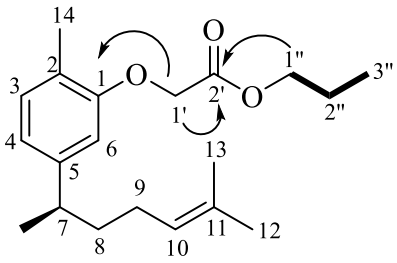

Figure 5.3: Key HMBC (arrows) and COSY (bold) correlations of derivative **(117)**

A molecular ion peak at *m/z* 318 was detected in the MS spectrum (**Appendix J4**) represents the mass of derivative **(117)**. The mass was higher than the expected molecular weight of derivative **(106)** by 16 amu, suggesting an oxygenation occurred in the reaction to form ester moiety in derivative **(117)**. The MS spectrum (**Appendix J4**) also reveals the presence of base peak at *m/z* 236 and fragment peak at *m/z* 193 as illustrated in **Scheme 5.5**. The loss of 2-methyl-pent-2-ene radical from XNT backbone to form benzylic cation (*m/z* 235) followed by hydrogen transfer caused by the self-CI of the fragment with other ions in the ion trap yielded the base peak at *m/z* 236.

The minor fragment at *m/z* 193 formed due to McLafferty rearrangement that is commonly observed in ester compounds consisted of linear alkyl chain with at least one γ-hydrogen. During the rearrangement process, the electron lone pair from the carbonyl group abstracted γ-hydrogen to form six-membered transition state. This process is followed by concurrent cleavage of the sigma bond between α- and β-position (Pavia et al., 2015), resulting in the loss of propene molecule. From thorough analysis of the spectral data obtained, it was concluded that the reaction unsuccessfully yielded the targeted derivative **(106)**, instead it yielded another derivative elucidated as propyl xanthorrhizyloxyacetate **(117)**.

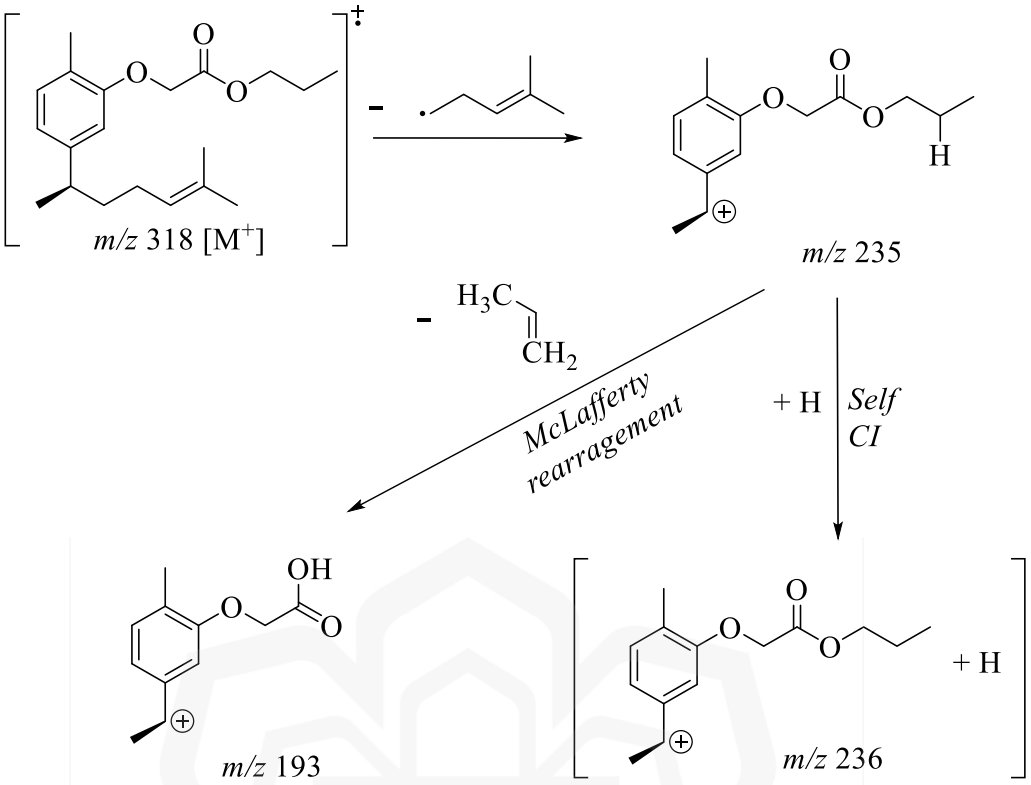

Scheme 5.5: Fragmentation pattern of derivative **(117)**

The proposed reaction mechanism to yield derivative **(117)** was illustrated in **Scheme 5.6**. Firstly, the carbonate ion from Cs_2CO_3 extracted phenolic hydrogen from XNT **(1)** to form phenoxide ion **(127)** and bicarbonate ion. The phenoxide ion **(131)** then attacked electrophilic carbon of tetrahydrofurfuryl chloride **(116)** through S_N2 reaction to form derivative **(106)**, while cesium chloride was removed as leaving group. However, the unexpected ester product synthesised indicated that derivative **(106)** underwent further reaction leading to formation of derivative **(117)**.

It is postulated that bicarbonate ion acted as nucleophile and attacked the methineoxy carbon, causing the tetrahydrofuran ring-opening to form intermediate **(132)**. Then, the reactive carbanion extracted a hydrogen from the hydrogen carbonate attached to intermediate **(132)** causing the loss of carbon dioxide **(133)** and cesium hydride **a**s leaving group. This concerted process leads to the formation of ester group of derivative **(117)**. Nevertheless, more studies are required to confirm the proposed reaction mechanism for the unexpected product. Mechanistic studies using density-

functional theory (DFT) calculations can help to validate the proposed reaction mechanism by calculating the activation energies of the reactants and transition state in chemical reactions (Momiyama et al., 2021).

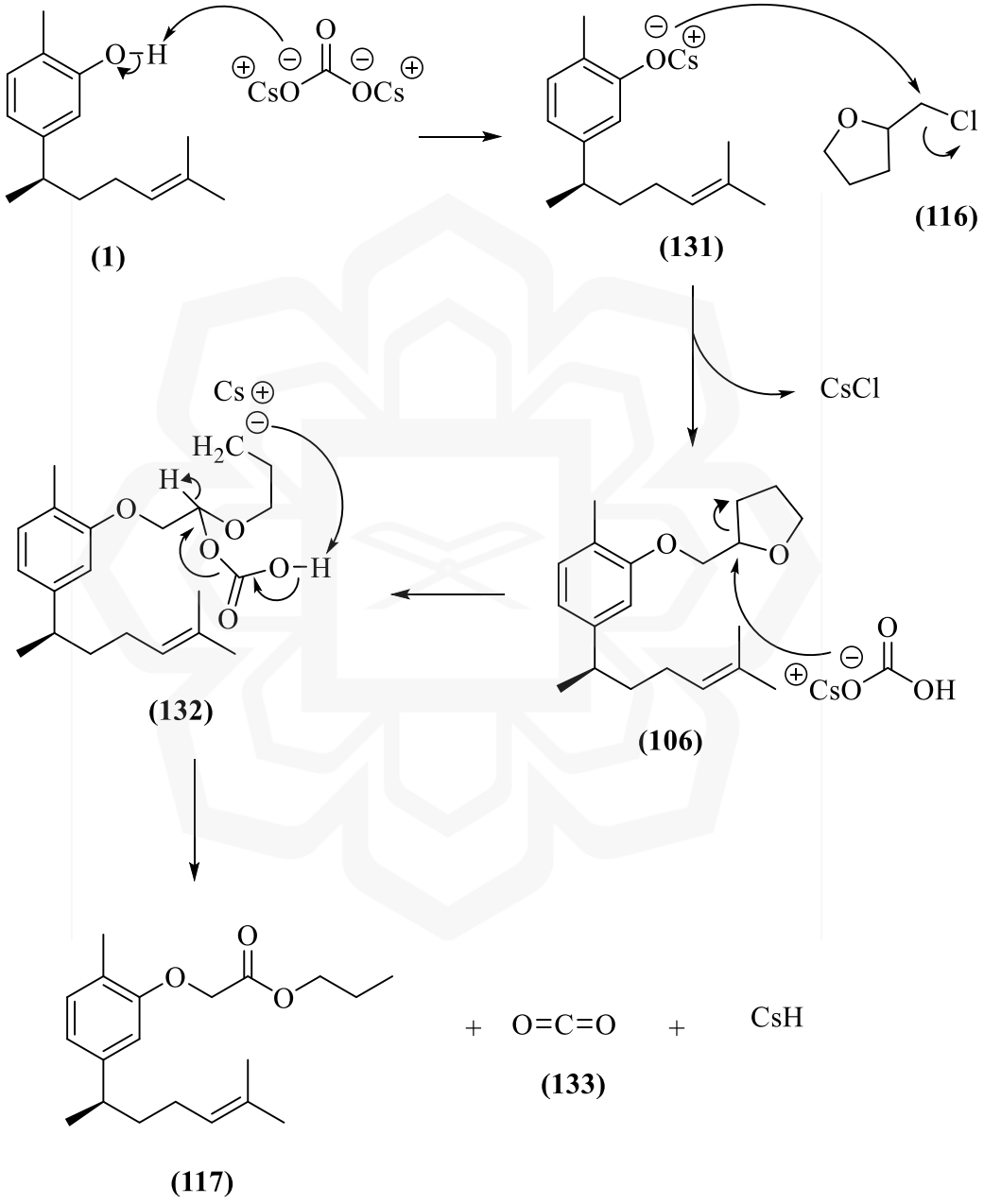

Scheme 5.6: Proposed reaction mechanism for formation of derivative **(117)**

5.4 ATTEMPTED SYNTHESIS OF XANTHORRHIZOL DERIVATIVES (107-110) AS LOX-3 INHIBITORS

Five derivatives were proposed as LOX-3 inhibitors, namely benzyl xanthorrhizyl ether **(76)**, 2-(xanthorrhizyloxy)ethyl carbamide **(107)**, *N*-(2-(xanthorrhizyloxy)ethyl)-1*H*-imidazole-4-carboxamide **(108)**, *N*-(2-(xanthorrhizyloxy)ethyl)-3-aminopropanamide **(109)** and 3-(xanthorrhizyloxy)propyl 1*H*-imidazole-4-carboxylate **(110)**. Derivative **(76)** was obtained from virtual screening approach and its synthesis was described in **Section 5.3**. Meanwhile, derivatives **(107-110)** were generated from *in silico* FBDD approach.

The synthesis of 2-(xanthorrhizyloxy)ethyl carbamide **(107)** was attempted using Williamson ether synthesis method as illustrated in **Scheme 5.7**. The reaction was carried out by reacting XNT **(1)** with *N*-(2-chloroethyl)urea **(118)** using K_2CO_3 in dry acetone. The reaction was carried out for 24 hours and monitored by using TLC with different solvent systems including *n*:hex:Et_2O (4:1), *n*:hex:EtOAc (4:1), $CHCl_3$:MeOH (4.5:0.5). However, no new spot was observed on the TLC plate, indicating unsuccessful reaction.

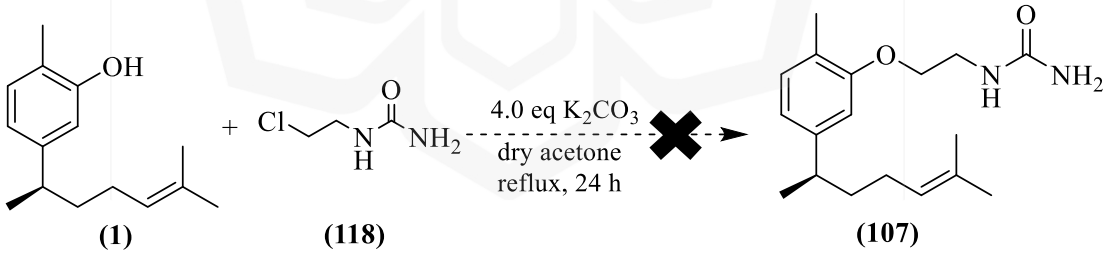

(1) **(118)** **(107)**

Scheme 5.7: Attempted synthesis of derivative **(107)**

The synthesis of *N*-(2-chloroethyl)-1*H*-imidazole-4-carboxamide **(121)** was carried out to be the starting material for synthesis of *N*-(2-(xanthorrhizyloxy)ethyl)-1*H*-imidazole-4-carboxamide **(108)**. The synthesis was conducted *via* Steglich esterification, involving the reaction between 4-imidazolecarboxylic acid **(119)** and ethylamine hydrochloride **(120)** with DCC as the coupling agent. DMAP was added in

catalytic amount for the formation of acylated pyridinium intermediate from *O*-acylisourea to prevent its the rearrangement to inactive *N*-acylurea (Jordan et al., 2021; Tsakos et al., 2015). The reaction was carried out in DMF for 18 hours.

The reaction mechanism for the formation of compound **(121)** was proposed based on the mechanism of Steglich esterification as depicted in **Scheme 5.8**. In this reaction, DCC abstracted the acidic hydrogen from 4-imidazole carboxylic acid **(118)** to form 4-imidazole carboxylate ion **(134)**. The nucleophilic carboxylate ion **(134)** then attacked the imine carbon of protonated DCC to form *O*-acylisourea intermediate **(135)**. Then, DMAP also served as a nucleophile attacked the carbonyl carbon of intermediate **(135)** resulting in the formation of intermediate **(136)**. Electron delocalisation of intermediate **(136)** afforded resonance-stabilised acyl pyridinium intermediate **(138)** and intermediate **(137)** as the leaving group. Then, ethylamine **(120)** attacked the carbonyl carbon of intermediate **(138)** to afford intermediate **(139)**. Intermediate **(139)** then underwent electron delocalisation and a proton transfer to intermediate **(137)** finally afforded compound **(121)**, DMAP and dicyclohexyl urea **(140)** as by-product.

The product was characterised by using ^{1}H NMR analysis (**Appendix K1**). The doublet of doublet of doublet signal appeared at δ_H 2.31 (J = 16.0, 12.5 and 3.5 Hz) was attributed to H-2". Meanwhile, the signal for proton H-1"b appeared as doublet of doublet of doublet of doublet peak (δ_H 4.14, J = 16.0, 12.5, 4.5, 3.8 Hz) due to coupling with H-2", H-1"a and NH. The multiplet peak at δ_H 3.72 was attributed to the geminal proton H-1"a. Aromatic protons of imidazole ring, H-5 and H-2 appeared at δ_H 7.40 and 7.95, respectively. The characteristic peaks observed in the ^{1}H NMR spectrum indicated successful synthesis of compound **(121)**. However, the multiplet peaks for dicyclohexyl protons from by-product DCU **(140)** were observed in the NMR spectrum at range δ_H 1 to 2 ppm (Ken et al., 2019) (**Appendix K2**). DCU **(140)** is insoluble in water and only partially soluble in many organic solvents, hence it is typically removed by filtration (Jordan et al., 2021). However, the trace amounts of DCU **(140)** were still difficult to remove, even *via* column chromatography (Tain et al., 2020) or recrystallisation (Tian et al., 2007). Therefore, other coupling agents such as 1-ethyl-3-(3-dimethylaminopropyl)carbodiimide (EDC) can be used as alternative for better efficiency in the synthesis process. Due to the low yield of compound **(121)** (8.39%), the next step to synthesis derivative **(108)** was not proceeded.

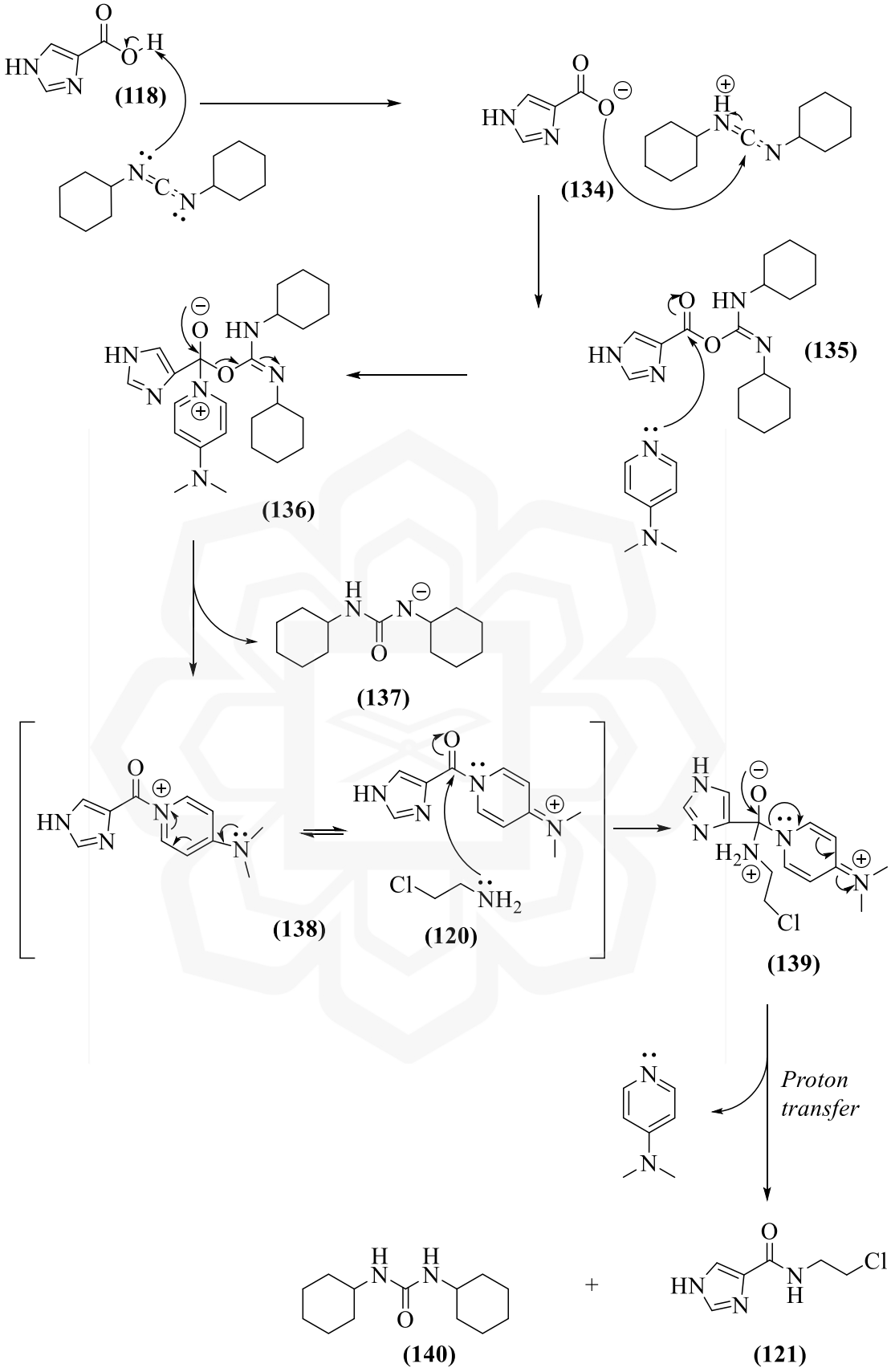

Scheme 5.8: Reaction mechanism for synthesis of compound **(121)**

The synthesis of *N*-(2-(xanthorrhizyloxy)ethyl)-3-aminopropanamide **(109)** required prior preparation of two compounds, namely *tert*-butyl-(3-((2-chloroethyl)amino)-3-oxopropyl)carbamate **(123)** and *tert*-butyl-(3-oxo-3-((2-xanthorrhizyloxyethyl)amino)propyl)carbamate **(124).** The synthesis of compound **(123)** was performed using Steglich esterification method using Boc-*β*-alanine **(122)** and ethylamine hydrochloride **(120)** with DCC, excess DIPEA and catalytic amount of DMAP **(Scheme 3.4)**. The reaction was conducted for 18 hours at room temperature in DCM. The crude product was purified to afford **(123)** as white crystal.

The IR spectrum **(Appendix L1)** of compound **(123)** showed the presence of two absorption peaks at 3325.58 and 3239.31 cm^{-1}, indicating the presence of two N-H functional groups from carbamate and amide moieties. The ^{1}H NMR analysis (**Appendix L3**) showed the appearance of a singlet peak at δ_H 1.44 (9H), assigned for *tert*-butyl protons of H-3, H-4 and H-5. Meanwhile, the appearance of a triplet signal (δ_H 2.62, J = 5.7 Hz) and a quartet signal (δ_H 3.41, J = 5.7 Hz) corresponded to protons H-2' and H-1', respectively. Two signals at δ_H 3.67 and 3.88 were ascribed for non-equivalent geminal protons H-1"a and H-1"b. The peaks for both N-H protons were also observed as broad singlet at δ_H 5.20 and 7.08.

The signal for H-2" appeared at δ_H 1.97 overlapped with the multiplet signals of dicyclohexyl protons from DCU **(140)** at δ_H 1 to 2 ppm (Ken et al., 2019) (**Appendix L2**). The analysis of ^{13}C NMR spectrum (**Appendix L4**) revealed the peak for carbonyl amide (C-3') and carbonyl ester (C-1) at δ_C 170.41 and 156.88, respectively. The peak for C-1 appeared to be more shielded as both oxygen and nitrogen are electron donating atoms, hence increased the electron density surrounding the carbonyl carbon. This increased the carbon's shielding effect and resulting it to be resonated at lower frequency. The peak at δ_C 25.69 was assigned to equivalent methyl carbons C-3, C-4 and C-5 from the *tert*-butyl moiety. Meanwhile, the signals at δ_C 33.21, 34.04, 48.35, and 49.19 were assigned to methylene carbons C-2', C-1', C-2" and C-1', respectively.

Compound **(123)** was reacted with XNT **(1)** with K_2CO_3 in dry acetone. Upon TLC monitoring, a new spot was observed with R_f value of 0.31 (*n*-hex:EtOAc, 4:1) upon staining with vanillin-suphuric acid reagent. Therefore, the purification using CC was performed to afford the product as colourless crystal. The ^{1}H NMR spectrum

(**Appendix M**) of the crystals showed the characteristics signals of XNT **(1)** protons (H-1 – H-15). However, there is no signal in the range of δ_H 3.2 to 3.8 that can be attributed to methyleneoxy protons H-2", which signifies the unsuccessful synthesis of derivative **(124)**. Moreover, the characteristics signals for protons from derivative **(123)** (H-1', H-2' and H-1", H-2"). The attempted reaction for the synthesis of compound **(124)** was illustrated in **Scheme 5.9**. Since the NMR analysis showed that the reaction failed to furnish compound **(124)**, the following reaction to afford final derivative **(109)** was not performed.

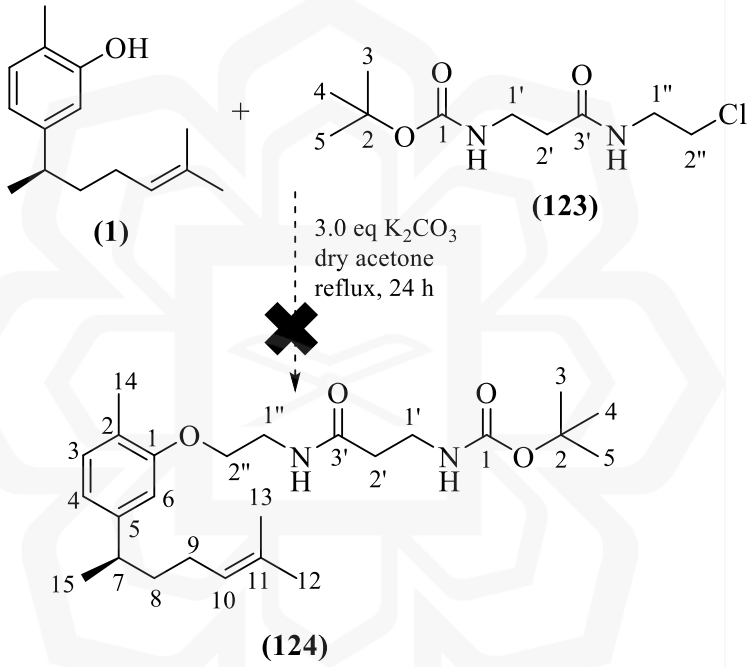

Scheme 5.9: Attempted synthesis of compound **(124)**

The synthesis of alkylating agent 3-chloropropyl-1*H*-imidazole-4-carboxylate **(126)** as the starting material for the synthesis of 3-(xanthorrhizyloxy)propyl 1*H*-imidazole-4-carboxamide **(110)**, was attempted. The attempt was carried out through the reaction of 4-imidazolecarboxylic acid **(119)** with 1-bromo-3-chloropropane **(125)** using Cs_2CO_3. Upon monitoring with TLC, a new spot was observed at R_f 0.76 with *n*-hex:EtOAc (1:4) as the solvent system. The crude product was purified using CC to afford colourless liquid. However, the ^{1}H NMR spectrum (**Appendix N**) showed no evidence for the formation of derivative **(126)**. The inconsistency of integration ratio

for signals assigned for imidazole protons (δ_H 7.62 to 7.68) and chloropropyl protons (δ_H 2.13 to 4.43) indicated that the product obtained may be present as the mixture of compound **(119)** and **(125)**, respectively. The attempt to synthesise compound **(126)** was depicted in **Scheme 5.10**.

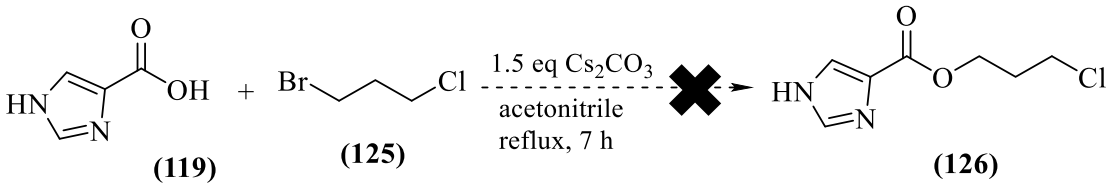

Scheme 5.10: Attempted synthesis of compound **(126)**

5.5 BIOLOGICAL ACTIVITIES OF XANTHORRHIZOL DERIVATIVES

The inhibitory activities of XNT **(1)** and derivatives **(76, 102-105**, **117)** were determined through *in vitro* Hyal-1 inhibitory enzymatic assay. Meanwhile, derivative **(76)** was subjected to *in vitro* LOX-3 enzyme assay to determine its inhibitory activity against LOX-3 enzyme.

5.5.1 *In Vitro* Inhibitory Activity Against Hyal-1 Enzyme

The inhibition of test compounds against the Hyal-1 enzyme were determined *via* turbidimetric method. **Figure 5.4** illustrates the reaction mechanism of Hyal-1 inhibitory action. HA is the substrate for Hyal-1 enzyme and will be digested in the reaction solution. The test compounds that can act as inhibitors will compete with HA and react with Hyal-1 enzyme to form Hyal-inhibitor complex. Upon addition of acidified serum albumin, the presence of undigested HA due to competitive inhibition resulted in the formation of turbid solution (Bailey & Levine, 1993). The absorbance of the turbid solution, which was measured at wavelength of 600 nm is directly proportional to the amount of undigested HA. Therefore, the higher the absorbance, the better the inhibitory activity of the test compounds against Hyal-1 enzyme.

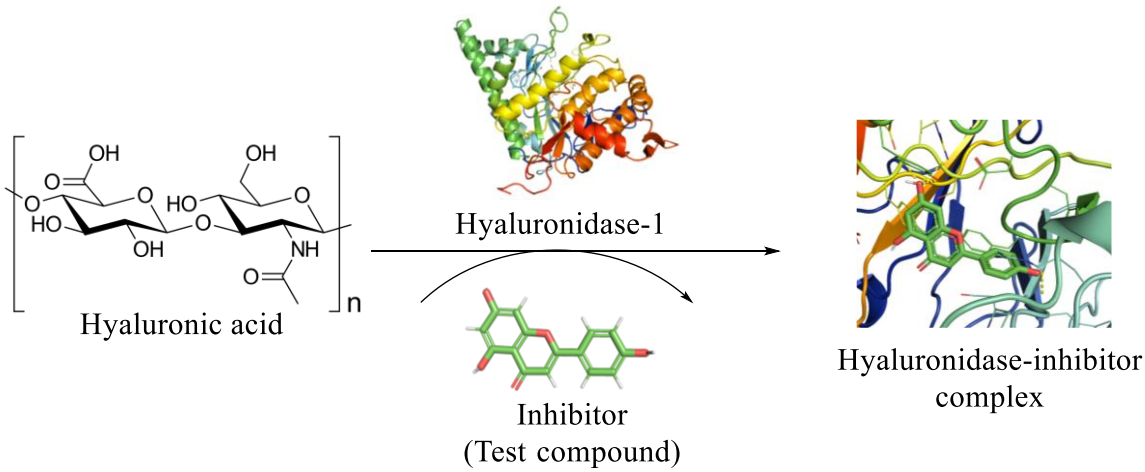

Figure 5.4: Competitive inhibition of Hyal-1 activity between HA and inhibitor

The percentage inhibition (I%) and IC_{50} values were tabulated in **Table 5.4**. The test compounds were tested at five different concentrations (400, 200, 100, 50, 25 µg/mL) and apigenin **(17)** was used as reference compound for the enzyme inhibitory activities. The test compounds that displayed percentage inhibition of 100% to 70% is classified as strong inhibitor, 69% to 40% as moderate inhibitor and 39% to 0% as weak inhibitor (Pisar & Mohd Hashim, 2023). The derivatives with *P* value less than 0.05 were considered statistically significant different compared to XNT **(1)** and apigenin **(17)**.

Derivatives **(76**, **102-104)** exhibited higher percentage inhibition, ranging from 46.59% to 95.37% compared to XNT **(1)** (12.43%) at 100 µg/mL indicating their improved activities from low to moderate inhibition. Derivative **(102)** displayed the strongest inhibitory activity with percentage inhibition 95.37% at 100 µg/mL, comparable to apigenin **(17)** (100%) at 250 µM (67.5 µg/mL). The most active derivative **(102)** displayed IC_{50} value of 44.45 µg/mL, which showed significant improved activity by 4.58-fold compared to XNT **(1)** (IC_{50} = 203.56 µg/mL). Derivatives **(76**, **103** and **104)** also exhibited enhanced inhibition compared to XNT **(1)** with IC_{50} value of 93.71, 66.20 and 57.56 µg/mL, respectively. However, these derivatives were still less potent compared to the positive control, apigenin **(17)** (IC_{50} = 27.07 µg/mL). Meanwhile, derivatives **(105)** and **(117)** possessed weak activity with percentage inhibition of 16.60% and 9.95%, respectively.

Table 5.4: Hyal-1 inhibitory activities

Compounds	Percentage inhibition (% ± S.E.M)		IC_{50} values
	100 µg/mL[a]	250 µM[b]	**(µg/mL ± S.E.M)**
(1)	12.43 ± 1.17	-	203.56 ± 9.67[d]
(76)	46.69 ± 3.07[c]	-	93.71 ± 5.79[cd]
(102)	95.37 ± 3.36[c]	-	44.45 ± 1.80[cd]
(103)	57.70 ± 6.90[c]	-	66.20 ± 6.83[cd]
(104)	65.20 ± 7.96[c]	-	57.56 ± 6.91[cd]
(105)	16.60 ± 1.05	-	>500[d]
(117)	9.95 ± 1.56	-	>500
Apigenin (17)	-	100	27.07 ± 0.88

Notes. The test compounds were prepared in the unit of µg/mL, the positive control was prepared in the unit of uM; [a]Data were expressed as mean ± S.E.M of three independent experiments performed in triplicate; [b]Data were expressed as mean ± S.E.M of six independent experiments performed in triplicate; Data was statistically significant different ($P < 0.05$) with [c]XNT **(1)** and [d]apigenin **(17)**.

The improved inhibitory activities of derivatives **(76, 102-104)** compared to XNT **(1)** were attributed to the modifications of hydroxyl group of R_1 in XNT **(1)** to different aromatic ring systems. The molecular docking results of the derivatives (**Section 4.2.1** and **4.3.1**) revealed that the aromatic rings substituents at R_1 position interacted with Asp129 and Glu131 residues. These amino acid residues contributed to the Hyal-1 inhibitory activity, thus, facilitated in blocking Hyal-1 enzyme from HA digestion. However, the binding energies displayed in molecular docking studies (**Section 4.2.1** and **4.3.1**) did not correlate with the IC_{50} values from the *in vitro* assay. For instance, derivatives **(104)** (-8.9 kcal/mol) and **(103)** (-8.2 kca1/mol) were expected to exhibit stronger inhibitory activities against Hyal-1 enzyme compared to derivative **(102)** (-7.9 kcal/mol) and apigenin **(17)** (-7.9 kcal/mol).

Instead, contradictory results were observed, whereby derivatives **(103** and **104)** exhibited lower percentage inhibition than derivative **(102)** and apigenin **(17)**. Derivative **(102)** exhibited higher binding energy of -7.9 kcal/mol against Hyal-1 enzyme in the molecular docking studies (**Section 4.3.1**) and exhibited the lowest IC_{50} value in *in vitro* assay (44.45 µg/mL). Although the binding energy value of derivative

(102) against Hyal enzyme is similar to the positive control apigenin **(17)**, it exhibited stronger inhibition in *in vitro* assay with IC_{50} value of 27.07 μg/mL. The lack of correlation between molecular docking and IC_{50} value prompted further analysis on the molecular interactions between derivative **(102)** and Hyal-1 enzyme.

The binding energy expressed in molecular docking was theoretically based on the scoring function that measured the strength of the binding pose between ligand and protein (Ramírez & Caballero, 2016). Moreover, molecular docking studies using AutoDock Vina only allowed for flexibility in the ligand conformation, while the receptor was kept rigid throughout the docking process (Che et al., 2023). In reality, the enzyme can undergo conformational changes upon ligand binding (Riziotis et al., 2022), and these factors suggested that molecular docking results alone are not sufficient to predict the experimental results of *in vitro* enzyme activity. Therefore, MD simulation study helped to address the limitations of docking by analysing the time-dependent behaviour of a protein-ligand complex. MD simulation analysis also considered the physical parameters such as temperature, solvent, and ions, which were not included in the docking studies (Tiwari & Singh, 2022).

5.5.2 *In Vitro* Inhibitory Activity Against LOX-3 Enzyme

5-LOX is one of the enzymes in eicosanoids synthesis pathway, which convert arachidonic acid to leukotrienes. Elevated levels of 5-LOX and leukotrienes are associated with asthma, rheumatoid arthritis, and tumour growth (Tian et al., 2020). Soybean LOX-3 was often used as the model for human 5-LOX, as both isoforms possessed structural similarity and mechanism of action (Muñoz-Ramírez et al., 2020).

In this assay, the LOX-3 inhibitory activities of the test compounds were measured using spectrophotometer method (Azhar-Ul-Haq et al., 2004). The assay reaction was initiated by linoleic acid substrate. In normal condition, LOX-3 enzyme will catalyse the oxidation of linoleic acid by molecular oxygen which resulted in the formation of conjugated diene product, 13*S*-HPODE (**Figure 5.5**). The absorbance of 13*S*-HPODE was measured at wavelength 234 nm. The presence of the test compound as competitive inhibitor for linoleic acid substrate can block the formation of 13*S*-

HPODE. Hence, the lower absorbance of the reaction mixture indicates better inhibitory activity against LOX-3 enzyme for the test compounds.

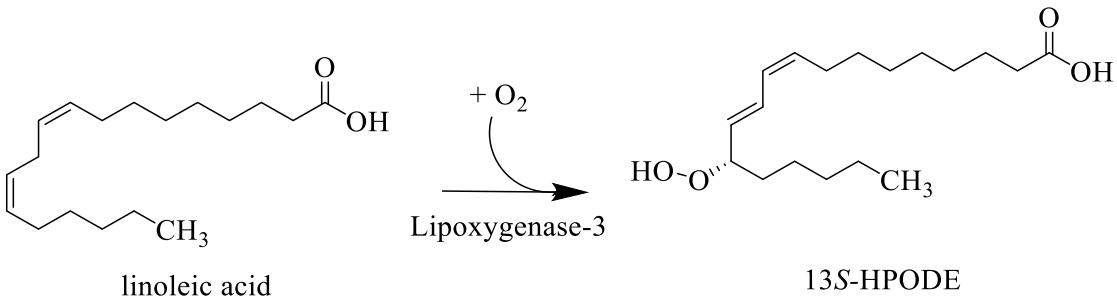

linoleic acid

13*S*-HPODE

Figure 5.5: Formation of 13*S*-HPODE from linoleic acid by LOX-3 enzyme

In this study, only XNT **(1)** and derivative **(76)** were subjected to *in vitro* LOX enzyme assay, since the synthesis of derivatives **(107-110)** were unsuccessful. A known potent inhibitor of LOX-3 enzyme called NDGA **(43)** was used as the positive control. The test compounds were tested at seven concentrations (400, 200, 100, 50, 25, 12.5 6.25 µg/mL) and the results were presented in **Table 5.5**. The test compounds with percentage inhibition of 100% to 70% indicated strong inhibitor, while percentage inhibition of 69% to 40% is classified as moderate inhibitor. Test compounds that exhibited percentage inhibition 39% to 0% is catagorised as weak inhibitor (Pisar & Mohd Hashim, 2023). Test compounds with *P* value less than 0.05 were considered as statistically significant different compared to XNT **(1)** and NDGA **(48)**. The statistical analysis using independent t-test showed that there were no significant difference in the percentage inhibition and IC_{50} value of derivative **(76)** compared to XNT **(1)**.

XNT **(1)** exhibited moderate activity (46.69%) at concentration 100 µg/mL with IC_{50} value of 142.34 µg/mL. Meanwhile, derivative **(76)** exhibited lower activity (12.43% at 100 µg/mL) compared to XNT **(1)** with IC_{50} value of 619.25 µg/mL. The decrement of the IC_{50} value by 4.35-fold compared to XNT **(1)** suggested that the modification of hydroxyl group to aromatic ring substituent did not improve the activity against the LOX-3 enzyme. This finding was not in agreement with molecular docking

studies in which derivative **(76)** exhibited stronger binding affinity (-8.6 kcal/mol) against LOX-3 enzyme compared to XNT **(1)** (-7.7 kcal/mol).

Table 5.5: LOX-3 inhibitory activities

Compounds	Percentage inhibition at 100 µg/mL (% ± S.E.M)	IC_{50} values (µg/mL ± S.E.M)
(1)	46.69 ± 3.07[b]	142.34 ± 10.19[b]
(76)	12.43 ± 1.17[b]	619.25 ± 91.18
NDGA (43)	99.42 ± 0.57	6.47 ± 0.47

Notes. All test compounds and positive control were prepared in the unit of µg/mL. Data were expressed as mean ± S.E.M of three independent experiments performed in triplicate; Data was statistically significant different ($P < 0.05$) with [a]XNT **(1)** and [b]NDGA **(48)**.

The contradictory results between binding energy from docking studies and experimental IC_{50} value of derivative **(76)** might be attributed to the hydrophobicity of its structure. The structure of derivative **(76)** which composed of two benzene rings, alkyl side chain, and only one oxygen atom from the ether functional group indicated that it lacks hydrogen bond donor or acceptor groups. The substitution of benzyloxy moiety at R_1 position in XNT **(1)** facilitated the establishment of hydrophobic interactions in the LOX-3 binding pocket with Trp519, Ile572 and Leu565 as discussed in **Section 4.2.2** (**Figure 4.11**). However, derivative **(76)** did not possess conventional hydrogen bond with the important amino acid residues in the hydrophilic regions **1** and **2** in the LOX-3 binding pocket compared to 13*S*-HPODE substrate (**Figure 5.6**).

Therefore, the weak inhibition of derivative **(76)** displayed in the *in vitro* assay despite strong binding energy in molecular docking was associated with the absence of hydrogen bonding interactions in hydrophilic regions **1** and **2**. This finding can also be justified through several reports that also highlights the importance of hydrogen bond interactions with amino acid residues Gln514, His518 (Lončarić et al., 2022), Ser510, Gln716 (Lavrentaki et al., 2023) and Arg726 (Ahmed et al., 2021) for LOX-3 inhibitory activities.

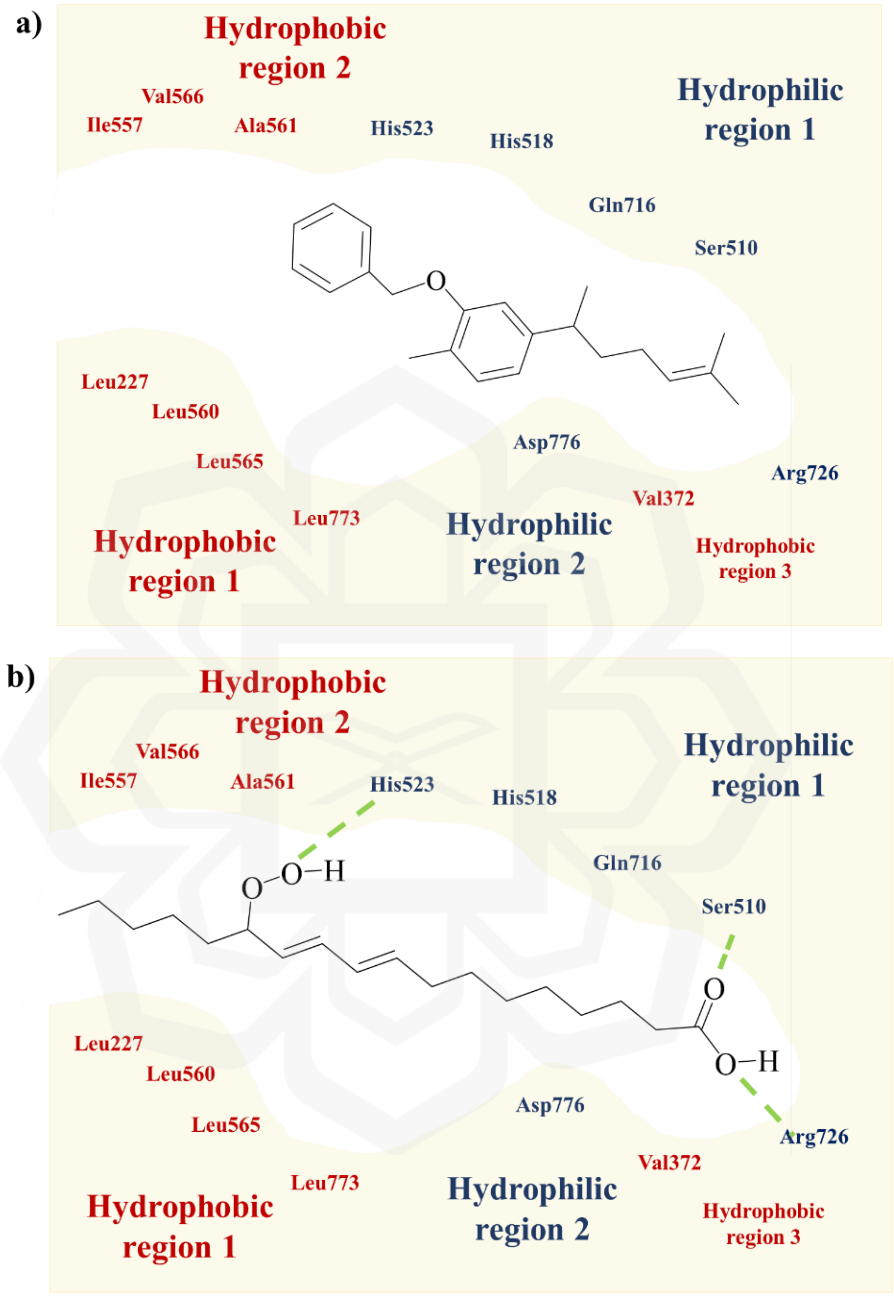

Figure 5.6: Schematic diagram of binding pose of a) derivative **(76)** and b) 13*S*-HPODE substrate in the LOX-3 enzyme binding pocket. The dashed line in green represents the hydrogen bonding interactions (Adapted from Ng et al. (2014)).

5.6 MOLECULAR DYNAMICS SIMULATION OF DERIVATIVE (102) AGAINST HYAL-1 ENZYME

In this study, MD simulation was performed to further elucidate the interaction between the protein-ligand complex of the most active compound in the *in vitro* assay, which was derivative **(102)** and positive control, apigenin **(17)** against Hyal-1 enzyme. The main difference between molecular docking and MD simulations is the time variable. The molecular docking study predicts the best binding conformation of ligand in the binding site and its affinity based on the calculation of binding energies. On the other hand, MD simulation monitors the conformational change of protein-ligand complex at different timescale. Therefore, MD simulations complement the data from molecular docking (Chen, 2015; Santos et al., 2019). In this study, the simulation time was set to 100 ns as previous MD simulation studies on Hyal-1 enzyme showed that 50 (Li et al., 2021) to 100 ns (Mancipe et al., 2023; Xu et al., 2024) is sufficient to observe the molecular changes that occurs upon ligand binding in the enzyme.

The overall stability of the protein-ligand complex can be observed through RMSD value. In general, higher RMSD value indicated the instability of the protein structure as the complex undergoes significant changes from its initial structure. Moreover, the deviation of ligand from the pocket due to inaccurate binding conformation or active site also contributed to the increase in the RMSD value. A value lower than 0.2 nm is a good criterion for the accurate ligand conformation in the binding site of the protein obtained from the molecular docking study (Liu et al., 2017).

The information on protein-ligand complex stability can be supplemented by radius of gyration (R_g), which defined as the distribution of atoms around the protein backbone and its axis (Sneha & George Priya Doss, 2016). The measure of R_g value accounts for global compactness of the protein. Hence, a stable complex should have low and steady R_g value throughout the simulation, indicating that no unfolding in the secondary or tertiary structure occurred upon ligand binding to the protein (Al-Karmalawy et al., 2021; Lemkul, 2019).

The mean RMSD value for the Hyal-1-derivative **(102)** complex was 0.17 ± 0.02 nm, comparable to Hyal-apigenin **(17)** complex (0.18 ± 0.03 nm). The Hyal-1-

derivative **(102)** complex achieved stable value after 25 ns (**Figure 5.7.a**). The RMSD of derivative **(102)** showed some fluctuations during the first 60 ns time (**Figure 5.7.b**), nevertheless achieved stability until the end of simulation with RMSD value of 0.18 ± 0.05 nm (**Table 5.6**). Meanwhile, RMSD of Hyal-1-apigenin **(17)** complex showed slight increment after 75 ns and remained constant until the end of simulation. Despite that, the RMSD value of apigenin **(17)** remained stable (0.09 ± 0.02) throughout the 100 ns, demonstrating its stability in Hyal-1 enzyme binding site (**Figure 5.7.b**). The stable RMSD value of apigenin **(17)** suggested that the fluctuations of the complex after 75 ns occurred globally, but no effect was imposed towards ligand binding. The minimal fluctuations of R_g value (**Figure 5.8**) for derivative **(102)** and apigenin **(17)** (22.7 and 22.8 nm, respectively) (**Table 5.6**) also indicated the Hyal-1 enzyme achieved stable conformation after ligands binding in the active pocket.

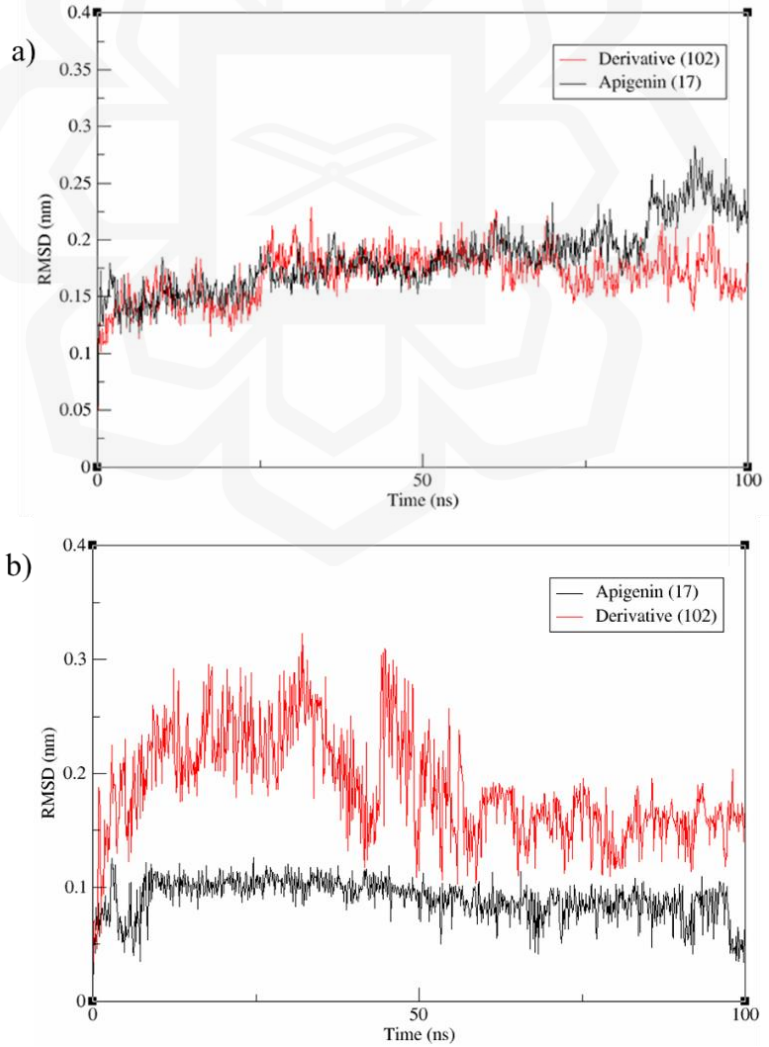

Figure 5.7: RMSD plot for a) Hyal-1-ligand complexes; b) ligand only

Table 5.6: Average RMSD and R_g values of derivative **(102)** and apigenin **(17)**

Analysis	Derivative (102)	Apigenin (17)
RMSD Hyal-1-ligand complex (nm)	0.17 ± 0.02	0.18 ± 0.03
RMSD ligand only (nm)	0.18 ± 0.05	0.09 ± 0.02
Radius of gyration (nm)	22.7 ± 0.01	22.8 ± 0.01

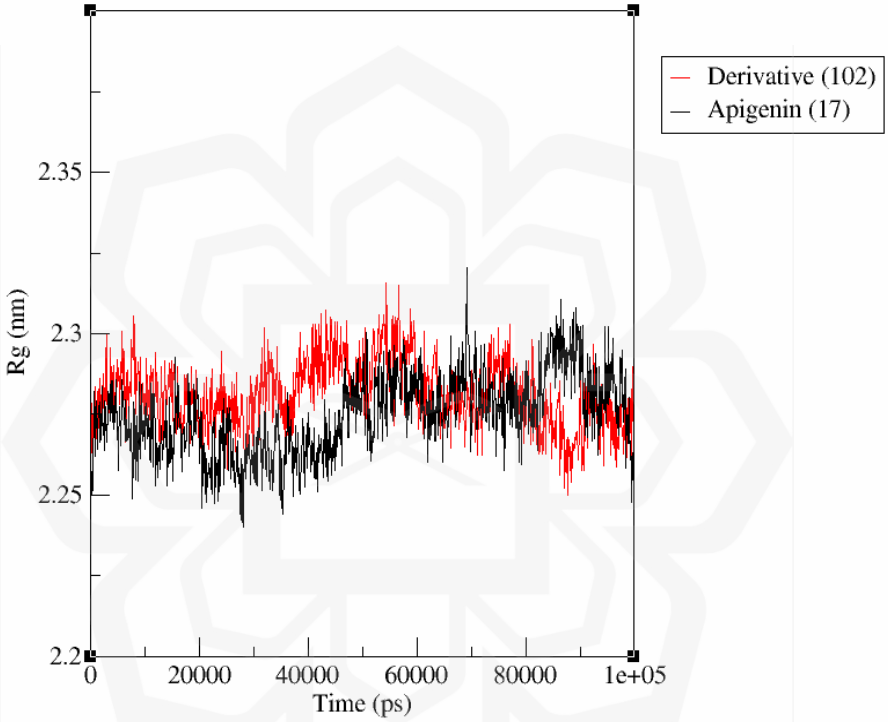

Figure 5.8: Radius of gyration plot for derivative **(102)** and apigenin **(17)**

The RMSF values of the systems was determined to check on the local effect of ligand binding on the amino acid residue. The graph for RMSF was plotted against residue number, where higher RMSF value of respective residue indicated that the residue has high flexibility during the simulation (Rashid et al., 2022). **Figure 5.9** depicted the RMSF values for residues of derivative **(102)** and apigenin **(17)** exhibited minor fluctuations along 100 ns simulations.

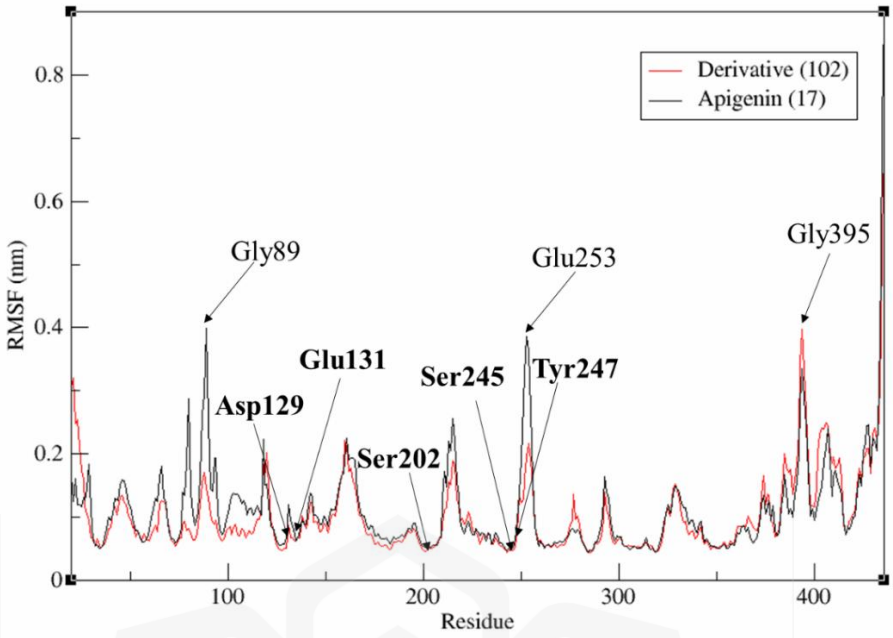

Figure 5.9: RMSF plot for derivative **(102)** and apigenin **(17)**. The important amino acid residues of Hyal-1 enzyme were shown in **bold**.

Higher flexibility can be observed for both compounds at residues Gly89, Glu253 and Gly395. These residues were not located around the binding site region; thus it did not pose local effect on the binding site. The important residues for enzyme activity in the binding site (Asp129, Glu131, Tyr202, Ser245 and Tyr247) possessed RMSF values lower than 0.2 nm. The minimal fluctuations upon ligand binding in the active site, reflected from the low RMSF value (**Figure 5.10**) suggested the rigidity of Hyal-1 binding pocket.

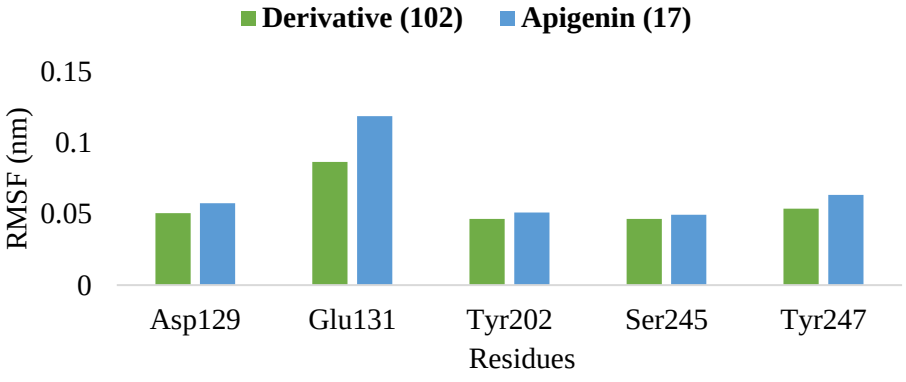

Figure 5.10: RMSF values of important residues for Hyal-1 enzyme

Hydrogen bonding interactions play a significant role in ligand binding and enzyme activities (Bulusu & Desiraju, 2020). Therefore, a closer look into the binding of the ligand in the binding site of Hyal-1 enzyme was evaluated with hydrogen bond analysis. This analysis represented the number of hydrogen bonds formed between ligands and Hyal-1 enzyme throughout the simulation.

The hydrogen bond plot as presented in **Figure 5.11** indicated that derivative **(102)** had lower hydrogen bond interactions with Hyal-1 enzyme. This can be seen by lower mean number of hydrogen bonds (0.19), compared to apigenin **(17)** (1.61). From the plot, it can be observed that derivative **(102)** did not exhibit significant hydrogen bond interactions during the first 60 ns time frame. After 60 ns, at least one hydrogen bond appeared in most of the time frames until the end of simulation.

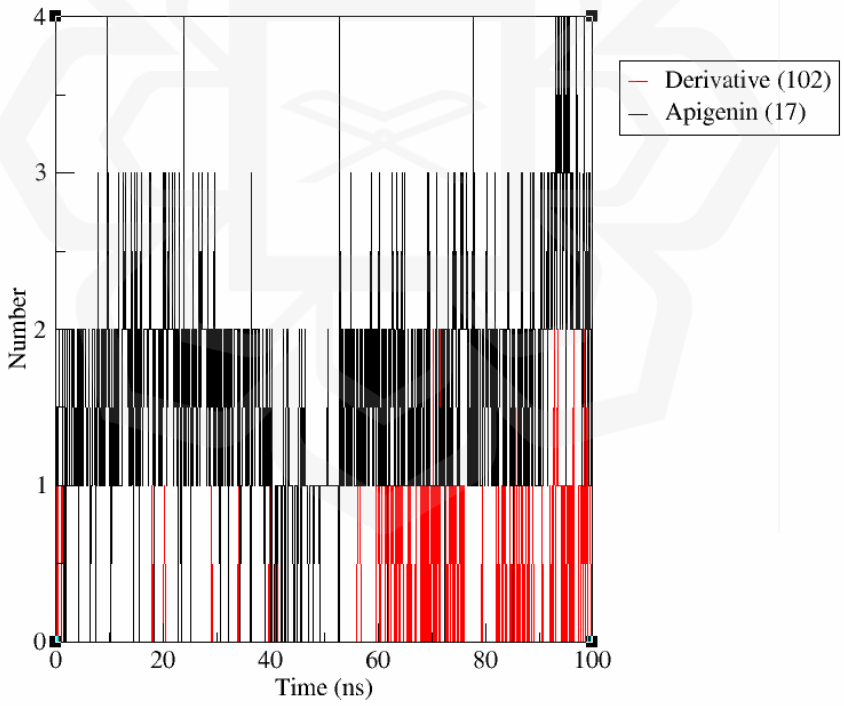

Figure 5.11: Number of hydrogen bonds of derivative **(102)** and apigenin **(17)**

The hydrogen bond analysis also indicated that apigenin **(17)** occupied the binding site of Hyal-1 enzyme *via* stronger hydrogen bond interactions compared to derivative **(102)**, as reflected in the higher number of hydrogen bonds (**Figure 5.11**),

and higher hydrogen bond occupancy with the important residues for enzyme activity (**Figure 5.12**). Therefore, it is inferred that apigenin **(17)** was able to exhibit stronger inhibition in the *in vitro* assay due to more significant hydrogen bonding interactions compared to derivative **(102)**. Apigenin **(17)** possessed five hydrogen bond acceptors and three hydrogen bond donors, hence it can interact with the active site of Hyal-1 enzyme through hydrogen bonding networks easily.

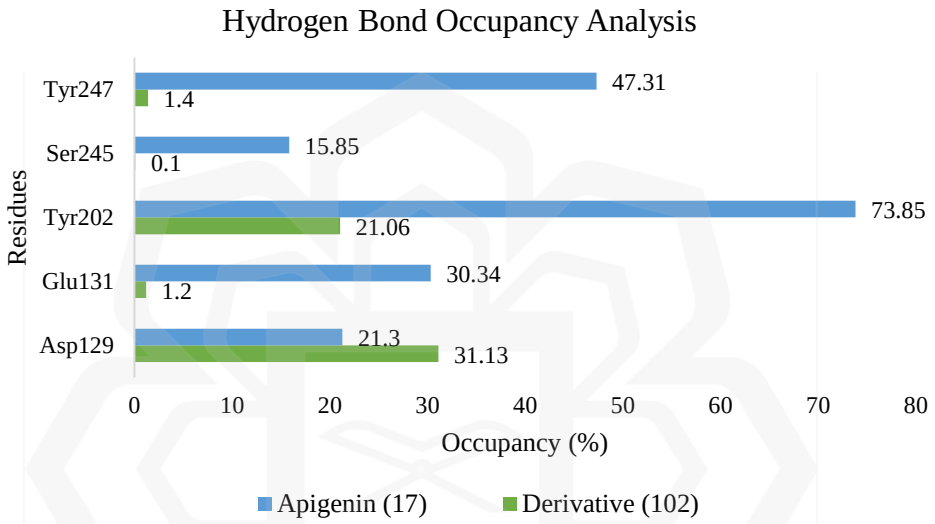

Figure 5.12: Hydrogen bond occupancy analysis of derivative **(102)** and apigenin **(17)**

Since the structure of derivative **(102)** with only one hydrogen bond donor and acceptors has lower chance of forming hydrogen bonding interactions with Hyal-1 enzyme, it was suggested that derivative **(102)** was stabilised in the binding site through hydrophobic and Van der Waals interactions. This inference was supported by the pair distance data. The distance between ligand and binding site of enzyme was plotted against the simulation time as depicted in **Figure 5.13**. It can be observed that derivative **(102)** was able to bound stably in the binding site with mean distance value of 0.21 ± 0.01 nm (**Table 5.7**).

The value for apigenin **(17)** (0.19 ± 0.01 nm) was slightly lower compared to derivative **(102)**, as hydrogen bonding interactions held apigenin **(17)** more strongly compared to other types of interactions, resulting in lower distance value. Moreover,

the visualisation of the simulation in VMD showed that derivative **(102)** did not deviate from the binding site of Hyal-1 enzyme throughout 100 ns simulation as depicted in **Figure 5.14**. Therefore, the MD simulation results suggest that although derivative **(102)** lacks strong hydrogen bond interactions, it achieved stabilisation in the Hyal-1 binding site through Van der Waals and hydrophobic interactions that were likely contributed to its good Hyal-1 inhibitory activity observed in the *in vitro* study.

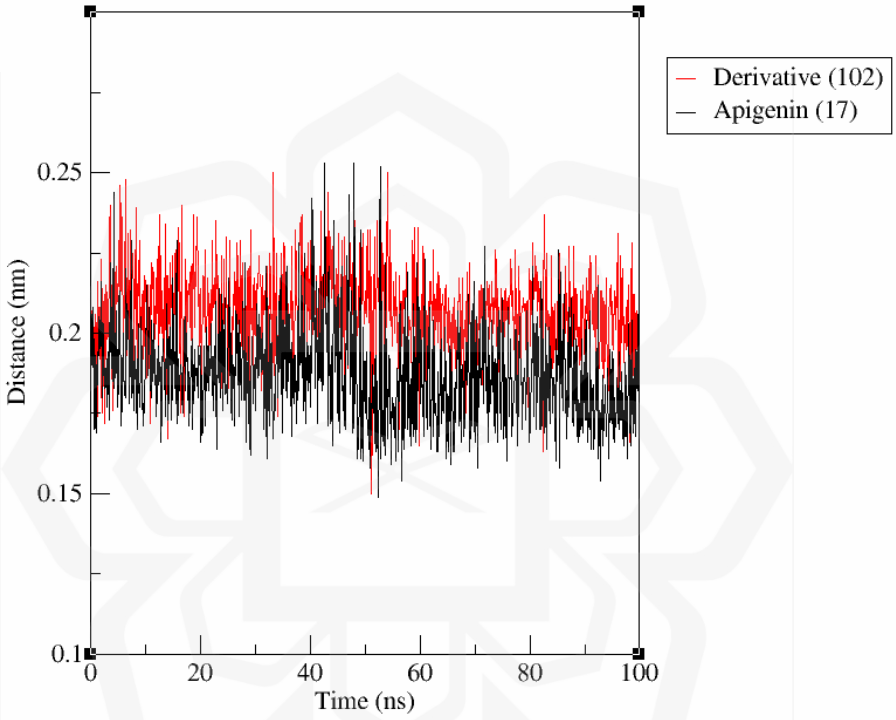

Figure 5.13: Distance graph of derivative **(102)** and apigenin **(17)** with Hyal-1 enzyme

Table 5.7: Distance between derivative **(102)** and apigenin **(17)** with the binding site of Hyal-1 enzyme

Compounds	Distance (nm)
Derivative (102)	0.21 ± 0.01
Apigenin (17)	0.19 ± 0.02

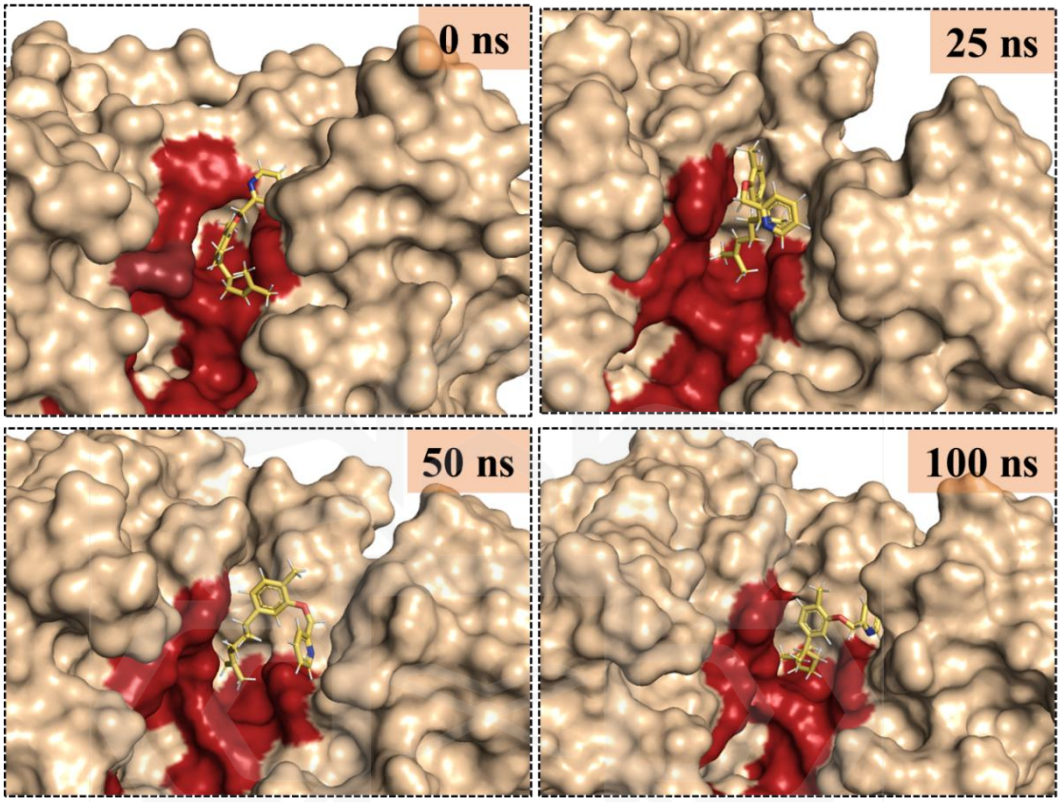

Figure 5.14: Visualisation state of derivative **(102)** (yellow) in binding site of Hyal-1 enzyme over 100 ns simulation.

CHAPTER 6

CONCLUSIONS AND RECOMMENDATIONS

6.1 CONCLUSIONS

Two computational approaches i.e virtual screening of XNT derivatives **(63-81**, **91-101)** and *in silico* FBDD had successfully furnished six new derivatives to be synthesised as potential Hyal-1 inhibitors. The XNT derivative were name of all new benzyl xanthorrhizyl ether **(76)**, (2-pyridinyl)methyl xanthorrhizyl ether **(102)**, 4-nitrobenzyl xanthorrhizyl ether **(103)**, 3-trifluoromethylbenzyl xanthorrhizyl ether **(104)**, (2-tetrahydro-2H-pyranyl)methyl xanthorrhizyl ether **(105)** and (2-tetrahydrofuranyl)methyl xanthorrhizyl ether **(106)**. However, the incorporation of different ring system substituted in the hydroxyl group of XNT **(1)** for each derivatives did not improve their drug-likeness properties compared to XNT **(1)**.

Derivatives **(76**, **102-106)** were successfully synthesised using Williamson ether synthesis reaction. On the other hand, the characterisation of product synthesised from reaction of XNT **(1)** with tetrahydrofurfuryl chloride **(116)** revealed the formation of an unexpected product, namely propyl 2-xanthorrhizyloxyacetate **(117)** was furnished instead of desired derivative **(106)**. All synthesised derivatives **(76**, **102-105**, **117)** were then subjected to *in vitro* assay to evaluate their inhibitory activities against Hyal-1 enzyme. Derivatives **(76**, **102-104)** exhibited stronger inhibitions against Hyal-1 enzyme compared to XNT **(1)** (203.56 µg/mL). Meanwhile, derivatives **(105)** and **(117)** had IC_{50} values higher than 500 µg/mL, therefore were considered as inactive.

Among all derivatives, derivative **(102)** exhibited strongest inhibition with IC_{50} value of 44.45 µg/mL. The trajectory analysis of derivative **(102)** determined *via* MD simulation revealed that it was bound stably to Hyal-1 enzyme throughout 100 ns simulation. Moreover, the lack of hydrogen bond occupancy of derivative **(102)** with the essential amino acid residues despite stable binding suggested that derivative **(102)** was stabilised in the active pocket through other type of interactions than hydrogen bonding, such as Van der Waals or hydrophobic interactions.

The virtual screening of published XNT derivatives **(63-81**, **91-101)** against soybean LOX-3 enzyme showed the potential of benzyl xanthorrhizyl ether **(76)** as LOX-3 inhibitor due to strong binding energy of -8.6 kcal/mol. Additionally, four XNT derivatives generated from *in silico* FBDD approach as potential LOX-3 inhibitors, namely 2-(xanthorrhizyloxy)ethyl carbamide **(107)**, *N*-(2-(xanthorrhizyloxy)ethyl)-1*H*-imidazole-4-carboxamide **(108)**, *N*-(2-(xanthorrhizyloxy)ethyl)-3-aminopropanamide **(109)** and 3-(xanthorrhizyloxy)propyl 1*H*-imidazole-4-carboxylate **(110)** were attempted to be synthesised. Derivatives **(107-110)** composed of polar functional groups such as ester and amide exhibited good drug-likeness properties and were predicted to have good absorption in gastrointestinal tract.

However, the attempted synthesis of derivatives **(107-110)** was unsuccessful. Therefore, only derivative **(76)** was subjected to *in vitro* LOX-3 assay. Derivative **(76)** displayed weaker inhibition towards LOX-3 enzyme with IC_{50} value of 619.25 µg/mL, compared to XNT (IC_{50} = 142.34 µg/mL). Since derivative **(76)** demonstrated low activity against LOX-3 enzyme, its further analysis using MD simulation was not performed.

6.2 FUTURE WORKS RECOMMENDATIONS

Several recommendations are proposed for the improvement on future works related to the synthesis of the derivatives and its biological evaluations. It is proposed that the synthesis of LOX-3 inhibitors are attempted using different coupling agent, EDC rather than DCC. This is because synthesis using EDC was reported to furnish the desired product with better yield and purity due to the water-soluble urea by-product that eases the process of purification. Moreover, the alkene functionality of XNT **(1)** structure can be explored to improve the ADME properties of the derivatives **(76**, **102-104)** as they possessed poor drug-likeness properties despite exhibiting good inhibitory activities against Hyal enzyme. Besides, mechanistic studies like DFT can be conducted to support the reaction mechanism proposed for the unexpected synthesis of derivative **(117)**. Lastly, binding interaction analysis using one frame from MD simulation can be performed to identify the type of interactions involved in the stabilisation of derivative **(102)** in the binding site of Hyal-1 enzyme.

REFERENCES

Abdelkhalek, A. S., Kothayer, H., Rezq, S., Orabi, K. Y., Romero, D. G., & El-Sabbagh, O. I. (2023). Synthesis of new multitarget-directed ligands containing thienopyrimidine nucleus for inhibition of 15-lipoxygenase, cyclooxygenases, and pro-inflammatory cytokines. *European Journal of Medicinal Chemistry*, *256*, 115443. https://doi.org/10.1016/j.ejmech.2023.115443

Abdullah, N. H., Thomas, N. F., Sivasothy, Y., Lee, V. S., Liew, S. Y., Noorbatcha, I. A., & Awang, K. (2016). Hyaluronidase inhibitory activity of pentacylic triterpenoids from *Prismatomeris tetrandra* (Roxb.) K. Schum: Isolation, synthesis and QSAR study. *International Journal of Molecular Sciences*, *17*(2). https://doi.org/10.3390/IJMS17020143

Aguilar, M. I., Delgado, G., Hernández, M. D. L., & Villarreal, M. L. (2001). Bioactive compounds from *Iostephane heterophylla* (Asteraceae). *Natural Product Letters*, *15*(2), 93–101. https://doi.org/10.1080/10575630108041265

Aguilar, M. I., Delgado, G., & Villarreal, M. L. (2001). New bioactive derivatives of xanthorrhizol. *Revista de La Sociedad Química de México*, *45*(2), 56–59.

Ahmad, I., Kuznetsov, A. E., Pirzada, A. S., Alsharif, K. F., Daglia, M., & Khan, H. (2023). Computational pharmacology and computational chemistry of 4-hydroxyisoleucine: Physicochemical, pharmacokinetic, and DFT-based approaches. *Frontiers in Chemistry*, *11*. https://doi.org/10.3389/fchem.2023.1145974

Ahmed, M., Maldonado, A. M., & Durrant, J. D. (2023). From byte to bench to bedside: molecular dynamics simulations and drug discovery. *BMC Biology*, *21*(1), 299. https://doi.org/10.1186/s12915-023-01791-z

Ahmed, M. N., Shabbir, S., Batool, B., Mahmood, T., Rashid, U., Yasin, K. A., Tahir, M. N., Cassará, M. L. A., & Gil, D. M. (2021). A new insight into non-covalent interactions in 1,4-disubstituted 1*H*-1,2,3-triazole: Synthesis, X-ray structure, DFT calculations, *in vitro* lipoxygenase inhibition (LOX) and *in silico* Studies. *Journal of Molecular Structure*, *1236*, 130283. https://doi.org/10.1016/j.molstruc.2021.130283

Al-Karmalawy, A. A., Dahab, M. A., Metwaly, A. M., Elhady, S. S., Elkaeed, E. B., Eissa, I. H., & Darwish, K. M. (2021). Molecular docking and dynamics simulation revealed the potential inhibitory activity of ACEIs against SARS-CoV-2 targeting the hACE2 receptor. *Frontiers in Chemistry*, *9*. https://doi.org/10.3389/fchem.2021.661230

Andola, P., Pagag, J., Laxman, D., & Guruprasad, L. (2022). Fragment-based inhibitor design for SARS-CoV2 main protease. *Structural Chemistry*, *33*(5), 1467–1487. https://doi.org/10.1007/s11224-022-01995-z

Arya, H., & Coumar, M. S. (2021). Lead identification and optimization. *The Design & Development of Novel Drugs and Vaccines*, 31–63. https://doi.org/10.1016/B978-0-12-821471-8.00004-0

Azhar-Ul-Haq, Malik, A., Anis, I., Khan, S. B., Ahmed, E., Ahmed, Z., Nawaz, S. A., & Choudhary, M. I. (2004). Enzymes inhibiting lignans from Vitex negundo. *Chemical & Pharmaceutical Bulletin*, *52*(11), 1269–1272. https://doi.org/10.1248/cpb.52.1269

Bailey, L. C., & Levine, N. A. (1993). Optimization of the USP assay for hyaluronidase. *Journal of Pharmaceutical and Biomedical Analysis*, *11*(4–5), 285–292. https://doi.org/10.1016/0731-7085(93)80019-W

Baeuer, P., Hess, B., & Lindahl, E. (n.d.). *GROMACS 2022 manual*. https://doi.org/10.5281/zenodo.6103568

Bhalani, D. V., Nutan, B., Kumar, A., & Singh Chandel, A. K. (2022). Bioavailability enhancement techniques for poorly aqueous soluble drugs and therapeutics. *Biomedicines*, *10*(9), 2055. https://doi.org/10.3390/biomedicines10092055

Bian, Y., & Xie, X. Q. (Sean). (2018). Computational fragment-based drug design: Current trends, strategies, and applications. *The AAPS Journal*, *20*(3), 59. https://doi.org/10.1208/S12248-018-0216-7

Bissaro, M., Sturlese, M., & Moro, S. (2020). The rise of molecular simulations in fragment-based drug design (FBDD): an overview. *Drug Discovery Today*, *25*(9), 1693–1701. https://doi.org/10.1016/j.drudis.2020.06.023

Bollag, G., Tsai, J., Zhang, J., Zhang, C., Ibrahim, P., Nolop, K., & Hirth, P. (2012). Vemurafenib: the first drug approved for BRAF-mutant cancer. *Nature Reviews Drug Discovery*, *11*(11), 873–886. https://doi.org/10.1038/nrd3847

Bol'shakov, O., Lebedyeva, I., & Katritzky, A. (2012). 17α-Ethynylestradiol peptide labeling by 'click' chemistry. *Synthesis*, *44*(18), 2926–2932. https://doi.org/10.1055/s-0032-1316702

Brian S. Furniss, Antony J. Hannaford, Peter W. G. Smith, & Austin R. Tatchell. (1989). *Vogel's textbook of practical organic chemistry* (5th ed.). Longman Scientific & Technical.

Brooks, B. R., Brooks, C. L., Mackerell, A. D., Nilsson, L., Petrella, R. J., Roux, B., Won, Y., Archontis, G., Bartels, C., Boresch, S., Caflisch, A., Caves, L., Cui, Q., Dinner, A. R., Feig, M., Fischer, S., Gao, J., Hodoscek, M., Im, W., … Karplus, M. (2009). CHARMM: The biomolecular simulation program. *Journal of Computational Chemistry*, *30*(10), 1545–1614. https://doi.org/10.1002/jcc.21287

Bulusu, G., & Desiraju, G. R. (2020). Strong and weak hydrogen bonds in protein–ligand recognition. *Journal of the Indian Institute of Science*, *100*(1), 31–41. https://doi.org/10.1007/s41745-019-00141-9

Chao, K. L., Muthukumar, L., & Herzberg, O. (2007). Structure of human hyaluronidase-1, a hyaluronan hydrolyzing enzyme involved in tumor growth and

angiogenesis. *Biochemistry*, *46*(23), 6911–6920. https://doi.org/10.1021/bi700382g

Che, X., Liu, Q., & Zhang, L. (2023). An accurate and universal protein-small molecule batch docking solution using Autodock Vina. *Results in Engineering*, *19*, 101335. https://doi.org/10.1016/j.rineng.2023.101335

Chen, Y.-C. (2015). Beware of docking! *Trends in Pharmacological Sciences*, *36*(2), 78–95. https://doi.org/10.1016/j.tips.2014.12.001

Chung, W. Y., Park, J. H., Kim, M. J., Kim, H. O., Hwang, J. K., Lee, S. K., & Park, K. K. (2007). Xanthorrhizol inhibits 12-O-tetradecanoylphorbol-13-acetate-induced acute inflammation and two-stage mouse skin carcinogenesis by blocking the expression of ornithine decarboxylase, cyclooxygenase-2 and inducible nitric oxide synthase through mitogen-activated protein kinases and/or the nuclear factor-kappa B. *Carcinogenesis*, *28*(6), 1224–1231. https://doi.org/10.1093/CARCIN/BGM005

Clark, D. E. (2011). What has polar surface area ever done for drug discovery? *Future Medicinal Chemistry*, *3*(4), 469–484. https://doi.org/10.4155/fmc.11.1

Congreve, M., Carr, R., Murray, C., & Jhoti, H. (2003). A "rule of three" for fragment-based lead discovery? *Drug Discovery Today*, *8*(19), 876–877. https://doi.org/10.1016/S1359-6446(03)02831-9

Daina, A., Michielin, O., & Zoete, V. (2017). SwissADME: a free web tool to evaluate pharmacokinetics, drug-likeness and medicinal chemistry friendliness of small molecules. *Scientific Reports*, *7*(1), 42717. https://doi.org/10.1038/srep42717

de Souza Neto, L. R., Moreira-Filho, J. T., Neves, B. J., Maidana, R. L. B. R., Guimarães, A. C. R., Furnham, N., Andrade, C. H., & Silva, F. P. (2020). *In silico* strategies to support fragment-to-lead optimization in drug discovery. *Frontiers in Chemistry*, *8*, 93. https://doi.org/10.3389/FCHEM.2020.00093

Deore, A. B., Dhumane, J. R., Wagh, H. V, & Sonawane, R. B. (2019). The stages of drug discovery and development process. *Asian Journal of Pharmaceutical Research and Development*, *7*(6), 62–67. https://doi.org/10.22270/AJPRD.V7I6.616

Dibyajyoti, S., Bin, E. T., & Swati, P. (2013). Bioinformatics:The effects on the cost of drug discovery. *Galle Medical Journal*, *18*(1), 44. https://doi.org/10.4038/GMJ.V18I1.5511

Dinata, D. I., Suryatno, H., Musfiroh, I., & Suherman, S. E. (2014). Molecular docking simulation of xanthorrhizol compounds derived from temulawak as antiinflammatory on enzymes COX-1 and COX-2. *Indonesian Journal of Pharmaceutical Science and Technology*, *1*(1), 7–13. https://doi.org/10.15416/IJPST.V1I1.7508

Dokoshi, T., Zhang, L. J., Nakatsuji, T., Adase, C. A., Sanford, J. A., Paladini, R. D., Tanaka, H., Fujiya, M., & Gallo, R. L. (2018). Hyaluronidase inhibits reactive

adipogenesis and inflammation of colon and skin. *JCI Insight*, *3*(21). https://doi.org/10.1172/JCI.INSIGHT.123072

Erlanson, D. A., Fesik, S. W., Hubbard, R. E., Jahnke, W., & Jhoti, H. (2016). Twenty years on: the impact of fragments on drug discovery. *Nature Reviews. Drug Discovery*, *15*(9), 605–619. https://doi.org/10.1038/NRD.2016.109

Fairbrother, W. J., Leverson, J. D., Sampath, D., & Souers, A. J. (2019). Discovery and development of Venetoclax, a selective antagonist of BCL-22. *Successful Drug Discovery* (pp. 225–245). Wiley. https://doi.org/10.1002/9783527814695.ch9

Fronza, M., Caetano, G. F., Leite, M. N., Bitencourt, C. S., Paula-Silva, F. W. G., Andrade, T. A. M., Frade, M. A. C., Merfort, I., & Faccioli, L. H. (2014). Hyaluronidase modulates inflammatory response and accelerates the cutaneous wound healing. *PLoS ONE*, *9*(11), 112297. https://doi.org/10.1371/JOURNAL.PONE.0112297

Furman, D., Campisi, J., Verdin, E., Carrera-Bastos, P., Targ, S., Franceschi, C., Ferrucci, L., Gilroy, D. W., Fasano, A., Miller, G. W., Miller, A. H., Mantovani, A., Weyand, C. M., Barzilai, N., Goronzy, J. J., Rando, T. A., Effros, R. B., Lucia, A., Kleinstreuer, N., & Slavich, G. M. (2019). Chronic inflammation in the etiology of disease across the life span. *Nature Medicine*, *25*(12), 1822. https://doi.org/10.1038/S41591-019-0675-0

Gadnayak, A., Dehury, B., Nayak, A., Jena, S., Sahoo, A., Panda, P. C., Ray, A., & Nayak, S. (2022). 'Mechanistic insights into 5-lipoxygenase inhibition by active principles derived from essential oils of Curcuma species: Molecular docking, ADMET analysis and molecular dynamic simulation study. *PLOS ONE*, *17*(7), e0271956. https://doi.org/10.1371/journal.pone.0271956

Garantziotis, S., & Savani, R. C. (2019). Hyaluronan biology: A complex balancing act of structure, function, location and context. *Matrix Biology: Journal of the International Society for Matrix Biology*, *78–79*, 1. https://doi.org/10.1016/J.MATBIO.2019.02.002

Ghansenyuy, S. Y., Eyong, K. O., Yemback, P., Mehreen, L., Nziko, V. de P. N., Ali, M. S., & Folefoc, G. N. (2023). Lipoxygenase inhibition and molecular docking studies of secondary metabolites from the leaves of *Alstonia scholaris*. *European Journal of Medicinal Chemistry Reports*, *9*, 100108. https://doi.org/10.1016/j.ejmcr.2023.100108

Giménez-Bastida, J. A., González-Sarrías, A., Laparra-Llopis, J. M., Schneider, C., & Espín, J. C. (2021). Targeting mammalian 5-lipoxygenase by dietary phenolics as an anti-inflammatory mechanism: A systematic review. *International Journal of Molecular Sciences*, *22*(15). https://doi.org/10.3390/IJMS22157937

Grasso, G., Di Gregorio, A., Mavkov, B., Piga, D., Labate, G. F. D., Danani, A., & Deriu, M. A. (2022). Fragmented blind docking: a novel protein–ligand binding prediction protocol. *Journal of Biomolecular Structure and Dynamics*, *40*(24), 13472–13481. https://doi.org/10.1080/07391102.2021.1988709

Goodsell, D. S., & Olson, A. J. (1990). Automated docking of substrates to proteins by simulated annealing. *Proteins: Structure, Function, and Bioinformatics*, *8*(3), 195–202. https://doi.org/10.1002/prot.340080302

Guo, Z. (2017). The modification of natural products for medical use. *Acta Pharmaceutica Sinica B*, *7*(2), 119–136. https://doi.org/10.1016/J.APSB.2016.06.003

Gupta, S., Baweja, G. S., Singh, S., Irani, M., Singh, R., & Asati, V. (2023). Integrated fragment-based drug design and virtual screening techniques for exploring the antidiabetic potential of thiazolidine-2,4-diones: Design, synthesis and in vivo studies. *European Journal of Medicinal Chemistry*, *261*, 115826. https://doi.org/10.1016/j.ejmech.2023.115826

Hanwell, M. D., Curtis, D. E., Lonie, D. C., Vandermeerschd, T., Zurek, E., & Hutchison, G. R. (2012). Avogadro: An advanced semantic chemical editor, visualization, and analysis platform. *Journal of Cheminformatics*, *4*(8), 1–17. https://doi.org/10.1186/1758-2946-4-17/FIGURES/14

Huang, H., Chen, J., Ren, J., Zhang, C., & Ji, F. (2019). Palladium(II)-catalyzed efficient synthesis of wedelolactone and evaluation as potential tyrosinase inhibitor. *Molecules*, *24*(22), 4130. https://doi.org/10.3390/molecules24224130

Hughes, J. P., Rees, S. S., Kalindjian, S. B., & Philpott, K. L. (2011). Principles of early drug discovery. *British Journal of Pharmacology*, *162*(6), 1239. https://doi.org/10.1111/J.1476-5381.2010.01127.X

Humphrey, W., Dalke, A., & Schulten, K. (1996). VMD: Visual molecular dynamics. *Journal of Molecular Graphics*, *14*(1), 33–38. https://doi.org/10.1016/0263-7855(96)00018-5

Isoyama, T., Thwaites, D., Selzer, M. G., Carey, R. I., Barbucci, R., & Lokeshwar, V. B. (2006). Differential selectivity of hyaluronidase inhibitors toward acidic and basic hyaluronidases. *Glycobiology*, *16*(1), 11–21. https://doi.org/10.1093/GLYCOB/CWJ036

Jameson, J. B., Kantz, A., Schultz, L., Kalyanaraman, C., Jacobson, M. P., Maloney, D. J., Jadhav, A., Simeonov, A., & Holman, T. R. (2014). A high throughput screen identifies potent and selective inhibitors to human epithelial 15-lipoxygenase-2. *PLoS ONE*, *9*(8), e104094. https://doi.org/10.1371/journal.pone.0104094

Jantan, I., Saputri, F. C., Qaisar, M. N., & Buang, F. (2012). Correlation between chemical composition of *Curcuma domestica* and *Curcuma xanthorrhiza* and their antioxidant effect on human low-density lipoprotein oxidation. *Evidence-Based Complementary and Alternative Medicine : ECAM*, *2012*. https://doi.org/10.1155/2012/438356

Jeffries, B., Wang, Z., Graton, J., Holland, S. D., Brind, T., Greenwood, R. D. R., Le Questel, J.-Y., Scott, J. S., Chiarparin, E., & Linclau, B. (2018). Reducing the lipophilicity of perfluoroalkyl groups by CF_2–F/CF_2–Me or CF_3/CH_3 Exchange.

Journal of Medicinal Chemistry, *61*(23), 10602–10618. https://doi.org/10.1021/acs.jmedchem.8b01222

Jo, S., Kim, T., Iyer, V. G., & Im, W. (2008). CHARMM-GUI: A web-based graphical user interface for CHARMM. *Journal of Computational Chemistry*, *29*(11), 1859–1865. https://doi.org/10.1002/jcc.20945

John, T. K., & Rao, G. S. K. (1985). Studies in terpenoids. Part LXIII. Absolute Configuration of naturally occuring (–)-Xanthorrhizol. *Indian Journal of Chemistry*, *24B*, 35–37.

Jordan, A., Whymark, K. D., Sydenham, J., & Sneddon, H. F. (2021). A solvent-reagent selection guide for Steglich-type esterification of carboxylic acids. *Green Chemistry*, *23*(17), 6405–6413. https://doi.org/10.1039/D1GC02251B

Karami, T. K., Hailu, S., Feng, S., Graham, R., & Gukasyan, H. J. (2022). Eyes on Lipinski's Rule of Five: A new "Rule of Thumb" for physicochemical design space of ophthalmic drugs. *Journal of Ocular Pharmacology and Therapeutics*, *38*(1), 43–55. https://doi.org/10.1089/jop.2021.0069

Ken, M. L., Tei, T., & Wan. M. Khairul. (2019). Synthesis and characterisation of N-analineferrocenylamide via carbodiimide coupling. *Malaysian Journal of Analytical Science*, *23*(2). https://doi.org/10.17576/mjas-2019-2302-02

Khammee, T., Rujitanapanich, S., Chunhakant, S., Jaratrungtawee, A., & Kuno, M. (2020). *In vitro* and *in silico* evaluations of chemical constituents from the rhizomes of *Aglaonema simplex* (Blume) Blume as Hyaluronidase Inhibitor. *Thai Journal of Science and Technology*, *9*(3), 269–277. https://doi.org/10.14456/TJST.2020.17

Kim, S., Kook, K. E., Kim, C., & Hwang, J. K. (2018). Inhibitory effects of Curcuma xanthorrhiza supercritical extract and xanthorrhizol on LPS-induced inflammation in HGF-1 Cells and RANKL-induced osteoclastogenesis in RAW264.7 cells. *Journal of Microbiology and Biotechnology*, *28*(8), 1270–1281. https://doi.org/10.4014/JMB.1803.03045

Koukoulitsa, C., Hadjipavlou–Litina, D., Geromichalos, G. D., & Skaltsa, H. (2007). Inhibitory effect on soybean lipoxygenase and docking studies of some secondary metabolites, isolated from *Origanum vulgare* L. ssp. *hirtum*. *Journal of Enzyme Inhibition and Medicinal Chemistry*, *22*(1), 99–104. https://doi.org/10.1080/14756360600991017

Kumar, A., Voet, A., & Zhang, K. Y. J. (2012). Fragment based drug design: From experimental to computational approaches. *Current Medicinal Chemistry*, *19*(30), 5128–5147. https://doi.org/10.2174/092986712803530467

Lamoree, B., & Hubbard, R. E. (2017). Current perspectives in fragment-based lead discovery (FBLD). *Essays in Biochemistry*, *61*(5), 453–464. https://doi.org/10.1042/EBC20170028

Lavrentaki, V., Kousaxidis, A., Theodosis-Nobelos, P., Papagiouvannis, G., Koutsopoulos, K., & Nicolaou, I. (2023). Design, synthesis, and pharmacological

evaluation of indazole carboxamides of N-substituted pyrrole derivatives as soybean lipoxygenase inhibitors. *Molecular Diversity*. https://doi.org/10.1007/s11030-023-10775-8

Lee, J. C., Oh, Y. S., Cho, S. H., & Lee, J. D. (1996). Efficient *in situ* esterification of carboxylic acids using cesium carbonate. *Organic Preparations and Procedures International*, *28*(4), 480–483. https://doi.org/10.1080/00304949609356558

Lee, J., Cheng, X., Swails, J. M., Yeom, M. S., Eastman, P. K., Lemkul, J. A., Wei, S., Buckner, J., Jeong, J. C., Qi, Y., Jo, S., Pande, V. S., Case, D. A., Brooks, C. L., MacKerell, A. D., Klauda, J. B., & Im, W. (2016). CHARMM-gui input generator for NAMD, GROMACS, AMBER, OpenMM, and CHARMM/OpenMM simulations using the CHARMM36 additive force field. *Journal of Chemical Theory and Computation*, *12*(1), 405–413. https://doi.org/10.1021/acs.jctc.5b00935

Lee, S. K., Hong, C. H., Huh, S. K., Kim, S. S., Oh, O. J., Min, H. Y., Park, K. K., Chung, W. Y., & Hwang, J. K. (2002). Suppressive effect of natural sesquiterpenoids on inducible cyclooxygenase (COX-2) and nitric oxide synthase (iNOS) activity in mouse macrophage cells. *Journal of Environmental Pathology, Toxicology and Oncology*, *21*(2), 141–148. https://doi.org/10.1615/JEnvironPatholToxicolOncol.v21.i2.70

Lemkul, J. (2019). From Proteins to Perturbed Hamiltonians: A suite of tutorials for the GROMACS-2018 molecular simulation package. *Living Journal of Computational Molecular Science*, *1*(1). https://doi.org/10.33011/livecoms.1.1.5068

Lengers, I., Herrmann, F., Le Borgne, M., & Jose, J. (2020). Improved surface display of human Hyal1 and identification of testosterone propionate and chicoric acid as new inhibitors. *Pharmaceuticals*, *13*(4), 1–18. https://doi.org/10.3390/PH13040054

Li, Q. (2020). Application of fragment-based drug discovery to versatile targets. *Frontiers in Molecular Biosciences*, *7*, 180. https://doi.org/10.3389/FMOLB.2020.00180/BIBTEX

Li, X., Liu, H., Yang, Z., Duan, H., Wang, Z., Cheng, Z., Song, Z., & Wu, X. (2021). Study on the interaction of hyaluronidase with certain flavonoids. *Journal of Molecular Structure*, *1241*, 130686. https://doi.org/10.1016/j.molstruc.2021.130686

Liao, W., Khoo, Y. W., Goh, J. W. K., & Wong, W.-S. F. (2019). Anti-oxidative and anti-inflammatory effects of Xanthorrhizol on aeroallergens-induced biological responses in vitro and ex vivo. *European Respiratory Journal*, *54*(suppl 63), PA4206. https://doi.org/10.1183/13993003.CONGRESS-2019.PA4206

Liao, W., & Wong, W. S. F. (2022). Anti-oxidative and anti-inflammatory properties of xanthorrhizol in airway inflammation. *Journal of Basic and Applied Pharmacology*, *2*(2), 74–87.

Lim, C. S., Jin, D. Q., Mok, H., Oh, S. J., Lee, J. U., Hwang, J. K., Ha, I., & Han, J. S. (2005). Antioxidant and antiinflammatory activities of xanthorrhizol in hippocampal neurons and primary cultured microglia. *Journal of Neuroscience Research*, *82*(6), 831–838. https://doi.org/10.1002/JNR.20692

Ling, S.-K., Tanaka, T., & Kouno, I. (2003). Effects of iridoids on lipoxygenase and hyaluronidase activities and their activation by β-glucosidase in the presence of amino acids. *Biological and Pharmaceutical Bulletin*, *26*(3), 352–356. https://doi.org/10.1248/bpb.26.352

Lipinski, C. A., Lombardo, F., Dominy, B. W., & Feeney, P. J. (2001). Experimental and computational approaches to estimate solubility and permeability in drug discovery and development settings 1PII of original article: S0169-409X(96)00423-1. The article was originally published in Advanced Drug Delivery Reviews 23 (1997) 3–25. 1. *Advanced Drug Delivery Reviews*, *46*(1–3), 3–26. https://doi.org/10.1016/S0169-409X(00)00129-0

Liu, J., Zhou, J., He, F., Gao, L., Wen, Y., Gao, L., Wang, P., Kang, D., & Hu, L. (2020). Design, synthesis and biological evaluation of novel indazole-based derivatives as potent HDAC inhibitors via fragment-based virtual screening. *European Journal of Medicinal Chemistry*, *192*, 112189. https://doi.org/10.1016/j.ejmech.2020.112189

Liu, K., Watanabe, E., & Kokubo, H. (2017). Exploring the stability of ligand binding modes to proteins by molecular dynamics simulations. *Journal of Computer-Aided Molecular Design*, *31*(2), 201–211. https://doi.org/10.1007/s10822-016-0005-2

Lončarić, M., Strelec, I., Pavić, V., Rastija, V., Karnaš, M., & Molnar, M. (2022). Green synthesis of thiazolidine-2,4-dione derivatives and their lipoxygenase inhibition activity with QSAR and molecular docking studies. *Frontiers in Chemistry*, *10*. https://doi.org/10.3389/fchem.2022.912822

Loureiro, D. R. P., Soares, J. X., Costa, J. C., Magalhães, Á. F., Azevedo, C. M. G., Pinto, M. M. M., & Afonso, C. M. M. (2019). Structures, activities and drug-likeness of anti-infective xanthone derivatives isolated from the marine environment: A review. *Molecules*, *24*(2), 243. https://doi.org/10.3390/molecules24020243

Lovering, F., Bikker, J., & Humblet, C. (2009). Escape from flatland: Increasing saturation as an approach to improving clinical success. *Journal of Medicinal Chemistry*, *52*(21), 6752–6756. https://doi.org/10.1021/jm901241e

Maghraby, M. T.-E., Abou-Ghadir, O. M. F., Abdel-Moty, S. G., Ali, A. Y., & Salem, O. I. A. (2020). Novel class of benzimidazole-thiazole hybrids: The privileged scaffolds of potent anti-inflammatory activity with dual inhibition of cyclooxygenase and 15-lipoxygenase enzymes. *Bioorganic & Medicinal Chemistry*, *28*(7), 115403. https://doi.org/10.1016/j.bmc.2020.115403

Mancipe, J. C., Vargas-Pinto, P., Rodríguez, O. E., Borrego-Muñoz, P., Castellanos Londoño, I., Ramírez, D., Piñeros, L. G., Mejía, M. C., & Pombo, L. M. (2023). Anti-Inflammatory Effect of izalpinin derived from *Chromolaena leivensis*: λ-

Carrageenan-induced paw edema and *in silico* model. *Molecules*, *28*(9), 3722. https://doi.org/10.3390/molecules28093722

Martel-Pelletier, J., Lajeunesse, D., Reboul, P., & Pelletier, J. P. (2003). Therapeutic role of dual inhibitors of 5-LOX and COX, selective and non-selective non-steroidal anti-inflammatory drugs. *Annals of the Rheumatic Diseases*, *62*(6), 501. https://doi.org/10.1136/ARD.62.6.501

McQuitty, C. E., Williams, R., Chokshi, S., & Urbani, L. (2020). Immunomodulatory role of the extracellular matrix within the liver disease microenvironment. *Frontiers in Immunology*, *11*. https://doi.org/10.3389/FIMMU.2020.574276

Mohs, R. C., & Greig, N. H. (2017). Drug discovery and development: Role of basic biological research. *Alzheimer's & Dementia: Translational Research & Clinical Interventions*, *3*(4), 651–657. https://doi.org/10.1016/j.trci.2017.10.005

Moinul, Md., Khatun, S., Amin, Sk. A., Jha, T., & Gayen, S. (2022). Recent trends in fragment-based anticancer drug design strategies against different targets: A mini-review. *Biochemical Pharmacology*, *206*, 115301. https://doi.org/10.1016/j.bcp.2022.115301

Momiyama, N., Honda, Y., Suzuki, T., & Jongwohan, C. (2021). Computational studies on reaction mechanisms and origin of stereoselectivity in the [1,3]-rearrangement of ene-aldimines. *Asian Journal of Organic Chemistry*, *10*(8), 2205–2212. https://doi.org/10.1002/ajoc.202100302

Morak-Młodawska, B., Jeleń, M., Martula, E., & Korlacki, R. (2023). Study of lipophilicity and ADME properties of 1,9-diazaphenothiazines with anticancer action. *International Journal of Molecular Sciences*, *24*(8), 6970. https://doi.org/10.3390/ijms24086970

Morikawa, T., Okugawa, S., Manse, Y., Muraoka, O., Yoshikawa, M., & Ninomiya, K. (2019). Quantitative determination of principal aporphine and benzylisoquinoline alkaloids due to blooming state in lotus flower (Flower buds of *Nelumbo nucifera*) and their hyaluronidase inhibitory activity. *Natural Product Communications*, *14*(6), 1–7. https://doi.org/10.1177/1934578X19857834

Muñoz-Ramírez, A., Mascayano-Collado, C., Barriga, A., Echeverría, J., & Urzúa, A. (2020). Inhibition of soybean 15-lipoxygenase and human 5-lipoxygenase by extracts of leaves, stem bark, phenols and catechols isolated from *Lithraea caustica* (Anacardiaceae). *Frontiers in Pharmacology*, *11*. https://doi.org/10.3389/fphar.2020.594257

Murata, T., Katagiri, T., Osaka, M., Yamauchi, S., Yoshimura, K., Kawada, M., Fujii, Y., Suzuki, Y., & Sasaki, K. (2021). Hyaluronidase and degranulation inhibitors from the edible roots of *Oenanthe javanica* including seric acids F and G that were obtained by heating. *Bioscience, Biotechnology, and Biochemistry*, *85*(2), 369–377. https://doi.org/10.1093/bbb/zbaa042

Ng, C., Rullah, K., Aluwi, M., Abas, F., Lam, K., Ismail, I., Narayanaswamy, R., Jamaludin, F., & Shaari, K. (2014). Synthesis and docking studies of 2,4,6-

trihydroxy-3-geranylacetophenone analogs as potential lipoxygenase inhibitor. *Molecules*, *19*(8), 11645–11659. https://doi.org/10.3390/molecules190811645

Ngai, M. H., & Sirat, H. M. (2004). Synthesis of several bisabolene sesquiterpenoids from xanthorrhizol isolated from *C. xanthorrhiza* and their bioactivities. *4th Annual National Science Fellowship Seminar*, *24*, 181–186.

Ngai, M. H., & Sirat, H. M. (2005). Synthesis of several bisabolane type sesquiterpenoids from xanthorrhizol. *Malaysian Journal of Chemistry*, *24*(1), 177–182.

Nguyen, H. T., Vu, T. Y., Chandi, V., Polimati, H., & Tatipamula, V. B. (2020). Dual COX and 5-LOX inhibition by clerodane diterpenes from seeds of Polyalthia longifolia (Sonn.) Thwaites. *Scientific Reports 2020 10:1*, *10*(1), 1–10. https://doi.org/10.1038/s41598-020-72840-8

Novartis. (2021, October 29). *FDA approves Novartis Scemblix® (asciminib), with novel mechanism of action for the treatment of chronic myeloid leukemia | Novartis*. https://www.novartis.com/news/media-releases/fda-approves-novartis-scemblix-asciminib-novel-mechanism-action-treatment-chronic-myeloid-leukemia

O'Boyle, N. M., Banck, M., James, C. A., Morley, C., Vandermeersch, T., & Hutchison, G. R. (2011). Open Babel: An open chemical toolbox. *Journal of Cheminformatics*, *3*(1), 33. https://doi.org/10.1186/1758-2946-3-33

Oon, S. F., Nallappan, M., Tee, T. T., Shohaimi, S., Kassim, N. K., Sa'ariwijaya, M. S. F., & Cheah, Y. H. (2015). Xanthorrhizol: A review of its pharmacological activities and anticancer properties. *Cancer Cell International*, *15*(1), 1–15. https://doi.org/10.1186/S12935-015-0255-4/TABLES/2

Osakwe, O. (2016). The significance of discovery screening and structure optimization studies. *Social Aspects of Drug Discovery, Development and Commercialization*, 109–128. https://doi.org/10.1016/B978-0-12-802220-7.00005-3

Pavia, D. L., Lampman, G. M., Kriz, G. S., & Vyvyan, J. R. (2015). *Introduction to Spectroscopy* (5th ed.). Cengage Learning.

Pintus, F., Floris, S., Fais, A., Era, B., Kumar, A., Gatto, G., Uriarte, E., & Matos, M. J. (2022). Hydroxy-3-phenylcoumarins as multitarget compounds for skin aging diseases: Synthesis, molecular docking and tyrosinase, elastase, collagenase and hyaluronidase inhibition, and sun protection factor. *Molecules*, *27*(20), 6914. https://doi.org/10.3390/molecules27206914

Pisar, M. M., & Mohd Hashim, S. N. A. (2023). Chapter 4 Bioassays: Antiinflammatory. In N. M. Yunos, M. Mokhtar, M. G. H. Khoo, & M. M. Pisar (Eds.), *A Laboratory Manual On Methods for Bioprospecting On Natural Products* (Vol. 1, pp. 71–89). Institut Penyelidikan Perhutanan Malaysia.

Purnamasari, Y., Hermawati, E., Mujahidin, D., Happyana, N., & Syah, Y. M. (2024). Xanthorrhizol derivatives and their biological properties as caspase-7 inhibitors. *Natural Product Research*, 1–9. https://doi.org/10.1080/14786419.2024.2302919

Qin, Y., Li, G., Wang, L., Yin, G., Zhang, X., Wang, H., Zheng, P., Hua, W., Cheng, Y., Zhao, Y., & Zhang, J. (2024). Modular preparation of biphenyl triazoles via click chemistry as non-competitive hyaluronidase inhibitors. *Bioorganic Chemistry*, *146*, 107291. https://doi.org/10.1016/j.bioorg.2024.107291

Qing, X., Wang, S., Yuan, Y., Pei, J., & Lai, L. (2021). *Multiple Target Drug Design Using LigBuilder 3* (pp. 279–298). https://doi.org/10.1007/978-1-0716-1209-5_16

Rachman, M., Piticchio, S., Majewski, M., & Barril, X. (2021). Fragment-to-lead tailored *in silico* design. *Drug Discovery Today: Technologies*, *40*, 44–57. https://doi.org/10.1016/j.ddtec.2021.08.005

Rahayu, M. D., Kusumaningrum, S., & Hayun, H. (2020). Synthesis of acetyl and benzoyl esters of xanthorrhizol and its oxidation products and evaluation of their inhibitory activity against nitric oxide production. *International Journal of Applied Pharmaceutics*, *12*(Special Issue 1), 135–138. https://doi.org/10.22159/IJAP.2020.V12S1.FF030

Rajalakshmi, R., Lalitha, P., Sharma, S. C., Rajiv, A., Chithambharan, A., & Ponnusamy, A. (2021). *In silico* studies: Physicochemical properties, drug score, toxicity predictions and molecular docking of organosulphur compounds against *Diabetes mellitus*. *Journal of Molecular Recognition*, *34*(11). https://doi.org/10.1002/jmr.2925

Ramírez, D., & Caballero, J. (2016). Is it reliable to use common molecular docking methods for comparing the binding affinities of enantiomer pairs for their protein target? *International Journal of Molecular Sciences*, *17*(4), 525. https://doi.org/10.3390/ijms17040525

Rashid, H. ur, Ahmad, N., Abdalla, M., Khan, K., Martines, M. A. U., & Shabana, S. (2022). Molecular docking and dynamic simulations of Cefixime, Etoposide and Nebrodenside A against the pathogenic proteins of SARS-CoV-2. *Journal of Molecular Structure*, *1247*, 131296. https://doi.org/10.1016/j.molstruc.2021.131296

Riziotis, I. G., Ribeiro, A. J. M., Borkakoti, N., & Thornton, J. M. (2022). Conformational variation in enzyme catalysis: A structural study on catalytic residues. *Journal of Molecular Biology*, *434*(7), 167517. https://doi.org/10.1016/j.jmb.2022.167517

Rossi, A., Pergola, C., Koeberle, A., Hoffmann, M., Dehm, F., Bramanti, P., Cuzzocrea, S., Werz, O., & Sautebin, L. (2010). The 5-lipoxygenase inhibitor, zileuton, suppresses prostaglandin biosynthesis by inhibition of arachidonic acid release in macrophages. *British Journal of Pharmacology*, *161*(3), 555. https://doi.org/10.1111/J.1476-5381.2010.00930.X

Santos, L. H. S., Ferreira, R. S., & Caffarena, E. R. (2019). *Integrating Molecular Docking and Molecular Dynamics Simulations* (pp. 13–34). https://doi.org/10.1007/978-1-4939-9752-7_2

Sardar, A., Abid, O.-R., Daud, S., Fakhar-e-Alam, M., Siddique, M. H., Ashraf, M., Shahid, W., Ejaz, S. A., Atif, M., Ahmad, S., Shafeeq, S., & Afzal, M. (2022). Design, synthesis, *in vitro* and *in silico* studies of naproxen derivatives as dual lipoxygenase and α-glucosidase inhibitors. *Journal of Saudi Chemical Society*, *26*(3), 101468. https://doi.org/10.1016/j.jscs.2022.101468

Sardar, A., Abid, O.-R., Daud, S., Shah, B. A., Shahid, W., Ashraf, M., Fatima, M., Ezzine, S., Wadood, A., Shareef, A., Al-Ghulikah, H. A., & Alissa, S. A. (2022). Identification of novel diclofenac acid and naproxen bearing hydrazones as 15-LOX inhibitors: Design, synthesis, in vitro evaluation, cytotoxicity, and in silico studies. *Arabian Journal of Chemistry*, *15*(12), 104300. https://doi.org/10.1016/j.arabjc.2022.104300

Schoepfer, J., Jahnke, W., Berellini, G., Buonamici, S., Cotesta, S., Cowan-Jacob, S. W., Dodd, S., Drueckes, P., Fabbro, D., Gabriel, T., Groell, J. M., Grotzfeld, R. M., Hassan, A. Q., Henry, C., Iyer, V., Jones, D., Lombardo, F., Loo, A., Manley, P. W., … Furet, P. (2018). Discovery of Asciminib (ABL001), an allosteric inhibitor of the tyrosine kinase activity of BCR-ABL1. *Journal of Medicinal Chemistry*, *61*(18), 8120–8135. https://doi.org/10.1021/acs.jmedchem.8b01040

Sheng, C., Dong, G., & Wang, C. (2015). *Computational Fragment-Based Drug Design* (pp. 189–215). https://doi.org/10.1007/7653_2015_51

Sirat, H. M., Hong, N. M., & Jauri, M. H. (2007). Chemistry of xanthorrhizol: synthesis of several bisabolane sesquiterpenoids from xanthorrhizol. *Tetrahedron Letters*, *48*(3), 457–460. https://doi.org/10.1016/j.tetlet.2006.11.051

Skrzypczak-Jankun, E., Bross, R. A., Carroll, R. T., Dunham, W. R., & Funk, M. O. (2001). Three-dimensional structure of a purple lipoxygenase. *Journal of the American Chemical Society*, *123*(44), 10814–10820. https://doi.org/10.1021/ja011759t

Sliwoski, G., Kothiwale, S., Meiler, J., & Lowe, E. W. (2014). Computational methods in drug discovery. *Pharmacological Reviews*, *66*(1), 334. https://doi.org/10.1124/PR.112.007336

Sneha, P., & George Priya Doss, C. (2016). *Molecular Dynamics* (pp. 181–224). https://doi.org/10.1016/bs.apcsb.2015.09.004

Sun, D., Gao, W., Hu, H., & Zhou, S. (2022). Why 90% of clinical drug development fails and how to improve it? *Acta Pharmaceutica Sinica B*, *12*(7), 3049–3062. https://doi.org/10.1016/j.apsb.2022.02.002

Sun, W., Liu, M., Li, Y., Hu, X., Chen, G., & Zhang, F. (2023). Xanthorrhizol inhibits mitochondrial damage, oxidative stress and inflammation in LPS-induced MLE-12 cells by regulating MAPK pathway. *Tissue and Cell*, *84*, 102170. https://doi.org/10.1016/j.tice.2023.102170

Tain, Y.-L., Jheng, L.-C., Chang, S. K. C., Chen, Y.-W., Huang, L.-T., Liao, J.-X., & Hou, C.-Y. (2020). Synthesis and characterization of novel resveratrol butyrate

esters that have the ability to prevent fat accumulation in a liver cell culture Model. *Molecules*, *25*(18), 4199. https://doi.org/10.3390/molecules25184199

Tian, W., Jiang, X., Kim, D., Guan, T., Nicolls, M. R., & Rockson, S. G. (2020). Leukotrienes in tumor-associated inflammation. *Frontiers in Pharmacology*, *11*. https://doi.org/10.3389/fphar.2020.01289

Tian, Z.-Y., Du, G.-J., Xie, S.-Q., Zhao, J., Gao, W.-Y., & Wang, C.-J. (2007). Synthesis and bioevaluation of 5-fluorouracil derivatives. *Molecules*, *12*(11), 2450–2457. https://doi.org/10.3390/12112450

Tiwari, A., & Singh, S. (2022). Computational approaches in drug designing. In *Bioinformatics* (pp. 207–217). Elsevier. https://doi.org/10.1016/B978-0-323-89775-4.00010-9

Torres, P. H. M., Sodero, A. C. R., Jofily, P., & Silva-Jr, F. P. (2019). Key Topics in Molecular Docking for Drug Design. *International Journal of Molecular Sciences*, *20*(18). https://doi.org/10.3390/IJMS20184574

Trott, O., & Olson, A. J. (2010). AutoDock Vina: Improving the speed and accuracy of docking with a new scoring function, efficient optimization, and multithreading. *Journal of Computational Chemistry*, *31*(2), 455–461. https://doi.org/10.1002/jcc.21334

Tsaioun, K., Bottlaender, M., & Mabondzo, A. (2009). ADDME – Avoiding Drug Development Mistakes Early: central nervous system drug discovery perspective. *BMC Neurology*, *9*(Suppl 1), S1. https://doi.org/10.1186/1471-2377-9-S1-S1

Tsakos, M., Schaffert, E. S., Clement, L. L., Villadsen, N. L., & Poulsen, T. B. (2015). Ester coupling reactions – an enduring challenge in the chemical synthesis of bioactive natural products. *Natural Product Reports*, *32*(4), 605–632. https://doi.org/10.1039/C4NP00106K

Usha, T., Shanmugarajan, D., Goyal, A. K., Kumar, C. S., & Middha, S. K. (2017). Recent updates on computer-aided drug discovery: Time for a paradigm shift. *Current Topics in Medicinal Chemistry*, *17*(30), 3296–3307. https://doi.org/10.2174/1568026618666180101163651

Veber, D. F., Johnson, S. R., Cheng, H.-Y., Smith, B. R., Ward, K. W., & Kopple, K. D. (2002). Molecular properties that influence the oral bioavailability of drug candidates. *Journal of Medicinal Chemistry*, *45*(12), 2615–2623. https://doi.org/10.1021/jm020017n

Villemagne, B., Faïon, L., Tangara, S., & Willand, N. (2023). Recent advances in Fragment-based strategies against tuberculosis. *European Journal of Medicinal Chemistry*, *258*, 115569. https://doi.org/10.1016/j.ejmech.2023.115569

Vo, N. N. Q., Nomura, Y., Muranaka, T., & Fukushima, E. O. (2019). Structure-activity relationships of pentacyclic triterpenoids as inhibitors of cyclooxygenase and lipoxygenase enzymes. *Journal of Natural Products*, *82*(12), 3311–3320. https://doi.org/10.1021/acs.jnatprod.9b00538

Wang, R., Gao, Y., & Lai, L. (2000). LigBuilder: A multi-purpose program for structure-based drug design. *Journal of Molecular Modeling*, *6*(7–8), 498–516. https://doi.org/10.1007/s0089400060498

Wang, S., König, G., Roth, H.-J., Fouché, M., Rodde, S., & Riniker, S. (2021). Effect of flexibility, lipophilicity, and the location of polar residues on the passive membrane permeability of a series of cyclic decapeptides. *Journal of Medicinal Chemistry*, *64*(17), 12761–12773. https://doi.org/10.1021/acs.jmedchem.1c00775

Wisastra, R., & Dekker, F. J. (2014). Inflammation, cancer and oxidative lipoxygenase activity are intimately linked. *Cancers*, *6*(3), 1500. https://doi.org/10.3390/CANCERS6031500

Wróbel-Biedrawa, D., Grabowska, K., Galanty, A., Sobolewska, D., Żmudzki, P., & Podolak, I. (2020). Anti-melanoma potential of two benzoquinone homologues embelin and rapanone - a comparative in vitro study. *Toxicology in Vitro*, *65*, 104826. https://doi.org/10.1016/j.tiv.2020.104826

Wu, F., Zhou, Y., Li, L., Shen, X., Chen, G., Wang, X., Liang, X., Tan, M., & Huang, Z. (2020). Computational approaches in preclinical studies on drug discovery and development. *Frontiers in Chemistry*, *8*. https://doi.org/10.3389/fchem.2020.00726

Xu, Y., Liang, X., & Hyun, C.-G. (2024). Isolation, characterization, genome annotation, and evaluation of hyaluronidase inhibitory activity in secondary metabolites of Brevibacillus sp. JNUCC 41: A comprehensive analysis through molecular docking and molecular dynamics simulation. *International Journal of Molecular Sciences*, *25*(9), 4611. https://doi.org/10.3390/ijms25094611

Xu, Y., Wang, S., Hu, Q., Gao, S., Ma, X., Zhang, W., Shen, Y., Chen, F., Lai, L., & Pei, J. (2018). CavityPlus: a web server for protein cavity detection with pharmacophore modelling, allosteric site identification and covalent ligand binding ability prediction. *Nucleic Acids Research*, *46*(Web Server issue), W374. https://doi.org/10.1093/NAR/GKY380

Yamaguchi, S., Kaneko, M., & Narukawa, M. (2021). Approval success rates of drug candidates based on target, action, modality, application, and their combinations. *Clinical and Translational Science*, *14*(3), 1113–1122. https://doi.org/10.1111/CTS.12980

Yang, C., Chen, E. A., & Zhang, Y. (2022). Protein–Ligand Docking in the Machine-Learning Era. *Molecules*, *27*(14), 4568. https://doi.org/10.3390/molecules27144568

Yu, W., & Mackerell, A. D. (2017). Computer-aided drug design methods. *Methods in Molecular Biology (Clifton, N.J.)*, *1520*, 85. https://doi.org/10.1007/978-1-4939-6634-9_5

Yu, W., Xiao, H., Lin, J., & Li, C. (2013). Discovery of novel STAT3 small molecule inhibitors via in silico site-directed fragment-based drug design. *Journal of Medicinal Chemistry*, *56*(11), 4402–4412. https://doi.org/10.1021/JM400080C

Yuan, Y., Pei, J., & Lai, L. (2011). LigBuilder 2: A practical *de novo* drug design approach. *Journal of Chemical Information and Modeling*, *51*(5), 1083–1091. https://doi.org/10.1021/ci100350u

Žádníková, P., Šínová, R., Pavlík, V., Šimek, M., Šafránková, B., Hermannová, M., Nešporová, K., & Velebný, V. (2022). The degradation of hyaluronan in the skin. *Biomolecules*, *12*(2), 251. https://doi.org/10.3390/biom12020251

Zhang, C., Ibrahim, P. N., Zhang, J., Burton, E. A., Habets, G., Zhang, Y., Powell, B., West, B. L., Matusow, B., Tsang, G., Shellooe, R., Carias, H., Nguyen, H., Marimuthu, A., Zhang, K. Y. J., Oh, A., Bremer, R., Hurt, C. R., Artis, D. R., … Bollag, G. (2013). Design and pharmacology of a highly specific dual FMS and KIT kinase inhibitor. *Proceedings of the National Academy of Sciences*, *110*(14), 5689–5694. https://doi.org/10.1073/pnas.1219457110

Zhang, L., Bharadwaj, A. G., Casper, A., Barkley, J., Barycki, J. J., & Simpson, M. A. (2009). Hyaluronidase activity of human Hyal1 requires active site acidic and tyrosine residues. *The Journal of Biological Chemistry*, *284*(14), 9433. https://doi.org/10.1074/JBC.M900210200

Zhang, W., Yuan, Y., Pei, J., & Lai, L. (2015). *CAVITY: Mapping the Druggable Binding Site*. 111–132. https://doi.org/10.1007/7653_2015_45

Zhou, M., Li, Y., Hou, H., Zou, W., Hu, L., Gong, L., Fan, W., Wang, R., Ibrahim, I. A. A., & Fan, S. (2022). Xanthorrhizol ameliorates oxidative stress and inflammation in freund's complete adjuvant-induced rheumatoid arthritis in rats. *Applied Biochemistry and Biotechnology*, *194*(12), 6423–6437. https://doi.org/10.1007/s12010-022-04091-4

APPENDICES

Appendix A: Molecular docking result of top fifty XNT derivatives as Hyal-1 inhibitors

Derivatives	SMILES notation	Binding energies (kcal/mol)
H013	NC1NC[C@@H](N1)COc1cc(ccc1C)[C@@H](CCC=C(C)C)C	-8.5
H515	OC[C@H]1OC[C@@H](N1)COc1cc(ccc1C)[C@@H](CCC=C(C)C)C	-8.5
H552	CC(=CCC[C@H](c1ccc(c(c1)OC[C@@H]1CNC[C@H]1C(=O)O)C)C)C	-8.5
H120	OC[C@H](C(=O)CCOc1cc(ccc1C)[C@@H](CCC=C(C)C)C)N	-8.3
H885	O=C1C[C@H]([C@@H](C1)COc1cc(ccc1C)[C@@H](CCC=C(C)C)C)O	-8.3
H207	O[C@H]1CC[C@@H](C1)COc1cc(ccc1C)[C@@H](CCC=C(C)C)C	-8.2
H507	OC[C@@H]1CNC[C@H]1COc1cc(ccc1C)[C@@H](CCC=C(C)C)C	-8.2
H730	NC[C@@H]1C=C[C@@H](C1)COc1cc(ccc1C)[C@@H](CCC=C(C)C)C	-8.2
H844	OC(=O)C/C=C\COc1cc(ccc1C)[C@@H](CCC=C(C)C)C	-8.2
H910	OC[C@@H]1NC[C@@H](OC1)COc1cc(ccc1C)[C@@H](CCC=C(C)C)C	-8.2
H938	O[C@H](CC(=O)N)CCOc1cc(ccc1C)[C@@H](CCC=C(C)C)C	-8.2
H983	CC(=CCC[C@H](c1ccc(c(c1)OCCCN=C(N)N)C)C)C	-8.2
H132	CC(=CCC[C@H](c1ccc(c(c1)OC[C@H]1NC[C@@H](C1)[NH3+])C)C)C	-8.1
H343	CC(=CCC[C@H](c1ccc(c(c1)OCC[C@H](c1nonc1)O)C)C)C	-8.1
H596	C=C[C@@H]1C=C[C@@H](C1)COc1cc(ccc1C)[C@@H](CCC=C(C)C)C	-8.1
H842	NC(=O)C/C=C\COc1cc(ccc1C)[C@@H](CCC=C(C)C)C	-8.1
H966	CC(=CCC[C@H](c1ccc(c(c1)OC[C@@H]1C[NH2+]C[C@H]1Cl)C)C)C	-8.1
H026	CC(=CCC[C@H](c1ccc(c(c1)OCC1C=CC=C1)C)C)C	-8.0
H242	F[C@@H]1C[NH2+][C@@H](C1)COc1cc(ccc1C)[C@@H](CCC=C(C)C)C	-8.0

H335	OC[C@@H]1C[NH2+]C[C@H]1COc1cc(ccc1C)[C@@H](CCC=C(C)C)C	-8.0
H486	O[C@H]1C[NH2+][C@@H](C1)COc1cc(ccc1C)[C@@H](CCC=C(C)C)C	-8.0
H571	NC(C/C=C\COc1cc(ccc1C)[C@@H](CCC=C(C)C)C)N	-8.0
H732	OC[C@H](/C=C\COc1cc(ccc1C)[C@@H](CCC=C(C)C)C)O	-8.0
H758	OC[C@@H]1CC[C@@H](O1)COc1cc(ccc1C)[C@@H](CCC=C(C)C)C	-8.0
H824	CC(=CCC[C@H](c1ccc(c(c1)OCCCc1ccno1)C)C)C	-8.0
H988	NC(=O)NCCCOc1cc(ccc1C)[C@@H](CCC=C(C)C)C	-8.0
H091	OC[C@@H]1CCC[C@H]1COc1cc(ccc1C)[C@@H](CCC=C(C)C)C	-7.9
H125	CC(=CCC[C@H](c1ccc(c(c1)OC[C@@H]1CCC[C@H]1O)C)C)C	-7.9
H131	F[C@@H]1CN[C@@H](C1)COc1cc(ccc1C)[C@@H](CCC=C(C)C)C	-7.9
H180	CC(=CCC[C@H](c1ccc(c(c1)OC/C=C\C(N)N)C)C)C	-7.9
H210	NC(NCCCOc1cc(ccc1C)[C@@H](CCC=C(C)C)C)N	-7.9
H266	O[C@H]1CN[C@@H](C1)COc1cc(ccc1C)[C@@H](CCC=C(C)C)C	-7.9
H310	NCC/C=C\COc1cc(ccc1C)[C@@H](CCC=C(C)C)C	-7.9
H371	CC(=CCC[C@H](c1ccc(c(c1)OC[C@H]1OC[C@H](C1)C(=O)O)C)C)C	-7.9
H378	CC(=CCC[C@H](c1ccc(c(c1)OC[C@@H]1CNC[C@H]1O)C)C)C	-7.9
H448	OC[C@@H]1OC[C@@H](N1)COc1cc(ccc1C)[C@@H](CCC=C(C)C)C	-7.9
H424	CC(=CCC[C@H](c1ccc(c(c1)OC[C@H]1CC[C@@H](C1)[NH3+])C)C)C	-7.9
H476	CC(=CCC[C@H](c1ccc(c(c1)OC[C@H]1C=C[C@H](C1)F)C)C)C	-7.9
H645	F[C@@H]1CO[C@@H](C1)COc1cc(ccc1C)[C@@H](CCC=C(C)C)C	-7.9
H672	C=C[C@@H]1CO[C@@H](C1)COc1cc(ccc1C)[C@@H](CCC=C(C)C)C	-7.9
H785	CC(=CCC[C@H](c1ccc(c(c1)OC[C@@H]1CNC[C@H]1[NH3+])C)C)C	-7.9
H819	CC(=CCC[C@H](c1ccc(c(c1)OC[C@@H]1COC[C@H]1Br)C)C)C	-7.9
H878	OC(=O)CCOCCOc1cc(ccc1C)[C@@H](CCC=C(C)C)C	-7.9

H908	C=C[C@@H]1CC[C@@H](O1)COc1cc(ccc1C)[C@@H](CCC=C(C)C)C	-7.9
H936	CC(=CCC[C@H](c1ccc(c(c1)OC[C@@H]1CCC[C@H]1[NH3+])C)C)C	-7.9
H187	F[C@H]1CC[C@@H](C1)COc1cc(ccc1C)[C@@H](CCC=C(C)C)C	-7.8
H646	[NH3+]CC1=N[C@H](CO1)COc1cc(ccc1C)[C@@H](CCC=C(C)C)C	-7.8
H780	NCNC/C=C\COc1cc(ccc1C)[C@@H](CCC=C(C)C)C	-7.8
H868	O[C@@H]1CO[C@H](C1)COc1cc(ccc1C)[C@@H](CCC=C(C)C)C	-7.8

Appendix B: Molecular docking results for top fifty derivatives as LOX-3 inhibitors

Derivatives	**SMILES notation**	**Binding energy (kcal/mol)**
L013	C=CCCOc1cc(ccc1C)[C@@H](CCC=C(C)C)C	-9.0
L995	CC[C@H]1C=CC(=C1)C(=O)CCOc1cc(ccc1C)[C@@H](CCC=C(C)C)C	-9.0
L168	C/C=C/CCCOc1cc(ccc1C)[C@@H](CCC=C(C)C)C	-8.9
L408	CC(=CCC[C@H](c1ccc(c(c1)OCCCC[C@H]1CCCN1)C)C)C	-8.9
L634	NC[C@H]1C=CC(=C1)C(=O)CCOc1cc(ccc1C)[C@@H](CCC=C(C)C)C	-8.9
L922	CC(=CCC[C@H](c1ccc(c(c1)OCCCC(=O)c1c[nH]cc1)C)C)C	-8.9
L1000	C#CC[C@@H]([C@@H]1CN1)CCOc1cc(ccc1C)[C@@H](CCC=C(C)C)C	-8.8
L159	C#CCCCCCOc1cc(ccc1C)[C@@H](CCC=C(C)C)C	-8.8
L224	CC(=CCC[C@H](c1ccc(c(c1)OCCOC[C@@H]1CCCC1=O)C)C)C	-8.8
L301	C#CCCCOc1cc(ccc1C)[C@@H](CCC=C(C)C)C	-8.8
L397	CCC/C=C\CCOc1cc(ccc1C)[C@@H](CCC=C(C)C)C	-8.8
L565	CC/C=C/C(=O)CCOc1cc(ccc1C)[C@@H](CCC=C(C)C)C	-8.8
L079	C/C=C/CCCCOc1cc(ccc1C)[C@@H](CCC=C(C)C)C	-8.7
L101	CC(=CCC[C@H](c1ccc(c(c1)OCCC(=O)n1ccccc1)C)C)C	-8.7

L248	NC(=N)NC/C=C\CCOc1cc(ccc1C)[C@@H](CCC=C(C)C)C	-8.7
L298	CC/C=C\CCCOc1cc(ccc1C)[C@@H](CCC=C(C)C)C	-8.7
L363	CC(=CCC[C@H](c1ccc(c(c1)OCCC(=O)C1=CCC=C1)C)C)C	-8.7
L437	CC(=CCC[C@H](c1ccc(c(c1)OCCNC[C@@H]1CCCC1=O)C)C)C	-8.7
L464	CC/C=C/CCCOc1cc(ccc1C)[C@@H](CCC=C(C)C)C	-8.7
L554	C=CCCCCCCOc1cc(ccc1C)[C@@H](CCC=C(C)C)C	-8.7
L694	CC(=CCC[C@H](c1ccc(c(c1)OCCCC(=O)c1n[nH]nn1)C)C)C	-8.7
L889	NC(=O)C/C=C\CCOc1cc(ccc1C)[C@@H](CCC=C(C)C)C	-8.7
L943	CC(=CCC[C@H](c1ccc(c(c1)OCCC(=O)C1=C[C@H](C=C1)F)C)C)C	-8.7
L992	C#CC[C@H](OC(=O)CO)CCOc1cc(ccc1C)[C@@H](CCC=C(C)C)C	-8.7
L056	CC(=CCC[C@H](c1ccc(c(c1)OCCc1cccc(n1)N)C)C)C	-8.6
L102	CC(=CCC[C@H](c1ccc(c(c1)OCCC(=O)C1=CCNN1)C)C)C	-8.6
L1041	OC(=O)C[C@H](/C=C\COc1cc(ccc1C)[C@@H](CCC=C(C)C)C)F	-8.6
L166	CC(=CCC[C@H](c1ccc(c(c1)OCC[C@@H](C[C@H]1CCC[NH2+]1)[NH3+])C)C)C	-8.6
L167	CNC(=O)CNC(=O)CCOc1cc(ccc1C)[C@@H](CCC=C(C)C)C	-8.6
L271	C[C@@H](c1ccc(c(c1)OCCC(=O)OCC#C)C)CCC=C(C)C	-8.6
L321	CC(=CCC[C@H](c1ccc(c(c1)OCCC(=O)c1ccc[nH]1)C)C)C	-8.6
L364	C#CC(=O)CCOc1cc(ccc1C)[C@@H](CCC=C(C)C)C	-8.6
L367	C=CCCCCCOc1cc(ccc1C)[C@@H](CCC=C(C)C)C	-8.6
L509	C/C=C\COC(=O)CCOc1cc(ccc1C)[C@@H](CCC=C(C)C)C	-8.6
L544	C[NH2+][C@H]1C=CC(=C1)C(=O)CCOc1cc(ccc1C)[C@@H](CCC=C(C)C)C	-8.6
L588	OC[C@H]1C=CC(=C1)C(=O)CCOc1cc(ccc1C)[C@@H](CCC=C(C)C)C	-8.6
L631	C#CC[C@@H](C(=O)N)CCOc1cc(ccc1C)[C@@H](CCC=C(C)C)C	-8.6
L636	CC(=CCC[C@H](c1ccc(c(c1)OC/C=C\CCC[C@@H]1CN1)C)C)C	-8.6

L676	CC(=CCC[C@H](c1ccc(c(c1)OCCOC[C@@H]1C=CC[C@H]1F)C)C)C	-8.6
L708	CN[C@H]1C=CC(=C1)C(=O)CCOc1cc(ccc1C)[C@@H](CCC=C(C)C)C	-8.6
L725	C=C[C@@H]([C@H]1C=CCC1)OCCOc1cc(ccc1C)[C@@H](CCC=C(C)C)C	-8.6
L823	CC(=CCC[C@H](c1ccc(c(c1)OCCC(=O)C1=C[C@H](C=C1)O)C)C)C	-8.6
L827	CCCCCCCOc1cc(ccc1C)[C@@H](CCC=C(C)C)C	-8.6
L843	C=C[C@H](CNC(=O)N)CCOc1cc(ccc1C)[C@@H](CCC=C(C)C)C	-8.6
L971	CCCC(=O)CCCOc1cc(ccc1C)[C@@H](CCC=C(C)C)C	-8.6
L001	CC(=CCC[C@H](c1ccc(c(c1)OCc1ccccc1)C)C)C	-8.5
L294	CCCC/C=C\COc1cc(ccc1C)[C@@H](CCC=C(C)C)C	-8.5
L637	CC/C=C\CCOc1cc(ccc1C)[C@@H](CCC=C(C)C)C	-8.5
L674	CC(=CCC[C@H](c1ccc(c(c1)OCCOC[C@@H]1C=CC[C@H]1F)C)C)C	-8.5
L963	CC(=CCC[C@H](c1ccc(c(c1)OCC/C=C/CC(=O)C)C)C)C	-8.5
L997	CC(=CCC[C@H](c1ccc(c(c1)OCCOC[C@@H]1C=CC[C@H]1[NH3+])C)C)C	-8.5

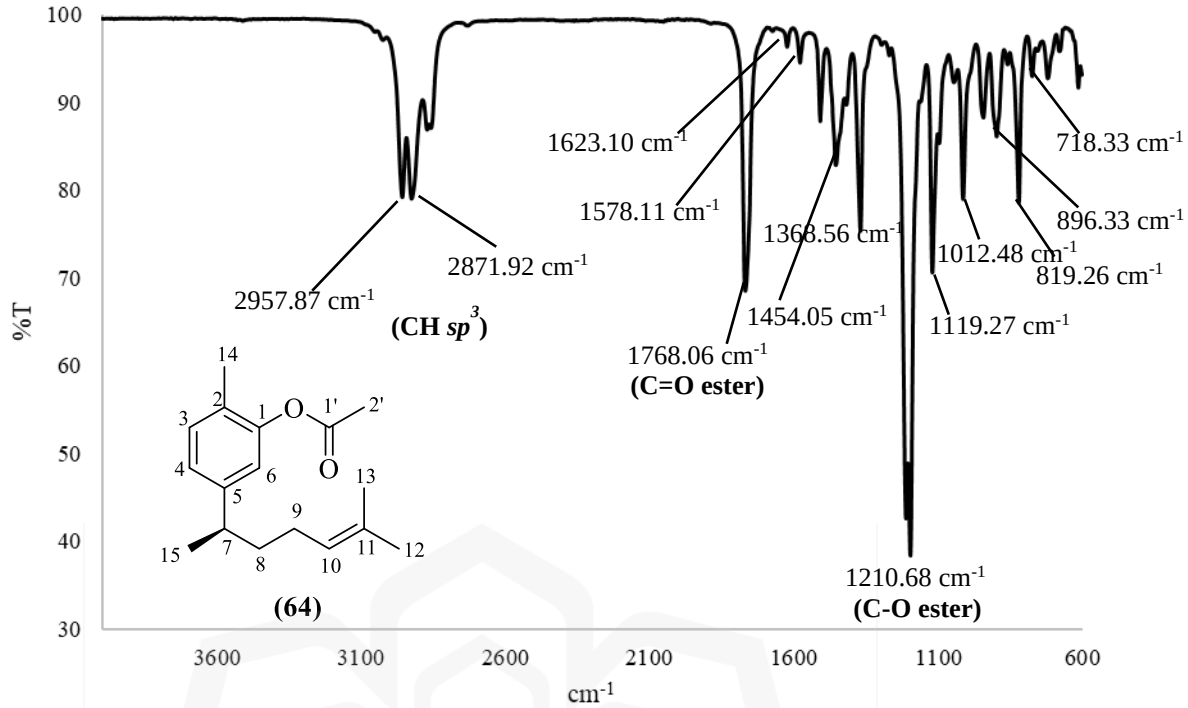

Appendix C1: ATR-IR spectrum of xanthorrhizyl acetate **(64)**

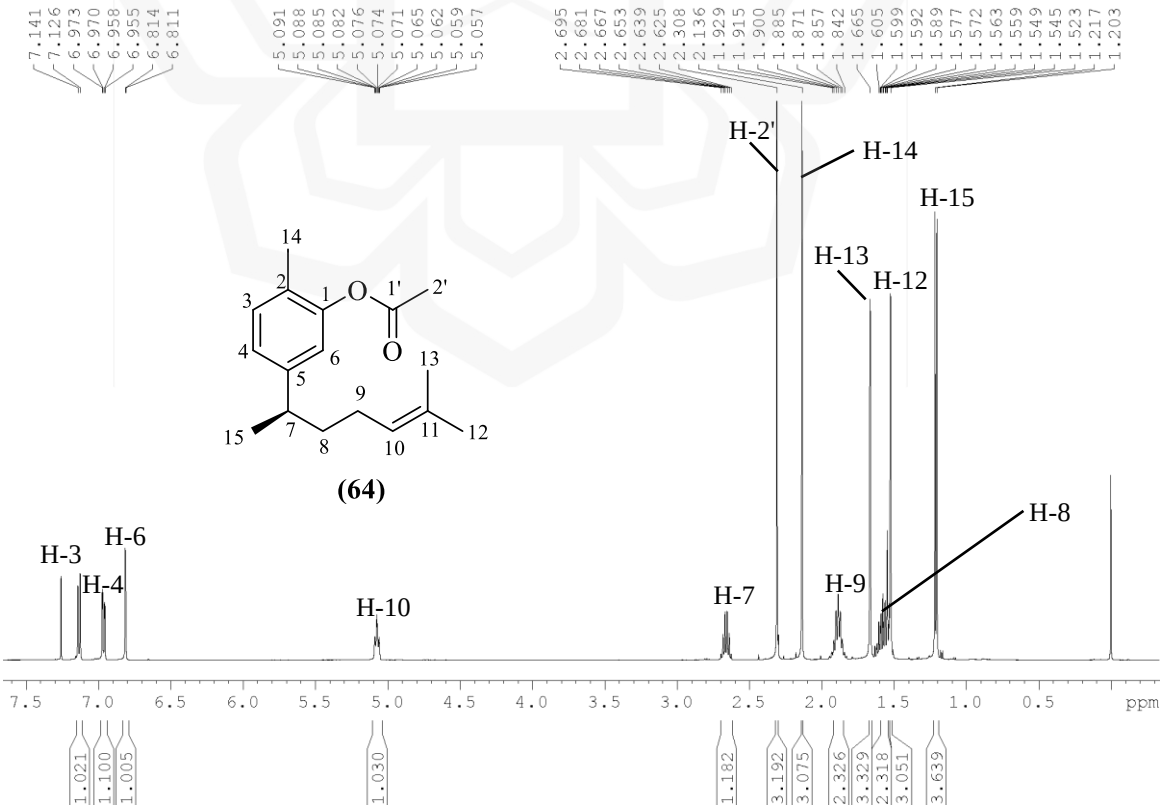

Appendix C2: ^{1}H NMR spectrum of xanthorrhizyl acetate **(64)**

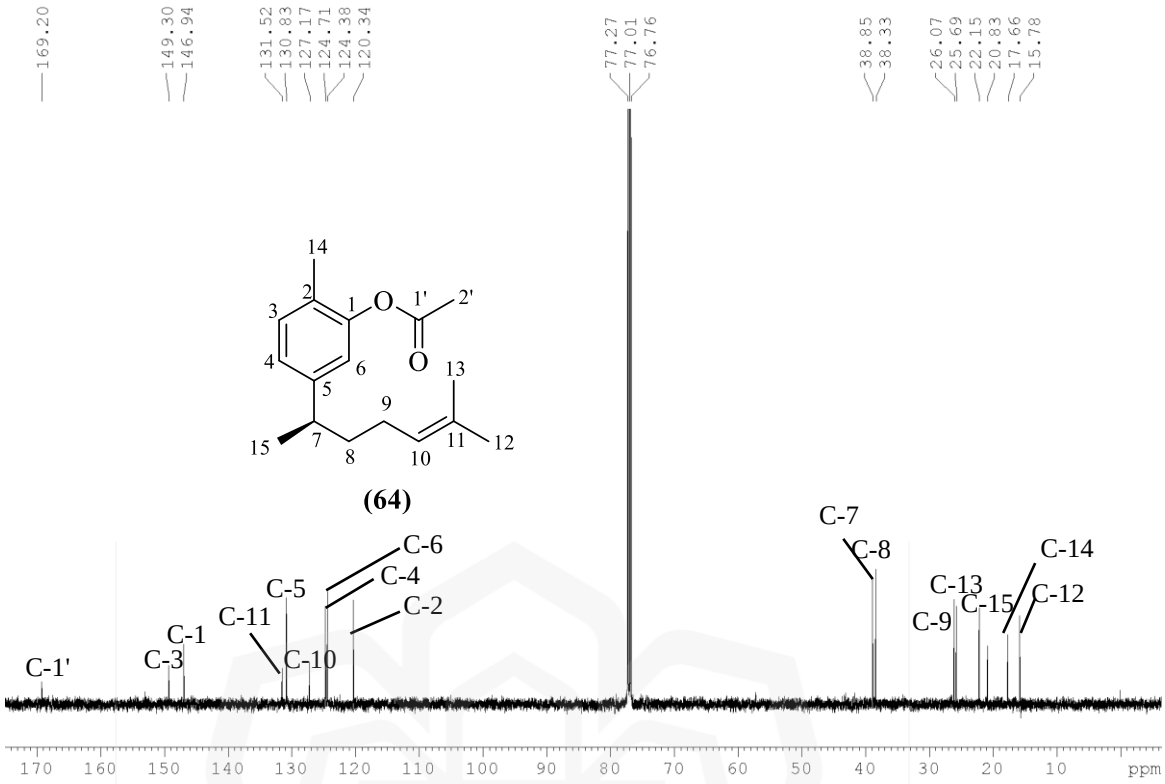

Appendix C3: ^{13}C NMR spectrum of xanthorrhizyl acetate **(64)**

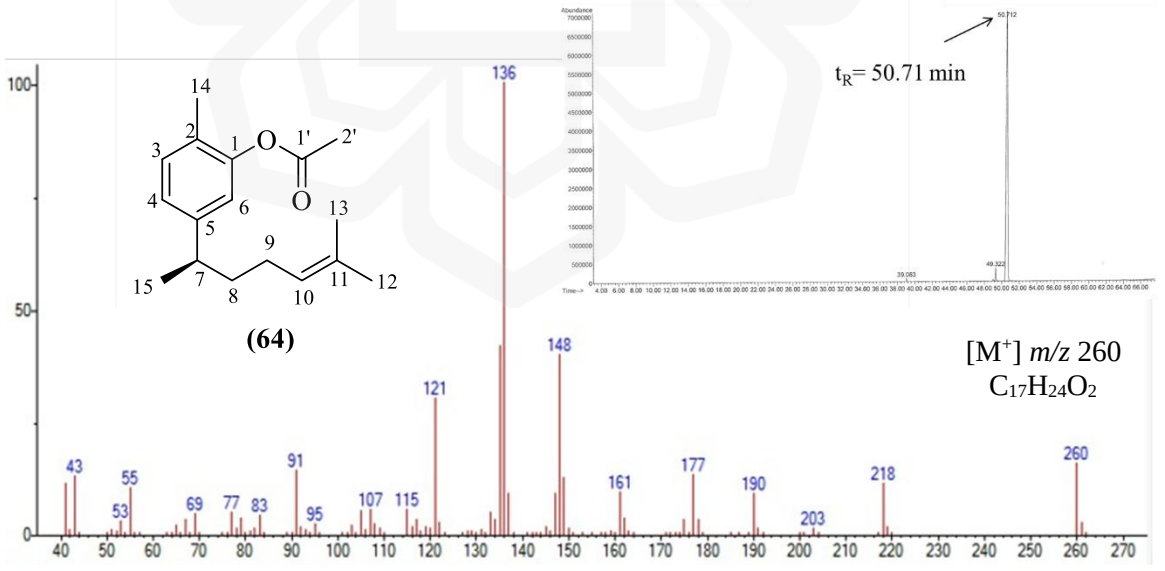

Appendix C4: GC-MS spectrum of xanthorrhizyl acetate **(64)**

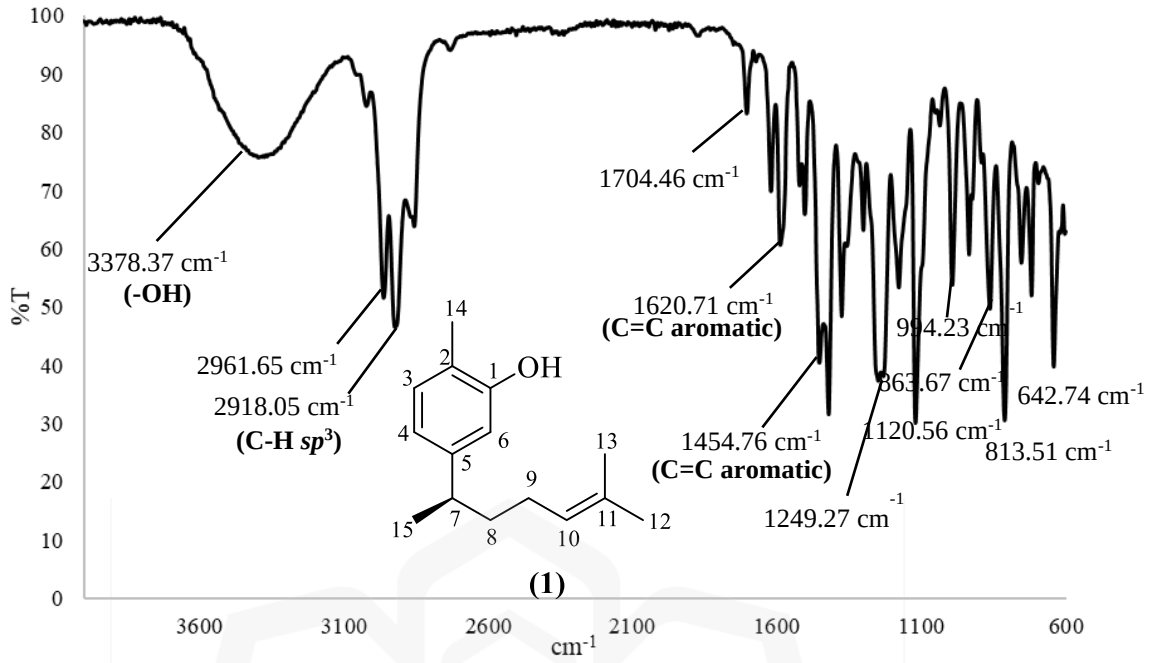

Appendix D1: ATR-IR spectrum of XNT **(1)**

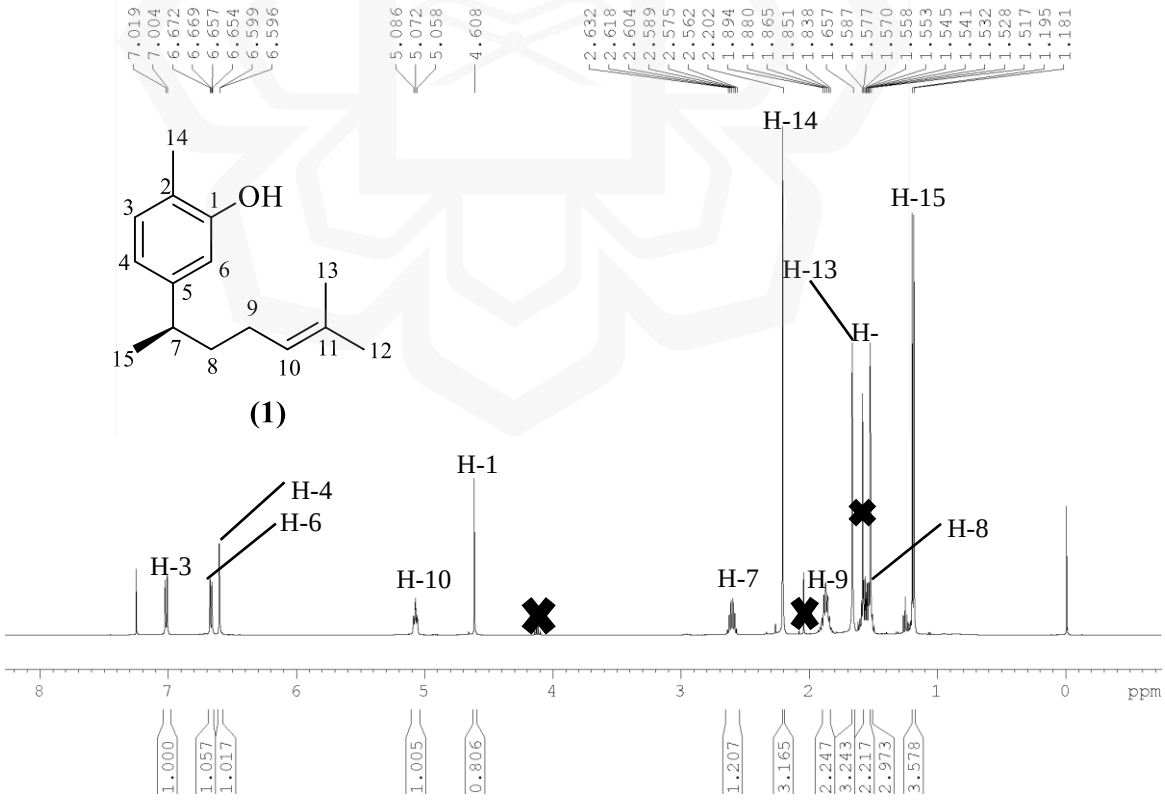

Appendix D2: ^{1}H NMR spectrum of XNT **(1)**

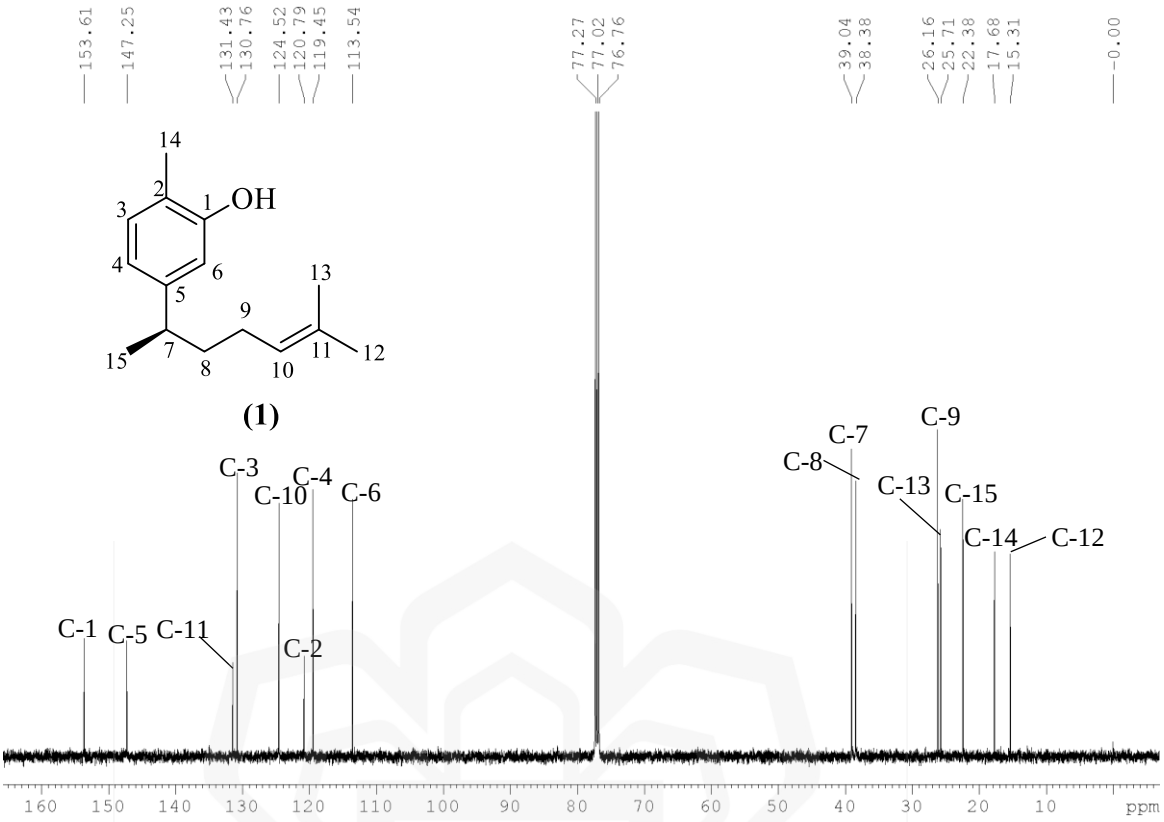

Appendix D3: ^{13}C NMR spectrum of XNT **(1)**

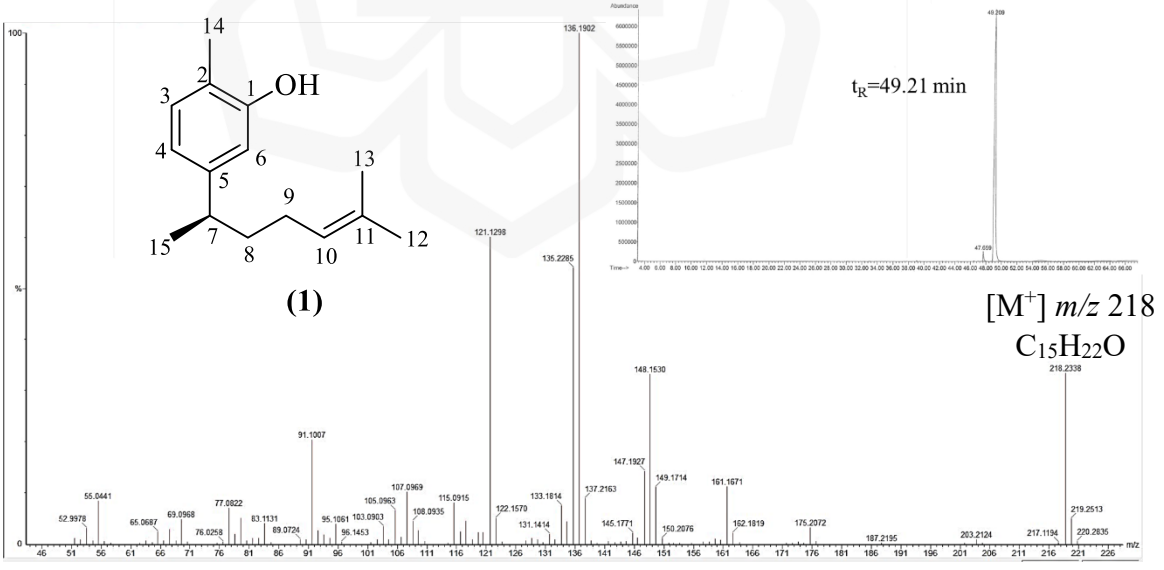

Appendix D4: GC-MS spectrum of XNT **(1)**

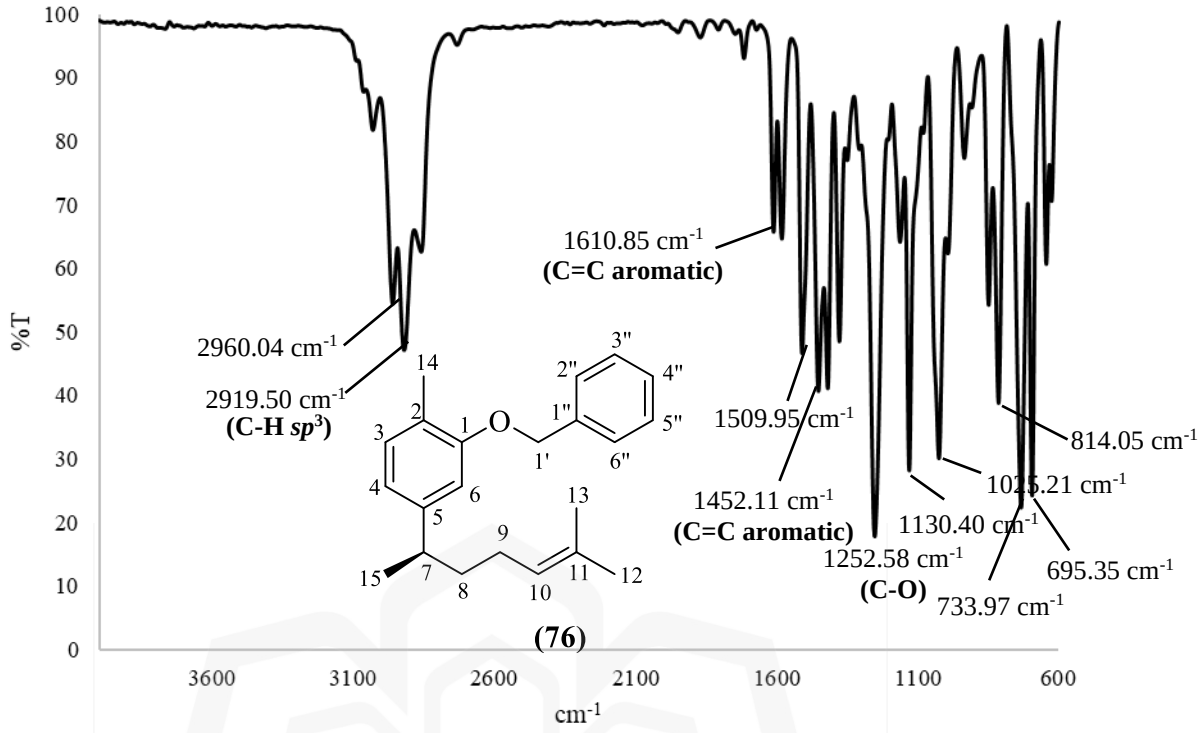

Appendix E1: ATR-IR spectrum of benzyl xanthorrhizyl ether **(76)**

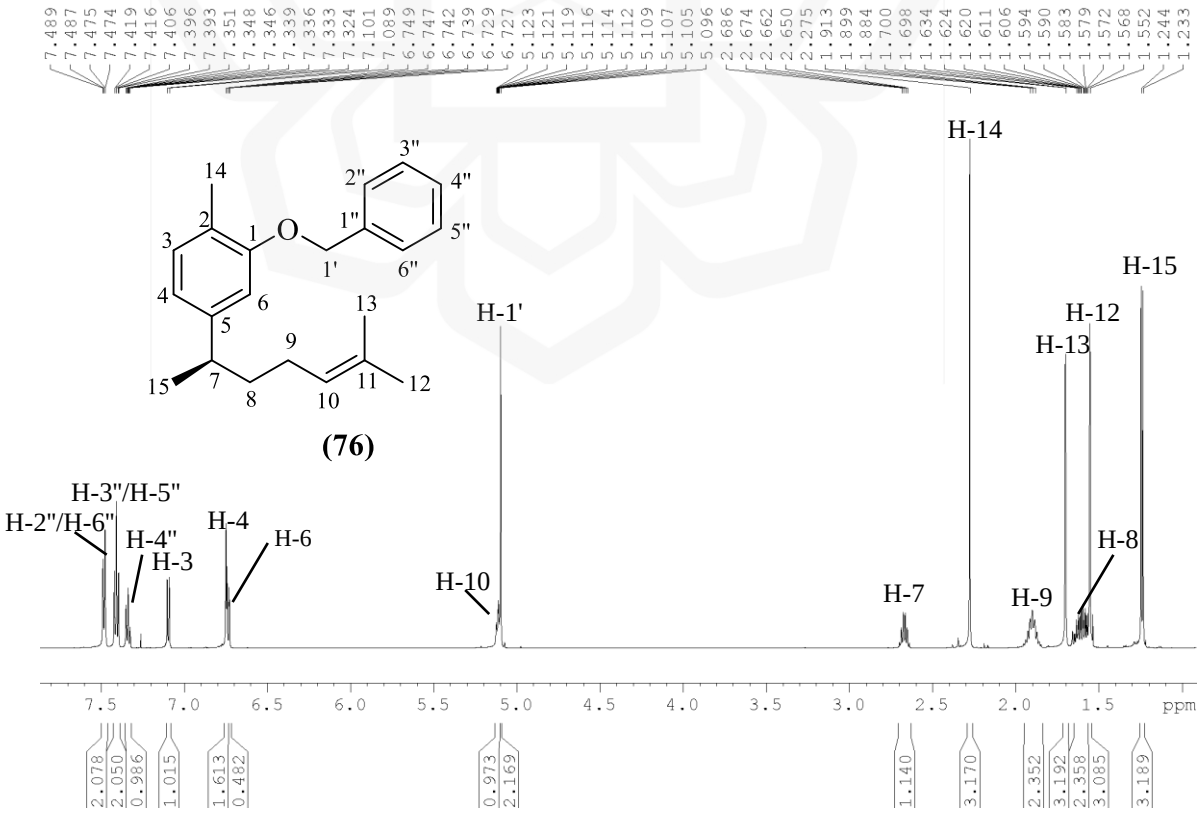

Appendix E2: ^{1}H NMR spectrum of benzyl xanthorrhizyl ether **(76)**

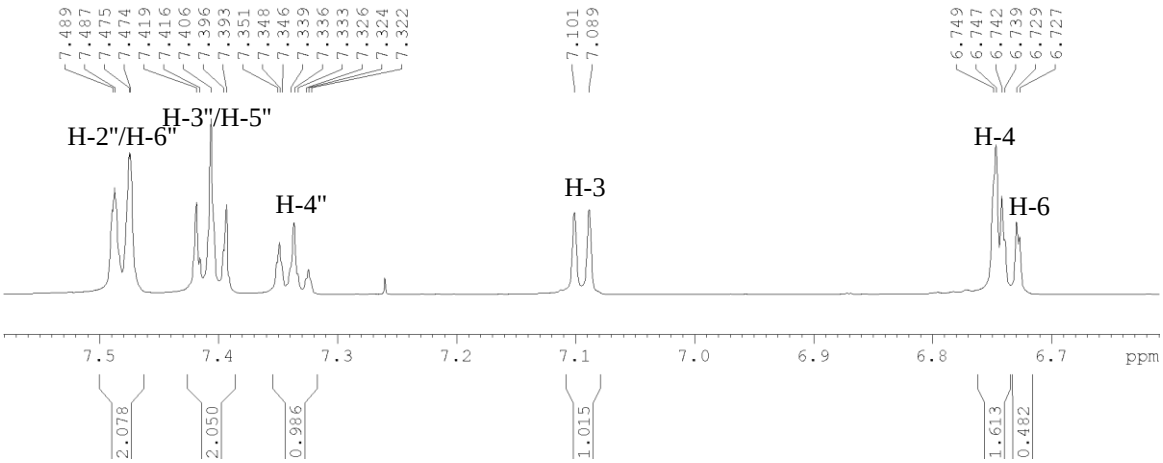

Appendix E3: ^{1}H NMR spectrum of benzyl xanthorrhizyl ether **(76)** (expansion)

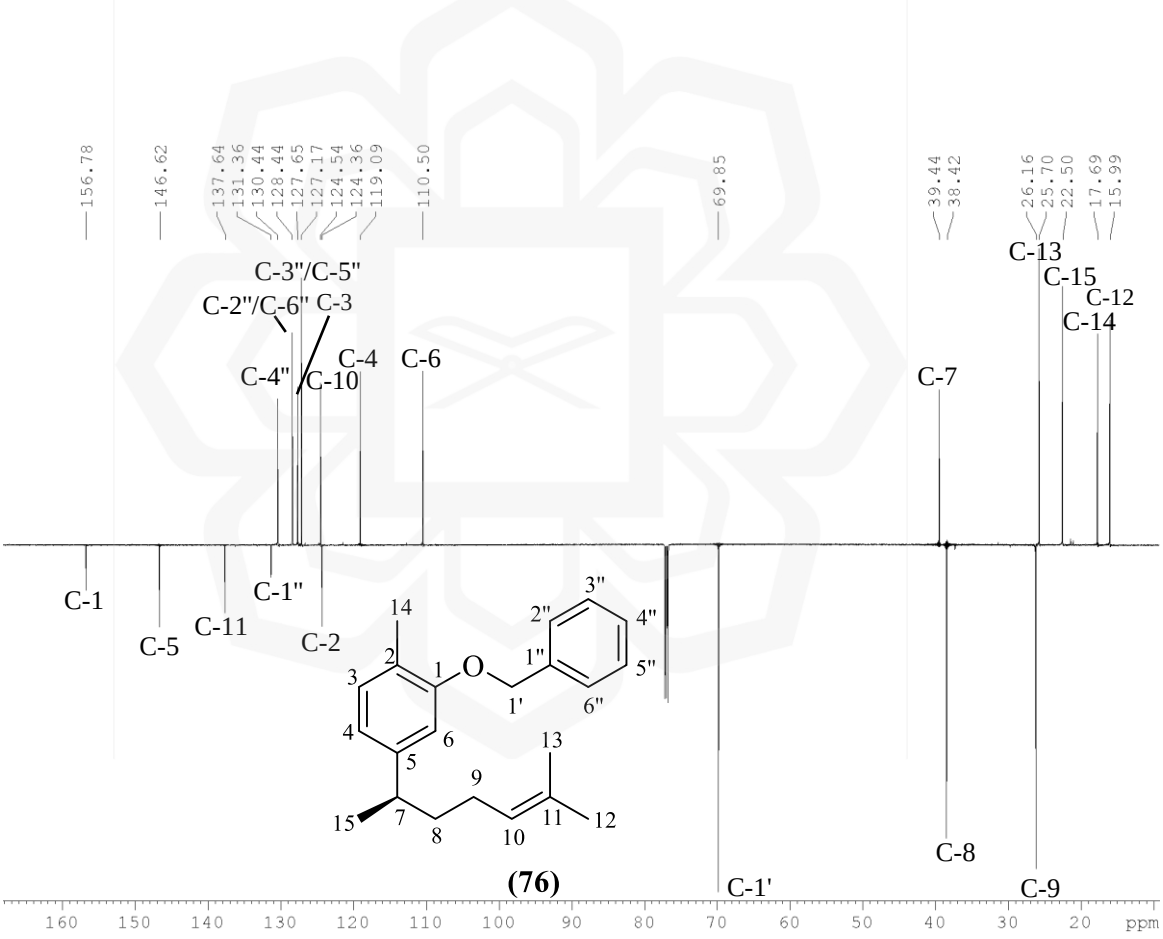

Appendix E4: DEPTQ spectrum of benzyl xanthorrhizyl ether **(76)**

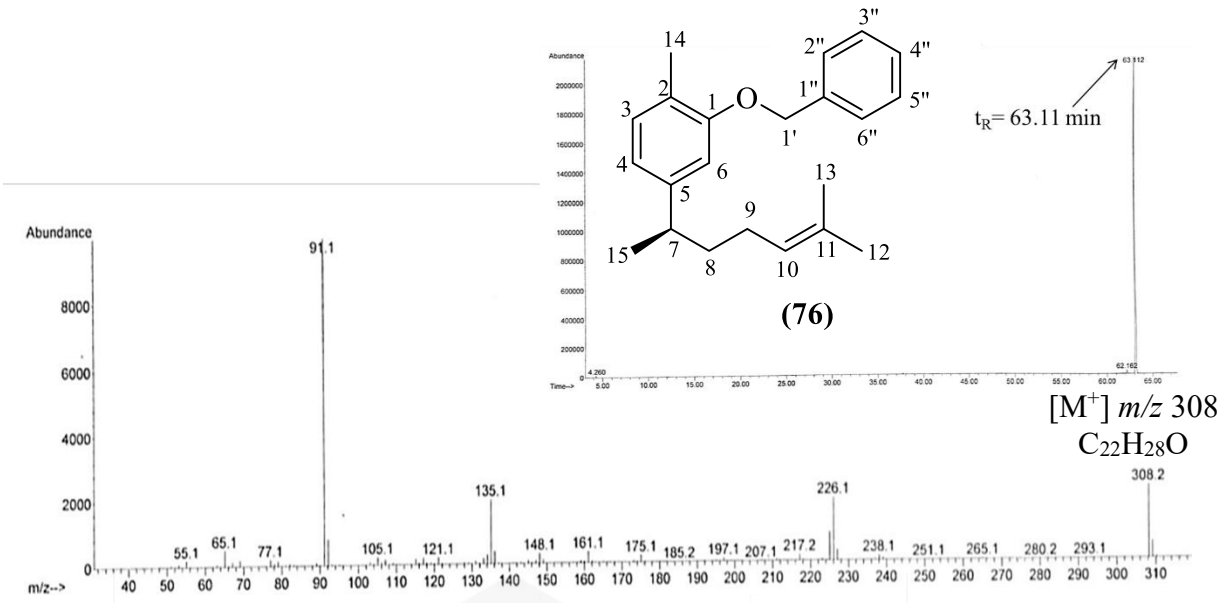

Appendix E5: GC-MS spectrum of benzyl xanthorrhizyl ether **(76)**

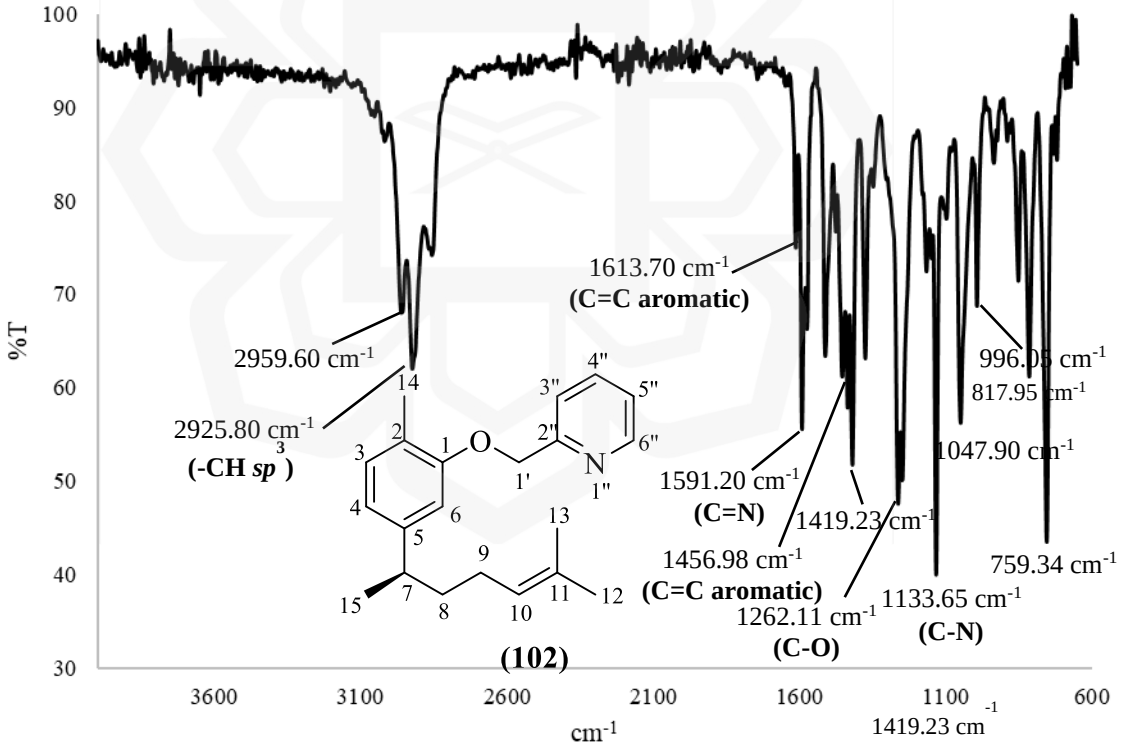

Appendix F1: ATR-IR spectrum of (2-pyridinyl)methyl xanthorrhizyl ether **(102)**

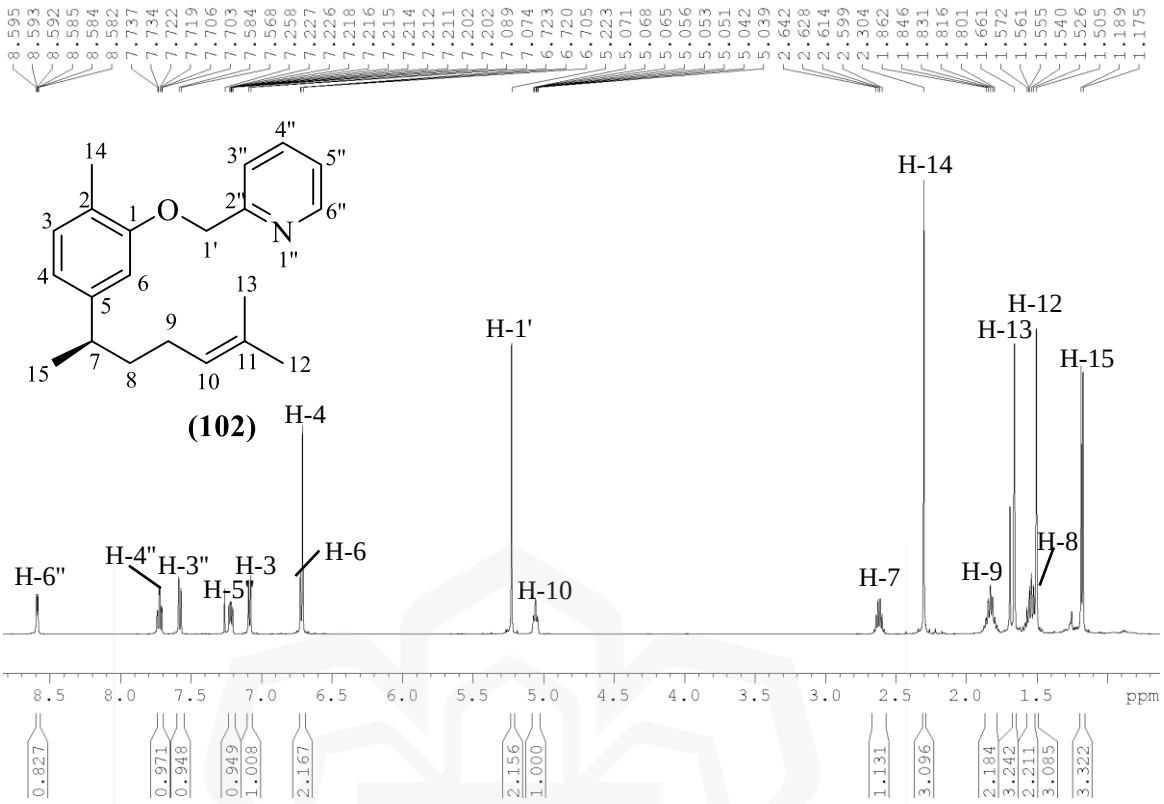

Appendix F2: ^{1}H NMR spectrum of (2-pyridinyl)methyl xanthorrhizyl ether **(102)**

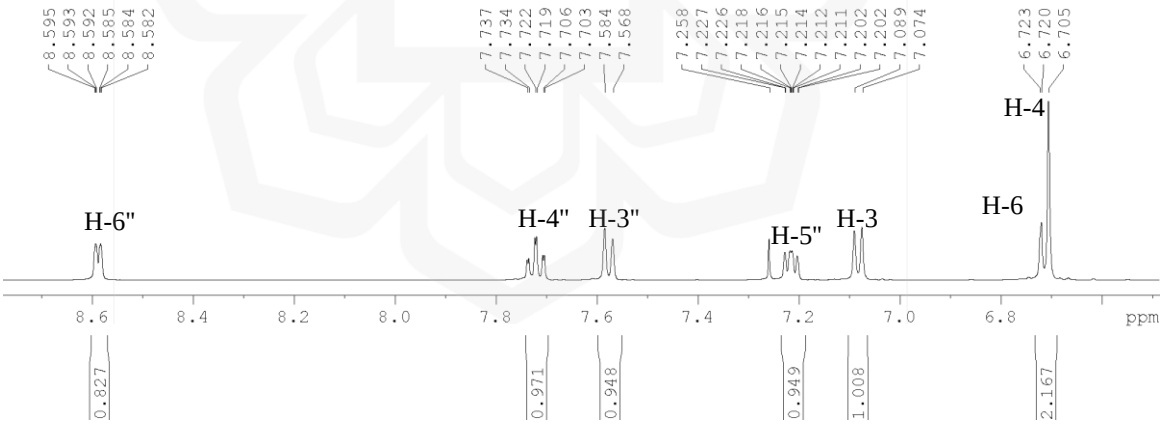

Appendix F3: ^{1}H NMR spectrum of (2-pyridinyl)methyl xanthorrhizyl ether **(102)** **(**expansion)

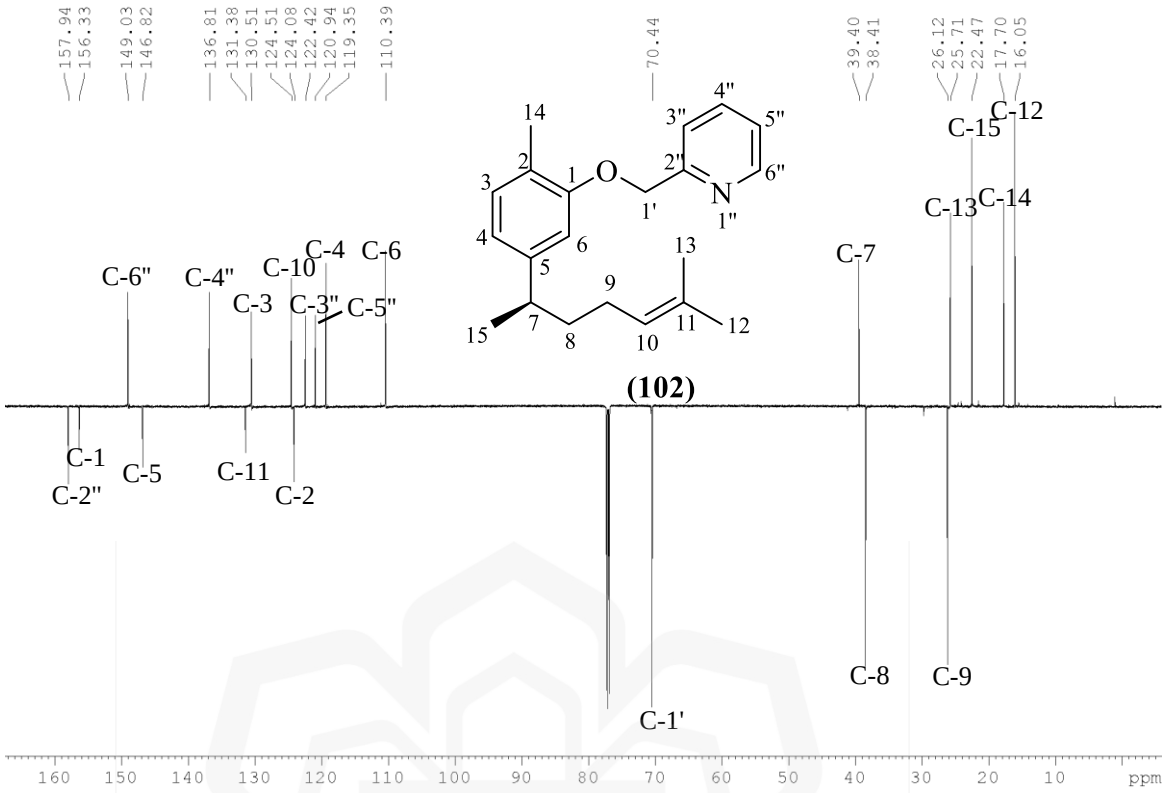

Appendix F4: DEPTQ spectrum of (2-pyridinyl)methyl xanthorrhizyl ether **(102)**

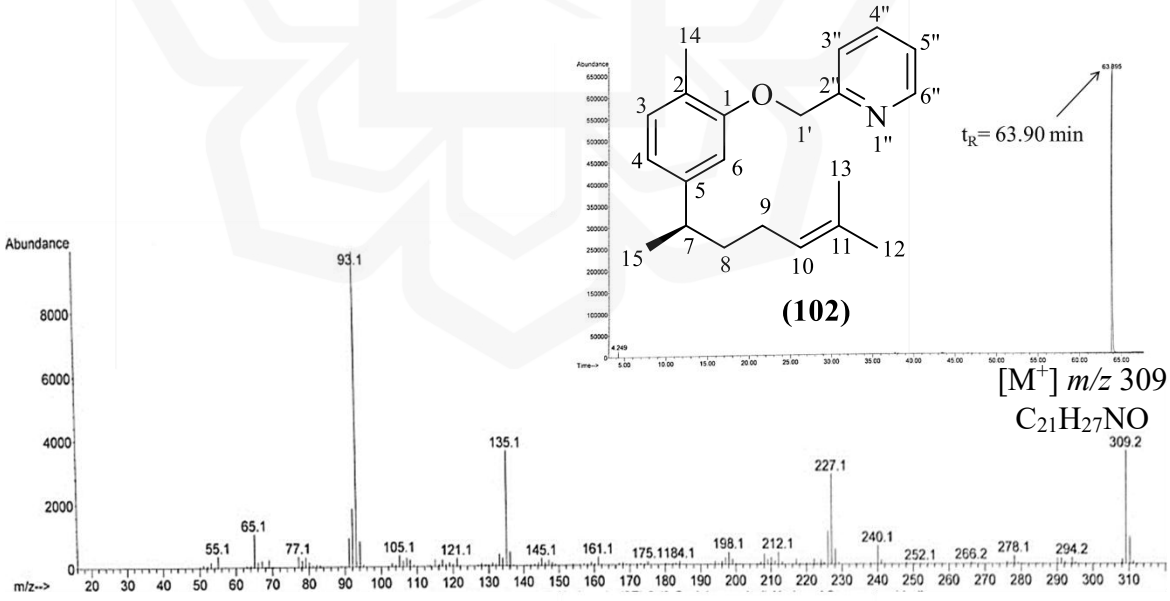

Appendix F5: GC-MS spectrum of (2-pyridinyl)methyl xanthorrhizyl ether **(102)**

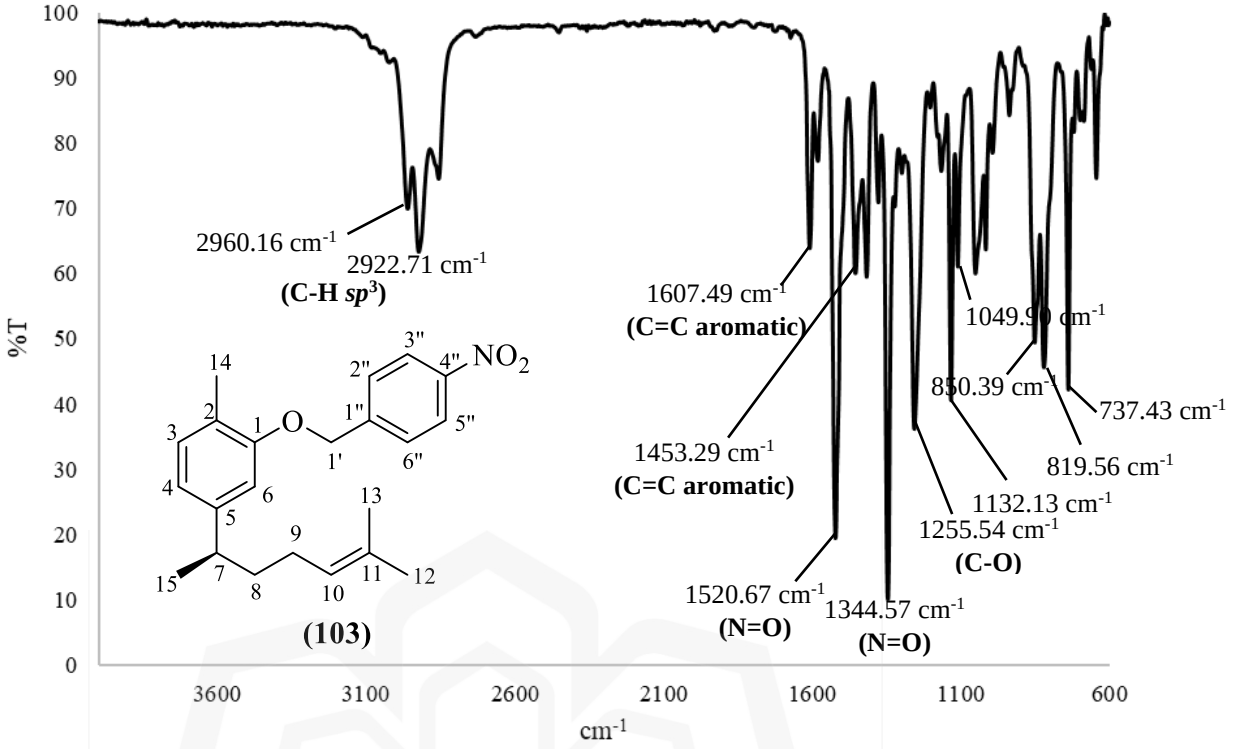

Appendix G1: ATR-IR spectrum of 4-nitrobenzyl xanthorrhizyl ether **(103)**

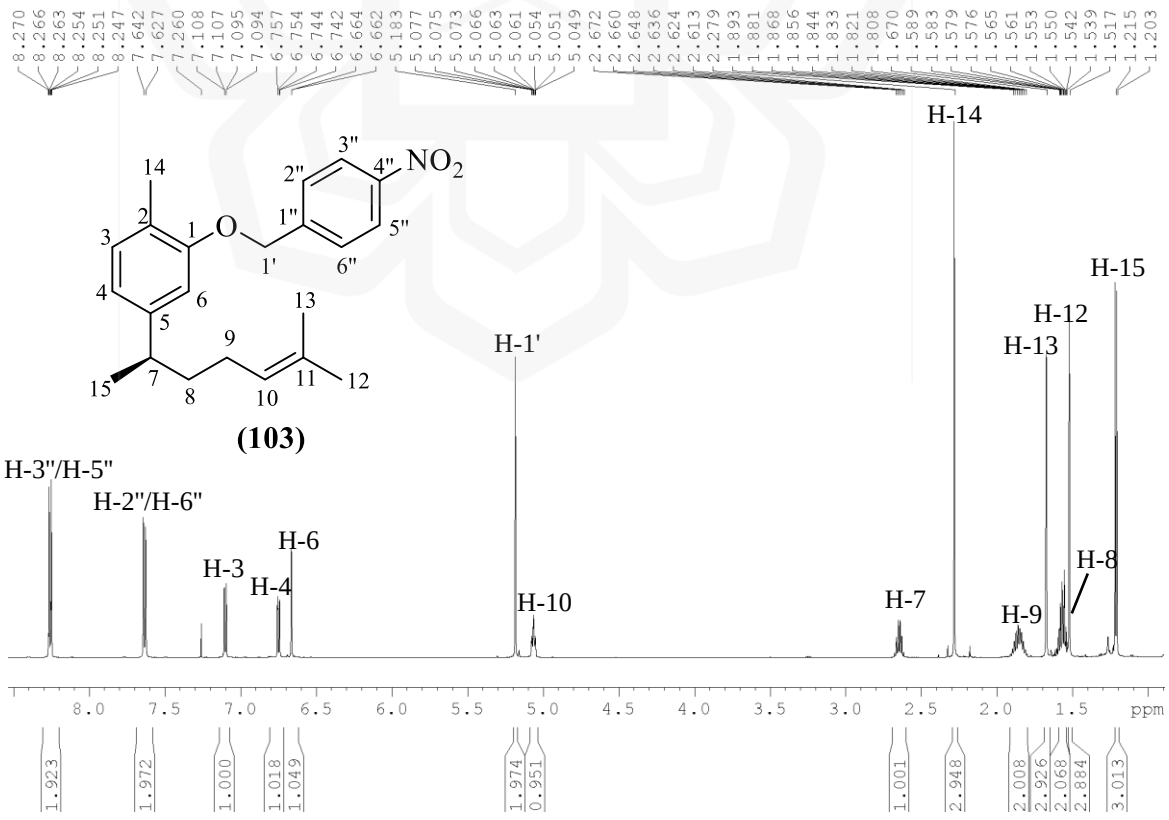

Appendix G2: ^{1}H NMR spectrum of 4-nitrobenzyl xanthorrhizyl ether **(103)**

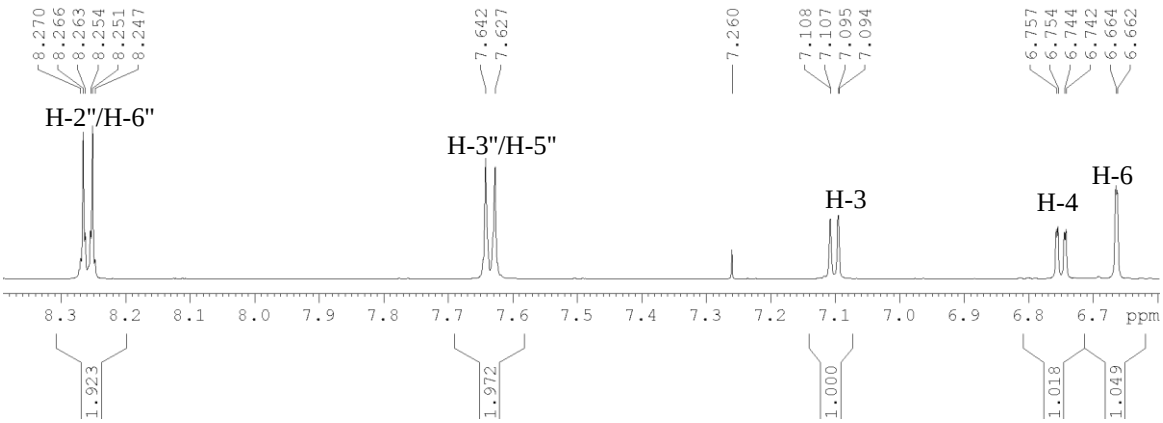

Appendix G3: ^{1}H NMR spectrum of 4-nitrobenzyl xanthorrhizyl ether **(103)** (expansion)

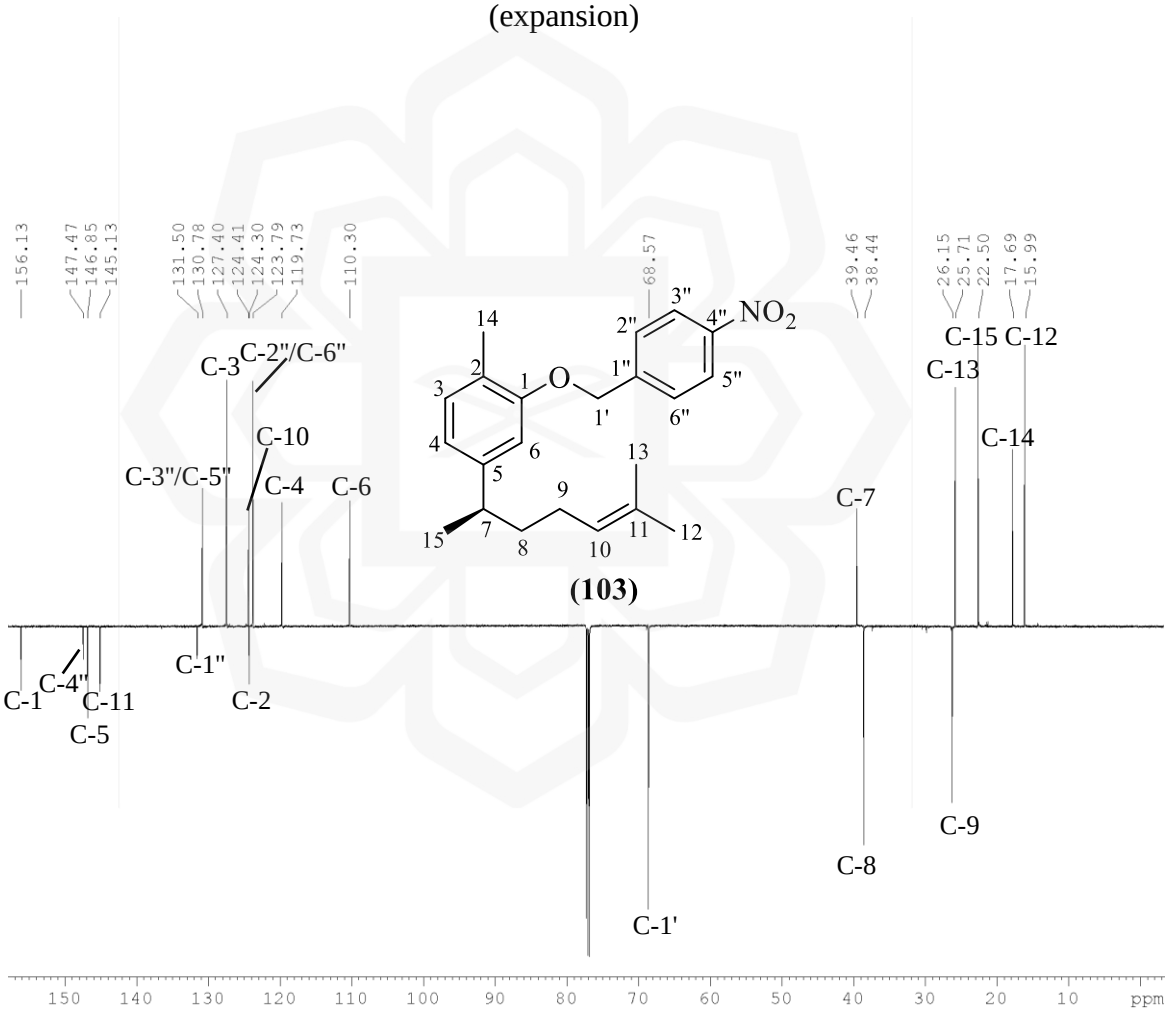

Appendix G4: DEPTQ spectrum of 4-nitrobenzyl xanthorrhizyl ether **(103)**

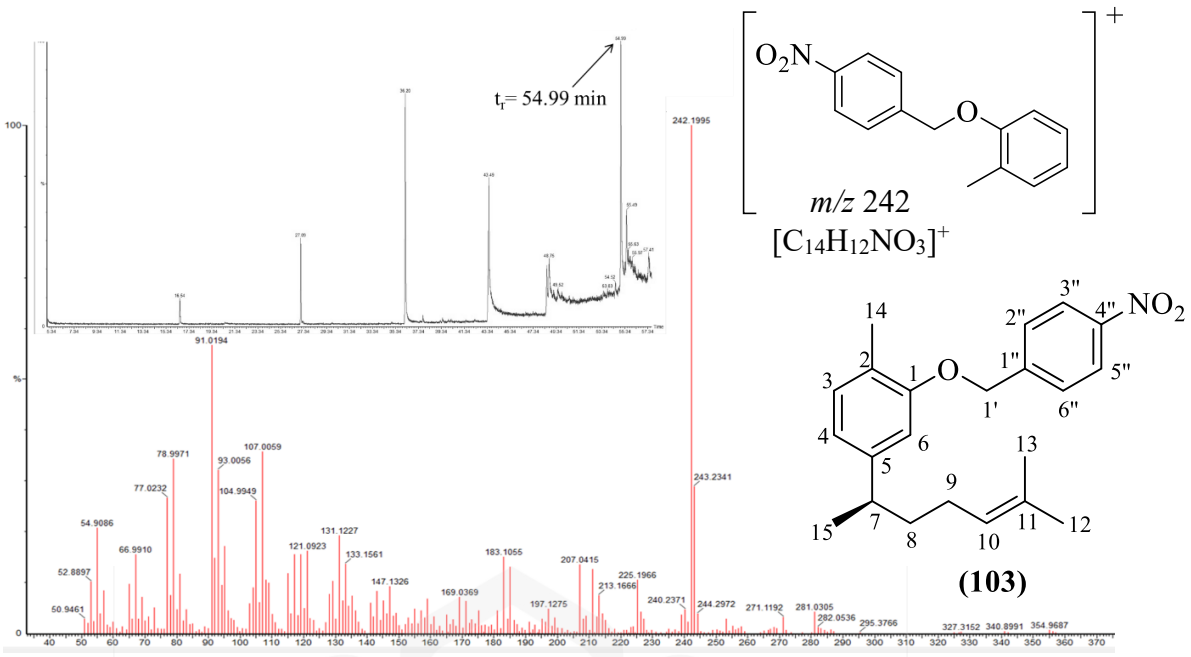

Appendix G5: GC-MS spectrum of 4-nitrobenzyl xanthorrhizyl ether **(103)**

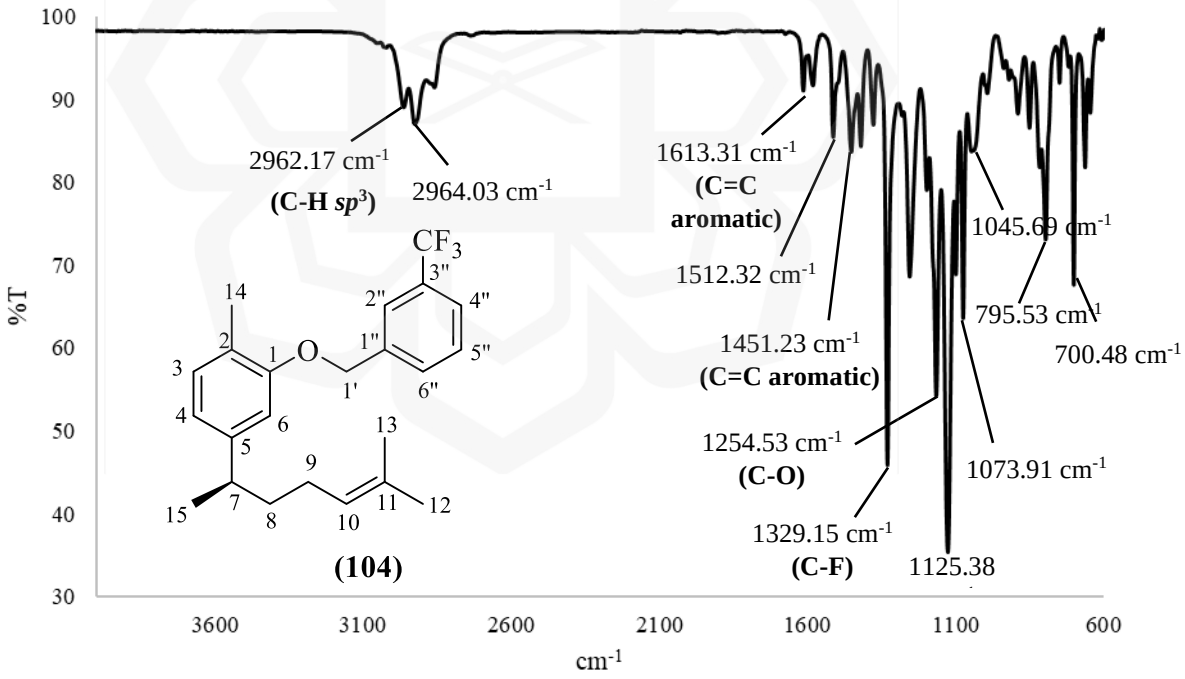

Appendix H1: ATR-IR spectrum of 3-trifluoromethylbenzyl xanthorrhizyl ether **(104)**

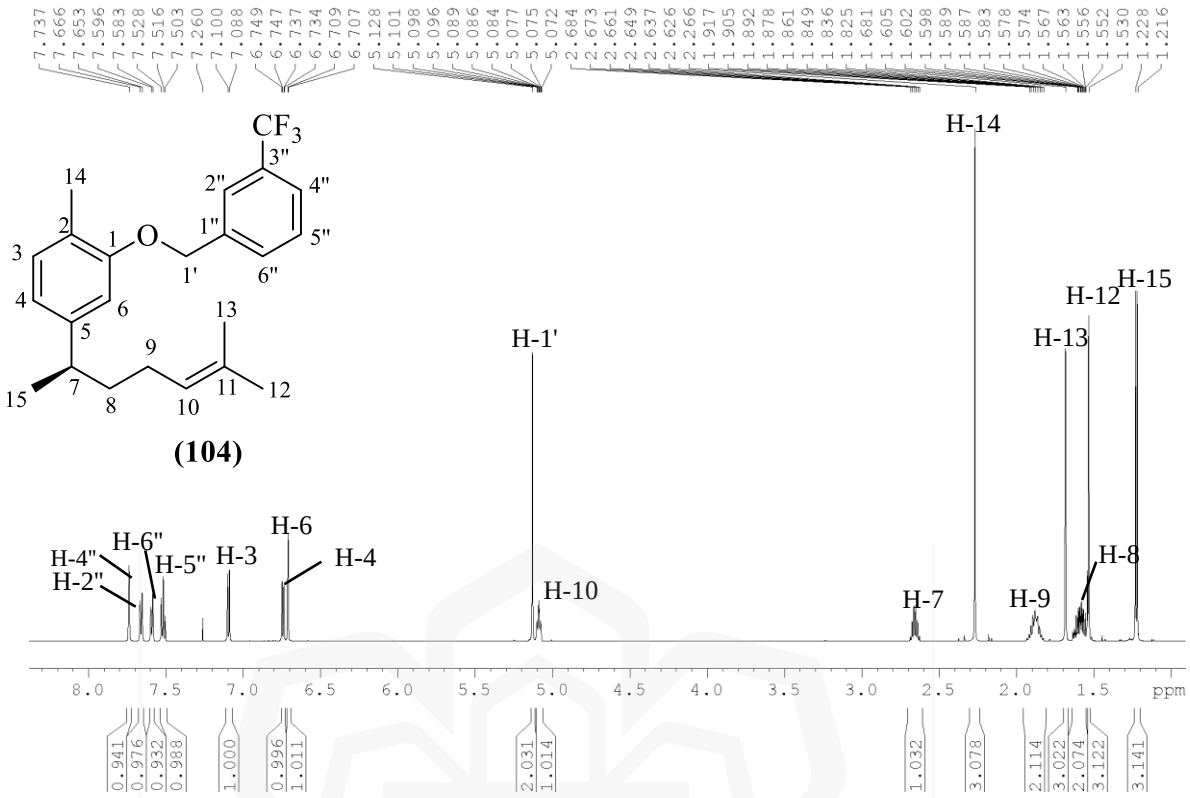

Appendix H2: ^{1}H NMR spectrum of 3-trifluoromethylbenzyl xanthorrhizyl ether **(104)**

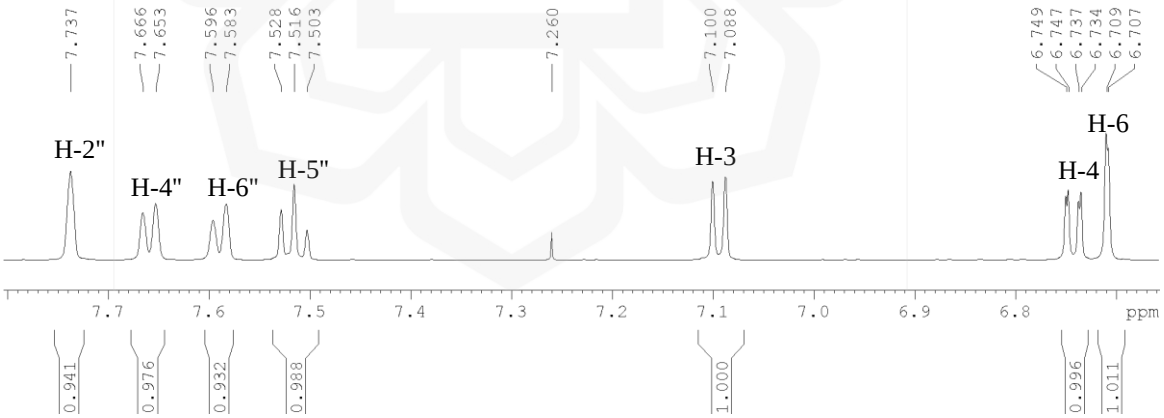

Appendix H3: ^{1}H NMR spectrum of 3-trifluoromethylbenzyl xanthorrhizyl ether (expansion) **(104)**

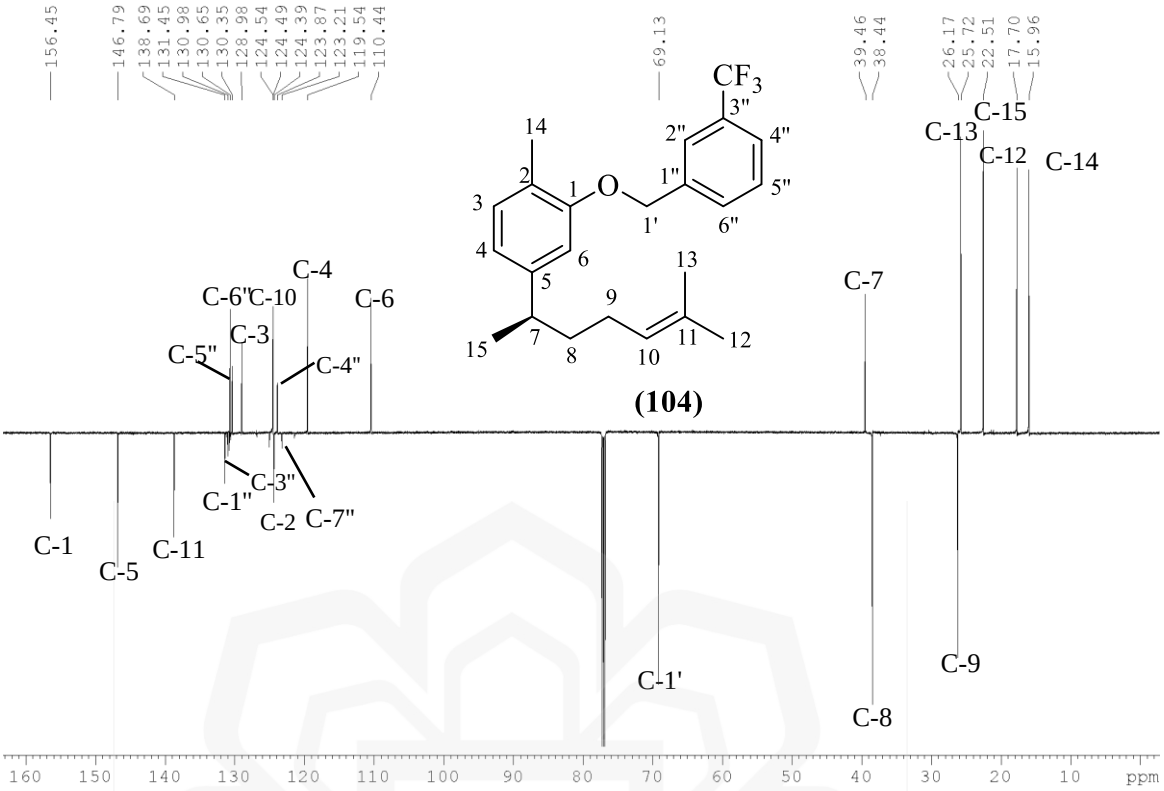

Appendix H4: DEPTQ spectrum of 3-trifluoromethylbenzyl xanthorrhizyl ether **(104)**

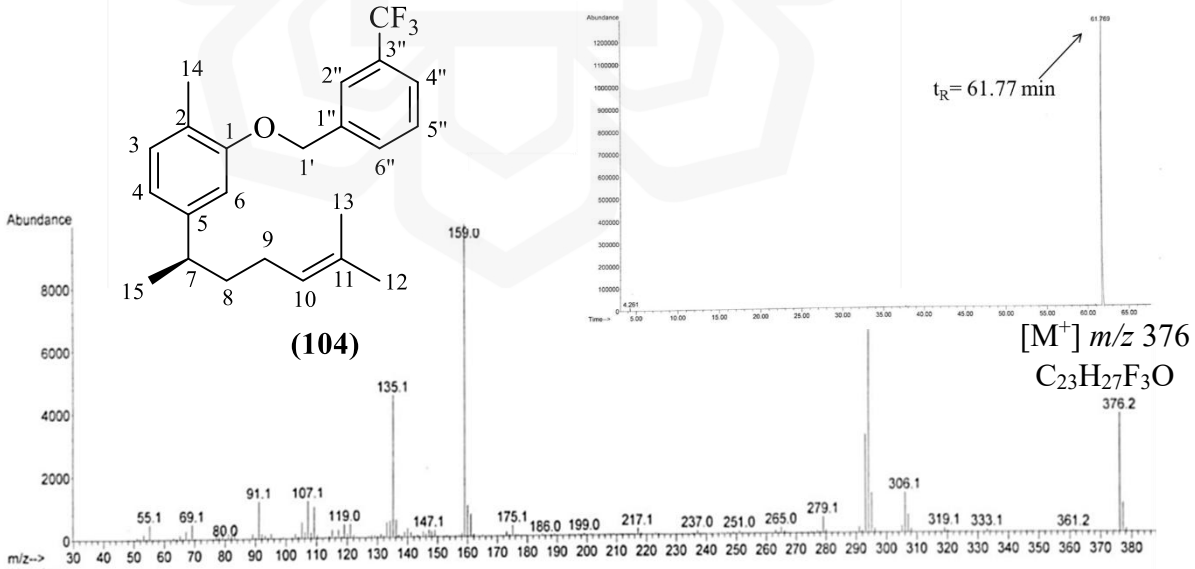

Appendix H5: GC-MS spectrum of 3-trifluoromethylbenzyl xanthorrhizyl ether **(104)**

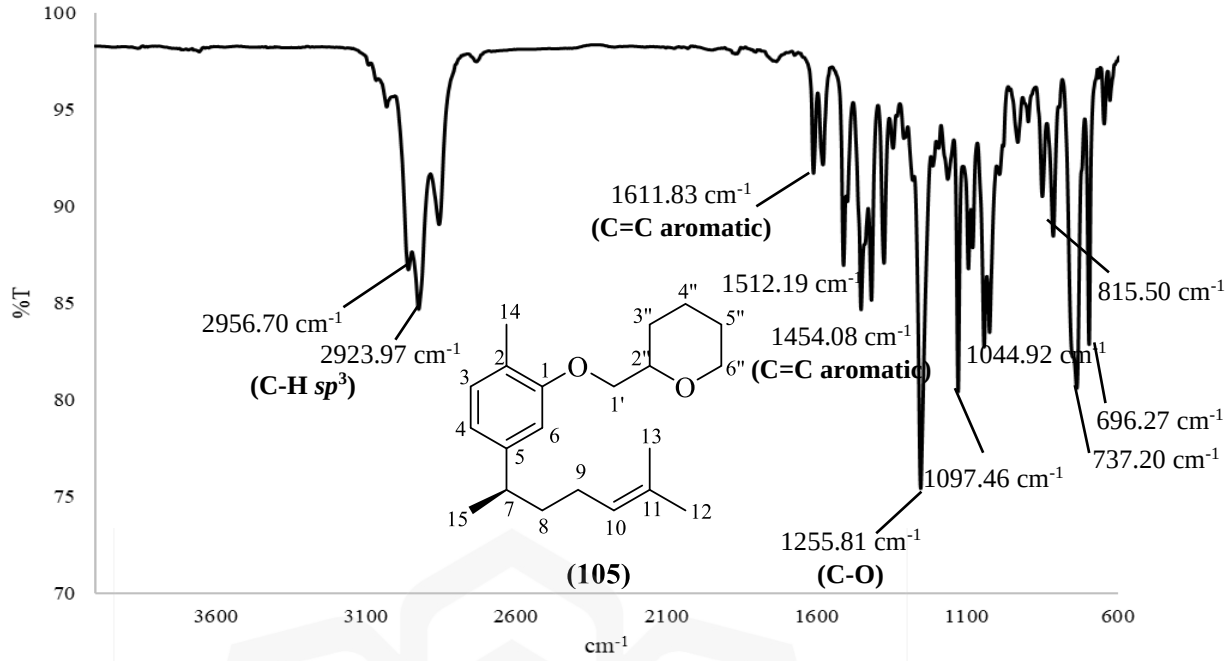

Appendix I1: ATR-IR spectrum of (2-tetrahydro-2*H*-pyranyl)methyl xanthorrhizyl ether **(105)**

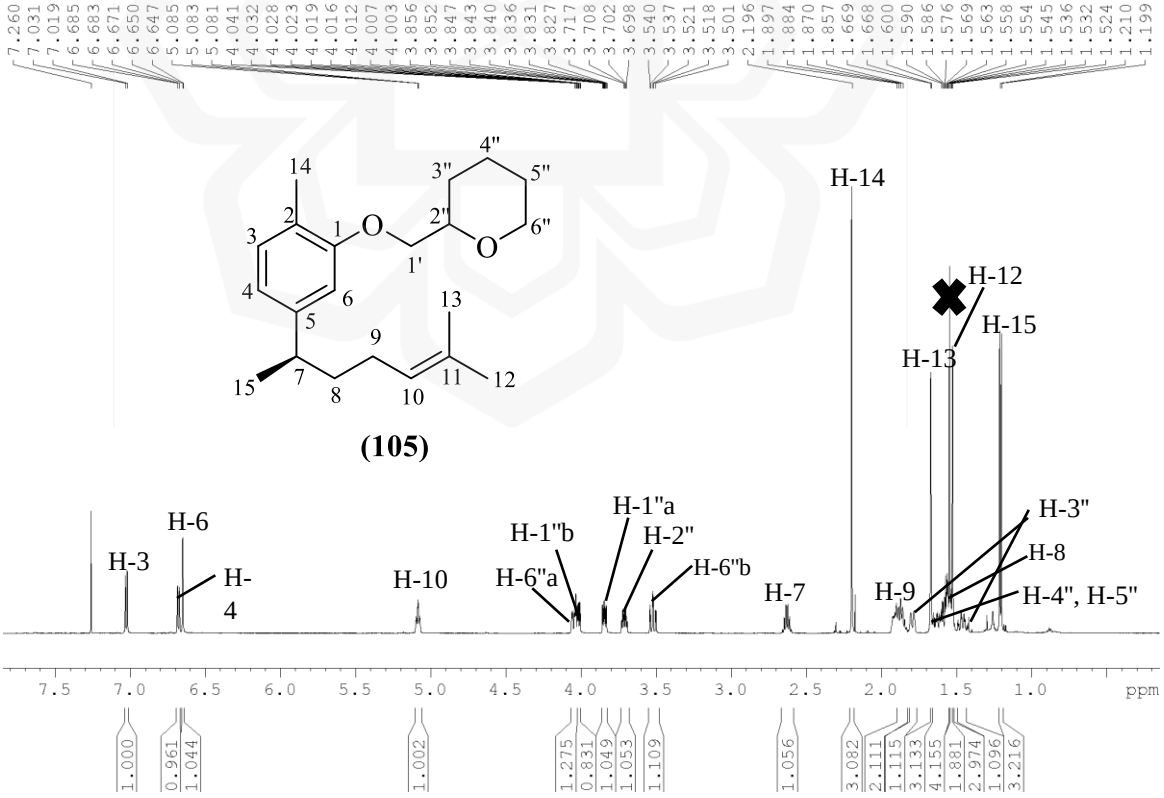

Appendix I2: [1]H NMR spectrum of (2-tetrahydro-2*H*-pyranyl)methyl xanthorrhizyl ether **(105)**

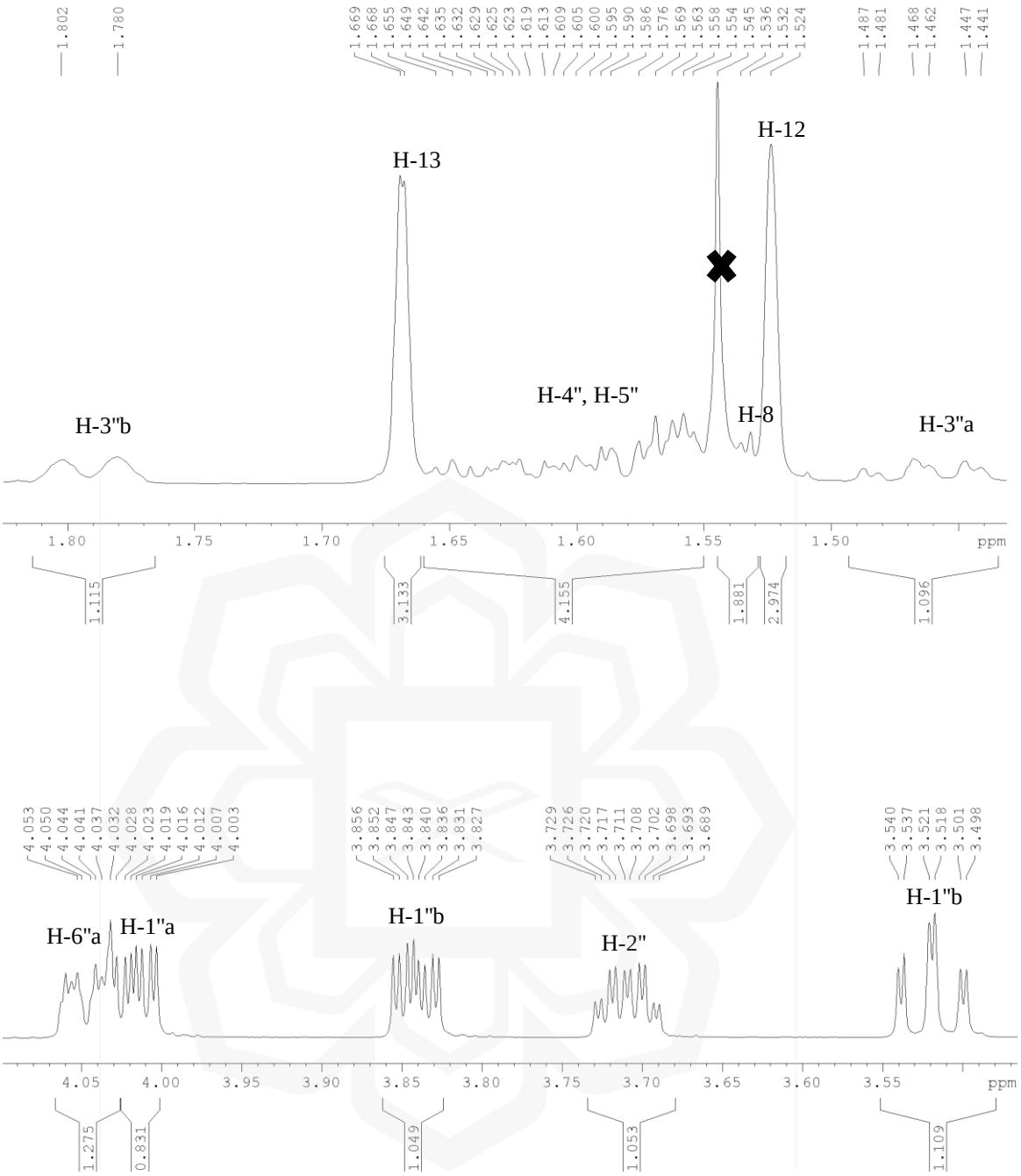

Appendix I3: ^{1}H NMR spectrum of (2-tetrahydro-2*H*-pyranyl)methyl xanthorrhizyl ether **(105)** (expansion)

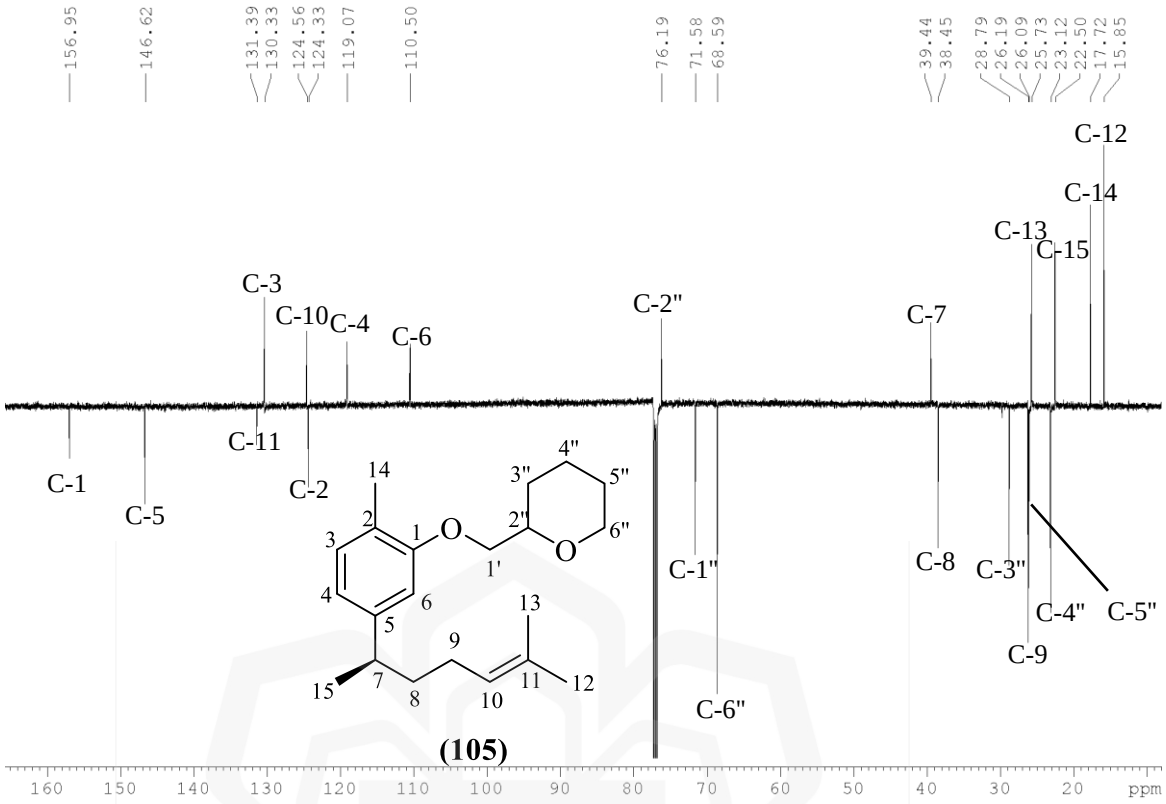

Appendix I4: DEPTQ spectrum of (2-tetrahydro-2*H*-pyranyl)methyl xanthorrhizyl ether **(105)**

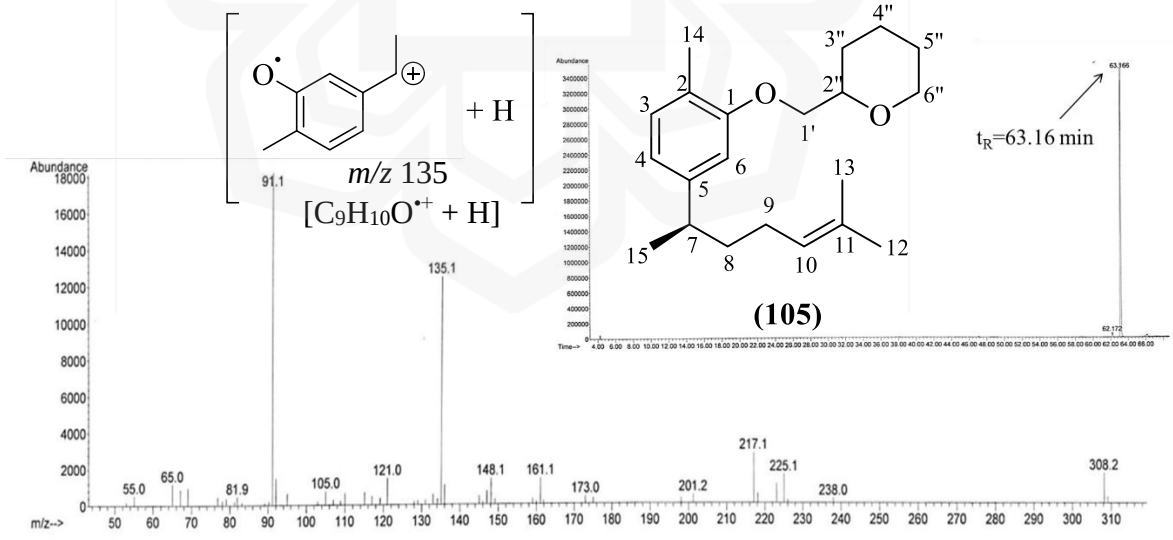

Appendix I5: GC-MS spectrum of (2-tetrahydro-2*H*-pyranyl)methyl xanthorrhizyl ether **(105)**

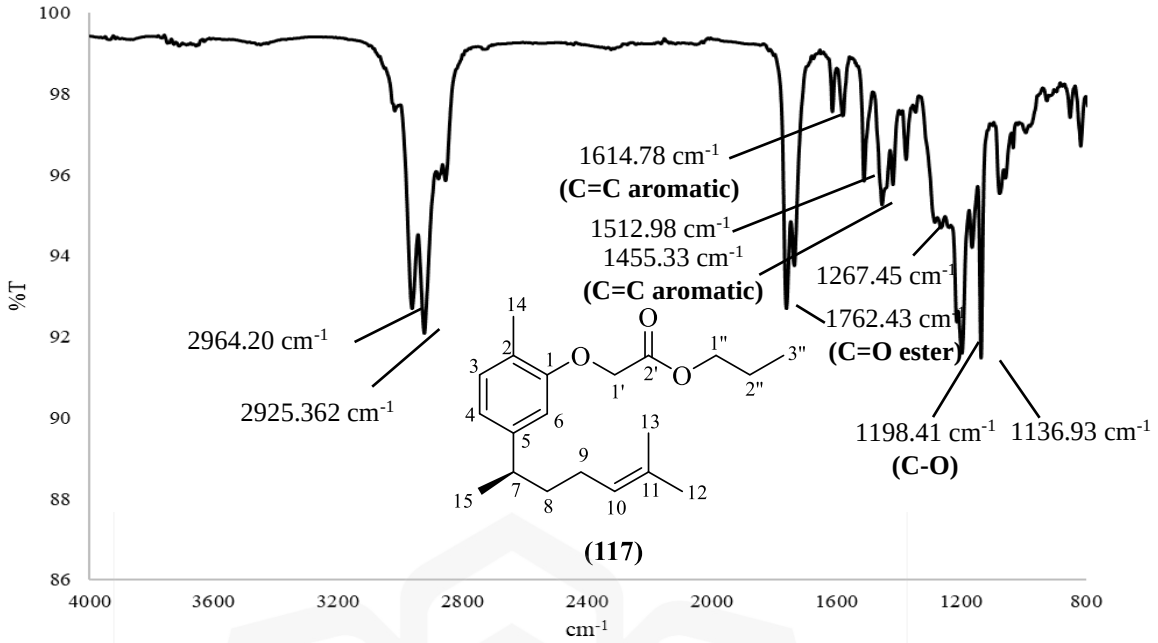

Appendix J1: ATR-IR spectrum of propyl xanthorrhizyloxyacetate **(117)**

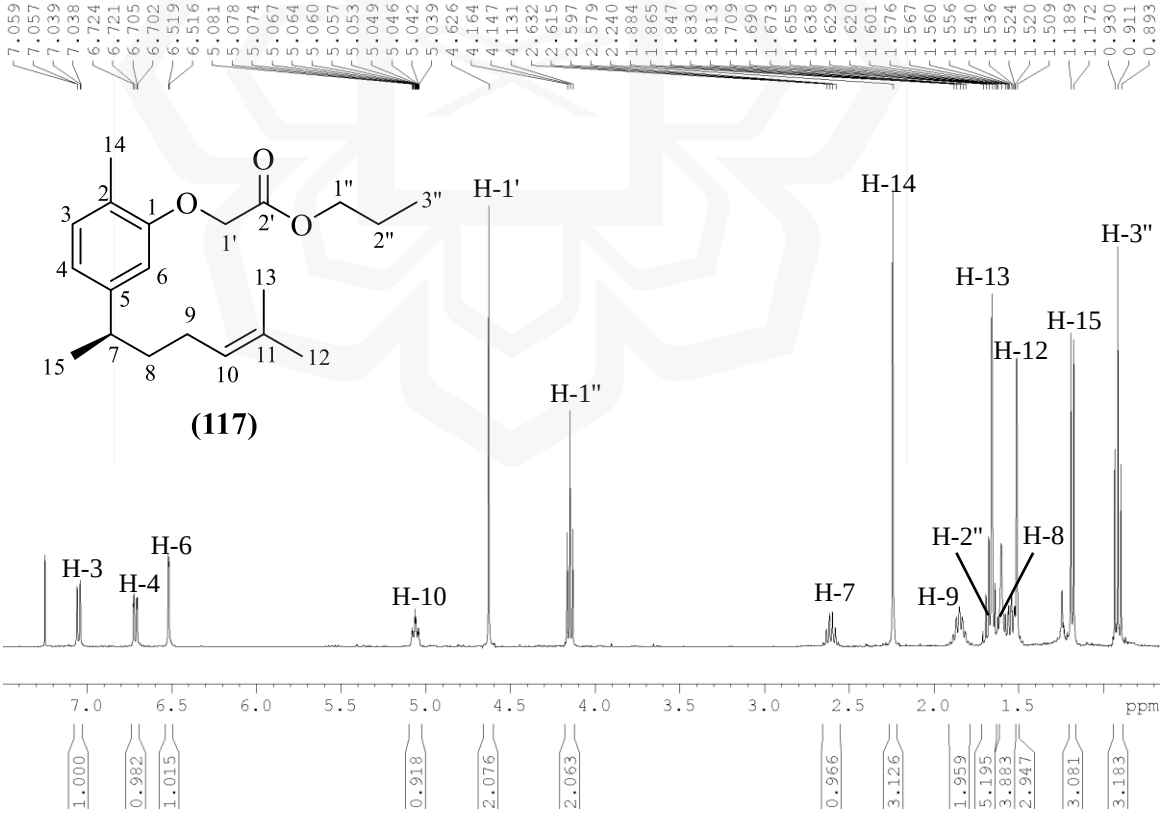

Appendix J2: ^{1}H NMR spectrum of propyl xanthorrhizyloxyacetate **(117)**

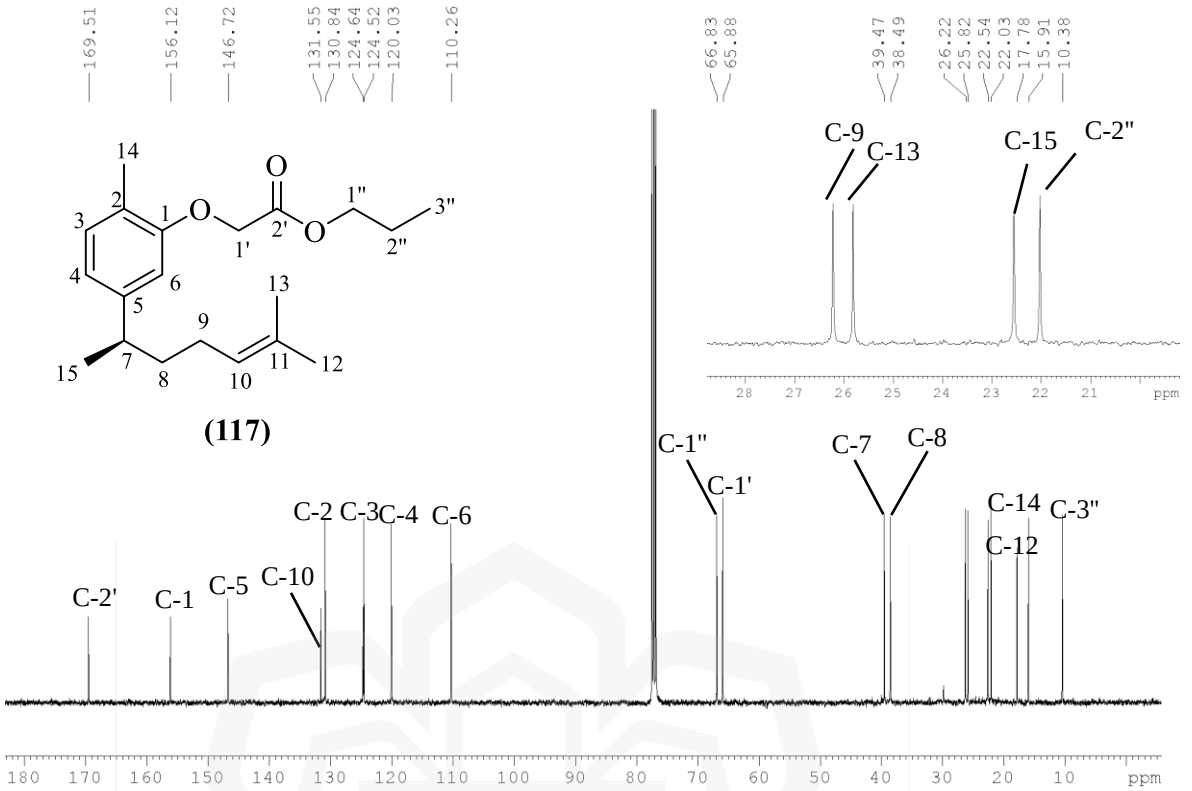

Appendix J3: ^{13}C NMR spectrum of propyl-2-xanthorrhizyloxyacetate **(117)**

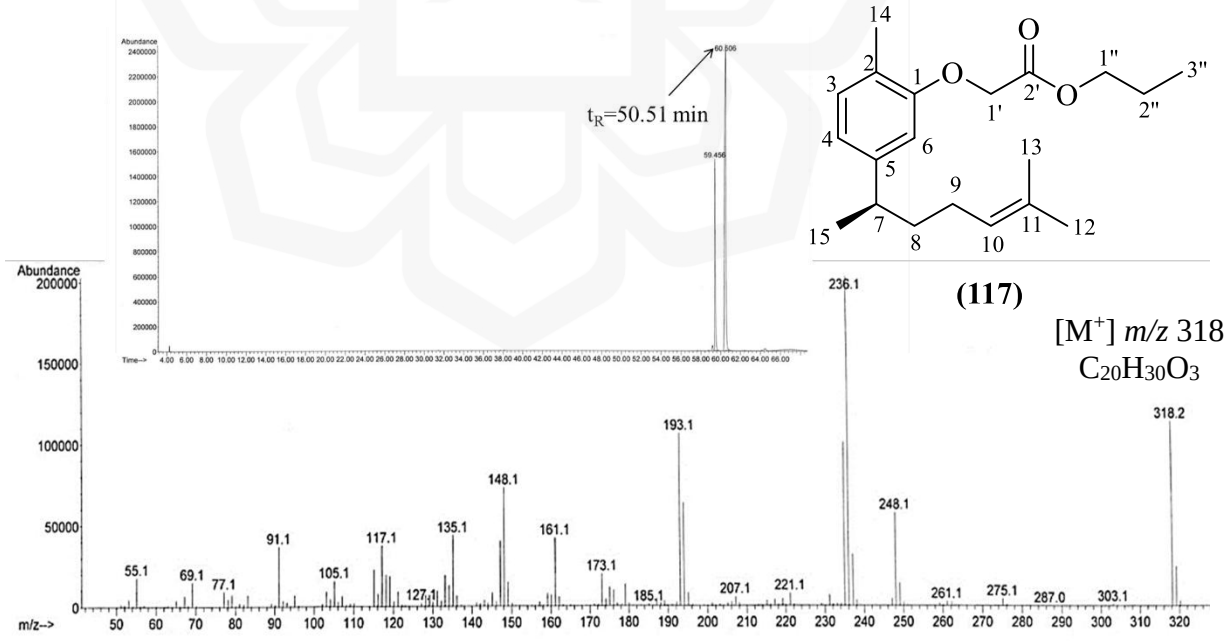

Appendix J4: GC-MS spectrum of propyl xanthorrhizyloxyacetate **(117)**

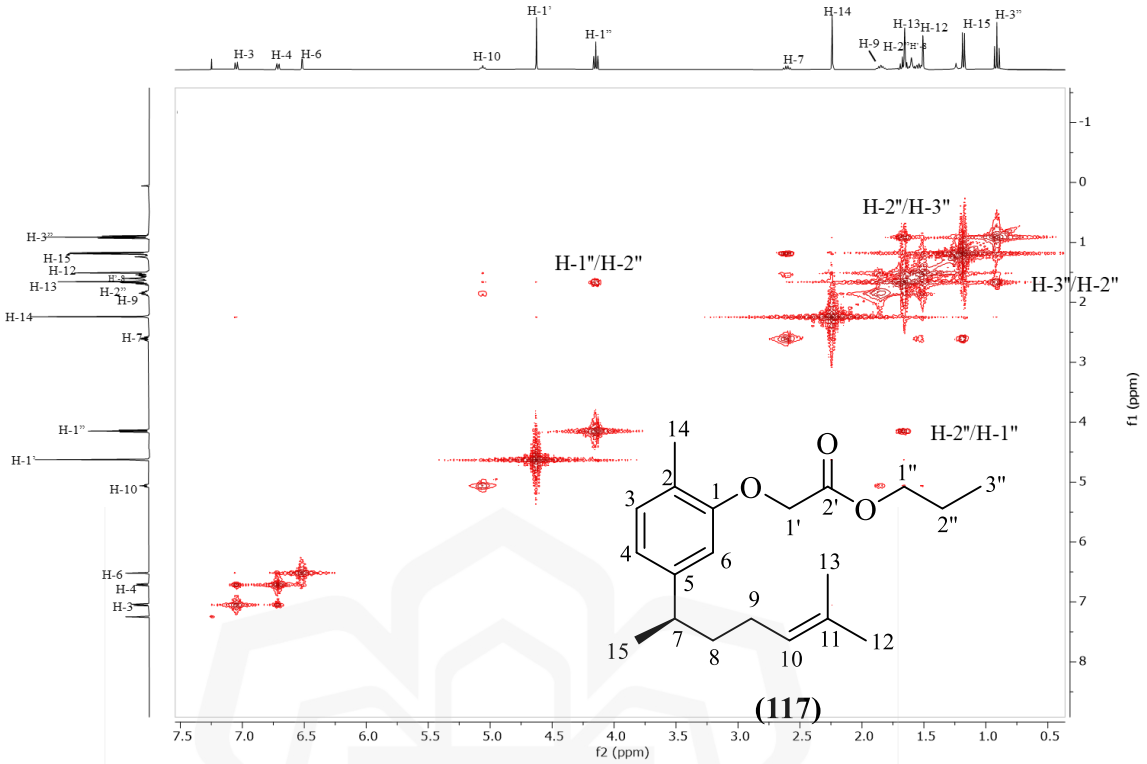

Appendix J5: COSY spectrum of propyl xanthorrhizyloxyacetate **(117)**

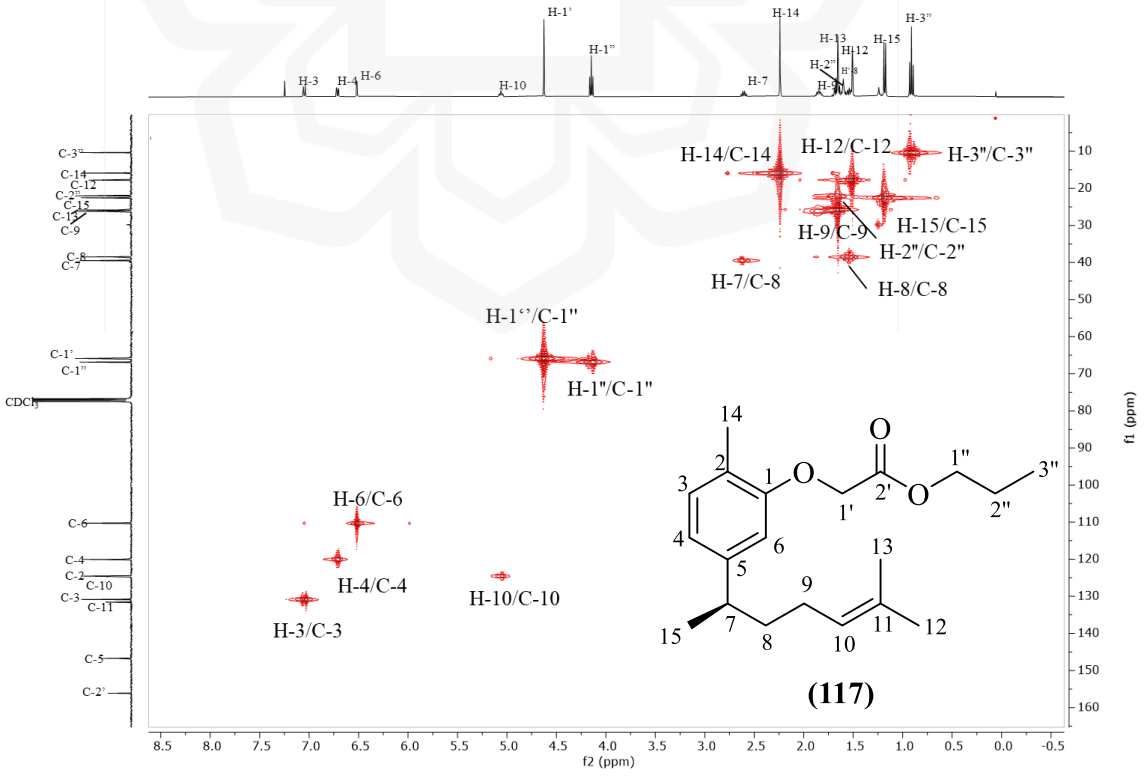

Appendix J6: HMQC spectrum of propyl xanthorrhizyloxyacetate **(117)**

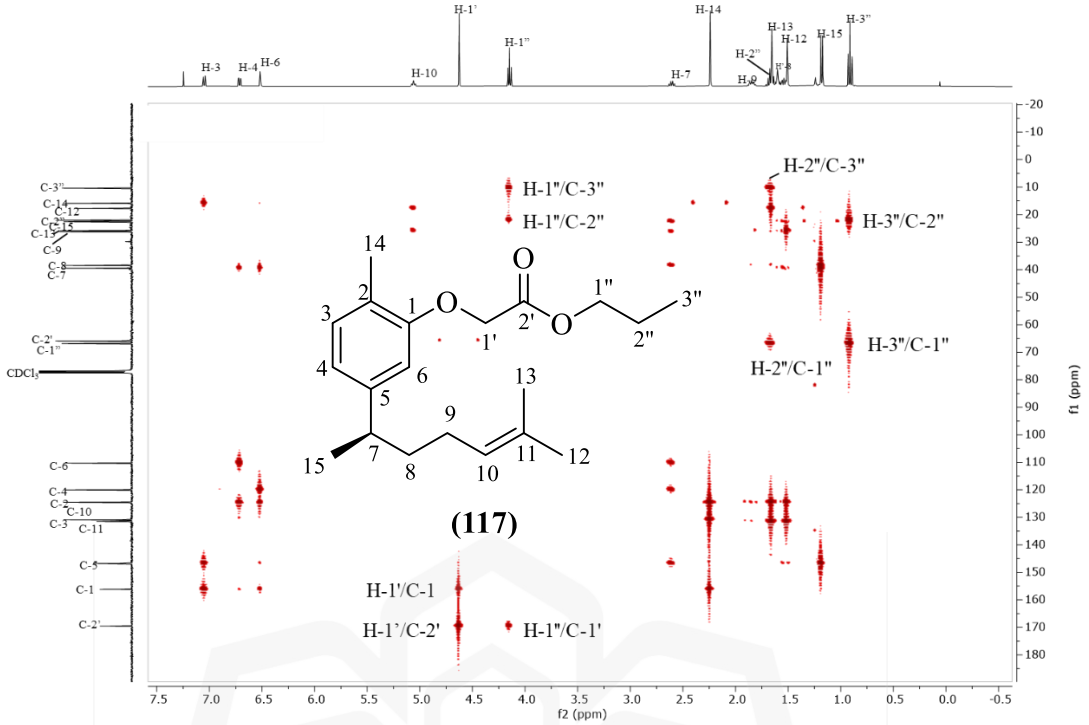

Appendix J7: HMBC spectrum of propyl-2-xanthorrhizyloxyacetate **(117)**

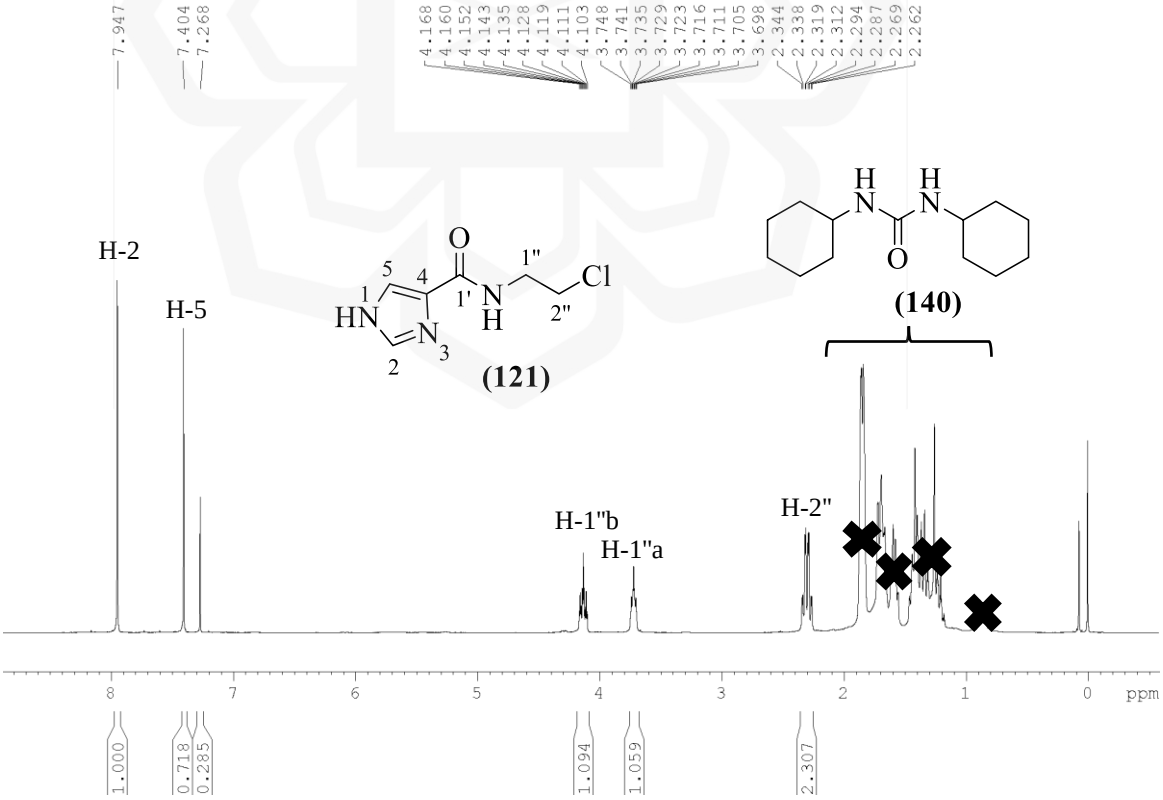

Appendix K1: ^{1}H NMR spectrum of *N*-(2-chloroethyl)-1*H*-imidazole-4-carboxamide **(121)**

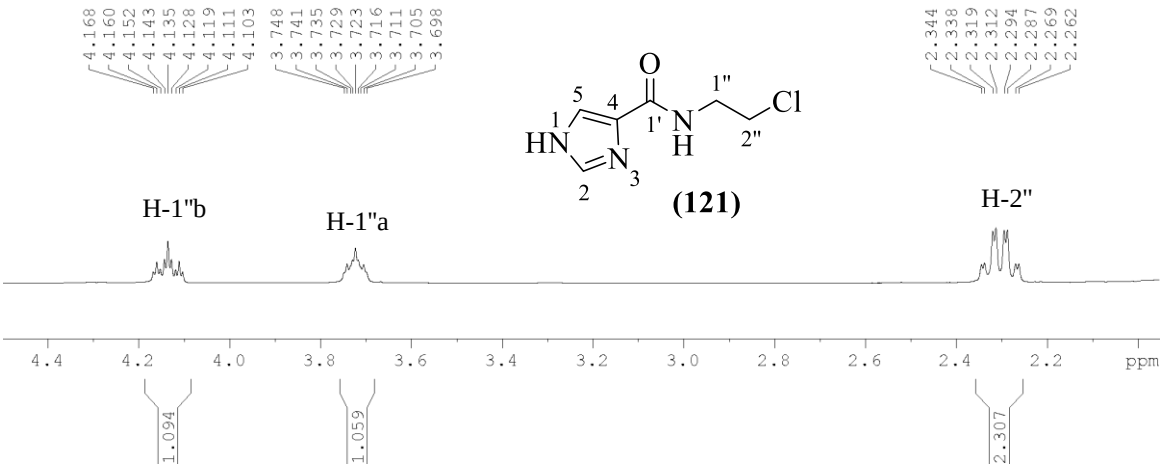

Appendix K2: ^{1}H NMR spectrum of *N*-(2-chloroethyl)-1*H*-imidazole-4-carboxamide **(121)** (expansion)

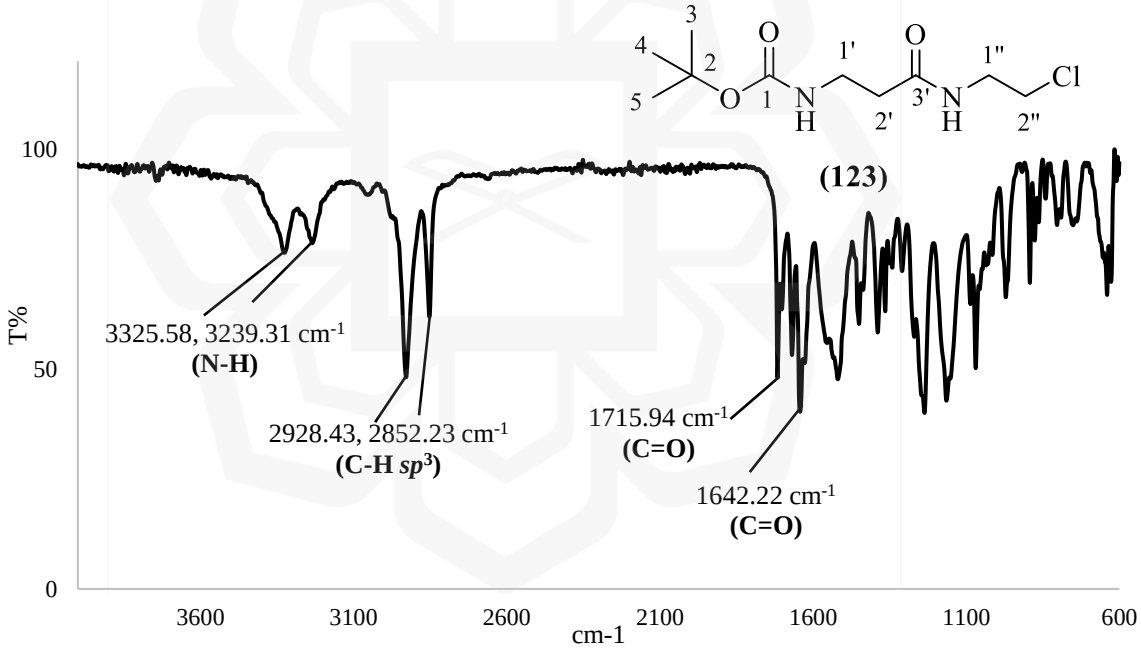

Appendix L1: ATR-IR spectrum of *tert*-butyl(3-((2-chloroethyl)amino)-3-oxopropyl)carbamate **(123)**

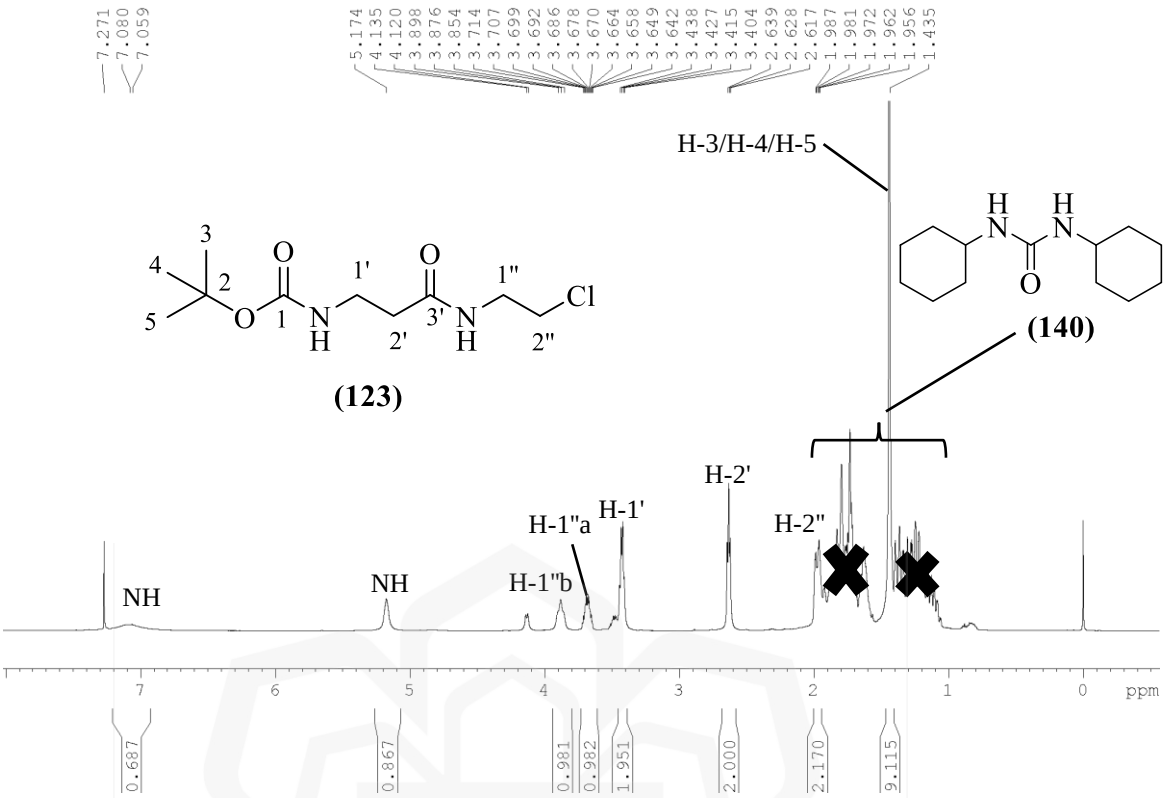

Appendix L2: ^{1}H NMR spectrum of *tert*-butyl (3-((2-chloroethyl)amino)-3-oxopropyl)carbamate **(123)**

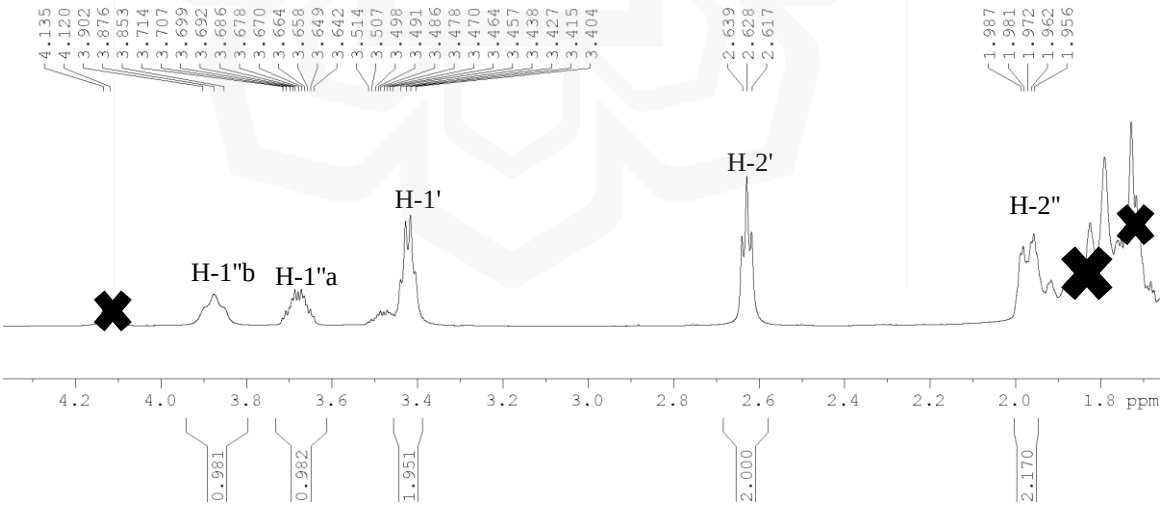

Appendix L3: ^{1}H NMR spectrum of *tert*-butyl (3-((2-chloroethyl)amino)-3-oxopropyl)carbamate **(123)** (expansion)

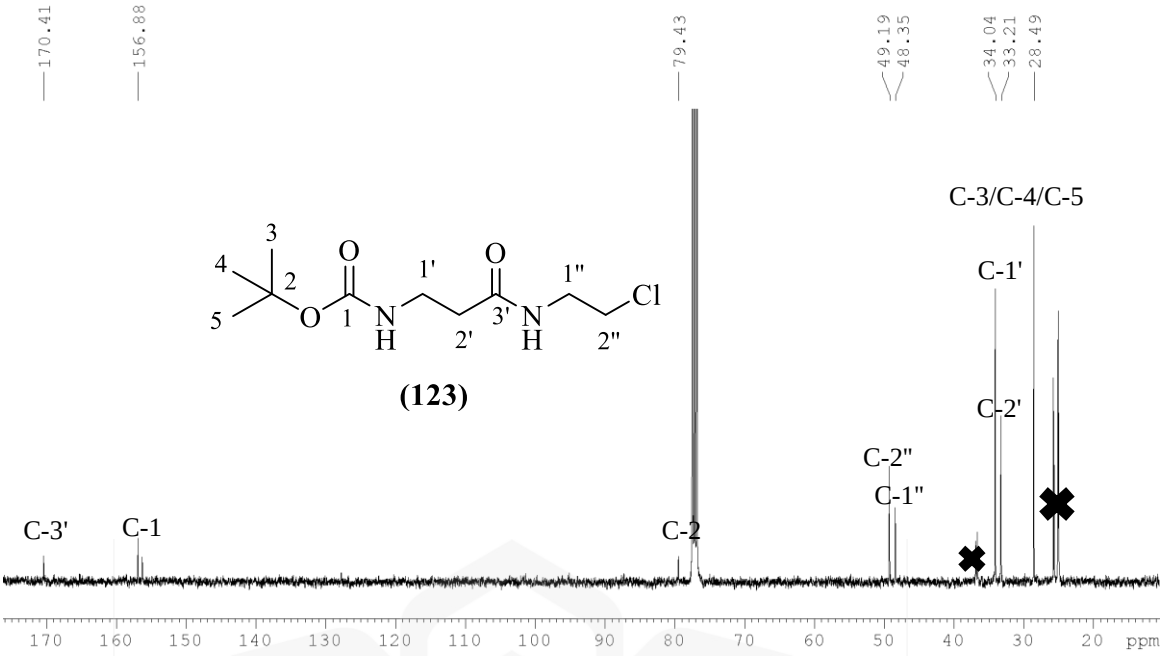

Appendix L4: ^{13}C NMR spectrum of *tert*-butyl (3-((2-chloroethyl)amino)-3-oxopropyl)carbamate **(123)**

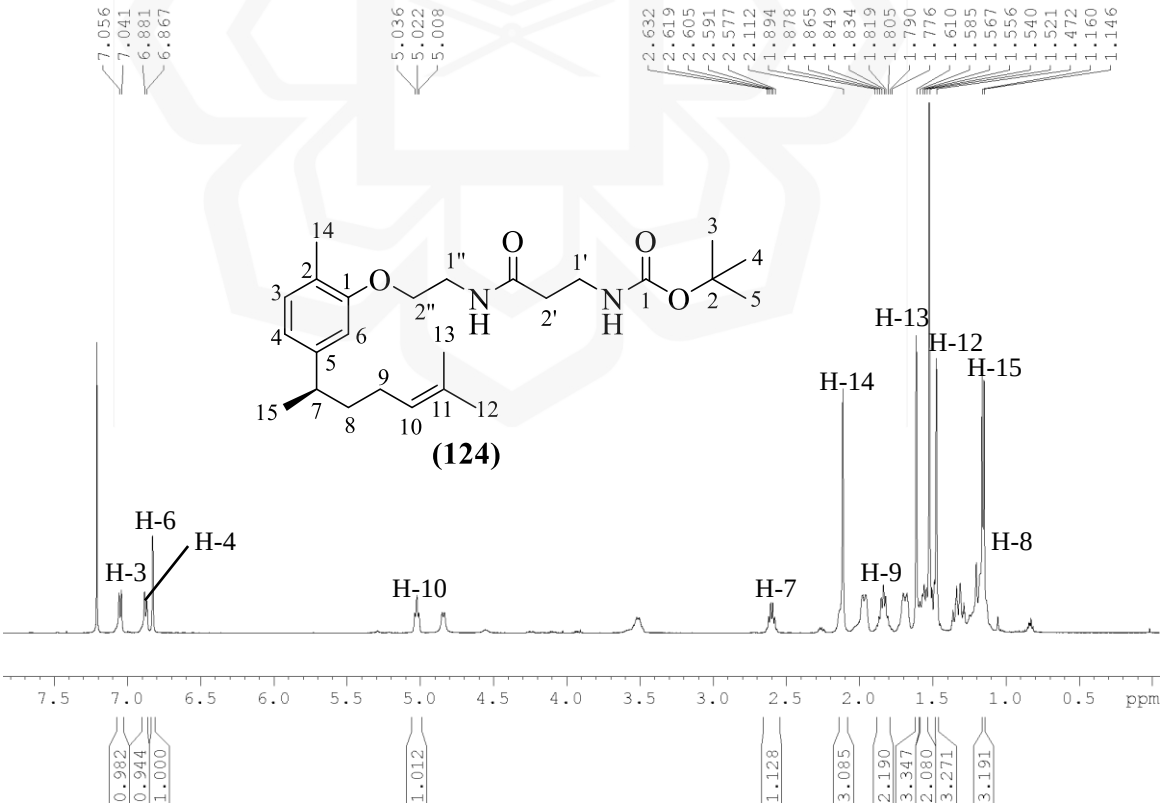

Appendix M: ^{1}H NMR spectrum for attempted synthesis of *tert*-butyl (3-oxo-3-((2-xanthorrhizyloxyethyl)amino)propyl)carbamate **(124)**

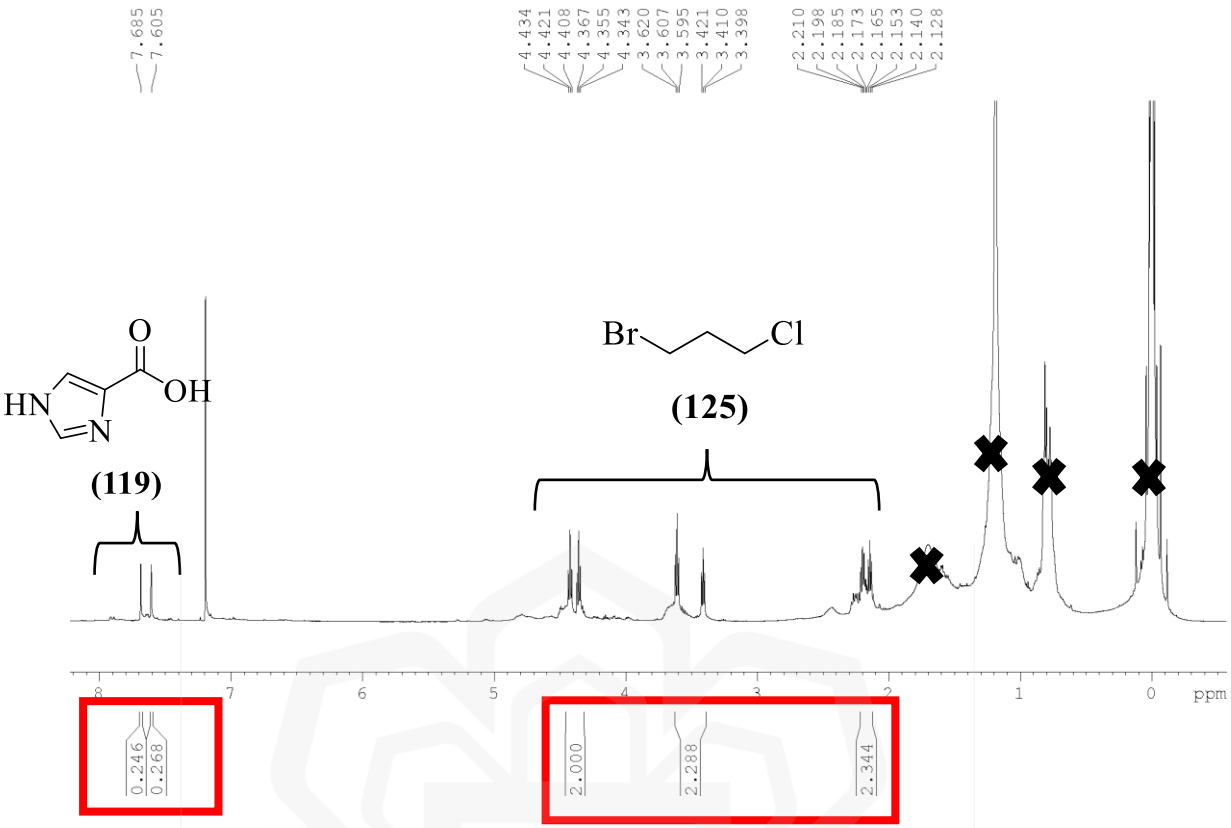

Appendix N: ^{1}H NMR spectrum of attempted synthesis of 3-chloropropyl-1*H*-imidazole-4-carboxylate **(126)**

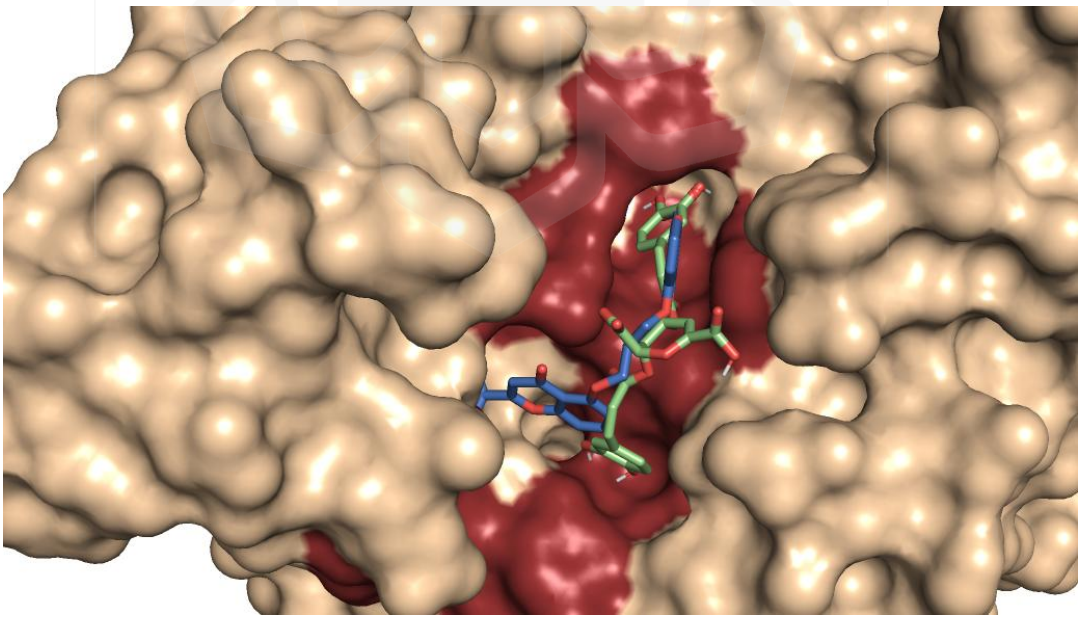

Appendix O1: Docking conformation of seric acid A **(26)** and disodium chromoglycate **(27)** in Hyal-1 binding site. The active site residues are coloured in maroon.

Appendix O2: Docking results of seric acid A **(26)** and disodium chromoglycate **(27)** against Hyal-1 enzyme

Compounds	Binding energies (kcal/mol)	Interacting amino acid residues
Seric acid A (26)	-8.8 ± 0.51	Tyr75, **Asp129**, **Glu131**, Trp141, **Tyr202***, Asp206*, Tyr210*, **Ser245***, **Tyr247***, Arg265*, Trp321
Disodium cromoglycate (27)	-8.3 ± 0.10	Tyr75*, **Asp129**, **Glu131**, Arg134, **Tyr202***, Phe204, **Tyr247***, Tyr286*, Trp321

Notes. The essential interacting amino acid residues were shown in **bold**. The hydrogen bonding interactions were marked with (*).